



NATO Security through Science Series - B:
Physics and Biophysics

Nuclear Science and Safety in Europe

Edited by
Tomas Čechák
László Jenkovszky
Iurii Karpenko

 Springer



*This publication
is supported by:*

The **NATO** Programme
for **Security through Science**

Nuclear Science and Safety in Europe

NATO Security through Science Series

This Series presents the results of scientific meetings supported under the NATO Programme for Security through Science (STS).

Meetings supported by the NATO STS Programme are in security-related priority areas of Defence Against Terrorism or Countering Other Threats to Security. The types of meeting supported are generally "Advanced Study Institutes" and "Advanced Research Workshops". The NATO STS Series collects together the results of these meetings. The meetings are co-organized by scientists from NATO countries and scientists from NATO's "Partner" or "Mediterranean Dialogue" countries. The observations and recommendations made at the meetings, as well as the contents of the volumes in the Series, reflect those of participants and contributors only; they should not necessarily be regarded as reflecting NATO views or policy.

Advanced Study Institutes (ASI) are high-level tutorial courses to convey the latest developments in a subject to an advanced-level audience

Advanced Research Workshops (ARW) are expert meetings where an intense but informal exchange of views at the frontiers of a subject aims at identifying directions for future action

Following a transformation of the programme in 2004 the Series has been re-named and re-organised. Recent volumes on topics not related to security, which result from meetings supported under the programme earlier, may be found in the NATO Science Series.

The Series is published by IOS Press, Amsterdam, and Springer, Dordrecht, in conjunction with the NATO Public Diplomacy Division.

Sub-Series

A. Chemistry and Biology	Springer
B. Physics and Biophysics	Springer
C. Environmental Security	Springer
D. Information and Communication Security	IOS Press
E. Human and Societal Dynamics	IOS Press

<http://www.nato.int/science>

<http://www.springer.com>

<http://www.iospress.nl>



Series B: Physics and Biophysics

Nuclear Science and Safety in Europe

edited by

Tomas Čechák

Czech Technical University,
Prague, Czech Republic

László Jenkovszky

Bogolyubov Institute for Theoretical Physics,
National Academy Sciences of Ukraine,
Kyiv, Ukraine

and

Iurii Karpenko

Shevchenko University of Kyiv,
Kyiv, Ukraine



Published in cooperation with NATO Public Diplomacy Division

Proceedings of the NATO Advanced Research Workshop on
Nuclear Science and Safety in Europe
Yalta, Crimea, Ukraine
10–16 September 2005

A C.I.P. Catalogue record for this book is available from the Library of Congress.

ISBN-10 1-4020-4964-1 (PB)
ISBN-13 978-1-4020-4964-4 (PB)
ISBN-10 1-4020-4963-3 (HB)
ISBN-13 978-1-4020-4963-7 (HB)
ISBN-10 1-4020-4965-X (e-book)
ISBN-13 978-1-4020-4965-1 (e-book)

Published by Springer,
P.O. Box 17, 3300 AA Dordrecht, The Netherlands.

www.springer.com

Printed on acid-free paper

All Rights Reserved

© 2006 Springer

No part of this work may be reproduced, stored in a retrieval system, or transmitted in any form or by any means, electronic, mechanical, photocopying, microfilming, recording or otherwise, without written permission from the Publisher, with the exception of any material supplied specifically for the purpose of being entered and executed on a computer system, for exclusive use by the purchaser of the work.

Printed in the Netherlands.

CONTENTS

Preface	ix
List of Contributors	xi

NUCLEAR SCIENCE

Vortices in the Fireballs Formed in Relativistic Nuclear Collisions <i>E. Pashitsky, D. Anchishkin, V. Malnev and R. Naryshkin</i>	3
Onset of Deconfinement and Critical Point – Future Ion Program at the CERN SPS <i>Marek Gaździcki</i>	27
Production and Study of Antihydrogen in the ATHENA Experiment <i>P. Genova, M. Amoretti, C. Amsler, G. Bonomi, P.D. Bowe, C. Canali, C. Carraro, C.L. Cesar, M. Charlton, M. Doser, A. Fontana, M.C. Fujiwara, R. Funakoshi, J.S. Hangst, R.S. Hayano, L.V. Jørgensen, A. Kellerbauer, V. Lagomarsino, R. Landua, E. Lodi Rizzini, M. Macrí, N. Madsen, G. Manuzio, D. Mitchard, P. Montagna, H. Pruys, C. Regenfus, A. Rotondi, G. Testera, A. Variola, L. Venturelli, Y. Yamazaki, D.P. van der Werf and N. Zurlo</i>	41
Critical Line of the Deconfinement Phase Transitions <i>Mark I. Gorenstein</i>	49
Multiple Production in Nuclear Collisions <i>A.B. Kaidalov</i>	69
An Experimental Proposal to Measure $K^+ \rightarrow \pi^+ \nu \bar{\nu}$ <i>Venelin Kozhuharov</i>	81
Low-energy Photon Scattering on a Polarizable Particle <i>S.A. Lukashovich and N.V. Maksimenko</i>	91
Fluctuations Near the Deconfinement Phase Transition Boundary <i>I.N. Mishustin</i>	99

Results from K2K and Status of T2K <i>Yuichi Oyama</i>	113
Hamiltonian Approach to Cosmological Perturbations in General Relativity <i>B.M. Barbashov, V.N. Pervushin, A.F. Zakharov and V.A. Zinchuk</i>	125
Recent Results from ep Interactions at HERA <i>Alessandro Polini</i>	137
Top Quark Physics from Tevatron to LHC <i>V. Šimák</i>	149
The QCD Analytic Perturbation Theory Description of Hadronic Contributions into Few Important Effects <i>I.L. Solovtsov, O.P. Solovtsova</i>	161
On Nature of Scalar and Tensor Mesons from the Analysis of Processes $\pi\pi \rightarrow \pi\pi, K\bar{K}, \eta\eta$ <i>Yu.S. Surovtsev, R. Kamiński, D. Krupa and M. Nagy</i>	169
New Proposal of Numerical Modelling of Bose-Einstein Correlations: Bose-Einstein Correlations from “within” <i>Oleg V. Utyuzh, Grzegorz Wilk and Zbigniew Włodarczyk</i>	175
Dissociation of Relativistic Nuclei in Peripheral Interactions in Nuclear Track Emulsion <i>P.I. Zarubin, D.A. Artemenkov, G.I. Orlova</i>	189
Cosmic Evolution as “Superfluid” Motion in GR <i>V.N. Pervushin, A.F. Zakharov and V.A. Zinchuk</i>	201

NUCLEAR SAFETY

The Uranium Mining and Storage of Nuclear Waste in Czech Republic <i>Tomáš Čechák and Jaroslav Klusoň</i>	207
Current State and the Future of Nuclear Energy <i>D.P. Belozorov and L.N. Davydov</i>	217
Fast Reactor Based on the Self-Sustained Regime of Nuclear Burning Wave <i>S.P. Fomin, Yu.P. Mel’nik, V.V. Pilipenko and N.F. Shul’ga</i>	239

On the Subcritical Amplifier of Neutron Flux Based on Enriched Uranium <i>V.A. Babenko, V.I. Gulik, L.L. Jenkovszky, V.N. Pavlovich and E.A. Pupirina</i>	253
Transmutation of Fission Products and Minor Actinides in a Subcritical Assembly Driven by a Neutron Generator <i>H.I. Kiyavitskaya, I.G. Serafimovich, V.V. Bournos, Yu.G. Fokov, S.V. Korneev, S.E. Mazanik A.A. Adamovich, C.C. Routkovskaia, A.V. Koulikovskaya, A.M. Khilmanovich, B.A. Martsynkevich, T.N. Korbut and S.E. Chigrinov</i>	265
Experiment and Radiation Safety at Colliders <i>V. Pugatch</i>	275
Authors Index	389
Subject Index	387

PREFACE

From September 10 to September 16, 2005 a NATO Advanced Research Workshop (ARW) on Nuclear Science and Safety in Europe was held in Yalta, Ukraine, in which 46 leading experts in the field of pure and applied nuclear physics from various countries participated.

The subject of the conference covered the recent results of theoretical and experimental studies in high-energy nuclear physics, accelerator technologies and nuclear technologies.

An important feature of the ARW was the interaction between nuclear physicists from East (former Soviet Union) and West (NATO countries).

Their collaboration on topical problems of nuclear science and its application, in particular in the utilization of the nuclear energy, storage and transmutation of the radioactive waste is an important premise for Europe's safety.

The present book contains a selection of invited talks at the ARW. They are grouped in two chapters, one on results of theoretical and experimental studies of nuclear forces (strong interaction physics), and the other on their possible applications. Here, of particular interest is the coverage of the recent developments in the construction of safe sub-critical (assemblies) reactors.

The contributions within each chapter are ordered alphabetically. To preserve the authenticity of the authors' contributions, we have minimized the editorial intervention in correcting only obvious misprints and style diversities.

We thank all the participants of the ARW, especially the authors of the present book, for their invaluable contribution to the success of the Workshop. The ARW was supported by NATO, grant # 981589.

LIST OF CONTRIBUTORS

D. Anchishkin

Bogolyubov Institute for Theoretical Physics
National Academy of Sciences of Ukraine
Kiev-143, 03680 UKRAINE

Tomás Čechák

Czech Technical University in Prague,
Faculty of Nuclear Sciences and Physical Engineering (FNSPE)
Brehova 7, 11519 Prague
CZECH REPUBLIC

L. Davydov

Akhiezer ITP, KFTI
Akademicheskaya Street 1
Kharkov, UKRAINE

S. Fomin

Akhiezer ITP, KFTI
Akademicheskaya Street 1
Kharkov, UKRAINE

M. Gaździcki

Institute für Kernphysik,
University of Frankfurt,
Max-von-Laue Str. 1
D-60438 Frankfurt
GERMANY

P. Genova

Dipartimento di Fisica Nucleare e Teorica
Via Bassi 6 - 27100 Pavia (PV)
ITALY

M. Gorenstein

Bogolyubov Institute for Theoretical Physics
National Academy of Sciences of Ukraine
Kiev-143, 03680 UKRAINE

L. Jenkovszky

Bogolyubov Institute for Theoretical Physics
National Academy of Sciences of Ukraine
Kiev-143, 03680 UKRAINE

A. Kaidalov

ITEP,
B. Cheremushkinskaya ulitsa 25,
117 259 Moscow
RUSSIA

H. Kiyavitskaya

Joint Institute for Power Nuclear Research
Acad. A.K. Krasin str. 99, Minsk
BELARUS

V. Kozhuharov

Atomic Physics Dep.
Faculty of Physics, University of Sofia
5 J. Bourchier Str., 1164 Sofia
BULGARIA

S. Lukashevich

Theoretical Physics Department
Gomel State University
Sovetskay str, 104,
246699, Gomel,
BELARUS

I. Mishustin

Institute for Theoretical Physics,
JWG University Frankfurt,
PF 111932
Robert-Mayer Str. 8-10
Frankfurt am Main 11
GERMANY

Y. Oyama

High Energy Accelerator Research Organisation (KEK)
Oho 1-1, Tsukuba Ibaraki 305-0801,
JAPAN

V. Pervushin

JINR, J. Curie 6,
Dubna, Moscow reg.
141980 RUSSIA

A. Polini

DESY F1,
Notkestrasse 85,
22607 Hamburg 52,
GERMANY

V. Pugatch

Institute for Nuclear Research,
National Academy of Sciences of Ukraine
Prospekt Nauki 47, Kiev-28,
03680 UKRAINE

V. Šimák

Institute of Physics of ASCR
Ostružinova 8,
Prague 10, CZ-10600
CZECH REPUBLIC

I. Solovtsov

International Center for Advanced Studies,
Gomel State Technical University,
Gomel, 246746
BELARUS

Yu. Surovtsev

JINR, J. Curie 6,
Dubna, Moscow reg.
141980 RUSSIA

G. Wilk

Soltan Institute for Nuclear Studies
Nuclear Theory Department (Zd-PVIII)
ul. Hoza 69; 00-681 Warsaw;
POLAND

P. Zarubin

JINR, J. Curie 6,
Dubna, Moscow reg.
141980 RUSSIA

V. Zinchuk

JINR, J. Curie 6,
Dubna, Moscow reg.
141980 RUSSIA

I.
Nuclear
Science

VORTICES IN THE FIREBALLS FORMED IN RELATIVISTIC NUCLEAR COLLISIONS

E. Pashitsky^{a,¶}, D. Anchishkin^{b,||}, V. Malnev^{c,**}, and R. Naryshkin^{c,††}
^a*Institute of Physics, Nat. Acad. Sci. of Ukraine, Kyiv 03028, Ukraine*
^b*Bogolyubov Institute for Theoretical Physics, Kyiv 03143, Ukraine*
^c*Kyiv National University, Physics Department, Kyiv 03022, Ukraine*

Abstract. On the base of the system of hydrodynamic equations we consider a model of formation and development of the hydrodynamic vortices in the nuclear matter during relativistic heavy-ion collisions, in astrophysical objects, and in powerful atmospheric phenomena such as typhoons and tornados. A new class of the analytic solutions of non-relativistic hydrodynamic equations for the incompressible liquid in the presence of a bulk sink are analyzed. The main feature of these solutions is that they describe non-stationary hydrodynamic vortices with the azimuth component of velocity exponentially or explosively growing with time. A necessary attribute of a system with such a behavior is a presence of a bulk sink, which provides the existence of the non-stationary vortex regime. These solutions are obtained by nullifying the terms in the Navier-Stokes equations, which describe viscous effects, exist and represent vortex structure with “rigid-body” rotation of the core and converging radial flows. With the help of our model we explain some typical features of the above physical systems from the unique point of view.

1. Introduction

Hydrodynamic vortices and vortex flows is rather common in nature. This is constantly confirmed by formation of the powerful atmospheric vortices, typhoons, tornados, and so on. An example of the gigantic vortex structure is the big “Red Spot” on the Jupiter surface that is observed by astronomers about a several centuries.

Why such hydrodynamic vortex structures exist for an appreciable length of time in liquids and gases in spite of a finite viscosity of these media? A possible answer to this question could be associated with realization of the profiles of hydrodynamical velocities that strongly reduce the affect of the

[¶] E-mail: pashitski@if.kiev.ua

^{||} E-mail: anch@bitp.kiev.ua

^{**} E-mail: malnev@univ.kiev.ua

^{††} E-mail: naryshkin@univ.kiev.ua

viscous terms in the Navier-Stokes equations. One example of a such durable motion is the axially-symmetrical Rankin vortex in an incompressible viscous liquid [1]. The velocity profile of this vortex has only one nonzero component – the azimuth component and describes the “rigid body” rotation in some cylindrical domain of an arbitrary radius and differential rotation (velocity is inversely proportional to a distance from the vortex center). This profile nullifies the terms with the first viscosity in the Navier-Stokes equation and satisfies the hydrodynamic equations of an incompressible liquid at a constant velocity of the vortex rotation. However, this motion turns out to be unstable because the first derivative of the azimuth velocity has a step at the border of the rigid body rotation. In the vicinity of this point, the viscous effects result in dissipation of the vortex kinetic energy and it diffuses in the space decaying with time. It is evident that the stationary or growing with time vortices may exist only at the expense of the external energy sources. Among all possible hydrodynamic flows and vortex motions in the incompressible liquid survive only those ones which have a comparatively small dissipation of energy.

We study a new class of solutions of non-relativistic hydrodynamic equations of a incompressible liquid with a bulk sink in a finite domain of the liquid with cylindrical or spherical symmetry. These solutions may be obtained by choosing the profiles of the hydrodynamic velocities that nullify the viscous terms in the Navier-Stokes equations [2]. We call them the quasi-dissipativeless solutions. They model the dynamical processes (nuclear, chemical reactions, phase transitions etc.), which move away out of the system, which performs a hydrodynamic motion, one or several species. The solutions under consideration describe the non-stationary hydrodynamic vortices with the exponentially growing velocity of rotation in some domain (core of the vortex) of the liquid with the bulk sink. The rotation acceleration of these vortices is a result of combined action of the convective and the Coriolis forces that appear due to the radial convergent flows into the bulk domain from the external region that support a constant density of the liquid. The acceleration of vortex motion may correspond to a regime of the nonlinear “explosive” instability in some special cases.

To our mind, the mechanism of formation and developing of this non-stationary hydrodynamic vortices could explain from the unique point of view a wide circle of the physical phenomena.

In this paper, we apply this hydrodynamic approach for description of:

- i) the rotational motion of nuclear matter, which appears in the relativistic collisions of heavy nuclei with an initial angular momentum;
- ii) the origination of non-dissipative hydrodynamic vortices in the liquid cores of planets and acceleration of the central cores of stars caused by thermonuclear reactions;

iii) the creation of powerful atmospheric vortices (whirlwinds, tornados, and typhoons).

2. The state of nuclear matter created in the relativistic nucleus-nucleus collisions

We consider the system, which is formed in the process of heavy nuclei collisions. Being accelerated to high energies ($E \gg 1$ GeV), heavy atomic nuclei with a charge $Z \gg 1$ gain the shape of ellipsoids of rotation, which are strongly contracted in the direction of motion due to the relativistic reduction of longitudinal sizes by the factor $\gamma = \sqrt{1 - v_0^2/c^2} \ll 1$ (where v_0 is the velocity of the colliding nuclei, and c is the velocity of light) (Fig. 1). A cluster of the dense hot nuclear matter (NM) that created in the nuclear collisions in the laboratory reference system takes the form of a thin disk with the initial radius $R_0 \sim 6-7$ fm = $6-7 \cdot 10^{-13}$ cm (for the nuclei of Au and Pb), the thickness $h_0 = \gamma R_0 \ll R_0$, and the total mass $\mu_0 = 2Am_N/\gamma$ (where A is atomic number, and m_N is nucleon mass). A high density of particles and their small mean free paths in the disk, its evolution on the initial stage $t < t_f$ (until the distances between particles becomes greater than the action radius of nuclear forces $r \sim \hbar/m_\pi c$, where $m_\pi \approx 140$ MeV/ c^2 — mass of a π -meson) can be described in the hydrodynamic approximation. According to [3], the cluster of NM begins one-dimensional expansion along the collision axis (Fig. 1) up to the freeze-out time of the order of $t_f \sim 10$ fm/c.

We consider the NM motion in the cylindrical coordinates with z axis along the collision line. The one-dimensionality of the expansion (along the z axis) allows us to assume that transverse hydrodynamic velocities (radial v_r and azimuthal v_φ components of the \mathbf{v}) are non-relativistic ones during the time, $t < t_f$. In addition, according to the Bjorken scenario of the one-dimensional expansion [4], majority of the particles is contained in the inner layers of the fireball and move with longitudinal velocities

$$v_z = \frac{z}{t}, \quad t > t_i \quad (t_i \ll t_f), \quad (1)$$

where $t_i = 0.1-0.3$ fm/c is a time of the formation of a fireball [5]. Only in a narrow external layer, the substance moves with velocities of the order of the velocity of light $v \rightarrow c$ (see Fig. 1).

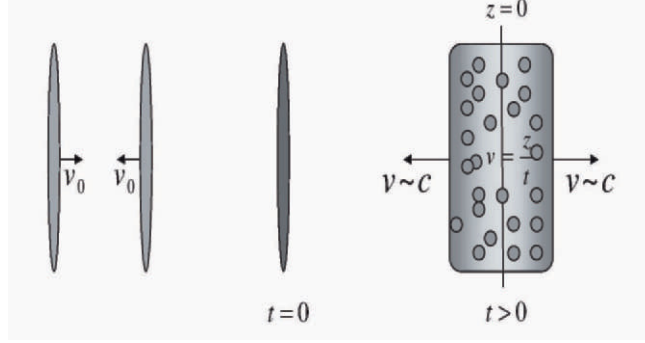


Figure 1. Sketch of the collision of relativistically contracted heavy nuclei. *Left figure*: nuclei before collision; *Figure in the center*: the nuclei just after overlapping, beginning of the formation of the fireball; *Right figure*: the fireball (cluster of hot and dense nuclear matter) which expands.

We consider such a region of a fireball or such a time of the hydrodynamic expansion, when the non-relativistic hydrodynamic description is valid for the longitudinal velocity v_z (in the Bjorken model, the duration of the formation of particles with great longitudinal momenta exceeds that for slow particles). In this case, we simplify our problem, which does not affect the qualitative behavior of the described hydrodynamic instability.

2.1. THE HYDRODYNAMIC INSTABILITY OF THE VORTEX MOTION IN NUCLEAR MATTER CREATED IN HEAVY-NUCLEI COLLISIONS

We describe the motion of NM with the help of the Navier–Stokes equation. In the cylindrical coordinate system it reads

$$\frac{\partial v_r}{\partial t} + (\mathbf{v}\nabla)v_r - \frac{v_\varphi^2}{r} = -\frac{1}{\rho}\frac{\partial p}{\partial r} + \nu\left[\Delta v_r - \frac{v_r}{r^2} - \frac{2}{r^2}\frac{\partial v_\varphi}{\partial\varphi}\right], \quad (2)$$

$$\frac{\partial v_\varphi}{\partial t} + (\mathbf{v}\nabla)v_\varphi + \frac{v_r v_\varphi}{r} = -\frac{1}{\rho r}\frac{\partial p}{\partial\varphi} + \nu\left[\Delta v_\varphi - \frac{v_\varphi}{r^2} + \frac{2}{r^2}\frac{\partial v_r}{\partial\varphi}\right], \quad (3)$$

$$\frac{\partial v_z}{\partial t} + (\mathbf{v}\nabla)v_z = -\frac{1}{\rho}\frac{\partial p}{\partial z} + \nu\Delta v_z, \quad (4)$$

where p is the pressure, ν is the coefficient of kinematic viscosity, and

$$(\mathbf{v}\nabla) = v_r\frac{\partial}{\partial r} + \frac{v_\varphi}{r}\frac{\partial}{\partial\varphi} + v_z\frac{\partial}{\partial z}, \quad \Delta = \frac{1}{r}\frac{\partial}{\partial r}\left(r\frac{\partial}{\partial r}\right) + \frac{1}{r^2}\frac{\partial^2}{\partial\varphi^2} + \frac{\partial^2}{\partial z^2}. \quad (5)$$

Different nuclear reactions are running in the fireball and accompanied by the escape of created products (secondary particles, γ -quanta, jets) and by a

decrease of the total mass of the fireball $\mu(t)$ with time. These processes may be described by the continuity equation with a bulk sink term, $q(\mathbf{r}, t)$,

$$\frac{\partial \rho}{\partial t} + \text{div}(\rho \mathbf{v}) = -q(r, t), \quad (6)$$

where $\rho(\mathbf{r}, t)$ is the density of NM. For the nuclear matter we may use the approximation of quasi-incompressible liquid. This means that in the process of hydrodynamic motion the following equation holds true

$$\frac{d\rho}{dt} = \frac{\partial \rho}{\partial t} + (\mathbf{v} \nabla) \rho = 0, \quad (7)$$

in comparison with the ordinary incompressible liquid with constant density now, $\rho(\mathbf{r}, t) \neq \text{const}$. We make one more assumption that the intensity of the bulk sink in (6) is proportional to the local fireball density, $q \propto \rho$. In this case, the continuity equation (6) for the incompressible NM can be represented as

$$\text{div} \mathbf{v} \equiv \frac{1}{r} \frac{\partial}{\partial r} (r v_r) + \frac{1}{r} \frac{\partial v_\phi}{\partial \phi} + \frac{\partial v_z}{\partial z} = -\frac{1}{\tau(t)}, \quad (8)$$

where the typical time $\tau = (q/\rho)^{-1}$ of the outflow of NM from a fireball at the expense of nuclear reactions (transformations of particles, annihilation, tunneling, etc.) depends on time only. The parameter τ can be estimated by the formula

$$\tau^{-1} = \sum_{\text{all processes}} \sigma_{\text{eff}} n v, \quad (9)$$

where σ_{eff} is the effective cross-section of inelastic processes or reactions, n is the bulk concentration of particles, and v is the mean velocity of the particles, which participate in the reactions. Expanding v_z in the vicinity, $z = 0$, in the middle cross-section of the fireball, where $v_z = 0$, and assuming that the fireball is rather thin, ($\gamma \ll 1$), we obtain

$$v_z(z, t) = \alpha(t) z. \quad (10)$$

Hence, according to the Bjorken model (1)

$$\alpha(t) = \frac{1}{t}, \quad t > t_1. \quad (11)$$

Doing in the same manner as while obtaining v_z (10), we can get the profiles of the transverse velocities proportional to a distance r from the z axis (where $v_r = 0$ and $v_\phi = 0$):

$$v_r(r, t) = -\beta(t) r, \quad v_\phi(r, t) = \Omega(t) r. \quad (12)$$

The negative sign of v_r corresponds to the convergent radial flow of NM in a fireball, which ensures the validity of the continuity equation (8) in the presence of a sink and the longitudinal expansion. We note that these profiles nullify the viscous terms in Navier–Stokes equations (3)-(4).

For the axisymmetric profiles of the velocity which are independent of the azimuthal angle φ , the equation of continuity (8) with regard for (10) and (12) leads to the relation

$$\alpha(t) - 2\beta(t) = -\frac{1}{\tau(t)}. \quad (13)$$

On the other hand, the component of azimuthal hydrodynamic velocity $v_\varphi(r, t) = \Omega(t)r$ describing the “rigid-body” rotation with unknown $\Omega(t)$ must satisfy the Navier–Stokes equation (3). Substitution (12) $v_r(r, t)$ and $v_\varphi(r, t)$ at $r \leq R(t)$, ($R(t)$ is a radius of the fireball at a moment time t), in (3) yields

$$\frac{d\Omega(t)}{dt} - 2\beta(t)\Omega(t) = 0. \quad (14)$$

The solution of this equation with account of (13) takes the form

$$\Omega(t) = \Omega_0 \exp \left\{ \int_{t_i}^t \left[\frac{1}{\tau(t')} + \alpha(t') \right] dt' \right\}, \quad (15)$$

where Ω_0 is an initial angular velocity of the rotation of nuclear matter. For the simplest case $\tau = \text{const}$, and in the Bjorken model where $\alpha(t) = 1/t$

$$\Omega(t) = \Omega_0 \frac{t}{t_i} \exp \left\{ \frac{t - t_i}{\tau} \right\}, \quad t > t_i. \quad (16)$$

This dependence describes the “exponential” hydrodynamic instability of the rotational motion of NM in the fireball provided that initial angular velocity, $\Omega_0 \neq 0$ (neglecting by the slow pre-exponential factor $\propto t$).

We connect the origin of nonzero Ω_0 with collisions of nuclei in highly excited rotational states with large orbital quantum numbers. Therefore, within the frame of the quasi-classical approximation there are some initial rotation of the nuclear matter with the hydrodynamic azimuthal velocity

$$v_{\varphi 0} = \Omega_0 r \quad (r \leq R_0), \quad (17)$$

where $R_0 = R(0)$ (initial radius of the fireball), Ω_0 is the initial angular velocity of rotation connected with the initial angular momentum of the fireball M_{z0} by the relation

$$M_{z0} = I_{z0}\Omega_0. \quad (18)$$

Here, I_{z0} is the initial moment of inertia. For the fireball in the form of a disk of a thickness $h_0 = \gamma R_0 \ll R_0$, it is equal to

$$I_{z0} = \frac{1}{2}\mu_0 R_0^2, \quad \mu_0 = \pi R_0^3 \gamma \rho_0, \quad (19)$$

where $\rho_0 = \mu_0 / \pi R_0^2 h_0$ is the initial density of NM.

The total mass of the fireball is given by

$$\mu(t) = \pi R^2(t) \int_{-h(t)/2}^{h(t)/2} \rho(z, t) dz, \quad (20)$$

where $h(t)$ is the fireball disk thickness and $\rho(z, t)$ is its density. The fireball transverse radius $R(t)$ and its mass $\mu(t)$ decrease with time.

We assume that the value of the integral

$$\int_{-h(t)/2}^{h(t)/2} \rho(z, t) dz \equiv \frac{\mu(t)}{\pi R^2(t)} = \frac{\mu_0}{\pi R_0^2} = \text{const}$$

is not changed during the expansion of the fireball, which would be fulfilled exactly upon the one-dimensional expansion in the absence of nuclear reactions, where $h(t)\rho(t) = h_0\rho_0 = \text{const}$. In this case, the decrease in $R(t)$ will occur only due to the presence of a bulk sink in the fireball (rather than at the expense of its expansion). This yields that the inertia moment drops proportionally to the fourth degree of the radius $R(t)$:

$$I_z(t) = \frac{1}{2}\mu(t)R^2(t) = \frac{\pi}{2}\rho_0 h_0 R^4(t). \quad (21)$$

By virtue of the law of conservation of the angular momentum $M_z = M_{z0} = \text{const}$ and according to (18), there exists the interrelation between the angular velocity of rotation of the cluster $\Omega(t)$ and its actual radius $R(t)$:

$$\Omega(t) = \Omega_0 \left[\frac{R_0}{R(t)} \right]^4. \quad (22)$$

According to (22), this corresponds to the exponential decrease (by neglecting the slower power behavior) of the cluster radius,

$$R(t) = R_0 \left(\frac{t_i}{t} \right)^{1/4} \exp \left\{ -\frac{t - t_i}{4\tau} \right\}, \quad t > t_i, \quad (23)$$

and to the exponential growth in time of the maximal azimuthal velocity of NM on the boundary of the cluster ($t > t_i$):

$$v_\varphi^{\max}(t) = \Omega(t)R(t) = \Omega_0 R_0 \left(\frac{t}{t_i} \right)^{3/4} \exp \left\{ \frac{3}{4} \frac{t - t_i}{\tau} \right\}. \quad (24)$$

The latter must lead to a change in the distributions of the momenta of outgoing secondary particles and to the appearance of the angular momentum in the distributions of those products of nuclear reactions which will take away a part of the rotational moment of the system with themselves.

For the velocity profiles (10)—(17), Eq. (2) defines a change in time of the radial pressure of NM in the cluster $r \leq R(t)$:

$$p(r, t) = p_0 + \frac{\rho r^2}{2} [\Omega^2(t) - \beta^2(t) + \dot{\beta}(t)], \quad (25)$$

where p_0 — pressure at $r = 0$, and the dot above a letter stands for the derivative with respect to time.

It is worth to note that, in the Bjorken model, the pressure turns out to be homogeneous along the axis of the expansion of NM by virtue of the equality $\dot{\alpha} = -1/t^2 = -\alpha^2$. With regard for (11) and (13), we get (at $\tau = \text{const}$):

$$p(r, z, t) = p_0 + \frac{\rho r^2}{2} \left[\Omega^2(t) - \frac{1}{4} \left(\frac{1}{t} + \frac{1}{\tau} \right)^2 - \frac{1}{2t^2} \right]. \quad (26)$$

Upon the noncentral collision of heavy nuclei (nonzero impact parameter), there appears the region of the overlapping of nuclei which is characterized by the asymmetry in the plane transverse to the collision axis. This leads to the appearance of the asymmetry of the spatial gradients of pressure and density, which causes the appearance of an asymmetry in the momentum distribution of particles [5]. In this case, the azimuthal angular distributions of secondary particles are usually represented by the formula [6]

$$\frac{dN}{d\varphi} = \frac{N_0}{2\pi} (1 + 2v_1 \cos \varphi + 2v_2 \cos 2\varphi + \dots). \quad (27)$$

The case with $v_2 \neq 0$ corresponds to the elliptic flow. The parameter v_2 depends monotonically on the transverse momentum of outgoing particles $p_{\perp} = \sqrt{p_r^2 + p_{\varphi}^2}$ and varies as follows: $v_2 = 0 \div 0.2$ [6]. We note that a similar azimuthal asymmetry indicates once more the presence of the effect of the collective character of the nuclear matter which is created in relativistic heavy-ion collisions and can be described in the hydrodynamic approximation.

The form of an axially nonsymmetric cluster of NM can be described as $R(t, \varphi) = R(t) (1 + \xi \cos 2\varphi)$, and its velocity components are

$$v_r(r, \varphi, t) = -\beta r (1 + \varepsilon \cos 2\varphi), \quad (28)$$

$$v_{\varphi}(r, \varphi, t) = \Omega r (1 + \delta \sin 2\varphi), \quad (29)$$

$$v_z(z, t) = \alpha z. \quad (30)$$

Here, $\xi(t), \varepsilon(t), \delta(t)$ — some functions of time. For such angular and radial dependences, the terms describing the viscosity in the Navier–Stokes equations are identically equal to zero under the condition $\beta\varepsilon = \Omega\delta$:

$$\nu \left[\frac{1}{r} \frac{\partial}{\partial r} \left(r \frac{\partial v_r}{\partial r} \right) + \frac{1}{r^2} \frac{\partial^2 v_r}{\partial \varphi^2} - \frac{v_r}{r^2} - \frac{2}{r^2} \frac{\partial v_\varphi}{\partial \varphi} \right] \equiv 0, \quad (31)$$

$$\nu \left[\frac{1}{r} \frac{\partial}{\partial r} \left(r \frac{\partial v_\varphi}{\partial r} \right) + \frac{1}{r^2} \frac{\partial^2 v_\varphi}{\partial \varphi^2} - \frac{v_\varphi}{r^2} + \frac{2}{r^2} \frac{\partial v_r}{\partial \varphi} \right] \equiv 0. \quad (32)$$

In this case, the equation of continuity (10) leads again to relation (13), and Eq. (3) yields (14).

Thus, in the hydrodynamic model under consideration, the noncentral character of the collisions of heavy nuclei does not practically affect the mechanism of development of a hydrodynamic rotational instability. The last is defined by the presence of the term describing a sink in the equation of continuity and by the initial nonzero vorticity of the cluster of NM and corresponds to the hydrodynamic velocity profiles which nullify the terms describing the viscosity in the Navier–Stokes equation.

3. Spherically symmetrical vortex structures in astrophysics (planets, stars)

In this section, we consider the possibility of existence of the dissipativeless vortex structures and the flow with zeroth viscosity in the spherically symmetric objects, particularly, in the planets and the Earth, where the melted liquid nucleus exists and in the central cores of stars and the Sun where the thermonuclear fusion reactions take place.

It is known, that in depths of the Earth and other planets of the Earth group the liquid cores exist. They consist of melted liquid minerals and metals. This core is enveloped by the rigid crust (lithosphere and asthenosphere) of a radius R_0 , and limited from inside by the surface of rigid core of a radius r_0 . On action of the gravity forces from other celestial bodies (in particular, for the Earth from the Moon and the Sun), the tidal waves may appear in the liquid cores that could cause breaks of the rigid crust forming powerful earthquakes.

We show that a spherical layer of the viscous liquid inside the liquid planet core in the domain $r_0 \leq r \leq R_0$ the close global hydrodynamical flows (three dimensional vortices) may appear that in the incompressible liquid correspond to the zeroth bulk viscosity and may be excited by the external gravitational fields. In stationary conditions, due to a finite viscosity and friction with the rigid walls, the liquid core of the planets must take part in

the daily rotation as a whole with a definite angular velocity Ω_0 (for the Earth $\Omega_0 \approx 7.3 \cdot 10^{-5} \text{ c}^{-1}$). The hydrodynamic azimuth velocity $v_{\varphi 0}$ of this “rigid” rotation of the liquid in the layer $r_0 \leq r \leq R_0$ with account of the spherically symmetric gravitational forces of the planet satisfies the following equations:

$$\frac{v_{\varphi 0}^2}{r} = \frac{1}{\rho} \frac{\partial P}{\partial r} + g(r), \quad v_{\varphi 0}^2 \cot \theta = \frac{1}{\rho} \frac{\partial P}{\partial \theta}, \quad (33)$$

where P and ρ are the equilibrium pressure and density of the liquid, $g(r) = \frac{4\pi}{3} G \rho r + g_0$ is the gravity acceleration inside the liquid core, $g_0 = GM_0/r_0^2$ is the gravity acceleration formed by the inner rigid core of a mass $M_0 = \frac{4\pi}{3} \rho_0 r_0^3$ and a density ρ_0 , G is the gravity constant, and θ is a polar angle of the spherical coordinates.

The stationary solutions that satisfy equations (33) take the following form

$$v_{\varphi 0}(r, \theta) = r\Omega_0 \sin \theta, \quad (34)$$

$$P(r, \theta) = P_0 + \frac{\rho r^2}{2} \left[\Omega_0^2 \sin^2 \theta - \frac{4\pi}{3} G \rho \right] - \rho g_0 r. \quad (35)$$

However, this ground state of the “solid” rotation may be perturbed by the external gravitational fields. To describe this perturbed hydrodynamic motion of the liquid in the domain $r_0 \leq r \leq R_0$ we apply equations of the Navier-Stokes and continuity equation for the incompressible viscous equation in the spherical coordinate system [2]. Keeping in mind that the radial velocity of the liquid v_r on the rigid walls at $r = r_0$ and $r = R_0$ must be zero, we set $v_r = 0$ in the whole bulk of the liquid core. In this case the hydrodynamic equations take the form:

$$-\frac{v_{\varphi}^2 + v_{\theta}^2}{r} = -\frac{1}{\rho} \frac{\partial P}{\partial r} - g(r) + \tilde{g}_r - \frac{2\nu}{r^2} \left[\frac{\partial v_{\theta}}{\partial \theta} + \frac{1}{\sin \theta} \frac{\partial v_{\varphi}}{\partial \varphi} + v_{\theta} \text{ctg} \theta \right], \quad (36)$$

$$\frac{\partial v_{\varphi}}{\partial t} + \frac{v_{\theta}}{r} \frac{\partial v_{\varphi}}{\partial \theta} + \frac{v_{\varphi}}{r \sin \theta} \frac{\partial v_{\varphi}}{\partial \varphi} + \frac{v_{\varphi} v_{\theta} \text{ctg} \theta}{r} = -\frac{1}{r \rho \sin \theta} \frac{\partial P}{\partial \varphi} + \tilde{g}_{\varphi} + \quad (37)$$

$$+ \nu \left[\frac{1}{r} \frac{\partial^2}{\partial r^2} (r v_{\varphi}) + \frac{1}{r^2 \sin^2 \theta} \frac{\partial^2 v_{\varphi}}{\partial \varphi^2} + \frac{1}{r^2 \sin \theta} \frac{\partial^2}{\partial \theta^2} (\sin \theta v_{\varphi}) + \frac{2 \cos \theta}{r^2 \sin^2 \theta} \frac{\partial v_{\theta}}{\partial \varphi} - \frac{v_{\varphi}}{r^2 \sin^2 \theta} \right], \quad (38)$$

$$\frac{\partial v_{\theta}}{\partial t} + \frac{v_{\varphi}}{r \sin \theta} \frac{\partial v_{\theta}}{\partial \varphi} + \frac{v_{\theta}}{r} \frac{\partial v_{\theta}}{\partial \theta} - \frac{v_{\varphi}^2 \text{ctg} \theta}{r} = -\frac{1}{r \rho} \frac{\partial P}{\partial \theta} + \tilde{g}_{\theta} + \nu \left[\frac{1}{r} \frac{\partial^2}{\partial r^2} (r v_{\theta}) + \frac{1}{r^2 \sin^2 \theta} \frac{\partial^2 v_{\theta}}{\partial \varphi^2} + \quad (39)$$

$$+ \frac{1}{r^2 \sin \theta} \frac{\partial^2}{\partial \theta^2} (\sin \theta v_{\theta}) - \frac{2 \cos \theta}{r^2 \sin^2 \theta} \frac{\partial v_{\varphi}}{\partial \varphi} - \frac{v_{\theta}}{r^2 \sin^2 \theta} \right]. \quad (40)$$

Here v_θ is the meridian velocity of the liquid, \widetilde{g}_r , \widetilde{g}_φ and \widetilde{g}_θ are the radial, azimuth, and meridian components of the perturbing acceleration that formed by the external gravity fields, respectively.

The continuity equation at $v_r = 0$ reduces to

$$\frac{\partial v_\theta}{\partial \theta} + \frac{1}{\sin \theta} \frac{\partial v_\varphi}{\partial \varphi} + v_\theta \cot \theta = 0. \quad (41)$$

According to equation (41), the expression in the square brackets with the coefficient of kinematic viscosity ν on the r.h.s. of equation (36) identically equals to zero. The continuity equation (41) is satisfied by the following angular dependencies of the angular velocities

$$v_\varphi(r, \theta, \varphi) = [r\Omega_0 + F(r)] \sin \theta + f(r) \cos \theta \cos \varphi, \quad (42)$$

$$v_\theta(r, \varphi) = f(r) \sin \varphi, \quad (43)$$

where $F(r)$ and $f(r)$ are arbitrary functions of r . Taking these functions in the form

$$F(r) = \Omega(r + \alpha/r^2), \quad f(r) = \omega(r + \beta/r^2), \quad (44)$$

where Ω and ω are some corrections to the constant angular velocity Ω_0 of the “rigid” rotation of the liquid and α i β are arbitrary parameters that are dictated by the boundary conditions the both expressions in the square brackets with ν in the right hand parts of equations (38) and (40). This means that the hydrodynamic flows with velocities (42) and (43) at the radial distribution (44) in the incompressible viscous liquid actually correspond to the zeroth bulk viscosity.

If we select parameters α and β equal to $\alpha = \beta = -R_0^3$, when the perturbed azimuth and meridional velocities equal to zero at $r = R_0$, then the friction between the liquid and the inner wall of rigid crust disappears. Moreover, if we assume that the rigid central planet core can rotate with the angular velocity different from the Ω_0 , then the friction between the liquid and rigid cores will be minimal at velocities that coincide at the point $r = r_0$. For example, on the equator at $\theta = \pi/2$ and $\varphi = 0$:

$$v_\varphi(r_0, \pi/2, 0) = [r_0\Omega_0 + \Omega(r_0 - R_0^3/r_0^2)]. \quad (45)$$

Now we show that these three dimensional global vortexes in the liquid cores of planets may be born under action of the external gravitational perturbations. Substituting expressions (42)—(44) at $\alpha = \beta = -R_0^3$ in equation (36) and taking account of the relation for the equilibrium state (34) and (35), for the perturbation of pressure \bar{P} we have the following equation:

$$r \left(1 - \frac{R_0^3}{r^3} \right)^2 [\Omega (2\Omega' + \Omega) \sin^2 \theta + 2\omega (\Omega' + \Omega) \sin \theta \cos \theta \cos \varphi + \omega^2 (\cos^2 \theta \cos^2 \varphi + \sin^2 \varphi)] \quad (46)$$

$$= -\frac{1}{r} \frac{\partial \tilde{P}}{\partial r} + \tilde{g}_r, \quad (47)$$

Let us consider the case of a maximum gravitational force acting on the Earth from the Moon and the Sun at the complete solar eclipse when the resultant gravitational potential is equal to

$$\Phi(r, \tilde{\theta}) = -G \left[\frac{M_1}{\sqrt{R_1^2 + r^2 - 2R_1 r \cos \tilde{\theta}}} + \frac{M_2}{\sqrt{R_2^2 + r^2 - 2R_2 r \cos \tilde{\theta}}} \right], \quad (48)$$

where M_1 i M_2 are the masses of the Sun and the Moon that are located at distances R_1 i R_2 from the Earth center respectively, \mathbf{r} is a radius-vector of an arbitrary point in the Earth bulk (in particular, in the liquid core $r < R_0$), and $\tilde{\theta}$ is the angle between vectors \mathbf{r} and $\mathbf{R}_{1,2}$. With account of the strong inequalities $R_0 \ll R_2 \ll R_1$ (at $M_1 \gg M_2$) keeping the terms of the second order of smallness, according to (48) we get

$$\Phi(r, \tilde{\theta}) \cong - \left[\Phi_0 + \Phi_1 r \cos \tilde{\theta} + \Phi_2 \frac{r^2}{2} (3 \cos^2 \tilde{\theta} - 1) \right], \quad (49)$$

where

$$\Phi_0 = G \left(\frac{M_1}{R_1} + \frac{M_2}{R_2} \right), \quad \Phi_1 = G \left(\frac{M_1}{R_1^2} + \frac{M_2}{R_2^2} \right), \quad \Phi_2 = G \left(\frac{M_1}{R_1^3} + \frac{M_2}{R_2^3} \right). \quad (50)$$

In the spherical coordinates with the polar axis coinciding with the Earth rotation axis, the angle $\tilde{\theta}$ can be expressed through the polar (θ i θ') and azimuth (φ i φ') angles of the vectors \mathbf{r} and $\mathbf{R}_{1,2}$ as follows

$$\cos \tilde{\theta} = \cos \theta \cos \theta' + \sin \theta \sin \theta' (\cos \varphi \cos \varphi' + \sin \varphi \sin \varphi'). \quad (51)$$

At the points of the Earth orbits (ecliptic) that corresponds to winter and summer solstice when the vectors $\mathbf{R}_{1,2}$ and the inclined axis of the Earth lies in the same plane so that $\varphi' = 0$, and $\theta' = \pi/2 - \theta_1$ (where θ_1 is the angle of Earth incline to the ecliptic plane), with the help (51) we get

$$\cos \tilde{\theta}(\theta, \varphi) = \cos \theta \sin \theta_1 + \sin \theta \cos \varphi \cos \theta_1. \quad (52)$$

At the points of spring and fall solstice when the vectors $\mathbf{R}_{1,2}$ under complete solar eclipse are directed so that $\varphi' = \theta' = \pi/2$, we have:

$$\cos \tilde{\theta}(\theta, \varphi) = \sin \theta \sin \varphi. \quad (53)$$

The perturbations of the gravity force with account of (49) and (52) or (53) may be calculated by using the formulas:

$$\tilde{g}_r = -\frac{\partial \Phi}{\partial r}, \quad \tilde{g}_\varphi = -\frac{1}{r \sin \theta} \frac{\partial \Phi}{\partial \varphi}, \quad \tilde{g}_\theta = -\frac{1}{r} \frac{\partial \Phi}{\partial \theta}. \quad (54)$$

In particular, for \tilde{g}_r according to (49) we get

$$\tilde{g}_r = \Phi_1 \cos \tilde{\theta}(\theta, \varphi) + \Phi_2 r [3 \cos^2 \tilde{\theta}(\theta, \varphi) - 1]. \quad (55)$$

With account of relations (52) and (53) we can see that the second term in (55) contains the same space—angular dependencies as the left hand part of the equation (47). In fact, according to (52) and (53), we obtain

$$\cos^2 \tilde{\theta} = \begin{cases} \cos^2 \theta \sin^2 \theta_1 + \sin \theta \cos \theta \cos \varphi \sin 2\theta_1 + \\ + (1 - \cos^2 \theta) \cos^2 \varphi \cos^2 \theta_1, \\ 1 - (\cos^2 \theta + \cos^2 \varphi) + \cos^2 \theta \cos^2 \varphi. \end{cases} \quad (56)$$

The correspondent terms in (56) with the angular dependencies of the type $\sin \theta \cos \theta \cos \varphi$ (at $\sin 2\theta_1$) and $\cos^2 \theta \cos^2 \varphi$ coincide in their structure with some terms in the left hand side of equation (47). In other words, a peculiar space—time resonance appears between the gravitation perturbations (55) and the dissipativeless hydrodynamic flows. It may excite these vortex flows in the liquid core of the Earth at the moments when the complete solar eclipse coincides with the above specified location of the Earth on the ecliptic.

The correspondent inhomogeneous perturbation of the pressure \tilde{P} must act on the rigid at $r = R_0$ and along with regular tidal waves can cause detraction (break) of the lithosphere forming conditions for appearance of the power earthquakes on the land or for birth of tsunami in an ocean, and amplification of the volcanic processes as well.

3.1. INFLUENCE OF THE THERMONUCLEAR REACTIONS ON THE HYDRODYNAMICS OF ROTATION OF THE CENTRAL CORE OF A STAR

It is known, that in the star central cores, particularly, in the sun, where the temperature could reach ten million degrees, the thermonuclear reaction resulting in transformation of hydrogen into helium take place. Formation of

one helium nucleus ${}^4\text{He}$ (or ${}^3\text{He}$) from four (or three) nuclei of hydrogen or protons H , leads to decreasing of the specific volume that occupies the fully ionized and compressed by the gravity forces hot hydrogen-helium plasma (analogously to the condensation process of water droplets). In other words, due to the thermonuclear fusion inside the star central core of a radius r_0 the bulk sink of substance appears. Under conditions of the dynamic and chemical equilibrium between the star core and its external envelop of a radius $R_0 > r_0$ convergent radial flows of hydrogen appear. They equalize the density and the chemical constitution of the plasma inside the star. If a typical time of the thermonuclear reactions is τ_0 , then at $\rho \approx \text{const}$ we can write the following effective continuity equation for the incompressible liquid (gas) with account of the spherical symmetry of the problem

$$\frac{\partial v_r}{\partial r} + \frac{2}{r}v_r = \begin{cases} -1/\tau_0, & r \leq r_0, \\ 0, & r_0 < r \leq R_0. \end{cases} \quad (57)$$

A solution of the equation (57) for the radial hydrodynamic velocity takes the form:

$$v_r = \begin{cases} -r/3\tau_0, & r \leq r_0, \\ -r_0^3/3\tau_0 r^2, & r_0 < r \leq R_0. \end{cases} \quad (58)$$

Below we neglect a high conductivity of the hot plasma and different electromagnetic effects and interactions with magnetic fields. In this situation, from the macroscopic point of view the hydrodynamic rotational motion of the dense electro-neutral plasma inside a spherically symmetric star can be approximately described by the conventional Navier-Stokes equations with account of the gravity forces. We can see that the radial dependencies (58) provide nullification of the term describing the bulk viscosity, i.e.

$$v_r \frac{\partial v_r}{\partial r} - \frac{v_\varphi^2}{r} = -\frac{1}{\rho} \frac{\partial P}{\partial r} - g(r). \quad (59)$$

On the other hand, if we chose the azimuth velocity v_φ in the form

$$v_\varphi(r, \theta) = \omega \sin \theta \begin{cases} r, & r \leq r_0, \\ r_0^2/r, & r_0 < r \leq R_0, \end{cases} \quad (60)$$

the term with the first viscosity will be nullified also. Substituting (58) and (60) into (59) and performing integration, we obtain the pressure distribution with account of gravitation inside the star:

$$P = \begin{cases} P_0 - \frac{\rho r^2}{2} \left[\frac{1}{9\tau_0^2} + \frac{4\pi}{3} G\rho - \omega^2 \sin^2 \theta \right], & r \leq r_0, \\ P_0 - \frac{\rho r^2}{2} \left[\frac{1}{9\tau_0^2} \frac{r_0^6}{r^6} + \frac{4\pi}{3} G\rho - \omega^2 \sin^2 \theta \right] - \\ -\rho g_0(r - r_0), & r_0 < r \leq R_0. \end{cases} \quad (61)$$

Here, for the sake of simplicity, we assume that the in the star bulk is homogeneous.

Substituting (60) in the l.h.s. of the second Navier-Stokes equation in spherical coordinates, we get:

$$\frac{d\omega}{dt} = \begin{cases} 2\omega/3\tau_0, & r \leq r_0, \\ 0, & r_0 < r \leq R_0. \end{cases} \quad (62)$$

From this at $\tau_0 = \text{const}$ we again obtain the exponential law of increasing of the angular velocity of “rigid” rotation of the substance in the bulk of the central core and a constant value of ω in the external domain:

$$\omega(t) = \begin{cases} \omega(0) e^{2t/3\tau_0}, & r \leq r_0, \\ \omega(0) = \text{const}, & r_0 < r \leq R_0. \end{cases} \quad (63)$$

This means that at the core border $r = r_0$ a step of the azimuth velocity increases in time:

$$\Delta v_\varphi(t) = [\omega(t) - \omega(0)]r_0 \sin \theta. \quad (64)$$

According to the calculations it causes the unstable surface perturbations and to development of the strong turbulence. This results in the stationary turbulent regime in some domain near the core border where at the expense of the anomalous turbulent viscosity $\nu^* \gg \nu$ when there is a constant difference between the velocities of rotation of the star central core and its envelop. The developed turbulent pulsations on the border between the core and its envelop may stimulate the active turbulence that is observed in the Sun atmosphere. However, an analysis of these phenomena with account of the Sun magnetic field perturbations requires the equations of magnetic hydrodynamics.

4. One-component liquid with accelerated flows: the mechanism of formation of a funnel and a windspout

One of the most interesting paradoxes in hydrodynamics is the so-called “funnel effect” (see [1, 7]). It is assumed, that this effect is caused by the conservation laws of the angular momenta of the incompressible liquid (gas) inside the given contour, and accompanied by the accelerated rotation of a vortex at concentration of vorticity a flow $\omega = \text{rot } \mathbf{v}$ due to the narrowing of the channel. Another approach to the problem of a funnel formation lies in the assumption (see [8]) about origination of the angular momentum at a zero initial vorticity as a result of instability of cylindrically-symmetric flow in a liquid (the flooded jet) in relation to axially-asymmetric left- and right-spiral perturbations with carrying out of rotation of a certain sign to the infinity at the expense of a flow (convective instability) and accumulation of a rotation motion of another sign (absolute instability).

Let us show, that there exist one more simple mechanism of a vortex formation in the incompressible liquid (gas), which is in a gravitational field and includes vertical ascending or descending flows, whose velocities depend on the coordinate z (along the vertical axis of a vortex). We consider Navier-Stokes equation for axially-symmetric motion of the incompressible viscous liquid (gas) in cylindrical coordinates:

$$\frac{\partial v_r}{\partial t} + v_r \frac{\partial v_r}{\partial r} - \frac{v_\varphi^2}{r} = -\frac{1}{\rho} \frac{\partial P}{\partial r} + \nu \left(\frac{\partial^2 v_r}{\partial r^2} + \frac{1}{r} \frac{\partial v_r}{\partial r} - \frac{v_r}{r^2} \right), \quad (65)$$

$$\frac{\partial v_\varphi}{\partial t} + v_r \frac{\partial v_\varphi}{\partial r} + \frac{v_r v_\varphi}{r} = \nu \left(\frac{\partial^2 v_\varphi}{\partial r^2} + \frac{1}{r} \frac{\partial v_\varphi}{\partial r} - \frac{v_\varphi}{r^2} \right), \quad (66)$$

$$\frac{\partial v_z}{\partial t} + v_r \frac{\partial v_z}{\partial r} + v_z \frac{\partial v_z}{\partial z} = -\frac{1}{\rho} \frac{\partial P}{\partial z} - g + \nu \left(\frac{\partial^2 v_z}{\partial r^2} + \frac{1}{r} \frac{\partial v_z}{\partial r} + \frac{\partial^2 v_z}{\partial z^2} \right), \quad (67)$$

where v_r, v_φ and v_z are radial, azimuthal and axial components of hydrodynamical velocity \mathbf{v} , P and ρ — pressure and density of a liquid (gas), $\nu = \eta/\rho$ — a coefficient of kinematic viscosity, and g — the gravity acceleration, which is directed opposite to axis z .

Equations (65)–(67) must be completed with the continuity equation

$$\operatorname{div} \mathbf{v} = \frac{\partial v_r}{\partial r} + \frac{v_r}{r} + \frac{\partial v_z}{\partial z} = 0. \quad (68)$$

Let us notice that in equations (65) and (66) the dependencies of v_r and v_φ on z are not taken into account for simplification reasons. We shall also notice, that despite the axial symmetry, the expression near the factor ν in the right hand parts of equations (65) and (66) we formally have a kind of the Laplace operator for a certain scalar complex function $f(r) e^{i\varphi}$, where the azimuthal angle φ plays a role of a phase, which by physical sense is similar to the well-known Berry phase.

In case of a plane vortical rotation, when $v_r = v_z = 0$, equations (65) and (66) become a form:

$$\frac{v_\varphi^2}{r} = \frac{1}{\rho} \frac{dP}{dr}, \quad (69)$$

$$\frac{\partial v_\varphi}{\partial t} = \nu \left(\frac{\partial^2 v_\varphi}{\partial r^2} + \frac{1}{r} \frac{\partial v_\varphi}{\partial r} - \frac{v_\varphi}{r^2} \right). \quad (70)$$

If a radial dependence of the azimuthal velocity $v_\varphi(r)$, according to the Rankine vortex model (see [1]), is chosen as

$$v_\varphi(r) = \begin{cases} \omega r, & r \leq R_0, \\ \omega R_0^2/r, & r > R_0, \end{cases} \quad (71)$$

than the right hand part of equation (70) equals identically to zero, what corresponds to the rotation of an incompressible liquid (gas) with a constant angular velocity $\omega = \text{const}$.

At this, a distribution of hydrodynamical pressure $P(r)$, according to (65), in the so-called cyclostrophic rotation regime has a form:

$$P(r) = \begin{cases} P_0 + \rho\omega^2 r^2/2, & r \leq R_0, \\ P_\infty - \rho\omega^2 R_0^4/2r^2, & r > R_0, \end{cases} \quad (72)$$

where $P_0 = (P_\infty - \rho\omega^2 R_0^2)$ is the pressure on the vortex axis, and P_∞ — the pressure on large distances (at $r \rightarrow \infty$).

In the Rankine model a radius of a vortex core R_0 is not determined, but if in a liquid (gas) a cylindrically-symmetric flow (the flooded jet) exists with a velocity v_z , than its radius will determine the size R_0 in (71). Let us assume, that the flow velocity depends linearly on the coordinate z and does not depend on r in the area $r \leq R_0$, i.e.

$$v_z(z) = \begin{cases} v_{z0} + \alpha z, & r \leq R_0, \\ 0, & r > R_0. \end{cases} \quad (73)$$

In this case the continuity equation (68) is satisfied for the following radial dependence of velocity v_r , continuous at $r = R_0$:

$$v_r(r) = \begin{cases} -\frac{1}{2}\alpha r, & r \leq R_0, \\ -\frac{1}{2}\alpha \frac{R_0^2}{r}, & r > R_0. \end{cases} \quad (74)$$

Let us notice, that the above mentioned structures of velocities (71), (73) and (74) nullify viscous terms in equations (65)–(67). At the same time, the diagonal components of the viscous stress tensor for these profiles are distinct from zero and result in the following expression for the change of kinetic energy of a vortex due to dissipation (by unit of length of a vortex along the axis z):

$$\left(\frac{dE_{\text{kin}}}{dt}\right)_{\text{dis}} = -4\pi\rho\nu \left[\frac{3}{2}\alpha^2 + \omega^2(0)\right] R_0^2. \quad (75)$$

Substituting expressions (71) and (74) in the equation (66), we get:

$$\frac{d\omega}{dt} = \begin{cases} \alpha\omega, & r \leq R_0, \\ 0, & r > R_0. \end{cases} \quad (76)$$

Equation (76) is a result of that in the inner region ($r \leq R_0$) the convertive and Coriolis forces at $v_r \neq 0$ are added up, but in the external region ($r > R_0$) they mutually compensate one another.

If the parameter α is constant in time ($\alpha = \text{const}$, $\frac{d\alpha}{dt} = 0$) and positive $\alpha > 0$, than from equation (76) it follows, that inside the area $r \leq R_0$ an angular velocity of a vortex grows in time due to the exponential law

$$\omega(t) = \omega(0) e^{\alpha t}, \quad (77)$$

provided that a nonzero initial vorticity $\omega(0) \neq 0$ exist in a liquid (gas), whereas in the external area $\omega = \omega(0) = \text{const}$. Thus, on the border of a vortex core $r = R_0$ a jump of azimuthal velocity, which exponentially grows in time, arises (see section 4).

Let us emphasize, that energy dissipation (75) at the non-stationary vortical motion does not depend on time t , and is determined only by the initial vorticity $2\omega(0)$. Thus, a dissipation remains small, despite the fast increase of an angular velocity of a “rigid-body” rotation of a vortex core. This means, that non-stationary vortices are not suppressed by the dissipation at the initial stage of their developments.

On the other hand, substituting (71), (73) and (74) in equations (65) and (67), we get the following equations for the determination of a pressure:

$$\frac{\partial P}{\partial r} = \begin{cases} \rho r \left[\omega^2(t) - \frac{\alpha^2(t)}{4} + \frac{1}{2} \frac{d\alpha}{dt} \right], & r \leq R_0, \\ \frac{\rho R_0^4}{r^3} \left[\omega^2(0) + \frac{\alpha^2(t)}{4} + \frac{1}{2} \frac{d\alpha}{dt} \frac{r^2}{R_0^2} \right], & r > R_0, \end{cases} \quad (78)$$

$$\frac{\partial P}{\partial z} = \begin{cases} -\rho \left[g + \alpha v_{z0} + z \left(\frac{d\alpha}{dt} + \alpha^2 \right) \right], & r \leq R_0, \\ -\rho g, & r > R_0. \end{cases} \quad (79)$$

Let us notice, that equations (78) and (79) indicate on the existence and increasing in time of step of the first derivatives of the pressure $\partial P/\partial r$ and $\partial P/\partial z$ on a surface of a vortex core $r = R_0$. From equation (79) a possibility of existence of the non-stationary solution with $\frac{d\alpha}{dt} \neq 0$ follows, namely:

$$\frac{d\alpha}{dt} + \alpha^2(t) = 0, \quad \frac{\partial P}{\partial z} \pm \rho g = 0. \quad (80)$$

The first equation (80) at $\alpha > 0$ has a solution:

$$\alpha(t) = \frac{\alpha_0}{1 + \alpha_0 t}, \quad \alpha_0 \equiv \alpha(0) > 0, \quad (81)$$

whereas the second equation (80) corresponds to hydrostatic pressure distribution in the whole space, and the sign (+) corresponds to an ascending flow (the axis z is directed upwards), and the sign (–) — to a descending flow (the

axis z is directed downwards). In this case equation (76) in the area $r \leq R_0$ has a solution

$$\omega(t) = \omega(0) \exp \left\{ \int_0^t \frac{\alpha_0 dt'}{1 + \alpha_0 t'} \right\} = \omega(0)(1 + \alpha_0 t), \quad (82)$$

which corresponds to the linear growth in time of velocity of a vortex rotation.

At last, we should notice that equation (76) under condition of $\alpha(t) = \omega(t) > 0$ takes a form:

$$\frac{d\omega}{dt} - \omega^2(t) = 0. \quad (83)$$

The solution of the nonlinear equation (83) corresponds to the so-called “explosive” instability:

$$\omega(t) \equiv \alpha(t) = \frac{\omega(0)}{1 - \omega(0)t}, \quad (84)$$

when in a final time interval $t_0 = 1/\omega(0) \equiv 1/\alpha(0)$ the angular velocity of a liquid rotation $\omega(t)$ and the derivative of the axial velocity on z , $\alpha(t) \equiv \partial v_z / \partial z$, rise formally to infinity, although they are actually limited from the above due to satisfying of the incompressibility condition of a liquid (see below).

The positive sign of α corresponds to the growth of velocity of a flow along the axis z directed by velocity v_{z0} . Thus, in a descending flow of a liquid which flows out through a hole at the bottom under the action of gravitation and accelerates along the axis z by a linear law (73), we get the exponential (77), linear (82), or “explosive” (84) laws of vortex rotation velocity growths in time. At this, the amount of a liquid, which flows out, is completely compensated by the inflow of the same amount of a liquid with velocity of a converging radial flow (74) from the surrounding volume, which is considered as an enough large reservoir of the substance.

Such a simple model explains the funnel formation in a bath at the opening of a hole or an whirlpool formation on a small river in the place of a sharp deepening of the bottom. The going out of exponential rotation velocity growth of a liquid (water) on the stationary regime is caused by the friction with a solid fixed surfaces, and also by the energy dissipation on the tangential step of the azimuthal velocity v_φ at the point $r = R_0$ (see below).

This model can also explain the origination of sandy tornados in deserts. Due to a strong heating by the sunlight of some sites of a surface of a sandy ground (the darkest or located perpendicularly to the solar rays), the nearby air gets warm locally and starts to rise upwards with acceleration under the action of the Archimedian force, as more light. If this acceleration in a quasi-stationary conditions corresponds approximately to the linear by z law (73), than at $\alpha > 0$ we again obtain the exponential law of rotation velocity growth of a vortex (77). At this, the accelerated decreasing in time of the pressure in

the vortex axis $r = 0$ with $\omega(t)$ and $\alpha(t)$ increasing leads to the suction of sand deep into the vortex and formation of a visible tornado, which is frequently observed in deserts.

4.1. FORMATION OF A TORNADO FUNNEL WITH ACCOUNT OF GRAVITY AND VERTICAL FLOWS OF AIR

As marked above, for flows of the air, which flow into a rain cloud of a cylindrical form at the time of its condensation, the following hydrodynamical velocities are characteristic:

$$v_r = \begin{cases} -\beta r, & r \leq R_0, \\ -\beta R_0^2/r, & r > R_0, \end{cases} \quad v_\varphi = \begin{cases} \omega r, & r \leq R_0, \\ \omega R_0^2/r, & r > R_0, \end{cases} \quad v_z = \begin{cases} v_{z0} + \alpha z, & r \leq R_0, \\ 0, & r > R_0, \end{cases} \quad (85)$$

where $2\beta = \alpha + |Q|/\rho$. In the case of exponential instability we have $\omega(t) = \omega(0) e^{2\beta t}$ (at $\alpha = \text{const}$ and $|Q| = \text{const}$). At this, bulk viscous forces in equations (65)–(67) equal identically to the zero, so that we get:

$$\frac{\partial P}{\partial r} = \begin{cases} \rho r [\omega^2(t) - \beta^2], & r \leq R_0, \\ \frac{\rho R_0^4}{r^3} [\omega^2(0) + \beta^2], & r > R_0, \end{cases} \quad (86)$$

$$\frac{\partial P}{\partial z} = \begin{cases} -\rho \tilde{g} - \rho \alpha^2 z, & \tilde{g} = g + \alpha v_{z0}, \quad r \leq R_0, \\ -\rho g, & r > R_0. \end{cases} \quad (87)$$

The integration of equations (86) and (87) determines a difference of the pressure between two arbitrary points

$$P_2 - P_1 = \begin{cases} -\rho \tilde{g}(z_2 - z_1) - \frac{\rho}{2} \alpha^2 (z_2^2 - z_1^2) + \frac{\rho}{2} [\omega^2(t) - \beta^2] (r_2^2 - r_1^2), & r_{1,2} \leq R_0, \\ -\rho \tilde{g}(z_2 - z_1) - \frac{\rho R_0^4}{2} [\omega^2(0) + \beta^2] \left(\frac{1}{r_2^2} - \frac{1}{r_1^2} \right), & r_{1,2} > R_0. \end{cases} \quad (88)$$

From (88) it follows, that the form of a surface of the constant pressure (an isobar), which corresponds to the point of water drops evaporation P_{evp} , in the internal area $r \leq R_0$ is determined by the equation

$$z^2(r, t) + \frac{2\tilde{g}}{\alpha^2} z(r, t) + \frac{R_0^2}{\alpha^2} [\omega^2(t) + \omega^2(0)] - \frac{r^2}{\alpha^2} [\omega^2(t) - \beta^2] - \frac{2(P_\infty - P_{\text{evp}})}{\rho \alpha^2} = 0, \quad (89)$$

where the coordinate z is counted from the initial flat surface $P_0 = P_\infty = P_{\text{evp}}$, and in the external area $r > R_0$ is set by the relation

$$z(r, t) = z_0(t) - \frac{[\omega^2(0) + \beta^2] R_0^4}{2gr^2} + \frac{(P_\infty - P_{\text{evp}})}{\rho g}, \quad (90)$$

where the function $z_0(t)$ is determined from the condition of isobar continuity in the point $r = R_0$. According to equation (89), we find value coordinates $z(r, t)$ in the point $r = R_0$:

$$z(R_0, t) = -\frac{\tilde{g}}{\alpha^2} + \sqrt{\frac{\tilde{g}^2}{\alpha^4} - \frac{[\omega^2(0) + \beta^2] R_0^2}{\alpha^2} + \frac{2(P_\infty - P_{\text{evp}})}{\rho\alpha^2}} = \text{const}, \quad (91)$$

so that

$$z_0 = z(R_0) + \frac{R_0^2}{2g} [\omega^2(0) + \beta^2] - \frac{(P_\infty - P_{\text{evp}})}{\rho g} = \text{const}, \quad (92)$$

i.e. in the external area $r > R_0$ a form of the isobar does not depend on time.

The coordinate of a point of the isobar on a vortex axis at $r = 0$, according to (89)–(92), is determined by the expression

$$z(0, t) = -\frac{\tilde{g}}{\alpha^2} + \sqrt{\frac{\tilde{g}^2}{\alpha^4} - \frac{R_0^2 [\omega^2(t) + \omega^2(0)]}{\alpha^2} + \frac{2(P_\infty - P_{\text{evp}})}{\rho\alpha^2}}. \quad (93)$$

From here it follows, that at $\tilde{g} > 0$, with growth of the angular velocity $\omega(t)$ in result of the exponential instability there is an increasing of the absolute value of the negative coordinate $z(0, t)$, what corresponds to the deepening of a minimum of function $z(r, t)$ in the area $z < 0$.

We can conclude, that the account of gravity and vertical flows allows to describe one of the main observable phenomena — a funnel formation on the bottom edge of a cloud during origination and development of tornados.

4.2. DISCUSSION OF APPLICABILITY OF THE DERIVED RESULTS FOR THE DESCRIPTION OF TORNADOS AND TYPHOONS

With the purpose of finding-out of applicability of the obtained new non-stationary solutions of Navier-Stokes and continuity equations for incompressible viscous media with a bulk sink and free inflow of the substance for the description of atmospheric vortices (tornados and typhoons) we will carry out numerical estimations of characteristic times of development of the considered above hydrodynamical instabilities of the vortical motion in conditions of intensive condensation of moisture inside a cloud.

Let us consider a round cylindrical cloud of a radius $R_0 \approx 1 \div 10$ km, which slowly rotates in the twirled air flow, with equal by order initial values of azimuthal and radial velocities on the border of a cloud $v_{r0} \approx v_{\varphi 0} \approx (1 \div 10)$ m/s. This corresponds to absolute values of initial angular velocity $\omega(0)$ and velocities of a converging radial flow β in the range $(10^{-4} \div 10^{-2})$ s⁻¹. At

humidity of atmospheric air of about 100%, its density almost twice exceeds density of the dry air $\rho = 1.3 \times 10^{-3} \text{ g/sm}^3$, so that the mentioned values of the parameter β are equivalent to capacities of a bulk sink Q due to condensation of a moisture of the order of $\sim 5 \times (10^{-7} \div 10^{-5}) \text{ g/s}\cdot\text{sm}^3$. In these conditions a characteristic time of acceleration of a vortex rotation in a result of exponential instability equals $\tau = 1/2\beta \approx (1 \div 100) \text{ min}$.

The maximal velocity of the order of c_s is reached for a time interval of $t \approx (3 \div 500) \text{ min}$. Typical observable times of origination and development of a tornado lie just in such a time interval (from several minutes to several hours).

For large-scale atmospheric vortices such as cyclones, hurricanes and typhoons, which originate in cloud masses with sizes of about 100 km and more, characteristic times of development of the instability increase by two – three orders and can reach several days, that also agrees with observable times of hurricane and typhoon existence. At the same time, the decreased pressure on the axis of a vortex caused by a cyclostrophic rotation regime explains the characteristic “suck” effect of a tornado.

Moreover, as it was marked above, in a two-phase system “air — water drops” a decreasing of the pressure below the boiling point of water at the given temperature should result in the termination of condensation of moisture and in evaporation of the drops. This explains the formation of a clear tornado “core” or a typhoon “eye” in the central part of a cloud system in the paraxial area of a vortex. Inside this area the velocity of a vortical rotation of the air slows down in time, as at a condition of $P < P_{\text{evp}}$ instead of a bulk sink ($Q < 0$) there is a source of a gas phase ($Q > 0$), and the parameter β changes its sign ($\beta < 0$), what corresponds to an exponential decelerating of the air. Such a condition of a dead calm is observed in the center “eye” of a typhoon.

It is possible to estimate the time of a tornado funnel contact with the surface of the Earth. In the case of exponential instability, at $z = -H$ (where H is the height of the bottom edge of a cloud above the ground), according to equation (93), at the conditions $\omega^2(t) \gg \beta^2$ and $\tilde{g}/\alpha^2 \gg H$ we find a time interval till this contact

$$t_H = \frac{1}{4\beta} \ln \left[\frac{\tilde{g}}{\omega^2(0)R_0^2} \right]. \quad (94)$$

At $H = 1 \text{ km}$ for the above mentioned values for $v_{\varphi 0}$ we get an estimation: $t_H \approx (1 \div 250) \text{ minutes}$, what in good correspondence with the observed phenomena.

5. Conclusions

In this paper a new class of exact solutions of hydrodynamics equations for an incompressible liquid (gas) at presence of a bulk sink and ascending flows of a substance has been considered. It is essential that one or several species of the system are gone under some dynamical process, for instance nuclear (chemical) reactions or phase transitions, from the general collective hydrodynamic motion. It is shown that those profiles, which nullify the terms in Navier-Stokes equation which describe viscous effects, exist and represent vortex structures with “rigid-body” rotation of the core and converging radial flows. In the case of constant bulk sink and inflow of the matter from the outside, the azimuthal velocity of a “rigid-body” rotation v_φ increases exponentially with time. At simultaneous infinite increasing of the sink and inflow rates, v_φ increases by scenario of the “explosive” instability when during a finite time interval the infinite rotation velocity is reached. We apply this hydrodynamic approach for description of the rotational motion of nuclear matter, which appears in the relativistic collisions of heavy nuclei with an initial angular momentum. We show that the acceleration of the rotation velocity of non-stationary vortices in nuclear matter has an explosive character.

On the basis of the developed theory of unstable hydrodynamical vortices an offered in [2] mechanism of origination and development of powerful atmospheric vortices — tornados and typhoons — during the intensive condensation of water vapor from the cooled below a dew point humid air at formation of dense rain clouds is considered. Within the framework of this mechanism it is possible to explain the basic characteristics of tornados and typhoons. Estimations of characteristic times of instability development of vortical motion are agreed by orders with the corresponding times of origination and existence of tornados (from several minutes till several hours) and typhoons (several days). With the account of gravity the given model describes the main phenomenon of a tornado — formation of a lengthening funnel on the bottom edge of a cloud in result of changing form of the surface of a constant pressure (isobar), that limits from the below the area of intensive condensation of moisture. The velocity step on the border of a tornado core results in the development of a strong turbulence, which can be described with the help of anomalous coefficient of turbulent viscosity, which in many orders exceeds the usual viscosity of the air.

Thus, the above considered non-stationary vortical structures are characteristic for all viscous liquids. In particular, in the classical hydrodynamics a favorable condition for the origination and existence of such vortices is nullification of the terms, which describe kinematic viscosity of the incom-

pressible liquid, in the cases of cylindrical and spherical symmetries. Such flows have the minimal energy dissipation, i.e. correspond to a peculiar “minimal entropy production principle”, and therefore relatively easily realize in the corresponding natural conditions.

References

- 1 *Kundu P.K.* Fluid Mechanics. — Academic Press, 1990.
- 2 *Pashitsky E.A.* Applied Hydromechanics **4** (76) (2002) 50 (in Russian).
- 3 *Landau L.D.*, *Izv. AN SSSR, Ser. Fiz.* **17** (1953) 51.
- 4 *Bjorken J.D.*, *Phys. Rev. D* **27** (1983) 140.
- 5 *McLerran L.*, *Pramana* **60** (2003) 575; [arXiv: hep-ph/0202025 (2002)].
- 6 *Adler C. et al.* (STAR Collaboration), *Phys. Rev. C* **66** (2002) 034904.
- 7 *Sedov L.I.* Mechanics of Continuum [in Russian]. — Moscow: Nauka, V.1 1983, V.2 1984.
- 8 *Gol’gshtik M.A., Shtern V.N., Yavorskii N.I.*, Viscous Flows with Paradoxical Properties [in Russian]. — Novosibirsk: Nauka, 1989.

ONSET OF DECONFINEMENT AND CRITICAL POINT – FUTURE ION PROGRAM AT THE CERN SPS

Marek Gaździcki (marek.gazdzicki@cern.ch)
*Institut für Kernphysik, University of Frankfurt, Germany and
Swietokrzyska Academy, Kielce, Poland*

Abstract. A new experimental program to study hadron production in collisions of nuclei at the CERN SPS is presented. It will focus on measurements of fluctuations and long correlations with the aim to identify properties of the onset of deconfinement and search for the critical point of strongly interacting matter.

Key words: quark-gluon plasma, deconfinement, critical point, relativistic nuclear collisions

1. Introduction

Over the 50 years of CERN history numerous experimental programs were devoted to a study of the properties of strong interactions [1]. Rich data on collisions of hadron and ion beams were collected. These results together with the data from other world laboratories have significant impact on our understanding of strong interactions and at the same time lead to new questions and define directions of future experimental and theoretical studies [2]. In particular, recently obtained exciting results [3, 4] on nucleus-nucleus collisions from the CERN SPS and the BNL RHIC suggest that the onset of deconfinement is located at the low SPS energies [5]. The most important open issues related to this finding are as follows. Is it possible to observe the predicted signals of the onset of deconfinement in fluctuations and anisotropic flow measurements? What is the nature of the transition from the anomalous energy dependence seen in the central Pb+Pb collisions at the SPS energies to the smooth dependence observed in p+p interactions? Does the critical point of strongly interacting matter exist and, if it does, where is it located?

In order to answer these questions it was proposed [6] to perform a sequence of new measurements of hadron production in collisions of protons and nuclei with nuclear targets at CERN by use of the upgraded NA49 apparatus [7].

The NA49 apparatus at the CERN SPS served during the last 10 years as a very reliable, large acceptance hadron spectrometer and delivered unique

high precision experimental data over the full range of SPS beams (from proton to lead) [8, 10] and energies (from 20A GeV to 200A GeV) [3, 4]. The most efficient and cost effective way to reach the physics goals of the proposed new experimental program is to use the upgraded NA49 detector, its reconstruction software and over many years accumulated experience in physics analysis.

The paper is organized as follows. The key physics questions addressed by the new program are formulated in Section 2. The basic requirements concerning the future measurements are discussed in Section 3. In Section 4 different experimental opportunities to study nucleus-nucleus collisions are briefly reviewed. The paper is closed by the summary, Section 5.

2. Key questions

One of the key issues of contemporary physics is the understanding of strong interactions and in particular the study of the properties of strongly interacting matter in equilibrium. What are the phases of this matter and how do the transitions between them look like are questions which motivate a broad experimental and theoretical effort. The study of high energy nucleus-nucleus collisions gives us a unique possibility to address these questions in well-controlled laboratory experiments.

2.1. ONSET OF DECONFINEMENT

Recent results [3, 4] on the energy dependence of hadron production in central Pb+Pb collisions at 20A, 30A, 40A, 80A and 158A GeV coming from the energy scan program at the CERN SPS serve as evidence for the existence of a transition to a new form of strongly interacting matter, the Quark Gluon Plasma (QGP) in nature [5]. Thus they are in agreement with the conjectures that at the top SPS and RHIC energies the matter created at the early stage of central Pb+Pb (Au+Au) collisions is in the state of QGP [11, 15]. The key results are summarized in Fig. 1.

The most dramatic effect can be seen in the energy dependence of the ratio $\langle K^+ \rangle / \langle \pi^+ \rangle$ of the mean multiplicities of K^+ and π^+ produced per event in central Pb+Pb collisions, which is plotted in the top panel of the figure. Following a fast threshold rise, the ratio passes through a sharp maximum in the SPS range and then seems to settle to a lower plateau value at higher energies. Kaons are the lightest strange hadrons and $\langle K^+ \rangle$ is equal to about half of the number of all anti-strange quarks produced in the collisions. Thus, the relative strangeness content of the produced matter passes through a sharp maximum at the SPS in nucleus-nucleus collisions. This feature is not observed for proton-proton reactions.

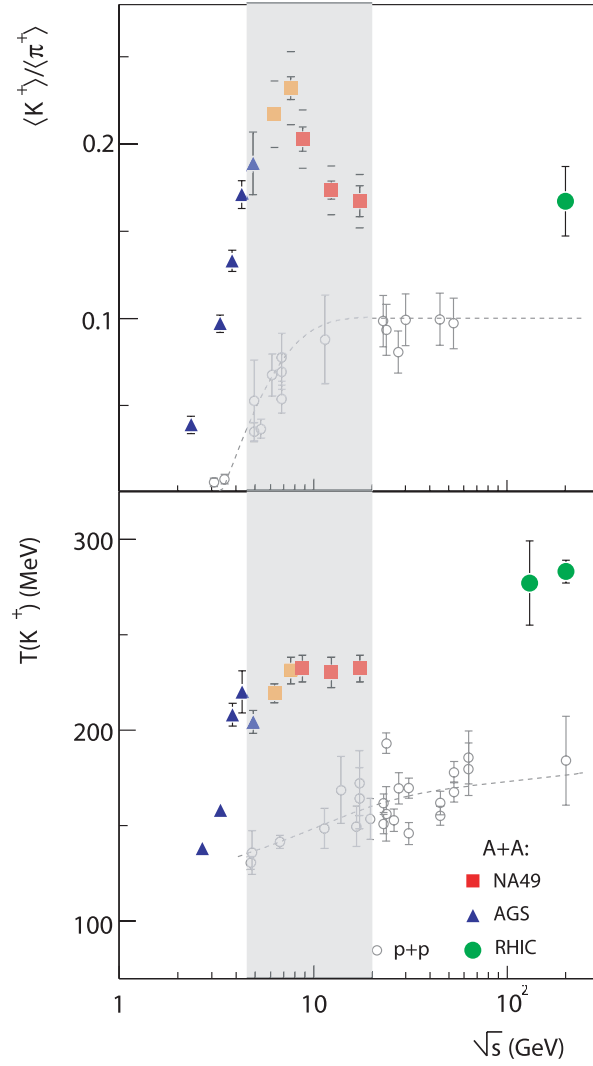


Figure 1. Collision energy dependence of the K^+ to π^+ ratio and the inverse slope parameter of the transverse mass spectra measured in central Pb+Pb and Au+Au collisions (solid symbols) compared to results from p+p reactions (open dots). The changes in the SPS energy range (solid squares) suggest the onset of the deconfinement phase transition. The energy region covered by the future measurements at the CERN SPS is indicated by the gray band.

A second important result is the constant value of the apparent temperature of K^+ mesons in central Pb+Pb collisions at low SPS energies as shown in the bottom panel of the figure. The plateau at the SPS energies is preceded by a steep rise of the apparent temperature at the AGS and followed by a further increase indicated by the RHIC data. Very different behaviour is measured in proton-proton interactions.

Presently, the sharp maximum and the following plateau in the energy dependence of the $\langle K^+ \rangle / \langle \pi^+ \rangle$ ratio has only been reproduced by the statistical model of the early stage [5] in which a first order phase transition is assumed. In this model the maximum reflects the decrease in the number ratio of strange to non-strange degrees of freedom and changes in their masses when deconfinement sets in. Moreover, the observed steepening of the increase in pion production is consistent with the expected excitation of the quark and gluon degrees of freedom. Finally, in the picture of the expanding fireball, the apparent temperature is related to the thermal motion of the particles and their collective expansion velocity. Collective expansion effects are expected to be important only in heavy ion collisions as they result from the pressure generated in the dense interacting matter. The stationary value of the apparent temperature of K^+ mesons may thus indicate an approximate constancy of the early stage temperature and pressure in the SPS energy range due to the coexistence of hadronic and deconfined phases, as in the case of the first order phase transition [19, 20].

Thus, the anomalies in the energy dependence of hadron production in central Pb+Pb collisions at the low SPS energies serve as evidence for the onset of deconfinement and the existence of QGP in nature. They are consistent with the hypotheses that the observed transition is of the first order. The anomalies are not observed in p+p interactions and they are not reproduced within hadronic models [21].

These results and their interpretation raise questions which can be answered only by new measurements. Two most important open problems are:

- is it possible to observe the predicted signals of the onset of deconfinement in fluctuations [23] and anisotropic flow [25]?
- what is the nature of the transition from the anomalous energy dependence measured in central Pb+Pb collisions at SPS energies to the smooth dependence measured in p+p interactions?

2.2. CRITICAL POINT

In the letter of Rajagopal, Shuryak, Stephanov and Wilczek addressed to the SPS Committee one reads: ... *Recent theoretical developments suggest that a key qualitative feature, namely a critical point (of strongly interacting matter)*

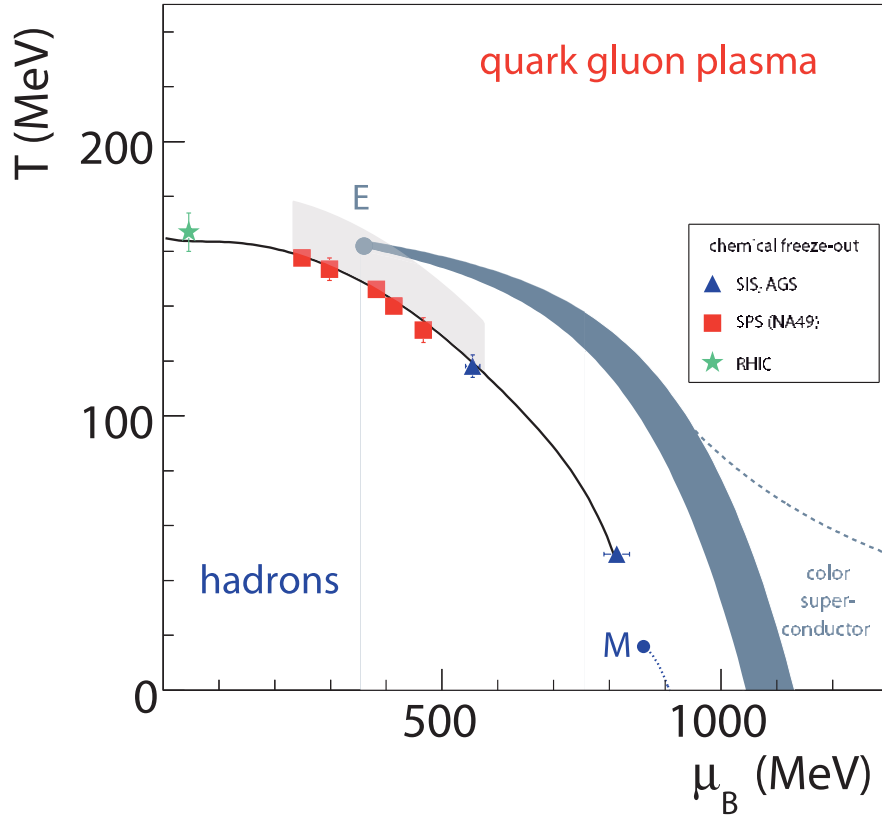


Figure 2. The hypothetical phase diagram of strongly interacting matter in the plane temperature, T , and baryonic chemical potential, μ_B . The end point **E** of the first order transition strip is the critical point of the second order. The chemical freeze-out points extracted from the analysis of hadron yields in central Pb+Pb (Au+Au) collisions at different energies are plotted by the solid symbols. The region covered by the future measurements at the CERN SPS is indicated by the gray band.

which in sense defines the landscape to be mapped, may be within reach of discovery and analysis by the SPS, if data is taken at several different energies. The discovery of the critical point would in stroke transform the map of the QCD phase diagram which we sketch below from one based only on reasonable inference from universality, lattice gauge theory and models into one within a solid experimental basis. ... More detailed argumentation is presented below.

Rich systematics of hadron multiplicities produced in nuclear collisions can be reasonably well described by hadron gas models [26, 27, 28]. Among the model parameters fitted to the data are temperature, T , and baryonic

chemical potential, μ_B , of the matter at the stage of the freeze-out of hadron composition (the chemical freeze-out). These parameters extracted for central Pb+Pb collisions at the CERN SPS energies are plotted in Fig. 2 together with the corresponding results for higher (RHIC) and lower (AGS, SIS) energies. With increasing collision energy T increases and μ_B decreases. A rapid increase of temperature is observed up to mid SPS energies, from the top SPS energy ($\sqrt{s_{NN}} = 17.2$ GeV) to the top RHIC energy ($\sqrt{s_{NN}} = 200$ GeV) the temperature increases only by about 10 MeV.

The sketch of the phase diagram of strongly interacting matter in the $(T - \mu_B)$ plane as suggested by QCD-based considerations [29, 30] is also shown in Fig. 2. To a large extent these predictions are qualitative, as QCD phenomenology at finite temperature and baryon number is one of the least explored domains of the theory. More quantitative results come from lattice QCD calculations which can be performed at $\mu_B = 0$. They strongly suggest a rapid crossover from the hadron gas to the QGP at the temperature $T_C = 170 - 190$ MeV [31, 32], which seems to be somewhat higher than the chemical freeze-out temperatures of central Pb+Pb collisions ($T = 150 - 170$ MeV) [33] at the top SPS and RHIC energies. The nature of the transition to QGP is expected to change due to the increasing baryo-chemical potential. At high potential the transition may be of the first order, where the end point of the first order transition domain, marked E in Fig. 2, is the critical point of the second order. Recently even richer structure of the phase transition to QGP was discussed within a statistical model of quark gluon bags [34]. It was suggested that the line of the first order phase transition at high μ_B is followed by the line of the second order phase transition at intermediate μ_B , and then by the lines of “higher order transitions” at low μ_B . A characteristic property of the second order phase transition (the critical point or line) is divergence of the susceptibilities. An important test for a second-order phase transition at the critical point is the validity of appropriate power laws in measurable quantities related to critical fluctuations. Techniques associated with such measurements in nuclear collisions have been developed recently [35] with emphasis on the sector of isoscalar di-pions (σ -mode) as required by the QCD conjecture for the critical end point in quark matter [29]. Employing such techniques in a study of nuclear collisions at different energies at the SPS and with nuclei of different sizes, the experiment may be confronted not only with the existence and location of the critical point but also with the size of critical fluctuations as given by the critical exponents of the QCD conjecture.

Thus when scanning the phase diagram a maximum of fluctuations located in a domain close to the critical point ($\Delta T \approx 15$ MeV and $\Delta\mu_B \approx 50$ MeV [36]) or the critical line should signal the second order phase transition. The position of the critical region is uncertain, but the best theoretical estimates based on lattice QCD calculations locate it at $T \approx 160$ MeV and

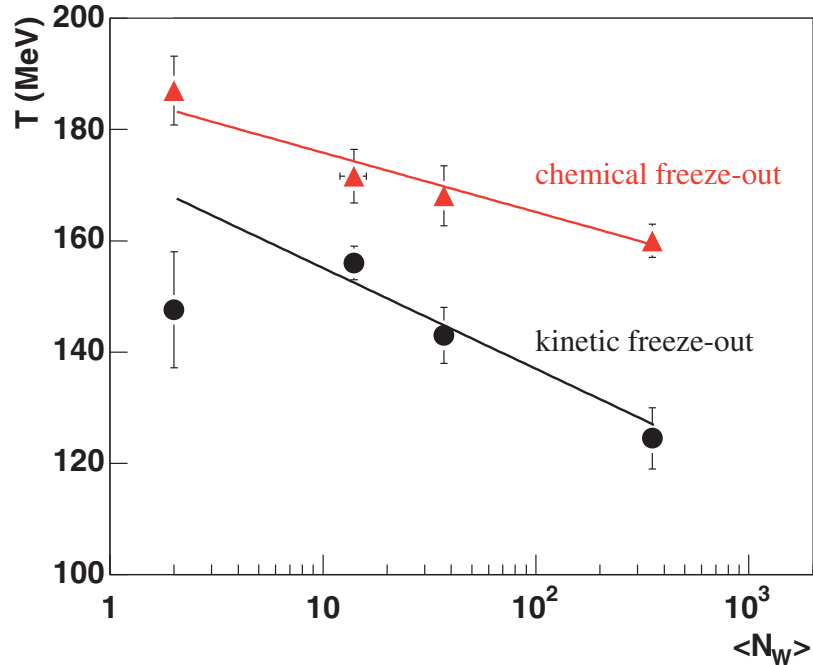


Figure 3. The dependence of the chemical and kinetic temperatures on the mean number of wounded nucleons for p+p, C+C, Si+Si and Pb+Pb collisions at 158A GeV.

$\mu_B \approx 360$ MeV [37, 38] as indicated in Fig. 2. It is thus in the vicinity of the chemical freeze-out points of central Pb+Pb collisions at the CERN SPS energies.

Pilot data [8] on interactions of light nuclei (Si+Si, C+C and p+p) taken by NA49 at 40A and 158A GeV indicate that the freeze-out temperature increases with decreasing mass number, A , of the colliding nuclei, see Fig. 3. This means that the scan in the collision energy and mass of the colliding nuclei allows us to scan the $(T - \mu_B)$ plane [39].

The experimental search for the critical point by investigating nuclear collisions is justified at energies higher than the energy of the onset of deconfinement. This is because the energy density at the early stage of the collision, which is relevant for the onset of deconfinement is higher than the energy density at the freeze-out, which is of the importance for the search for the critical point. The only anomalies possibly related to the onset of deconfinement are

measured at $\sqrt{s_{NN}} \approx 8$ GeV (see Fig. 1). This limits a search for the critical point to an energy range $\sqrt{s_{NN}} > 8$ GeV. Fortunately, as discussed above and illustrated in Fig. 2, the best theoretical predictions locate the critical point in the $(T - \mu_B)$ region accessible in nuclear collisions in this energy range. Thus the new measurements at the CERN SPS can answer the fundamental question:

- does the critical point of strongly interacting matter exist in nature and, if it does, where is it located?

3. General requirements

The physics goals of the new experimental program with nuclear beams at the CERN SPS presented in the previous section require the energy scan in the whole SPS energy range (10A-200A GeV) with light and intermediate mass nuclei. The measurements should be focused on the precise study of fluctuations and anisotropic flow. The first NA49 results on these subjects [40, 41, 42, 43, 44] suggest, in fact, presence of interesting effects for collisions with moderate number of participant nucleons and/or at low collision energies. However, a very limited set of data and serious resolution and acceptance limitations do not allow firm conclusions. The general physics needs when confronted with the NA49 results and experience suggest improvements of the current performance of the NA49 apparatus.

1. The event collection rate should be significantly increased in order to allow a fast registration of a sufficient statistics for a large number of different reactions (A , $\sqrt{s_{NN}}$).
2. The resolution in the event centrality determination based on the measurement of the energy of projectile spectator nucleons should be improved. This is important for high precision measurements of the event-by-event fluctuations.
3. The acceptance of the measurements of charged hadrons has to be increased and made as uniform as possible.

With this improved set-up we intend to register C+C, Si+Si and In+In collisions at 10A, 20A, 30A, 40A, 80A, 158A GeV and a typical number of recorded events per reaction is $2 \cdot 10^6$.

4. Experimental landscape

High energy nucleus-nucleus collisions have been studied experimentally since the beginning of 1970s in several international and national laboratories. Present and future accelerator facilities for relativistic nuclear beams are

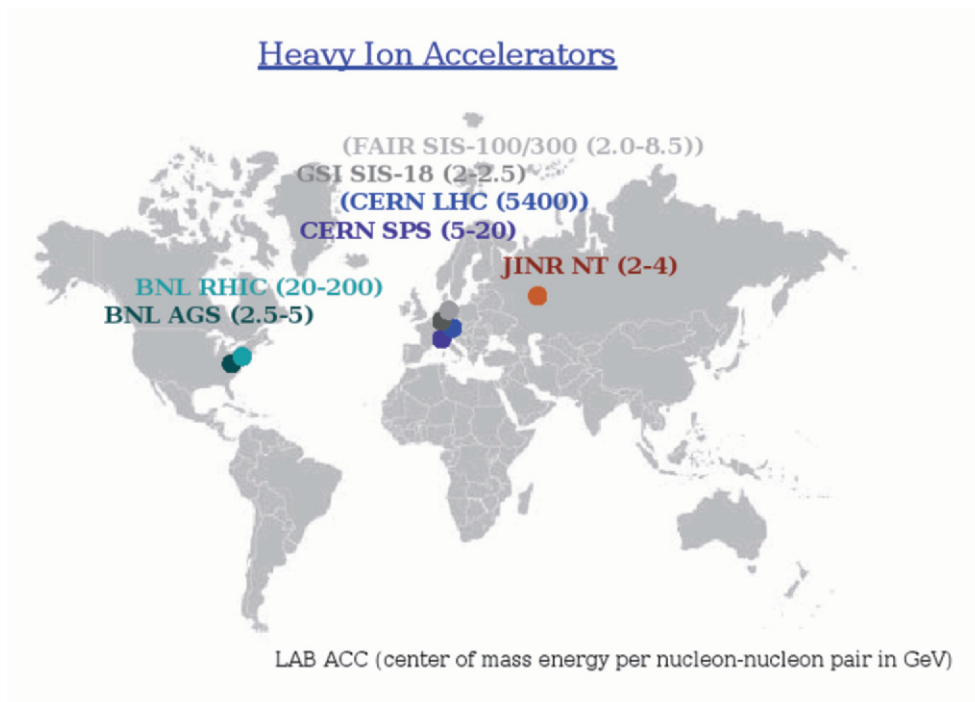


Figure 4. The present and future accelerators of relativistic nuclear beams. For each facility the name of the laboratory, the name of the accelerator and the energy range (center of mass energy per nucleon-nucleon pair in GeV) are given.

summarized in Fig. 4, where their nominal energy range is also given. They are ordered according to the top collision energy in Fig. 5. The basic physics of the strongly interacting matter which is related to a given energy domain is also given in Fig. 5.

In addition to the CERN SPS the physics of the onset of deconfinement and the critical point can be studied at the BNL RHIC [45].

Up to now the experiments at RHIC were performed in the collider mode in the energy range $\sqrt{s_{NN}} = 20 - 200$ GeV. It seems, however, plausible to run RHIC even at significantly lower energies [46], down to $\sqrt{s_{NN}} \approx 5$ GeV, and thus cover the SPS energy range. The advantages of this potential RHIC program would be:

- a broad collision energy range covered by a single experimental facility which yields small relative systematic errors of the resulting energy dependence of hadron production properties,
- a uniform and almost complete acceptance around midrapidity, provided the existing STAR apparatus is used in this study; it is important for the measurements of the anisotropic flow.

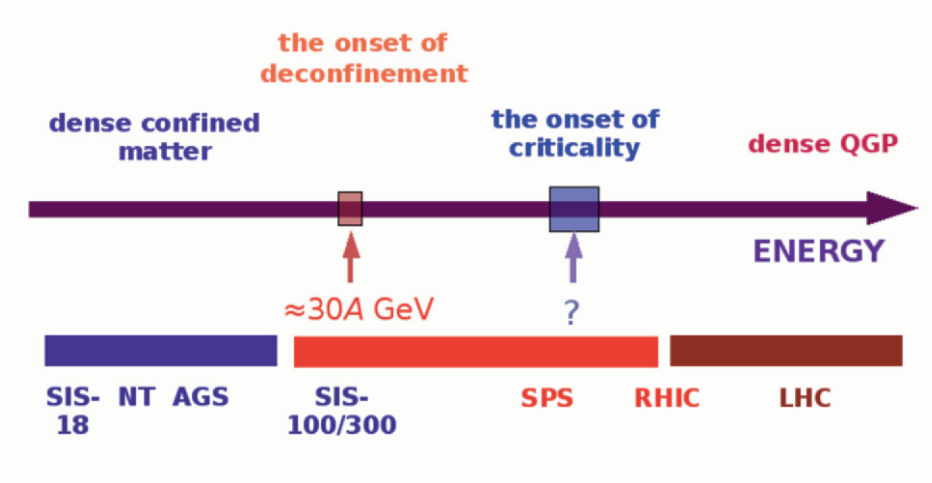


Figure 5. The accelerators of relativistic nuclear beams ordered according to the top collision energy and the basic physics of strongly interacting matter related to a given energy domain. The central horizontal bar indicates the energy range of the CERN SPS.

However, running experiments in the collider mode does not allow a measurement of the spectator fragments and thus a selection of events with a fixed number of interacting nucleons. The latter is important for event-by-event fluctuation studies, in particular fluctuations of extensive variables like particle multiplicity [43].

The RHIC accelerator can be used also as a fixed target machine. In this case the top energy is $\sqrt{s_{NN}} \approx 14$ GeV and the existing BRAHMS detector can be used for measurements of inclusive identified hadron spectra [45]. This option is considered as a possible fast cross-check of the NA49 results.

In view of the importance of the physics of the onset of deconfinement and the critical point it appears desirable to perform the experiments in both centers. The expected results will be complementary in the important aspects of fluctuations and anisotropic flow. The partial overlap of the results will allow the necessary experimental cross-checks.

5. Summary

The recent experimental and theoretical findings strongly suggest that a further study of nuclear collisions in the CERN SPS energy range is of particular importance. The new measurements can answer the questions concerning the nature of the onset of deconfinement and the existence and location of the critical point.

Consequently, a new experimental program to study hadron production in collisions of nuclei at the CERN SPS is proposed. It will focus on measurements of fluctuations and long correlations in C+C, Si+Si and In+In interactions at 10A, 20A, 30A, 40A, 80A and 158A GeV with the aim to identify properties of the onset of deconfinement and search for the critical point of strongly interacting matter. A parallel complementary effort at the BNL RHIC is strongly recommended.

Acknowledgements

This work is based on the Letter of Intent prepared by the NA49-future Collaboration. It was partly supported by Virtual Institute of Strongly Interacting Matter (VI-146) of Helmholtz Association, Germany.

References

- 1 R. Aymar et al., Phys. Rept. **403-404**, 1 (2004).
- 2 J. Dainton et al., [The CERN SPS and PS Committee], CERN-SPSC-2005-010, SPSC-M-730 (2005).
- 3 S. V. Afanasiev *et al.* [The NA49 Collaboration], Phys. Rev. C **66**, 054902 (2002) [arxiv:nucl-ex/0205002].
- 4 M. Gazdzicki *et al.* [NA49 Collaboration], J. Phys. G **30**, S701 (2004) [arXiv:nucl-ex/0403023].
- 5 M. Gazdzicki and M. I. Gorenstein, Acta Phys. Polon. B **30**, 2705 (1999) [arXiv:hep-ph/9803462].
- 6 J. Bartke et al., *A new experimental programme with nuclei and proton beams at the CERN SPS*, CERN-SPSC-2003-038(SPSC-EOI-01) and presentations at the Villars workshop 2004; N. Antoniou et al., *Study of hadron production in collisions of protons and nuclei at the CERN SPS*, the Letter of Intent in preparation.
- 7 S. Afanasev *et al.* [NA49 Collaboration], Nucl. Instrum. Meth. A **430**, 210 (1999).
- 8 C. Alt *et al.* [NA49 Collaboration], Phys. Rev. Lett. **94**, 052301 (2005) [arXiv:nucl-ex/0406031] and
- 9 P. Dinkelaker [NA49 Collaboration], J. Phys. G **31**, S1131 (2005).
- 10 C. Alt, arXiv:hep-ex/0510009.
- 11 U. W. Heinz and M. Jacob, arXiv:nucl-th/0002042,
- 12 J. Rafelski and B. Muller, Phys. Rev. Lett. **48**, 1066 (1982) [Erratum-ibid. **56**, 2334 (1986)],
- 13 T. Matsui and H. Satz, Phys. Lett. B **178**, 416 (1986),
- 14 F. Becattini, L. Maiani, F. Piccinini, A. D. Polosa and V. Riquer, arXiv:hep-ph/0508188.
- 15 I. Arsene *et al.* [BRAHMS Collaboration], Nucl. Phys. A **757**, 1 (2005) [arXiv:nucl-ex/0410020],
- 16 B. B. Back *et al.*, Nucl. Phys. A **757**, 28 (2005) [arXiv:nucl-ex/0410022],

- 17 J. Adams *et al.* [STAR Collaboration], Nucl. Phys. A **757**, 102 (2005) [arXiv:nucl-ex/0501009],
- 18 K. Adcox *et al.* [PHENIX Collaboration], Nucl. Phys. A **757**, 184 (2005) [arXiv:nucl-ex/0410003],
- 19 M. I. Gorenstein, M. Gazdzicki and K. A. Bugaev, Phys. Lett. B **567**, 175 (2003) [arXiv:hep-ph/0303041].
- 20 Y. Hama, F. Grassi, O. Socolowski, T. Kodama, M. Gazdzicki and M. Gorenstein, Acta Phys. Polon. B **35**, 179 (2004).
- 21 E. L. Bratkovskaya *et al.*, Phys. Rev. C **69**, 054907 (2004) [arXiv:nucl-th/0402026],
- 22 J. Cleymans and K. Redlich, Phys. Rev. C **60**, 054908 (1999) [arXiv:nucl-th/9903063].
- 23 M. Gazdzicki, M. I. Gorenstein and S. Mrowczynski, Phys. Lett. B **585**, 115 (2004) [arXiv:hep-ph/0304052] and
- 24 M. I. Gorenstein, M. Gazdzicki and O. S. Zozulya, Phys. Lett. B **585**, 237 (2004) [arXiv:hep-ph/0309142].
- 25 P. F. Kolb, J. Sollfrank and U. W. Heinz, Phys. Rev. C **62**, 054909 (2000) [arXiv:hep-ph/0006129].
- 26 J. Cleymans and K. Redlich, Nucl. Phys. A **661**, 379 (1999) [arXiv:nucl-th/9906065].
- 27 P. Braun-Munzinger, K. Redlich and J. Stachel, arXiv:nucl-th/0304013.
- 28 F. Becattini and U. W. Heinz, Z. Phys. C **76**, 269 (1997) [Erratum-ibid. C **76**, 578 (1997)] [arXiv:hep-ph/9702274] and F. Becattini, M. Gazdzicki and J. Sollfrank, Eur. Phys. J. C **5**, 143 (1998) [arXiv:hep-ph/9710529].
- 29 K. Rajagopal and F. Wilczek, arXiv:hep-ph/0011333.
- 30 M. A. Stephanov, arXiv:hep-ph/0402115.
- 31 F. Karsch, J. Phys. G **31**, S633 (2005) [arXiv:hep-lat/0412038].
- 32 S. D. Katz, arXiv:hep-ph/0511166.
- 33 F. Becattini, J. Manninen and M. Gazdzicki, arXiv:hep-ph/0511092.
- 34 M. I. Gorenstein, M. Gazdzicki and W. Greiner, Phys. Rev. C **72**, 024909 (2005) [arXiv:nucl-th/0505050].
- 35 N. G. Antoniou, Y. F. Contoyiannis, F. K. Diakonou, A. I. Karanikas, C. N. Ktorides, Nucl. Phys. A **693**, 799 (2001), N. G. Antoniou, F. K. Diakonou, G. Mavromanolakis, Nucl. Phys. A **761**, 149 (2005)
- 36 Y. Hatta and T. Ikeda, Phys. Rev. D **67**, 014028 (2003) [arXiv:hep-ph/0210284].
- 37 Z. Fodor and S. D. Katz, JHEP **0404**, 050 (2004) [arXiv:hep-lat/0402006].
- 38 C. R. Allton *et al.*, Phys. Rev. D **71**, 054508 (2005) [arXiv:hep-lat/0501030].
- 39 M. A. Stephanov, K. Rajagopal and E. V. Shuryak, Phys. Rev. D **60**, 114028 (1999) [arXiv:hep-ph/9903292].
- 40 C. Alt *et al.* [NA49 Collaboration], Phys. Rev. C **68**, 034903 (2003) [arXiv:nucl-ex/0303001].
- 41 T. Anticic *et al.* [NA49 Collaboration], Phys. Rev. C **70**, 034902 (2004) [arXiv:hep-ex/0311009].
- 42 M. Rybczynski *et al.* [NA49 Collaboration], J. Phys. Conf. Ser. **5**, 74 (2005) [arXiv:nucl-ex/0409009].

- 43 M. Gazdzicki and M. Gorenstein, arXiv:hep-ph/0511058.
- 44 C. Roland *et al.* [NA49 Collaboration], J. Phys. G **30**, S1381 (2004) [arXiv:nucl-ex/0403035].
- 45 G. Stephans, Proceedings of the Quark Matter 2005, August 2005, Budapest, Hungary.
- 46 T. Satogata, private communication.

PRODUCTION AND STUDY OF ANTIHYDROGEN IN THE ATHENA EXPERIMENT

P. Genova^{a,b}, M. Amoretti^c, C. Amsler^d, G. Bonomi^e, P. D. Bowe^f,
C. Canali^{c,g}, C. Carraro^{c,g}, C. L. Cesar^h, M. Charltonⁱ, M. Doser^e,
A. Fontana^{a,b}, M. C. Fujiwara^{j,k}, R. Funakoshi^k, J. S. Hangst^f,
R. S. Hayano^k, L. V. Jørgensenⁱ, A. Kellerbauer^e, V. Lagomarsino^{c,g},
R. Landua^e, E. Lodi Rizzini^{a,l}, M. Macri^c, N. Madsen^f, G. Manuzio^{c,g},
D. Mitchardⁱ, P. Montagna^{a,b}, H. Pruys^e, C. Regenfus^e, A. Rotondi^{a,b},
G. Testera^{c,g}, A. Variola^c, L. Venturelli^{a,l}, Y. Yamazaki^{j,m}, D. P. van der
Werfⁱ, N. Zurlo^{a,l}

^a *Dipartimento di Fisica Nucleare e Teorica, Università di Pavia, 27100 Pavia, Italy*

^b *Istituto Nazionale di Fisica Nucleare, Sezione di Pavia, 27100 Pavia, Italy*

^c *Istituto Nazionale di Fisica Nucleare, Sezione di Genova, 16146 Genova, Italy*

^d *Physik-Institut, Zürich University, CH-8057 Zürich, Switzerland*

^e *PH Department, CERN, 1211 Geneva 23, Switzerland*

^f *Department of Physics and Astronomy, University of Aarhus, 8000 Aarhus C, Denmark*

^g *Dipartimento di Fisica, Università di Genova, 16146 Genova, Italy*

^h *Instituto de Fisica, Universidade Federal do Rio de Janeiro, Rio de Janeiro 21945-970, Brazil*

ⁱ *Department of Physics, University of Wales Swansea, Swansea SA2 8PP, UK*

^j *Atomic Physics Laboratory, RIKEN, Saitama 351-0198, Japan*

^k *Department of Physics, University of Tokyo, Tokyo 113-0033, Japan*

^l *Dipartimento di Chimica e Fisica per l'Ingegneria e per i Materiali, Università di Brescia, 25123 Brescia, Italy*

^m *Graduate School of Arts and Sciences, University of Tokyo, Tokyo, 153-8902, Japan*

Abstract. In the last three years of data taking, the ATHENA experiment at the CERN Antiproton Decelerator facility has been able to produce large amounts of antihydrogen atoms and to study the formation process in detail. Moreover, in 2004, ATHENA tried to produce antihydrogen by means of laser stimulation. In this contribution we summarize the main results obtained and the progress made in analysing the results of the laser experiment.

1. Main goals of the experiment

The motivation for antihydrogen production is mainly related to two different kinds of study of great interest for fundamental physics: testing CPT symmetry in the $\text{H}-\bar{\text{H}}$ system and studying the gravitational acceleration constant of $\bar{\text{H}}$. The CPT theorem, which states the conservation of the product, in any order, of the three quantum operators T (time reversal), C (charge conjugation) and P (parity), is well established both theoretically and experimentally [1, 2, 3]. As a consequence of this theorem, for each particle there must be an antiparticle, that is a particle with opposite electric charge, opposite internal quantum numbers, opposite magnetic moment, same total lifetime and same inertial mass. The experimental tests of this theorem are based on high precision measurements of these quantities, in particular we recall the experiments on the mass difference between K and $\bar{\text{K}}^0$ [3] and the charge-to-mass ratio difference between proton and antiproton [4].

With the mind open to new physics, one may look at the key assumptions of the CPT theorem and notice that it is based on the standard Quantum Field Theory - in particular it assumes point like space time - which may not be ultimately true. Moreover, there are theoretical models which, while preserving microcausality and renormalizability, violate CPT invariance, see e. g. [5]. The comparison of the spectral lines of antihydrogen with those of hydrogen provides a unique benchmark for a high precision CPT test. In the case of hydrogen, 10^{-14} precision has been achieved for 1s-2s spectroscopy [6]. A spectroscopic test is not model dependent as the $\text{K}\bar{\text{K}}^0$ mass experiment, which assumes a standard model evolution of kaons to derive a suitable figure of merit to be compared with experimental data [7].

Another interesting topic is related to the gravitational behaviour of antiparticles inside the Earth's field. According to the Equivalence Principle the gravitational mass of a particle does not depend upon its properties, so it should be the same in the case of a particle or an antiparticle. Nevertheless no test of the gravitational mass of neutral antimatter has ever been done. Non standard theories have been proposed, implying differences in the gravitational mass of antiparticles with respect to particles, see [8, 9] for summaries of this work. A neutral system as antihydrogen, being free from disturbing effects due to the electric fields, is ideal to set reliable experimental limits to any antigravity evidence.

These two ultimate goals were not attained by the ATHENA experiment, although ATHENA was able to make the first step in this

direction, by establishing the production of cold antihydrogen and making studies on the physical properties of the produced antiatoms.

2. Apparatus description and evidence for antihydrogen production

The apparatus used to produce and detect antihydrogen consists of three charged particle traps, of the Penning type, and an annihilation detector (for a detailed description of the ATHENA apparatus see [10]). On one side a trap is used to confine and cool the antiprotons coming from the Antiproton Decelerator (left side of figure 1), whereas on the other side the positrons coming from a 1.2 GBq radioactive ^{22}Na source are accumulated in a second Penning trap. In order to make antihydrogen both antiprotons and positrons are transferred and simultaneously confined in a third trap - the mixing trap - placed near the antiproton trap. The mixing and the antiproton trap electrodes are placed inside a 3 T superconducting magnet. The ambient temperature inside the mixing trap is around 15 K and the typical residual gas pressure is lower than 10^{-11} mbar. Usually in the mixing trap around 10^4 antiprotons interact with a positron plasma containing up to 10^8 positrons. The positron plasma is monitored by exciting its normal modes with a radiofrequency electric field. Typical parameters were 2.5 mm radius, 3.2 cm length and $2.5 \cdot 10^8 \text{ cm}^{-3}$ density [11, 12].

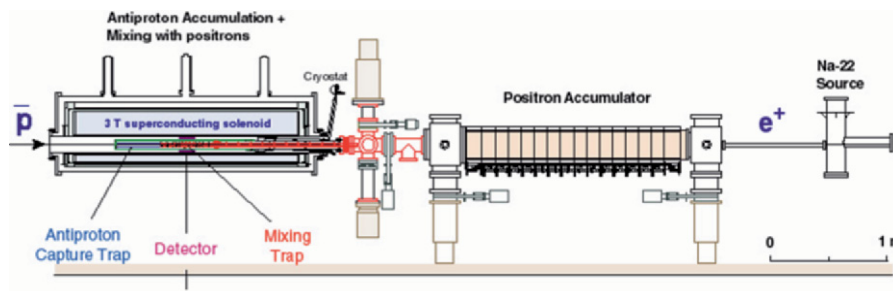


Figure 1. Sketch of the ATHENA apparatus.

The typical mixing procedure - *cold mixing* - consists of injecting first the positrons in the mixing trap and keeping them confined, then injecting the antiprotons and keeping the two clouds confined by using the so-called *nested trap* electrode potential configuration, see fig. 2 [13]. In this way the antiprotons can interact with the positron plasma. If $\bar{\text{H}}$ is formed, it is not confined by the electric and magnetic fields and it moves along a straight line towards the trap electrodes, annihilating on them.

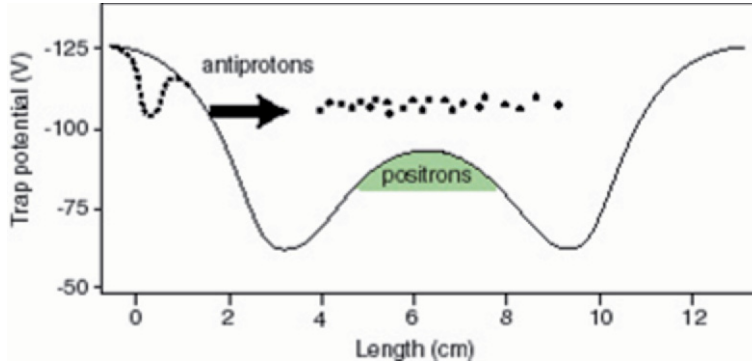


Figure 2. Nested trap potential configuration.

In order to detect antihydrogen production, the annihilation detector is placed just outside the trap electrodes. It consists of 2 layers of microstrip silicon detectors, for charged particle tracking, and 192 CsI crystals, which constitute a high granularity electromagnetic calorimeter (each crystal has dimensions $1.7 \text{ cm} \times 1.75 \text{ cm} \times 1.3 \text{ cm}$). The antihydrogen signature is the space and time coincidence of the nucleon-antiproton and electron-positron annihilations. The former annihilation produces neutral and charged pions, while the latter produces two back-to-back 511 keV photons. By using the silicon detectors, it is possible to reconstruct the charged pion tracks and hence the nucleon-antiproton annihilation vertex, while the 511 keV photons are detected by the calibrated crystals.

Given an antiproton annihilation vertex and two crystals hit by 511 keV photons, one may consider the distance between the centres of these two crystals and the antiproton vertex, expecting a small value in case of antihydrogen production. By considering the cosine of the angle between the segments joining the antiproton vertex with the 511 keV crystals' centres, one expects a peak at $\cos(\theta) = -1$ in case of antihydrogen production, but a uniform distribution otherwise. Figure 3 [14] shows the histogram of this variable for the standard *cold mixing* runs of 2002, superimposed with the so called *hot mixing* runs. In the *cold mixing* runs, we followed the standard procedure described here (positron temperature $\simeq 15 \text{ K}$), whereas in the *hot mixing* runs the positrons were heated with a radiofrequency electric field stimulating the quadrupole resonance mode (positron temperature up to $\simeq 3500 \text{ K}$). Due to the variation of the antihydrogen formation cross section - assuming it equal to the known hydrogen one - the higher the relative energy between the positrons and the antiprotons, the lower the antihydrogen formation probability. The *hot mixing* is thus a perfect

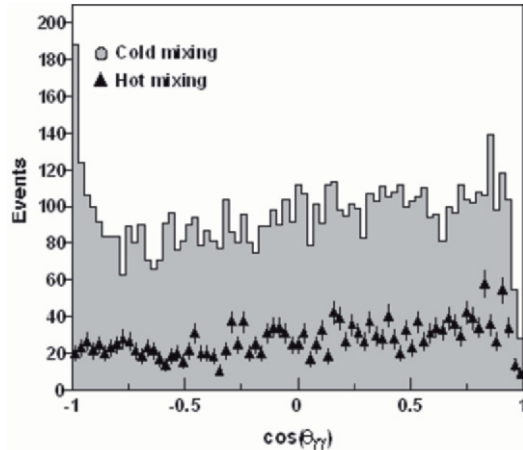


Figure 3. Opening angle distribution for *cold mixing* and *hot mixing* (triangles) [14].

background for antihydrogen production, having just the same conditions of *cold mixing*, with the $\bar{\text{H}}$ signal totally suppressed. As fig. 3 shows, in experimental data, there is a clear $\bar{\text{H}}$ signal for *cold mixing*, but no signal in case of *hot mixing*. Monte Carlo simulations of the detector are also in agreement with these data.

Further evidence of $\bar{\text{H}}$ production is based on the different distributions of the annihilations in cases of *cold mixing* and *hot mixing*. In the former case a substantially isotropic distribution is observed with maximum intensity on a ring which corresponds to the trap wall, whereas for the latter the annihilations are mainly in the centre of the trap (see fig. 4). This is in agreement with antihydrogen production during *cold mixing* and no $\bar{\text{H}}$ production during *hot mixing*, whose annihilations in the centre are $\bar{\text{p}}$, not $\bar{\text{H}}$, annihilations (possibly on residual gas or ions confined in the trap).

Furthermore the time distribution of the triggers is very different in the two cases (see fig. 5) with a peak followed by a gradual decay in case of *cold mixing*. The trigger distribution and the trigger peak rate have been studied at various heating intensities, i. e. heating the positron plasma with different RF voltages. This corresponds to different relative antiproton-positron energies, allowing a study of the dependence of antihydrogen production on the positron energy. The known $\bar{\text{H}}$ formation mechanisms are the two-body - “spontaneous radiative” - recombination $e^+ + \bar{\text{p}} \rightarrow \bar{\text{H}} + \gamma$ and the three-body recombination $e^+ + e^+ + \bar{\text{p}} \rightarrow \bar{\text{H}} + e^+$. Since the cross sections of these processes scale differently with the positron temperature, the dominant process may be

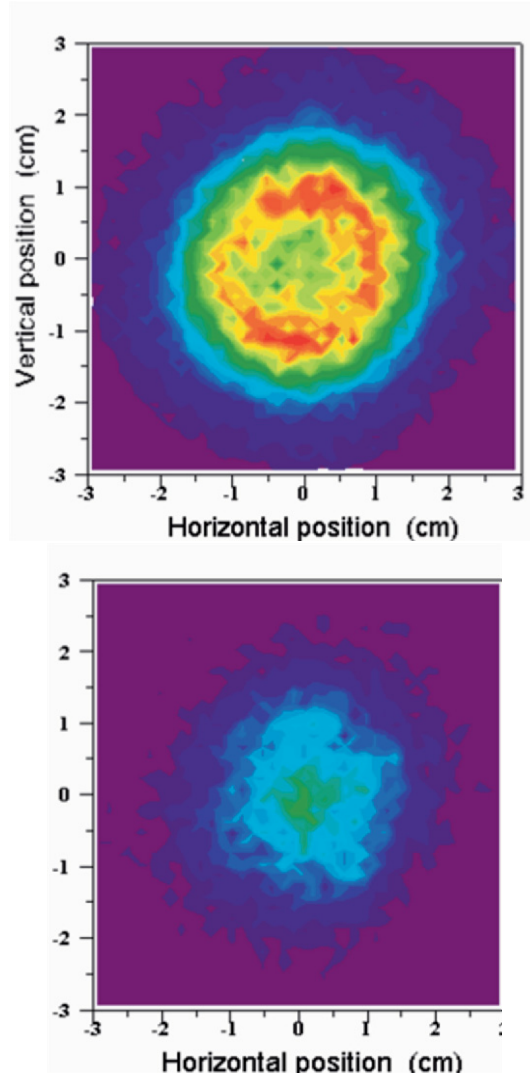


Figure 4. x-y vertex distribution for *cold mixing* - left - and *hot mixing* - right.

isolated by studying the temperature dependence. However, our data are not in agreement with a simple scaling law and the experimental peak rate is higher than the value expected by two-body process only [15]. This suggests a more complicated role of the recombination process, for which the scaling law is a rough approximation and whose theoretical calculation requires dedicated simulations to take properly into account, amongst other things, re-ionization processes and finite plasma dimensions [16].

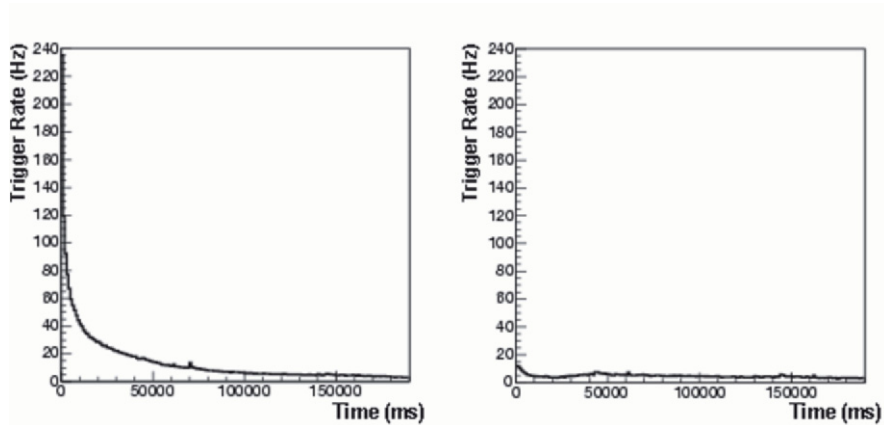


Figure 5. Trigger distribution for *cold mixing* - left - and *hot mixing* - right.

3. Laser stimulated recombination experiment

During 2004 we introduced a laser beam in the antihydrogen mixing region, in order to trigger the reaction $e^+ + \bar{p} + n\gamma \rightarrow \bar{H} + (n+1)\gamma$. We used a CO₂ continuous wave laser, tuned at 10.96 μm wavelength, to stimulate the transition from continuum to the $n = 11$ antihydrogen bound state. Theoretical studies on laser stimulated recombination indicate this frequency as well suited for enhanced production, with an expected stimulated rate higher than 60 Hz [17]. The laser is properly focused into the mixing region, with a peak intensity of 160 W/cm² at 10 W power, and chopped at a frequency of 25 Hz. In this way, during the same *cold mixing* run, it is possible to alternate laser ON and laser OFF conditions (presence/absence of the laser beam) and study the differences. During the laser runs, we observe a slight increase in the ambient temperature inside the nested trap and no vacuum deterioration.

In our preliminary analysis, we see no effect on the vertex temporal distribution due to the presence of the laser (the vertex distribution in the presence of the laser is statistically compatible with the distribution in the absence of the laser).

This result is confirmed by a study of the opening angle distribution for standard *cold mixing*, for laser ON and laser OFF data. There is still evidence of \bar{H} production, but no clear enhancement. In the two samples the peaks at $\cos\theta = -1$ are compatible as well as the variable peak/*plateau*, the *plateau* being the average of the counts in the region $-0.9 < \cos\theta < 0.8$, where there is low \bar{H} production (the analysis is still in progress).

4. Conclusion

We have briefly reviewed some interesting results obtained by the ATHENA experiment. $\bar{\text{H}}$ production has been firmly established and the first studies on the produced antiatoms have been performed. No enhancement of $\bar{\text{H}}$ production was obtained with a laser beam tuned at $\sim 11 \mu\text{m}$, which seems to suggest that the dominant formation process is not the two-body one. These results and the ATHENA experience will be a useful guide and reference for the next generation of antihydrogen experiments.

References

- 1 G. Lüders, *Ann. Phys.* **21** (1957).
- 2 R. Jost, *Helv. Phys. Acta* **30** (1957).
- 3 A. Angelopoulos et al., *Phys. Lett.* **B471** (1999).
- 4 G. Gabrielse et al., *Phys. Rev. Lett.* **82** (1999).
- 5 R. Bluhm, V. A. Kostelecký, N. Russel, *Phys. Rev.* **D57** (1998).
- 6 M. Niering et al., *Phys. Rev. Lett.* **84** (2000).
- 7 Shabalin E. 1994, *Phys. At. Nuclei* **57** (1994).
- 8 M. M. Nieto, *Phys. Rep.* **205** (1991).
- 9 M. M. Nieto, *Phys. Rep.* **216** (1992).
- 10 ATHENA Collab., M. Amoretti et al., *Nucl. Instr. Methods* **A518** (2004).
- 11 ATHENA Collab.: M. Amoretti et al., *Physics of Plasmas* **10** (2003).
- 12 ATHENA Collab.: M. Amoretti et al., *Phys. Rev. Lett.* **91** (2003).
- 13 G. Gabrielse, S. Rolston, L. Haarsma, W. Kells *Phys. Lett.* **A129** (1988).
- 14 ATHENA Collab.: M. Amoretti et al., *Nature* **419** (2002).
- 15 ATHENA Collab.: M. Amoretti et al., *Phys. Lett.* **B583** (2004) 59.
- 16 F. Robicheaux, *Phys. Rev.* **A70** (2004).
- 17 M. V. Ryabinina, L. Melnikov, *Nucl. Instr. Meth.* **B214** (2004).

CRITICAL LINE OF THE DECONFINEMENT PHASE TRANSITIONS

Mark I. Gorenstein

Bogolyubov Institute for Theoretical Physics, Kiev, Ukraine

Abstract. Phase diagram of strongly interacting matter is discussed within the exactly solvable statistical model of the quark-gluon bags. The model predicts two phases of matter: the hadron gas at a low temperature T and baryonic chemical potential μ_B , and the quark-gluon gas at a high T and/or μ_B . The nature of the phase transition depends on a form of the bag mass-volume spectrum (its pre-exponential factor), which is expected to change with the μ_B/T ratio. It is therefore likely that the line of the 1st order transition at a high μ_B/T ratio is followed by the line of the 2nd order phase transition at an intermediate μ_B/T , and then by the lines of "higher order transitions" at a low μ_B/T . This talk is based on a recent paper (Gorenstein, Gaździcki, and Greiner, 2005).

1. Introduction

Investigation of the properties of strongly interacting matter at a high energy density is one of the most important subjects of the contemporary physics. In particular, the hypothesis that at high energy densities the matter is in the form of quark-gluon plasma (QGP) (Collins and Perry, 1975) rather than a gas of hadrons (HG) motivated a first stage of the broad experimental program of study of ultra-relativistic nucleus–nucleus collisions. Over the last 20 years rich data were collected by experiments located at Alternating Gradient Synchrotron (AGS) and Relativistic Heavy Ion Collider (RHIC) in Brookhaven National Laboratory, USA and at Super Proton Synchrotron (SPS) in CERN, Switzerland. The results indicate that the properties of the created matter change rapidly in the region of the low SPS energies (Afnasiev et al., 2002; Gaździcki et al., 2004), $E_{lab} = 30 - 80$ GeV/nucleon. The observed effects are suggestive of a transition, or perhaps rapid cross-over, from a hadron gas to a new form of strongly interacting matter (Gaździcki and Gorenstein, 1999; Gorenstein et al., 2003).

What are the properties of the transition between the two phases of strongly interacting matter? This question motivates the second stage of the investigation of nucleus-nucleus collisions. Based on the numerous examples of the well-known substances a conjecture was formulated, see review paper

(Stephanov, 2004) and references there in, that the transition from HG to QGP is a 1st order phase transition at low values of a temperature T and a high baryo-chemical potential μ_B and it is a rapid cross-over at a high T and a low μ_B . The end point of the 1st order phase transition line is expected to be the 2nd order critical point. This hypothesis seems to be supported by QCD-based qualitative considerations (Stephanov, 2004) and first semi-quantitative lattice QCD calculations (Fodor and Katz, 2002; Karsch et al., 2004). The properties of the deconfinement phase transition are, however, far from being well established. This stimulates our study of the transition domain within the statistical model of quark-gluon bags.

The bag model (Chodos et al., 1974) was invented in order to describe the hadron spectrum, the hadron masses and their proper volumes. This model is also successfully used for a description of the deconfined phase, see e.g. (Shuryak, 1980; Cleymans et al., 1986). Thus the model suggests a possibility for a unified treatment of both phases. Any configuration of the system and, therefore, each term in the system partition function, can be regarded as a many-bag state both below and above the transition domain.

The important properties of the statistical bootstrap model with the van der Waals repulsion are summarized in Sect. 2. In Sect. 3 the statistical model of the quark-gluon bags is presented. Within this model properties of the transition region for $\mu_B = 0$ are studied in Sect. 4 and the analysis is extended to the complete $T - \mu_B$ plane in Sect. 5. The paper is closed by the summary and outlook given in Sect. 6.

2. Statistical bootstrap model and van der Waals repulsion

The grand canonical partition function for an ideal Boltzmann gas of particles of mass m and a number of internal degrees of freedom (a degeneracy factor) g , in a volume V and at a temperature T is given by:

$$\begin{aligned} Z(V, T) &= \sum_{N=0}^{\infty} \frac{1}{N!} \prod_{j=1}^N \int \frac{gV d^3k_j}{(2\pi)^3} \exp \left[- \frac{(k_j^2 + m^2)^{1/2}}{T} \right] \\ &= \sum_{N=0}^{\infty} \frac{[V g\phi(T, m)]^N}{N!} = \exp[Vg\phi(T, m)], \end{aligned} \quad (1)$$

where

$$\phi(T, m) \equiv \frac{1}{2\pi^2} \int_0^{\infty} k^2 dk \exp \left[- \frac{(k^2 + m^2)^{1/2}}{T} \right] = \frac{m^2 T}{2\pi^2} K_2 \left(\frac{m}{T} \right) \quad (2)$$

and K_2 is the modified Bessel function. The function $\phi(T, m)$ is equal to the particle number density:

$$n(T) \equiv \frac{\bar{N}(V, T)}{V} = g\phi(T, m). \quad (3)$$

The ideal gas pressure and energy density can be derived from Eq. (1) as:

$$p(T) \equiv T \frac{\ln Z(V, T)}{V} = T g\phi(T, m), \quad (4)$$

$$\varepsilon(T) \equiv T \frac{dp}{dT} - p(T) = T^2 g \frac{d\phi(T, m)}{dT}. \quad (5)$$

One can easily generalize the ideal gas formulation (1) to the mixture of particles with masses m_1, \dots, m_n and degeneracy factors g_1, \dots, g_n :

$$\begin{aligned} Z(V, T) &= \sum_{N_1=0}^{\infty} \dots \sum_{N_n=0}^{\infty} \frac{[Vg_1\phi(T, m_1)]^{N_1}}{N_1!} \dots \frac{[Vg_n\phi(T, m_n)]^{N_n}}{N_n!} \\ &= \exp \left[V \sum_{j=1}^n g_j \phi(T, m_j) \right]. \end{aligned} \quad (6)$$

The sum over different particle species j can be extended to infinity. It is convenient to introduce the mass spectrum density $\rho(m)$, so that $\rho(m)dm$ gives the number of different particle mass states in the interval $[m, m + dm]$, i.e. $\sum_{j=1}^{\infty} g_j \dots = \int_0^{\infty} dm \dots \rho(m)$. In this case the pressure and the energy density are given by:

$$p(T) = T \int_0^{\infty} dm \rho(m) \phi(T, m), \quad \varepsilon(T) = T^2 \int_0^{\infty} dm \rho(m) \frac{d\phi(T, m)}{dT}. \quad (7)$$

Eqs. (7) were introduced by Hagedorn (Hagedorn, 1965) for the mass spectrum increasing exponentially for $m \rightarrow \infty$:

$$\rho(m) \simeq C m^{-a} \exp(bm), \quad (8)$$

where a, b and C are model parameters. This form of the spectrum (8) was further derived from the statistical bootstrap model (Frautschi, 1971). It can be shown, that within this model the temperature $T_H \equiv 1/b$ (the ‘‘Hagedorn temperature’’) is the maximum temperature of the matter. The behavior of thermodynamical functions (7) with the mass spectrum (8) depends crucially on the parameter a . In particular, in the limit $T \rightarrow T_H$ the pressure and the energy density approach:

$$p, \varepsilon \rightarrow \infty, \quad \text{for } a \leq \frac{5}{2}; \quad (9)$$

$$p \rightarrow \text{const}, \varepsilon \rightarrow \infty, \quad \text{for } \frac{5}{2} \leq a \leq \frac{7}{2}; \quad (10)$$

$$p, \varepsilon \rightarrow \text{const}, \quad \text{for } a > \frac{7}{2}. \quad (11)$$

Up to here all particles including those with $m \rightarrow \infty$ were treated as point-like objects. Clearly this is an unrealistic feature of the statistical bootstrap model. It can be overcome by introduction of hadron proper volumes which simultaneously mimic the repulsive interactions between hadrons. The van der Waals excluded volume procedure can be applied for this purpose (Gorenstein et al., 1981). Other approaches were also discussed (Hagedorn and Rafelski, 1980; Kapusta, 1981). The volume V of the ideal gas (1) is substituted by the “available volume” $V - v_o N$, where v_o is a parameter which corresponds to a particle proper volume. The partition function then reads:

$$Z(V, T) = \sum_{N=0}^{\infty} \frac{[(V - v_o N) g\phi(T, m)]^N}{N!} \theta(V - v_o N). \quad (12)$$

The pressure of the van der Waals gas can be calculated from the partition function (12) by use of its Laplace transform (Gorenstein et al., 1981; Rischke et al., 1991):

$$\hat{Z}(s, T) \equiv \int_0^{\infty} dV \exp(-sV) Z(V, T) = \frac{1}{s - \exp(-v_o s) g\phi(T, m)}. \quad (13)$$

In the thermodynamic limit, $V \rightarrow \infty$, the partition function behaves as $Z(V, T) \simeq \exp[pV/T]$. An exponentially increasing $Z(V, T)$ generates the farthest-right singularity $s^* = p/T$ of the function $\hat{Z}(s, T)$ in variable s . This is because the integral over V in Eq. (13) diverges at its upper limit for $s < p/T$. Consequently, the pressure can be expressed as

$$p(T) = T \lim_{V \rightarrow \infty} \frac{\ln Z(V, T)}{V} = T s^*(T), \quad (14)$$

and the farthest-right singularity s^* of $\hat{Z}(s, T)$ (13) can be calculated from the transcendental equation (Gorenstein et al., 1981; Rischke et al., 1991):

$$s^*(T) = \exp[-v_o s^*(T)] g\phi(T, m). \quad (15)$$

Note that the singularity s^* is not related to phase transitions in the system. Such a singularity exists for any statistical system. For example, for the ideal gas ($v_o = 0$ in Eq. (15)) $s^* = g\phi(T, m)$ and thus from Eq. (14) one gets $p = T g\phi(T, m)$ which corresponds to the ideal gas equation of state (4).

3. Gas of quark-gluon bags

The van der Waals gas consisting of n hadronic species, which are called bags in what follows. is considered in this section. Its partition function reads:

$$Z(V, T) = \sum_{N_1=0}^{\infty} \dots \sum_{N_n=0}^{\infty} \frac{[(V - v_1 N_1 - \dots - v_n N_n) g_1 \phi(T, m_1)]^{N_1}}{N_1!} \times \dots \quad (16)$$

$$\dots \times \frac{[(V - v_1 N_1 - \dots - v_n N_n) g_n \phi(T, m_n)]^{N_n}}{N_n!} \theta(V - v_1 N_1 - \dots - v_n N_n) ,$$

where $(m_1, v_1), \dots, (m_n, v_n)$ are the masses and volumes of the bags. The Laplace transformation of Eq. (16) gives

$$\hat{Z}(s, T) = \left[s - \sum_{j=1}^n \exp(-v_j s) g_j \phi(T, m_j) \right]^{-1} . \quad (17)$$

As long as the number of types of bags, n , is finite, the only possible singularity of $\hat{Z}(s, T)$ (17) is its pole. However, in the case of an infinite number of types of bags the second singularity of $\hat{Z}(s, T)$ may appear. This case is discussed in what follows.

Introducing the bag mass-volume spectrum, $\rho(m, v)$, so that $\rho(m, v) dm dv$ gives the number of bag states in the mass-volume interval $[m, v; m + dm, v + dv]$, the sum over different bag states in definition of $Z(V, T)$ can be replaced by the integral, $\sum_{j=1}^{\infty} g_j \dots = \int_0^{\infty} dm dv \dots \rho(m, v)$. Then, the Laplace transform of $Z(V, T)$ reads (Gorenstein et al., 1981):

$$\hat{Z}(s, T) \equiv \int_0^{\infty} dV \exp(-sV) Z(V, T) = [s - f(T, s)]^{-1} , \quad (18)$$

where

$$f(T, s) = \int_0^{\infty} dm dv \rho(m, v) \exp(-vs) \phi(T, m) . \quad (19)$$

The pressure is again given by the farthest-right singularity: $p(T) = T s^*(T)$. One evident singular point of $\hat{Z}(s, T)$ (18) is the pole singularity, $s_H(T)$:

$$s_H(T) = f(T, s_H(T)) . \quad (20)$$

As mentioned above this is the only singularity of $\hat{Z}(s, T)$ if one restricts the mass-volume bag spectrum to a finite number of states. For an infinite number of mass-volume states the second singular point of $\hat{Z}(s, T)$ (18), $s_Q(T)$, can emerge, which is due to a possible singularity of the function $f(T, s)$ (19) itself. The system pressure takes then the form:

$$p(T) = T s^*(T) = T \cdot \max\{s_H(T), s_Q(T)\} , \quad (21)$$

and thus the farthest-right singularity $s^*(T)$ of $\hat{Z}(s, T)$ (18) can be either the pole singularity $s_H(T)$ (20) or the $s_Q(T)$ singularity of the function $f(T, s)$ (19) itself. The mathematical mechanism for possible phase transition (PT) in our model is the ‘‘collision’’ of the two singularities, i.e. $s_H(T) = s_Q(T)$ at PT temperature $T = T_C$ (see Fig. 1). In physical terms this can be interpreted as the existence of two phases of matter, namely, the hadron gas with the pressure, $p_H = T s_H(T)$, and the quark gluon plasma with the pressure $p_Q = T s_Q(T)$. At a given temperature T the system prefers to stay in a phase with the higher pressure. The pressures of both phases are equal at the PT temperature T_C .

An important feature of this modeling of the phase transition should be stressed here. The transition, and thus the occurrence of the two phases of matter, appears as a direct consequence of the postulated general partition function (a single equation of state). Further on, the properties of the transition, e.g. its location and order, follow from the partition function and are not assumed. This can be confronted with the well-known phenomenological construction of the phase transition, in which the existence of the two different phases of matter and the nature of the transition between them are postulated.

The crucial ingredient of the model presented here which defines the presence, location and the order of the PT is the form of the mass-volume spectrum of bags $\rho(m, v)$. In the region where both m and v are large it can be described within the bag model (Chodos et al., 1974). In the simplest case of a bag filled with the non-interacting massless quarks and gluons one finds (Gorenstein et al., 1982):

$$\rho(m, v) \simeq C v^\gamma (m - Bv)^\delta \exp \left[\frac{4}{3} \sigma_Q^{1/4} v^{1/4} (m - Bv)^{3/4} \right], \quad (22)$$

where C , γ , δ and B , the so-called bag constant, $B \approx 400 \text{ MeV/fm}^3$ (Shuryak, 1980), are the model parameters and

$$\sigma_Q = \frac{\pi^2}{30} \left(g_g + \frac{7}{8} g_{q\bar{q}} \right) = \frac{\pi^2}{30} \left(2 \cdot 8 + \frac{7}{8} \cdot 2 \cdot 2 \cdot 3 \cdot 3 \right) = \frac{\pi^2}{30} \frac{95}{2} \quad (23)$$

is the Stefan-Boltzmann constant counting gluons (spin, color) and (anti-) quarks (spin, color and u , d , s -flavor) degrees of freedom. This is the asymptotic expression assumed to be valid for a sufficiently large volume and mass of a bag, $v > V_0$ and $m > Bv + M_0$. The validity limits can be estimated to be $V_0 \approx 1 \text{ fm}^3$ and $M_0 \approx 2 \text{ GeV}$ (Gorenstein and Lipskih, 1983; Gorenstein, 1984). The mass-volume spectrum function:

$$\rho_H(m, v) = \sum_{j=1}^n g_j \delta(m - m_j) \delta(v - v_j) \quad (24)$$

should be added to $\rho(m, v)$ in order to reproduce the known low-lying hadron states located at $v < V_0$ and $m < BV_0 + M_0$. The mass spectra of the resonances are described by the Breit-Wigner functions. Consequently, a general form of $f(T, s)$ (19) reads:

$$\begin{aligned} f(T, s) &\equiv f_H(T, s) + f_Q(T, s) \\ &= \sum_{j=1}^n g_j \exp(-v_j s) \phi(T, m_j) + \int_{V_0}^{\infty} dv \int_{M_0+Bv}^{\infty} dm \rho(m, v) \exp(-sv) \phi(T, m), \end{aligned} \quad (25)$$

where $\rho(m, v)$ is given by Eq. (22).

The behavior of $f_Q(T, s)$ is discussed in the following. The integral over mass in Eq. (25) can be calculated by the steepest decent estimate. Using the asymptotic expansion of the K_2 -function one finds $\phi(T, m) \simeq (mT/2\pi)^{3/2} \exp(-m/T)$ for $m \gg T$. A factor exponential in m in the last term of Eq. (25) is given by:

$$\exp\left[-\frac{m}{T} + \frac{4}{3}\sigma_Q^{1/4}v^{1/4}(m-Bv)^{3/4}\right] \equiv \exp[U(m)]. \quad (26)$$

The function $U(m)$ has a maximum at:

$$m_0 = \sigma_Q T^4 v + Bv. \quad (27)$$

Presenting $U(m)$ as

$$U(m) \simeq U(m_0) + \frac{1}{2} \left(\frac{d^2 U}{dm^2} \right)_{m=m_0} (m - m_0)^2 = vs_Q(T) - \frac{(m - m_0)^2}{8\sigma_Q v T^5}, \quad (28)$$

with

$$s_Q(T) \equiv \frac{1}{3} \sigma_Q T^3 - \frac{B}{T}, \quad (29)$$

one finds

$$f_Q(T, s) \simeq u(T) \int_{V_0}^{\infty} dv v^{2+\gamma+\delta} \exp[-v(s - s_Q(T))], \quad (30)$$

where $u(T) = C\pi^{-1}\sigma_Q^{\delta+1/2} T^{4+4\delta} (\sigma_Q T^4 + B)^{3/2}$. The function $f_Q(T, s)$ (30) has the singular point $s = s_Q$ because for $s < s_Q$ the integral over dv diverges at its upper limit.

The first term of Eq. (25), f_H , represents the contribution of a finite number of low-lying hadron states. This function has no s -singularities at any temperature T . The integration over the region $m, v \rightarrow \infty$ generates the singularity $s_Q(T)$ (29) of the $f_Q(T, s)$ function (30). As follows from the discussion below this singularity should be associated with the QGP phase.

By construction the function $f(T, s)$ (19) is a positive one, so that $s_H(T)$ (20) is also positive. On the other hand, it can be seen from Eq. (29) that at a low T $s_Q(T) < 0$. Therefore, $s_H > s_Q$ at small T , and according to Eq. (21) it follows:

$$p(T) = T s_H, \quad \varepsilon(T) = T^2 \frac{ds_H}{dT}. \quad (31)$$

The system of the quark-gluon bags is in a hadron phase.

If two singularities “collide”, $T = T_C$ and $s_H(T_C) = s_Q(T_C)$, the singularity $s_Q(T)$ can become the farthest-right singularity at $T > T_C$. In Fig. 1 the dependence of the function $f(T, s)$ on s and its singularities are sketched for $T_1 < T_2 = T_C < T_3$. The thermodynamical functions defined by the singularity $s_Q(T)$ are:

$$p(T) = T s_Q = \frac{\sigma_Q}{3} T^4 - B, \quad \varepsilon(T) = T^2 \frac{ds_Q}{dT} = \sigma_Q T^4 + B \quad (32)$$

and thus they describe the QGP phase.

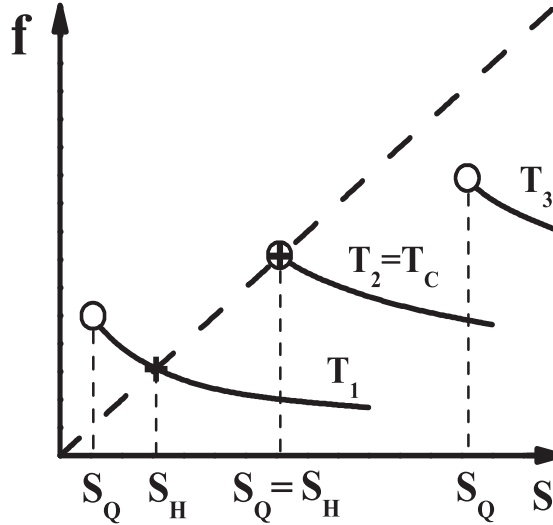


Figure 1. The dependence of $f(T, s)$ on s for three different temperatures: $T_1 < T_2 = T_C < T_3$ (solid lines). The pole singularity s_H and the singularity s_Q are denoted by circles and crosses, respectively. A PT corresponds to the “collision” of two singularities $s_H = s_Q$ at the temperature T_C .

The existence and the order of the phase transition depend on the values of the parameters of the model. From Eq. (30) follows that a PT exists, i.e. $s^* = s_Q$ at high T , provided $\gamma + \delta < -3$ (otherwise $f(T, s_Q) = \infty$, and $s_H > s_Q$ for all T , for illustration see Fig. 2, left).

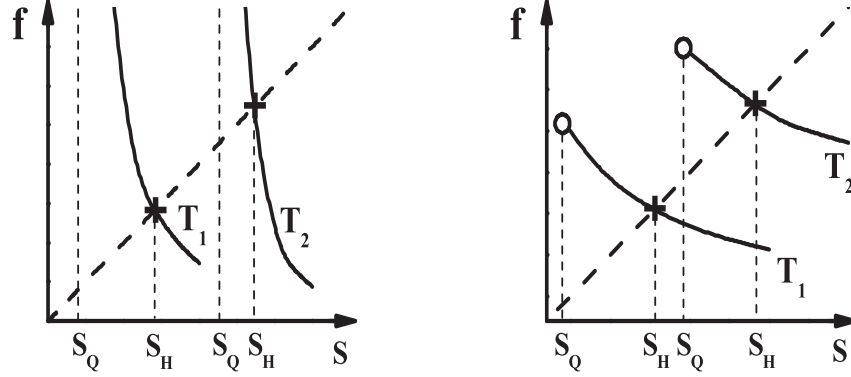


Figure 2. The dependence of $f(T, s)$ on s for two different temperatures, $T_1 < T_2$ (solid lines). The figures demonstrate the absence of the PT in the model if $f(T, s_Q) = \infty$ (left), or if $f(T, s_Q) > s_Q$ at all T (right).

In addition it is required that $f(T, s_Q) < s_Q(T)$ at $T \rightarrow \infty$, (otherwise $s^* = s_H > s_Q$ for all T , for illustration see Fig. 2, right). For $\gamma + \delta < -3$ one finds $f_Q(T, s_Q) \propto T^{10+4\delta}$ at $T \rightarrow \infty$. On the other hand, $s_Q(T) \propto T^3$ at a high T and therefore $\delta < -7/4$. Consequently the general conditions for the existence of any phase transition in the model are:

$$\gamma < -\frac{5}{4}, \quad \delta < -\frac{7}{4}. \quad (33)$$

4. First, second, and higher order phase transitions

In this section the order of the PT in the system of quark-gluon bags is discussed.

The 1st order PT takes place at $T = T_C$ provided $s_Q(T_C) = s_H(T_C)$ and:

$$\left(\frac{ds_Q}{dT}\right)_{T=T_C} > \left(\frac{ds_H}{dT}\right)_{T=T_C}. \quad (34)$$

Thus the energy density $\varepsilon = T^2 ds/dT$ has discontinuity (latent heat) at the 1st order PT. Its dependence on T is shown in Fig. 3, left. In calculating ds_H/dT it is important to note that the function $s_H(T)$ (20) is only defined for $T \leq T_C$, i.e. for $s_H(T) \geq s_Q(T)$.

The 2nd order PT takes place at $T = T_C$ provided $s_Q(T_C) = s_H(T_C)$ and:

$$\left(\frac{ds_Q}{dT}\right)_{T=T_C} = \left(\frac{ds_H}{dT}\right)_{T=T_C}, \quad \left(\frac{d^2s_H}{dT^2}\right)_{T=T_C} \neq \left(\frac{d^2s_Q}{dT^2}\right)_{T=T_C}. \quad (35)$$

Hence the energy density is a continuous function of T , but its first derivate has a discontinuity, for illustration see Fig. 3, right.

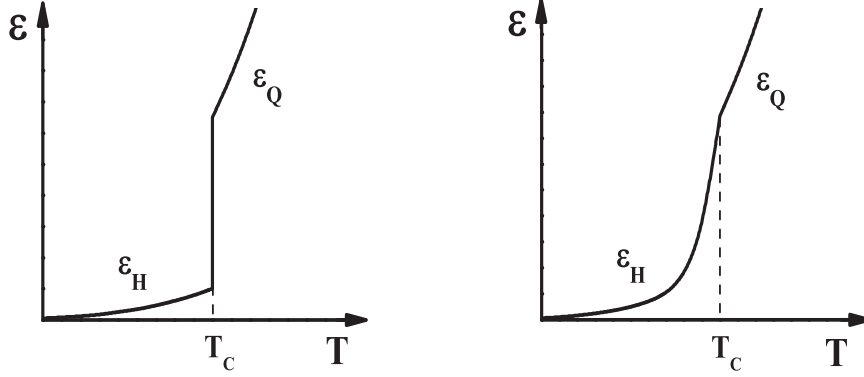


Figure 3. The dependence of the energy density ε on temperature for the 1st (left) and 2nd (right) order PT. The energy density $\varepsilon(T)$ has a discontinuity at $T = T_C$ for the 1st order PT whereas for the 2nd order PT $\varepsilon(T)$ is a continuous function of T , but $d\varepsilon/dT$ has a discontinuity at $T = T_C$.

What is the order of the PT in the model? To answer this question Eq. (20) should be rewritten as:

$$s_H = f_H + u \int_{V_o}^{\infty} dv v^{-\alpha} \exp[-v(s_H - s_Q)] , \quad (36)$$

where $\alpha \equiv -(\gamma + \delta + 2) > 1$. Differentiating both sides with respect to T (the prime denotes the d/dT derivative) one gets:

$$\begin{aligned} s'_H &= f'_H + u' \int_{V_o}^{\infty} dv v^{-\alpha} \exp[-v(s_H - s_Q)] \\ &+ u \int_{V_o}^{\infty} dv v^{-\alpha+1} (s'_Q - s'_H) \exp[-v(s_H - s_Q)] , \end{aligned} \quad (37)$$

from which follows:

$$s'_H = \frac{G + F \cdot s'_Q}{1 + F} , \quad (38)$$

where

$$\begin{aligned} G &\equiv f'_H + u' \int_{V_o}^{\infty} dv v^{-\alpha} \exp[-v(s_H - s_Q)] , \\ F &\equiv u \int_{V_o}^{\infty} dv v^{-\alpha+1} \exp[-v(s_H - s_Q)] . \end{aligned} \quad (39)$$

It is easy to see that the transition is of the 1st order, i.e. $s'_Q(T_C) > s'_H(T_C)$, provided $\alpha > 2$. The 2nd or higher order phase transition takes place provided

$s'_Q(T_C) = s'_H(T_C)$ at $T = T_C$. This condition is satisfied when $F(T)$ diverges to infinity at $T \rightarrow (T_C - 0)$, i.e. for T approaching T_C from below.

One notes that the exponential factor in $\rho(m, v)$ (22) generates the singularity $s_Q(T)$ (29) of the $\hat{Z}(s, T)$ function (18). Due to this there is a possibility of a phase transition in the model. Whether it does exist and what the order is depends on the values of the parameters γ and δ in the pre-exponential power-like factor, $v^\gamma(m - Bv)^\delta$, of the mass-volume bag spectrum $\rho(m, v)$ (22). This resembles the case of the statistical bootstrap model discussed in Sec. II. The limiting temperature $T_H = 1/b$ appears because of the exponentially increasing factor $\exp(bm)$, in the mass spectrum (8), but the thermodynamical behavior (9-11) at $T = T_H$ depends crucially on the value of the parameter a in the pre-exponential factor, m^{-a} (8).

What is the physical difference between $\alpha > 2$ and $1 < \alpha \leq 2$ in the model? From Eq. (36) it follows that the volume distribution function of quark-gluon bags at $T < T_C$ has the form

$$W(v) \propto v^{-\alpha} \exp[-v(s_H - s_Q)] . \quad (40)$$

Consequently the average bag volume:

$$\bar{v} = \int_{V_o}^{\infty} dv v W(v) , \quad (41)$$

at $T \rightarrow (T_C - 0)$ approaches:

$$\bar{v} = \text{const} , \quad \text{for } \alpha > 2 ; \quad (42)$$

$$\bar{v} \rightarrow \infty , \quad \text{for } 1 < \alpha \leq 2 . \quad (43)$$

Thus in the vicinity of the 1st order PT the finite volume bags (hadrons) dominate at $T < T_C$. There is a single infinite volume bag (QGP) at $T > T_C$ and a mixed phase at $T = T_C$ (Gorenstein et al., 1998). For the 2nd order and/or ‘‘higher order transitions’’ the dominant bag configurations include the large volume bags already in a hadron phase $T < T_C$, and the average bag volume increases to infinity at $T \rightarrow (T_C - 0)$.

The condition for the 2nd order PT can be derived as following. The integral for the function F reads

$$\int_{V_o}^{\infty} dv v^{-\alpha+1} \exp[-v(s_H - s_Q)] = (s_H - s_Q)^{-2+\alpha} \Gamma[2 - \alpha, (s_H - s_Q)V_o] ,$$

where $\Gamma(k, x)$ is the incomplete Gamma-function. Thus using Eq. (38) one finds at $T \rightarrow (T_C - 0)$:

$$s'_Q - s'_H \propto (s_H - s_Q)^{2-\alpha} , \quad \text{for } \alpha < 2 , \quad (44)$$

$$s'_Q - s'_H \propto -\ln^{-1}(s_H - s_Q) , \quad \text{for } \alpha = 2 , \quad (45)$$

and consequently:

$$s''_H - s''_Q \propto (s_H - s_Q)^{3-2\alpha} \quad \text{for} \quad \alpha < 2; \quad (46)$$

$$s''_H - s''_Q \propto -\frac{\ln^{-3}(s_H - s_Q)}{s_H - s_Q} \quad \text{for} \quad \alpha = 2. \quad (47)$$

Therefore for $3/2 < \alpha \leq 2$ the 2^{nd} order PT with $s''_H(T_C) = \infty$ takes place whereas for $\alpha = 3/2$ the 2^{nd} order PT with the finite value of $s''_H(T_C)$ is observed. The dependence of the specific heat $C \equiv d\varepsilon/dT$ on T is shown in Fig. 4, left.

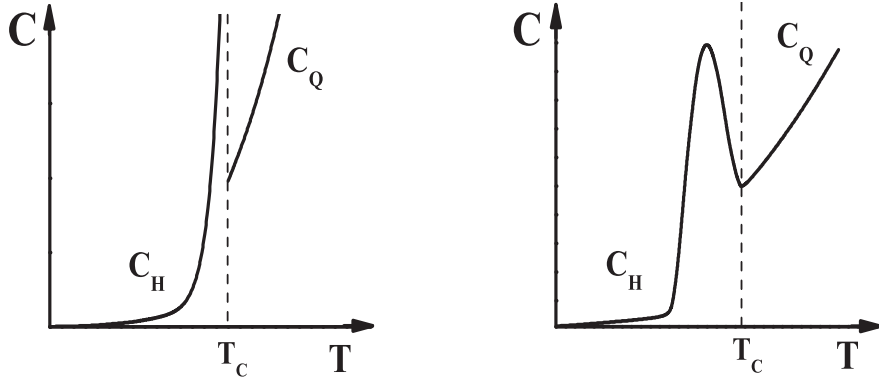


Figure 4. The dependence of the specific heat on temperature for the 2^{nd} order PT (left) and for the 3^{rd} order PT (right). Large values of C in the hadron phase reflect the fact that large derivative $d\varepsilon_H/dT$ at T close to T_C is needed for the 2^{nd} and 3^{rd} order PT to reach the value of $\varepsilon_Q(T_C)$ without energy density discontinuity.

An infinite value of a specific heat C at $T \rightarrow (T_C - 0)$ obtained within the model for $3/2 < \alpha \leq 2$ is typical for the 2^{nd} order PTs.

From Eq. (46) it follows that $s''_H(T_C) = s''_Q(T_C)$ for $\alpha < 3/2$. Using Eqs. (44, 46) one finds at $T \rightarrow (T_C - 0)$:

$$s'''_H - s'''_Q \propto (s_H - s_Q)^{4-3\alpha}. \quad (48)$$

Thus, for $4/3 \leq \alpha < 3/2$ there is a 3^{rd} order transition with $s_Q(T_C) = s_H(T_C)$ and:

$$s'_H(T_C) = s'_Q(T_C), \quad s''_H(T_C) = s''_Q(T_C), \quad s'''_H(T_C) \neq s'''_Q(T_C), \quad (49)$$

with $s'''_H(T_C) = \infty$ for $4/3 < \alpha < 3/2$ and with a finite value of $s'''_H(T_C)$ for $\alpha = 4/3$. The dependence of the specific heat $C \equiv d\varepsilon/dT$ on temperature for the 3^{rd} order transition is shown in Fig. 4, right.

By calculating higher order derivatives of s_H and s_Q with respect to T it can be shown that for $(n+1)/n \leq \alpha < n/(n-1)$ ($n = 4, 5, \dots$) there is a n^{th} order transition with $s_Q(T_C) = s_H(T_C)$ and:

$$s'_H(T_C) = s'_Q(T_C), \dots s_H^{(n-1)}(T_C) = s_Q^{(n-1)}(T_C), s_H^{(n)}(T_C) \neq s_Q^{(n)}(T_C), \quad (50)$$

with $s_H^{(n)}(T_C) = \infty$ for $(n+1)/n < \alpha < n/(n-1)$ and with a finite value of $s_H^{(n)}(T_C)$ for $\alpha = (n+1)/n$.

The 3rd and higher order PTs correspond to a continuous specific heat function C with its maximum at T near T_C (see Fig. 4, right). This maximum appears due to the fact that large values of derivative $d\varepsilon_H/dT$ at T close to T_C are needed to reach the value of $\varepsilon_Q(T_C)$ without discontinuities of energy density and specific heat. The so called crossover point is usually defined as a position of this maximum. Note that in the present model the maximum of a specific heat is always inside the hadron phase.

5. Non-zero baryonic number

At a non-zero baryonic density the grand canonical partition function for the system of quark-gluon bags can be presented in the form

$$Z(V, T, \mu_B) \equiv \sum_{b=-\infty}^{\infty} \exp\left(\frac{b\mu_B}{T}\right) Z(V, T, B), \quad (51)$$

where μ_B is the baryonic chemical potential (for simplicity strangeness is neglected in the initial discussion). The Laplace transform of $Z(V, T, \mu_B)$ (51) reads (Gorenstein et al., 1998)

$$\hat{Z}(s, T, \mu_B) \equiv \int_0^{\infty} dV \exp(-sV) Z(V, T, \mu_B) = \frac{1}{s - f(s, T, \mu_B)}, \quad (52)$$

where

$$f(T, \mu_B, s) = f_H(T, \mu_B, s) + \int_{V_o}^{\infty} dv \int_{M_o+Bv}^{\infty} dm \rho(m, v; \mu_B/T) \exp(-sv) \phi(T, m), \quad (53)$$

with

$$f_H(T, \mu_B, s) = \sum_{j=1}^n g_j \exp\left(\frac{b_j \mu_B}{T}\right) \exp(-v_j s) \phi(T, m_j), \quad (54)$$

$$\rho(m, v; \mu_B/T) \equiv \sum_{b=-\infty}^{\infty} \exp\left(\frac{b\mu_B}{T}\right) \rho(m, v; b). \quad (55)$$

Similar to the case of $\mu_B = 0$ discussed in the previous sections one finds that the pressure is defined by the farthest-right singularity, s^* :

$$p(T, \mu_B) = \lim_{V \rightarrow \infty} \frac{T}{V} \ln Z(V, T, \mu_B) = T s^*(T, \mu_B) = T \cdot \max\{s_H, s_Q\}, \quad (56)$$

and it can be either given by the pole singularity, s_H :

$$s_H(T, \mu_B) = f(s_H, T, \mu_B), \quad (57)$$

or the singularity s_Q of the function $f(s, T, \mu_B)$ (53) itself:

$$\begin{aligned} s_Q(T, \mu_B) &= \frac{\pi^2}{90} T^3 \left[\frac{95}{2} + \frac{10}{\pi^2} \left(\frac{\mu_B}{T} \right)^2 + \frac{5}{9\pi^4} \left(\frac{\mu_B}{T} \right)^4 \right] - \frac{B}{T} \\ &\equiv \frac{1}{3} \bar{\sigma}_Q(\mu_B) T^3 - \frac{B}{T}. \end{aligned} \quad (58)$$

Note that for $\mu_B = 0$ Eq. (58) is transformed back to $s_Q(T)$ (29), as $\bar{\sigma}_Q(\mu_B = 0) = \sigma_Q$. The energy density and baryonic number density are equal to

$$\varepsilon(T, \mu_B) = T^2 \frac{\partial s^*(T, \mu_B)}{\partial T} + T \mu_B \frac{\partial s^*(T, \mu_B)}{\partial \mu_B}, \quad (59)$$

$$n_B(T, \mu_B) = T \frac{\partial s^*(T, \mu_B)}{\partial \mu_B}. \quad (60)$$

The second term in Eq. (53), the function $f_Q(T, \mu_B, s)$, can be approximated as

$$f_Q(T, s, \mu_B) \simeq u(T, \mu_B/T) \int_{V_0}^{\infty} dv v^{-\alpha} \exp[-v(s - s_Q(T, \mu_B))], \quad (61)$$

i.e., it has the same form as $f_Q(T, s)$ (30). At $\mu_B/T = \text{const}$ and $T \rightarrow \infty$ one finds $s_Q(T, \mu_B) \propto T^3$ and $u(T, \mu_B/T) \propto T^{10+4\delta}$. This is the same behavior as in the case of $\mu_B = 0$, (30). At a small T and μ_B one finds $s_H > s_Q$, so that the farthest-right singularity s^* equals to s_H . This pole-like singularity, $s_H(T, \mu_B)$, of the function $\hat{Z}(s, T, \mu_B)$ (52) should be compared with the singularity $s_Q(T, \mu_B)$ of the function $f_Q(T, s, \mu_B)$ (53) itself. The dependence of s_Q on the variables T and μ_B is known in an explicit form (58). If conditions (33) are satisfied it can be shown that with an increasing T along the lines of $\mu_B/T = \text{const}$ one reaches the point $T_C(\mu_B)$ at which the two singularities collide, $s_Q = s_H$, and $s_Q(T, \mu_B)$ becomes the farthest-right singularity of the function $\hat{Z}(s, T, \mu_B)$ (52) at $T \rightarrow \infty$ and fixed μ_B/T . Therefore, the line of phase transitions $s_H(T, \mu_B) = s_Q(T, \mu_B)$ appears in the $T - \mu_B$ plane. Below the phase transition line one observes $s_H(T, \mu_B) > s_Q(T, \mu_B)$ and the system is in a hadron phase. Above this line the singularity $s_Q(T, \mu_B)$ becomes the

farthest-right singularity of the function $\hat{Z}(s, T, \mu_B)$ (52) and the system is in a QGP phase. The corresponding thermodynamical functions are given by:

$$p(T, \mu_B) = T s_Q(T, \mu_B) = \frac{\pi^2}{90} \cdot \frac{95}{2} T^4 + \frac{1}{9} \mu_B^2 T^2 + \frac{1}{162\pi^2} \mu_B^4 - B, \quad (62)$$

$$\varepsilon(T, \mu_B) = T^2 \frac{\partial s_Q(T, \mu_B)}{\partial T} + T \mu_B \frac{\partial s_Q(T, \mu_B)}{\partial \mu_B} = 3 p(T, \mu_B) + 4B, \quad (63)$$

$$n_B(T, \mu_B) = T \frac{\partial s_Q(T, \mu_B)}{\partial \mu_B} = \frac{2}{9} \mu_B T^2 + \frac{2}{81\pi^2} \mu_B^3. \quad (64)$$

The analysis similar to that in the previous section leads to the conclusion that one has the 1st order PT for $\alpha > 2$ in Eq. (61), for $3/2 \leq \alpha \leq 2$ there is the 2nd order PT, and, in general, for $(n+1)/n \leq \alpha < n/(n-1)$ ($n = 3, 4, \dots$) there is a n^{th} order transition. Note that $s_H(T, \mu_B)$ found from by Eq. (57) is only weakly dependent on α . This means that for $\alpha > 1$ the hadron gas pressure $p_H = T s_H$ and thus the position of the phase transition line,

$$s_H(T, \mu_B) = s_Q(T, \mu_B), \quad (65)$$

in the $T - \mu_B$ plane is not affected by the contribution from the large volume bags. The main contribution to s_H (57) comes from small mass (volume) bags, i.e. from known hadrons included in f_H (54). This is valid for all $\alpha > 1$, so that the line (65) calculated within the model is similar for transitions of different orders. On the other hand, the behavior of the derivatives of s_H (57) with respect to T and/or μ_B near the critical line (65), and thus the order of the phase transition, may crucially depend on the contributions from the quark-gluon bags with $v \rightarrow \infty$. For $\alpha > 2$ one observes the 1st order PT, but for $1 < \alpha \leq 2$ the 2nd and higher order PTs are found. In this latter case the energy density, baryonic number density and entropy density have significant contribution from the large volume bags in the hadron phase near the PT line (65).

The actual structure of the ‘‘critical’’ line on the $T - \mu_B$ plane is defined by a dependence of the parameter α on the μ_B/T ratio. This dependence can not be reliably evaluated within the model and thus an external information is needed in order to locate the predicted ‘‘critical’’ line in the phase diagram. The lattice QCD calculations indicate that at zero μ_B there is rapid but smooth cross-over. Thus this suggests a choice $1 < \alpha < 3/2$ at $\mu_B = 0$, i.e. the transition is of the 3rd or a higher order. Numerous models predict the strong 1st order PT at a high μ_B/T ratio, thus $\alpha > 2$ should be selected in this domain. As a simple example in which the above conditions are satisfied one may consider a linear dependence, $\alpha = \alpha_0 + \alpha_1 \mu_B/T$, where $\alpha_0 = 1 + \epsilon$ ($0 < \epsilon \ll 1$) and $\alpha_1 \approx 0.5$. Then the line of the 1st order PT at a high μ_B/T

ends at the point $\mu_B/T \approx 2$, where the line of the 2nd order PT starts. Further on at $\mu_B/T \approx 1$ the lines of the 3rd and higher order transitions follow on the “critical” line. This hypothetical “critical” line of the deconfinement phase transition in the $T - \mu_B$ plane is shown in Fig. 5.

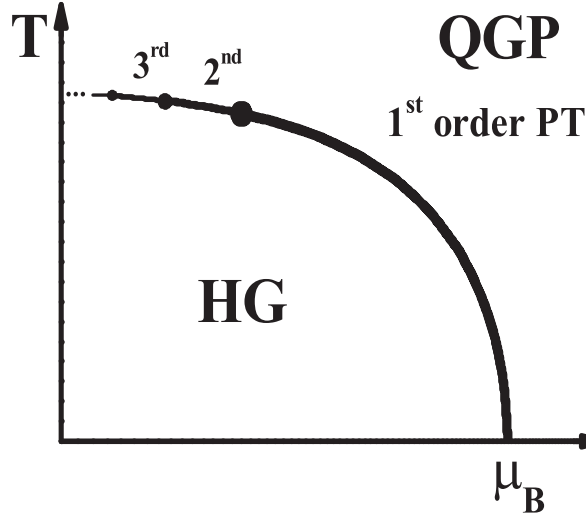


Figure 5. The hypothetical phase diagram of strongly interacting matter in the $T - \mu_B$ plane within the quark-gluon bag model. The influence of strangeness is neglected. The line of the 1st order phase transition at a high μ_B/T ratio is followed by the line of the 2nd order PT at an intermediate μ_B/T values and by the lines of higher order PTs at a low μ_B/T .

In the case of the non-zero strange chemical potential μ_S the pole singularity, s_H , and the singularity s_Q become dependent on μ_S . The system created in nucleus-nucleus collisions has zero net strangeness and consequently,

$$n_S(T, \mu_B, \mu_S) = T \frac{\partial s^*(T, \mu_B, \mu_S)}{\partial \mu_S} = 0. \quad (66)$$

At a small T and μ_B , when $s_H > s_Q$, Eq. (66) with $s^* = s_H$ defines the strange chemical potential $\mu_S = \mu_S^H(T, \mu_B)$ which guarantees a zero value of the net strangeness density in a hadron phase. When the singularity s_Q becomes the farthest-right singularity the requirement of zero net strangeness (66) with $s^* = s_Q$ leads to $\mu_S = \mu_S^Q = \mu_B/3$. The functions $\mu_S^H(T, \mu_B)$ and $\mu_S^Q(T, \mu_B) = \mu_B/3$ are different. Consequently, the line (65) of the 1st order PT in the $T - \mu_B$ plane is transformed into a “strip” (Lee and Heinz, 1993). The phase diagram in which influence of the strangeness is taken into account is shown schematically in Fig. 5.

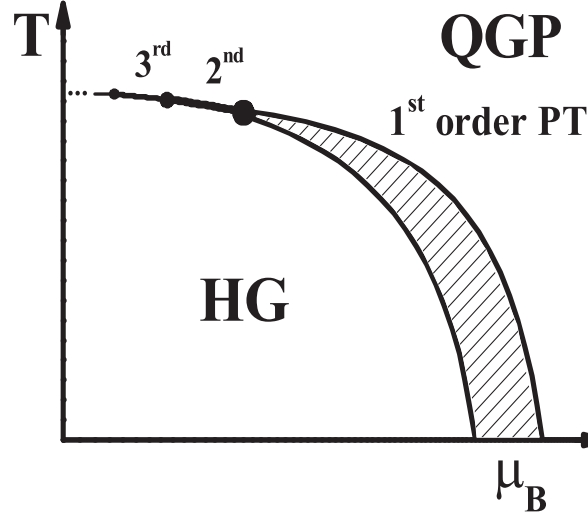


Figure 6. The hypothetical phase diagram of strongly interacting matter in the $T - \mu_B$ plane with strangeness taken into account. The line of the 1st order phase transition is transformed into a “strip”. For further details see caption of Fig. 5.

The lower and upper limits of the “strip” are defined, respectively, by the conditions:

$$s_H(T, \mu_B, \mu_S^H) = s_Q(T, \mu_B, \mu_S^H), \quad s_Q(T, \mu_B, \mu_S^Q) = s_H(T, \mu_B, \mu_S^Q). \quad (67)$$

The T and μ_B values inside the “strip” correspond to the mixed HG-QGP phase for which the following conditions have to be satisfied:

$$s_H(T, \mu_B, \mu_S) = s_Q(T, \mu_B, \mu_S), \quad (68)$$

$$n_S^{mix} \equiv \delta \cdot n_S^Q + (1 - \delta) \cdot n_S^H = \delta \cdot T \frac{\partial s_Q}{\partial \mu_S} + (1 - \delta) \cdot T \frac{\partial s_H}{\partial \mu_S} = 0, \quad (69)$$

where δ is a fraction of the mixed phase volume occupied by the QGP. Eq. (68) reflect the Gibbs equilibrium between the two phases: the thermal equilibrium (equal temperatures), the mechanical equilibrium (equal pressures), the chemical equilibrium (equal chemical potentials). The net strangeness does not vanish in each phase separately, but the total net strangeness of the mixed phase (69) is equal to zero. This means the strangeness–anti-strangeness separation inside the mixed phase (Greiner et al., 1987). The line (65) for the 2nd and higher order PTs (i.e. for $1 < \alpha \leq 2$) remains unchanged as μ_S^H becomes equal to μ_S^Q along this line.

6. Summary and outlook

The phase diagram of strongly interacting matter was studied within the exactly solvable statistical model of the quark-gluon bags. The model predicts two phases of matter: the hadron gas at a low temperature T and baryonic chemical potential μ_B , and the quark-gluon gas at a high T and/or μ_B . The order of the phase transition is expected to alter with a change of the μ_B/T ratio. The line of the 1st order transition at a high μ_B/T is followed by the line of the 2nd order phase transition at an intermediate μ_B/T , and then by the lines of the “higher order transitions” at a low μ_B/T . The condition of the strangeness conservation transforms the 1st order transition line into the “strip” in which the strange chemical potential varies between the QGP and HG values.

In the high and low temperature domains the approach presented here reduces to two well known and successful models: the hadron gas model and the bag model of QGP. Thus, one may hope the obtained results concerning properties of the phase transition region may reflect the basic features of nature.

Clearly, a further development of the model is possible and required. It is necessary to perform quantitative calculations using known hadron states. These calculations should allow to establish a relation between the model parameters and the T and μ_B values and hence locate the critical line in the $T - \mu_B$ plane. Further on one should investigate various possibilities to study experimentally a rich structure of the transition line predicted by the model.

Acknowledgments

I am grateful to Marek Gaździcki and Walter Greiner for collaboration. I am also thankful to V.V. Begun, C. Greiner, E.V. Shuryak, M. Stephanov, and I. Zakout for useful comments. The work was supported by US Civilian Research and Development Foundation (CRDF) Cooperative Grants Program, Project Agreement UKP1-2613-KV-04.

References

- Gorenstein, Mark I., Gaździcki, Marek, and Greiner, Walter (2005) Critical Line of the Deconfinement Phase Transitions, *Phys. Rev. C* **72**, 024909.
- Collins, J. C. and Perry, M. J. (1975) Superdense Matter: Neutrons Or Asymptotically Free Quarks? *Phys. Rev. Lett.* **34**, 1353.
- Afanasiev, S.V., *et al.* (2002) Energy dependence of pion and kaon production in central Pb + Pb collisions, *Phys. Rev. C* **66**, 054902.
- Gaździcki, M., *et al.* (2004) Report from NA49, *J. Phys.* **G 30**, S701.
- Gaździcki, M. and Gorenstein, M.I. (1999), On the early stage of nucleus nucleus collisions, *Acta Phys. Polon.* **B 30**, 2705.

- Gorenstein M.I., Gaździcki M., and Bugaev K.A. (2003) Transverse activity of kaons and the deconfinement phase transition in nucleus nucleus collisions, *Phys. Lett.* **B 567**, 175.
- Stephanov, M. (2004) The phase diagram of QCD and the critical point, *Acta Phys. Polon.* **B 35**, 2939.
- Fodor, Z. and S. D. Katz, S.D. (2002) Lattice determination of the critical point of QCD at finite T and μ , *JHEP* **0203**, 014.
- F. Karsch, F., *et al.* (2004) Where is the chiral critical point in 3-flavor QCD? *Nucl. Phys. Proc. Suppl.* **129**, 614.
- Chodos, A., *et al.* (1974) *Phys. Rev.* **D 9**, 3471.
- Shuryak, E.V. (1980) *Phys. Rep.* **61**, 71.
- Cleymmans, J., Gavai, R.V., and Suhonen, E. (1986) *Phys. Rep.* **130**, 217.
- Hagedorn, R. (1965) *Nuovo Cimento Suppl.* **3**, 147.
- Frautschi, S. (1971) *Phys. Rev.* **D 3**, 2821.
- Gorenstein, M.I., Petrov, V.K., Zinovjev, G.M. (1981) Phase transition in the hadron gas model, *Phys. Lett.* **B 106**, 327.
- Hagedorn, R. and Rafelski, J. (1980) *Phys. Lett.* **B 97**, 136.
- Kapusta, J.I. (1981) *Phys. Rev.* **D 23**, 2444.
- Rischke, D.H. , Gorenstein, M.I., Stöcker, H., and Greiner, W. (1991) Excluded volume effects for the nuclear matter equation of state, *Z. Phys.* **C 51**, 485.
- Gorenstein, M.I., *et al.* (1982) Exactly solvable model of phase transition between hadron and quark gluon matter, *Teor. Mat. Fiz. (Russ)* **52** 346.
- Gorenstein, M.I. and Lipskih, S.I. (1983) SU(3) color in the phase transition between hadronic and quark-gluon matter, *Yad. Fiz. (Russ)* **38**, 1262.
- Gorenstein, M.I. (1984) Absence of limiting temperature and phase transitions in the Van-der-Waals models of hadronic gas, *Yad. Fiz. (Russ)* **39** 712.
- Gorenstein, M.I., Greiner W., and Yang, Shin Nan (1998) Phase transition in the gas of bags, *J. Phys.* **G 24**, 725.
- Gorenstein, M.I., Lipskih, S.I., and Zinovjev, G.M. (1984) Model of deconfinement phase transition in baryonic quark-gluon bag system, *Z. Phys.* **C 22**, 189.
- Lee, K.S. and Heinz, U. (1993) *Phys. Rev.* **D 47**, 2068.
- Greiner, C., Koch, P., and Stöcker, H. (1987) *Phys. Rev. Lett.* **58**, 1825.

MULTIPLE PRODUCTION IN NUCLEAR COLLISIONS

A.B. Kaidalov (kaidalov@itep.ru)

*Institute of Theoretical and Experimental Physics, B. Cheremushkinskaya
25, 117259, Moscow, Russia*

Abstract. The approach to interactions of hadrons, virtual photons and nuclei with nuclei, proposed by Gribov, is reviewed and applied to description of nuclear structure functions in the small x region and heavy ion collisions. The problem of saturation of parton densities in deep inelastic scattering (DIS) in the limit $x \rightarrow 0$ is discussed and its relation to heavy ion collisions at very high energies is investigated. It is emphasized that the shadowing effects are important in a definite kinematical region. It is shown that the prediction of the Glauber model for densities of hadrons produced in the central rapidity region in nucleus–nucleus interactions are modified due to shadowing of small- x -partons. Calculations show that shadowing effects are important at RHIC energies, but the “saturation” at these energies is not achieved yet. Production of particles with large transverse momenta and jets both in Au-Au and D-Au collisions is discussed.

Key words: nuclear interactions, shadowing

1. Introduction

Interactions of nuclei at high energies can provide an important information on properties of the Quantum Chromodynamics (QCD) at high temperature and densities. Heavy ion collisions are considered as a tool to produce and study a new state of matter : the quark-gluon plasma (QGP).

In this paper I shall use the approach to nuclear interactions, proposed by Gribov [1], At very high energies the colliding nuclei are complicated states of partons (quarks and gluons). The modification of parton distributions inside nuclei is a very interesting phenomenon. This modification in the region of small x -Bjorken due to effects of shadowing is related to the problem of “saturation” of parton densities in the limit $x \rightarrow 0$. The “saturation” of partons plays an important role in heavy ions collisions at very high energies. Gribov’s approach allows one to calculate nuclear shadowing in the small x region and to relate these effects to particle production in heavy ion collisions.

I shall extensively use AGK-cutting rules [2] and Gribov reggeon diagram technique to calculate inclusive particle spectra and particle densities in the central rapidity region for heavy-ions collisions. The values of particle and energy densities are very important for the problem of creation of the quark-gluon plasma in heavy-ions collisions.

In the first part of the paper (Section 2) I shall shortly review Gribov's approach to high-energy interactions of hadrons with nuclei [1] and note the difference in the space-time picture of interactions at low and high energies. The difference between the Glauber approximation [3] and the general Gribov theory will be emphasized.

Investigation of the deep inelastic scattering (DIS) in the region of small x -Bjorken gives an important information on the behavior of partonic densities. Experimental data on small- x DIS obtained at HERA [4] show that distributions of quarks and gluons have a fast increase as x decreases up to values $\sim 10^{-4}$. In reggeon theory this increase is related to an intercept of the leading Pomeron singularity $\alpha_P(0)$: $xq(x)$ or $xg(x) \sim \frac{1}{x^\Delta}$, where $\Delta \equiv \alpha_P(0) - 1$. There are good reasons to believe that this fast increase will be modified for even smaller values of x due to influence of unitarity effects. In the limit $x \rightarrow 0$ partonic distributions $xq(x)(xg(x))$ reach the limit of "saturation" and increase only as powers of $\ln \frac{1}{x}$. The problem of "saturation" is even more important in heavy ions collisions, where densities of partons in colliding nuclei are very large. This problem has been studied in QCD perturbation theory [5] and partonic configurations, which include nonlinear effects in QCD evolution, were called "color glass condensate" [6]. However the pattern of "saturation" is much more general.

In Section 3 I shall review theoretical approaches to the origin of the pomeron in QCD.

The problem of small x behavior in DIS will be considered in Section 4 and the model [7] based on reggeon theory and dipole picture of interaction of virtual photons with nucleons will be outlined. This model gives a self consistent description of structure functions of a proton and diffraction dissociation of a photon in a broad region of virtualities Q^2 . I shall discuss the pattern of "saturation" in this model.

It will be shown in Section 5 that the reggeon approach to interactions with nuclei allows to calculate shadowing effects in the small x region for structure functions of nuclei.

Production of hadrons and jets in heavy ions collisions is described in Section 6. It is emphasized that the coherence condition strongly limits the kinematic region where the shadowing effects for inclusive cross sections are important. In the same approach, which leads to description of nuclear structure functions, it is shown that the shadowing

effect in heavy ions collisions leads to a sizable reduction of inclusive particle spectra in comparison with the Glauber model already at RHIC energies. Theoretical predictions agree to the existing experimental data. It is emphasized, however, that at RHIC (and even LHC) energies the situation is far from the “saturation” limit. The effects, which lead to a suppression of production for particles with large p_{\perp} at RHIC, are discussed.

2. Gribov theory of high-energy nuclear interactions

In classical papers of Gribov [1] it was shown how to incorporate the Glauber model [3] for interactions of hadrons with nuclei into a general framework of relativistic quantum theory. Consider an amplitude of elastic scattering for high-energy hadron–nucleus interactions. In the Glauber model it is described by successive rescatterings of initial hadron on nucleons of the nucleus. However, as was emphasized by Gribov [1, 8], the space–time picture of the interaction at high-energy $E > m_h \mu R_A$ (μ is a characteristic hadronic scale $\sim 1 \text{ GeV}$ and R_A is the radius of the nucleus) is completely different from this simple picture. It corresponds to coherent interactions of a fluctuation of the initial hadron, which is “prepared” long before its interaction with the nucleus. A very important result of Gribov [1] is that nevertheless the elastic hA –amplitude can be written as a sum of the diagrams with elastic rescatterings, which give the same result as Glauber model, plus all possible diffractive excitations of the initial hadron. At not too high energies $E_L \sim 10^2 \text{ GeV}$ these terms lead to corrections to the Glauber approximation of 10 – 20% for the total hA cross section.

We will show below that at very high energies and for inclusive cross sections this modification of the Glauber approximation is very important. The difference between Glauber model and Gribov’s theory is essential for understanding shadowing corrections for structure functions of nuclei related to hard processes on nuclei and for many aspects of multiparticle production on nuclei [9].

An important consequence of the space–time structure of interactions of hadrons with nuclei is the theorem, based on AGK–cutting rules [2], that for inclusive cross sections all rescatterings cancel with each other and these cross sections are determined by the diagrams of impulse approximation. Note, however, that this result, valid asymptotically in the central rapidity region, only applies to the diagrams of the Glauber–type, i.e. when masses of diffractive intermediate states are limited and do not increase with energy. As a result, the inclusive cross

section for production of a hadron a is expressed, for a given impact parameter b , in terms of inclusive cross section for hN interactions

$$E \frac{d^3 \sigma_{hA}^a(b)}{d^3 p} = T_A(b) E \frac{d^3 \sigma_{hN}^a}{d^3 p} \quad (1)$$

where $T_A(b)$ is the nuclear profile function $T_A(b) = \int dz \rho_A(r)$, and $\rho_A(r)$ is the nuclear density, ($\int d^2 b T_A(b) = A$). After integration over b we get

$$E \frac{d^3 \sigma_{hA}^a}{d^3 p} = A E \frac{d^3 \sigma_{hN}^a}{d^3 p} \quad (2)$$

For inclusive cross sections in nucleus-nucleus $A_1 A_2$ -collisions the result of the Glauber approximation is very simple to formulate due to the AGK cancellation theorem. It is possible to prove, for an arbitrary number of interactions of nucleons of both nuclei, that all rescatterings cancel in the same way as for hA -interactions. Thus a natural generalization of eq. (1) for inclusive spectra of hadrons produced in the central rapidity region in nucleus-nucleus interactions takes place in the Glauber approximation

$$E \frac{d^3 \sigma_{A_1 A_2}^a(b)}{d^3 p} = T_{A_1 A_2}(b) E \frac{d^3 \sigma_{NN}^a}{d^3 p} \quad (3)$$

where $T_{A_1 A_2}(b) = \int d^2 s T_{A_1}(\vec{s}) T_{A_2}(\vec{b} - \vec{s})$.

The densities of charged particles can be obtained from eq.(3) by dividing it by the total inelastic cross section of nucleus-nucleus interaction. For example

$$\frac{dn_{A_1 A_2}^{ch}(b)}{dy} = \frac{T_{A_1 A_2}(b)}{\sigma_{A_1 A_2}^{in}} \sigma_{NN}^{in} \frac{dn_{NN}^{ch}}{dy} = n_{A_1 A_2}(b) \frac{dn_{NN}^{ch}}{dy} \quad (4)$$

In the following we shall use these results to calculate particle densities in the central rapidity region at high energies.

3. Pomeron and small- x physics

Scattering amplitude of a virtual photon on a proton target at fixed virtuality Q^2 and very high c.m. energy W is described in reggeon theory by exchange of the pomeron pole and multi pomeron cuts. An increase of the structure function $F_2(x, Q^2)$ as $x \approx \frac{Q^2}{W^2} \rightarrow 0$ in pole approximation $\sim \frac{1}{x^\Delta}$, where $\Delta \equiv \alpha_P(0) - 1$. At large Q^2 $F_2(x, Q^2) \sim \sum_i e_i^2 x (q_i(x, Q^2) + \bar{q}_i(x, Q^2))$. Where $q_i(x, Q^2)$ is the distribution of quarks

of flavor i . Thus for $\Delta > 0$ density of partons increases as $x \rightarrow 0$. The value of Δ was calculated in QCD perturbation theory. Summation of the leading $\ln \frac{1}{x}$ leads to the BFKL [10] pomeron with the value of $\Delta = \frac{12\ln 2}{\pi} \alpha_s \approx 0.5$, which corresponds to a very fast increase of parton densities. In this leading approximation the pomeron corresponds to a cut in j -plane. In the next to leading approximation the leading singularity is the Regge pole ¹ and the value of Δ is substantially decreases to the values $\Delta = 0.15 \div 0.25$ [11]. This leading pole strongly depends on nonperturbative region of small momentum transfer [12]. A connection of the pomeron with spectrum of glueballs and the role of nonperturbative effects were studied in ref. [13], using the method of vacuum correlators [14]. It was shown [13] that confinement effects and mixing of gluonic and $q\bar{q}$ -Regge-trajectories are important for the value of the intercept of the pomeron trajectory. The pomeron pole with $\Delta > 0$ leads for $s \equiv W^2 \rightarrow \infty$ to a violation of s-channel unitarity. It is well known that the unitarity is restored if the multi-pomeron exchanges in the t-channel are taken into account. In the following I will use for this intercept the value $\Delta \approx 0.2$, found from analysis of experimental data on high-energy hadronic interactions with an account of multi pomeron contributions [15].

4. Models for small- x DIS

Experimental data at HERA [4] show that distributions of quarks and gluons have a fast rise as x decreases. For parametrization of $F_2(x, Q^2)$ at small $x \sim \frac{1}{x^\Delta}$ data demonstrate that Δ increases with Q^2 and is close to 0.2 at $Q^2 \sim 10 \text{ GeV}^2$. This was interpreted in ref. [16] as a consequence of decrease of multi-pomeron contributions as Q^2 increases. A similar interpretation in terms of “saturation” of parton densities has been proposed by Golec-Biernat and Wusthoff (GBW) [17]. In the pomeron theory the multi-pomeron contributions are related to diffractive production processes and for self consistency it is important to describe simultaneously total cross sections (structure functions) and diffractive processes. At high energies virtual photons dissociate first to $q\bar{q}$ -pairs, which interact with a target. For small relative transverse distance r_\perp between q and \bar{q} such a dipole has a small ($\sim r_\perp^2$) total interaction cross section and small diffraction dissociation cross section. On the other hand for large size pair these cross sections are not small. As a result the role of multi-pomeron rescatterings decreases as Q^2 increases. Explicit models, which take these effects into account, have

¹ There is a sequence of poles in j -plane concentrated at point $j=1$

been constructed in the framework of the reggeon theory [7]. Contribution of small size configurations to $\sigma_s(tot)$ has been described in QCD perturbation theory in the form similar to the one used in ref. [17].

Contributions of large distance dipoles were described in the same framework as hadronic interactions. An important difference from GBW-model is that the model [7] corresponds to summation of a certain class of reggeon diagrams and formulas for cross sections $\sigma(b, r, s, Q^2)$ are given in the impact parameter representation. Also the fan-type diagrams with triple Pomeron interaction are included [7]. This leads to a qualitative difference with GBW-model in the pattern of “saturation” for very small $x (x \leq 10^{-5})$.² In particular in the “saturation” region cross sections of $q\bar{q}$ -pairs with a target does not tend to a constant (as in GBW-model), but have the Froissart type increase $\sim \ln^2 \frac{1}{x}$. This is due to a logarithmic increase of the interaction radius and is out of scope of QCD perturbation theory.

5. Structure functions of nuclei in the shadowing region

Study of nuclear structure functions in the small- x region provides an important information on unitarity effects for dense partonic systems. The total cross section of a virtual photon-nucleus interaction can be written as a series in number of rescatterings on nucleons of a nucleus

$$\sigma_{\gamma^*A}^{(tot)} = \sigma_{\gamma^*A}^{(1)} + \sigma_{\gamma^*A}^{(2)} + \dots \quad (5)$$

The first term corresponds to a sum of incoherent interactions and is equal to

$$\sigma_{\gamma^*A}^{(1)} = A\sigma_{\gamma^*N}$$

The second term describes the shadowing and according to Gribov theory [1] can be expressed in terms of cross section of diffraction dissociation of a photon on a nucleon target

$$\sigma^{(2)} = -4\pi \int d^2b T_A^2(b) \int dM^2 \frac{d\sigma_{\gamma^*N}^{DD}(t=0)}{dM^2 dt} f_A(t_{min}) \quad (6)$$

The minimal value of momentum transfer t_{min} to nucleons depends on the longitudinal fraction of momentum transfer $x_P = \frac{Q^2+M^2}{s} = \frac{x}{\beta}$, where $\beta = \frac{Q^2}{Q^2+M^2}$.

$$t_{min} = -x_P^2 m_N^2$$

² Models of ref. [7] as well as GBW-model [17] give a good description of HERA data on structure functions F_2 and diffractive production.

I would like to emphasize that the shadowing effects are different from zero only in the region of very small x_P or x , where $t_{min} \ll \frac{1}{R_A^2}$ (R_A is the nuclear radius). The same condition of coherence corresponds to lifetimes of the initial hadronic fluctuation $\tau_h \sim \frac{1}{m_N x}$ much larger than radius of a nucleus. These well known conditions for existence of shadowing are important also for heavy ion collisions (see below). Higher order rescatterings are model dependent. In refs. [18, 19] they were calculated in the Schwimmer model [20], where

$$F_{2A}/F_{2N} = \int d^2b \frac{T_A(b)}{1 + F(x, Q^2)T_A(b)} \quad (7)$$

with $F(x, Q^2) = 4\pi \int dM^2 \left(d\sigma_{\gamma^*N}^{DD}(t=0)/dM^2 dt \right) \times (f_A(t_{min})/\sigma_{\gamma^*N}(x, Q^2))$. Using an information on diffraction dissociation in γ^*N -collisions it is possible to calculate nuclear structure functions in a good agreement with experimental data [18, 19](see also [21]). These calculations show that the shadowing effects increase as x decreases in the region $x < 0.1$. The shadowing correction $\sigma^{(2)}/\sigma^{(1)}$ increases with atomic number $\sim A^{1/3}$, but in the region of $x \sim 10^{-2}$ relevant for RHIC energies (see below) and for $Q^2 \sim 1 \text{ GeV}^2$ a decrease of F_{2A} due to shadowing is less than 25% even for heavy nuclei (Au).

Thus the shadowing effects for distributions of quarks (which are directly measured in DIS) can be well described theoretically and prediction for smaller x , relevant for LHC energies, look reliable. Information on shadowing effects for gluons is more limited. This information can be obtained from the data on ‘‘gluonic content’’ of the pomeron [22], using the same method as for quarks. Recent calculations [23] show that qualitatively shadowing for gluons has similar behavior as the one for quarks, but the function $F(x, Q^2)$ in eq.(7) is about 50% larger for gluons..

6. Heavy ions collisions

In heavy ion collisions the problem of shadowing of soft partons of colliding nuclei is very important. This phenomenon takes place only in the kinematic region where longitudinal momentum fractions of soft partons satisfy to the condition $x_i \ll 1/m_N R_A$ ($i = 1, 2$) discussed in the previous Section. Values of x_i can be determined from the kinematic conditions

$$x_1 \cdot x_2 = \frac{M_{\perp}^2}{s}; \quad x_1 - x_2 = x_F \quad (7)$$

where M_{\perp} is the transverse mass of the system produced in the collision and x_F is its Feynman x .

For example at RHIC energy $\sqrt{s} = 200 \text{ GeV}$ in the central rapidity region ($x_F \approx 0$) the shadowing for Au-Au collisions is possible only for transverse momenta less than several GeV.

It is possible to calculate the shadowing effects for inclusive densities of produced particles using the Gribov approach [1] to nuclear interactions. For the models of the Glauber-type, which do not take into account interactions between Pomerons, the AGK theorem [2] takes place. As a result simple equations (3),(4) are valid.

It was emphasized in the Section 2, that eqs.(3),(4) are valid in the Glauber model for $x_F \approx 0$ in the limit $s \rightarrow \infty$. For finite energies there are corrections due to energy-momentum conservation effects [24].

In reggeon theory the shadowing effects discussed above are related to diagrams with interactions between Pomerons. They lead to a substantial decrease of particle densities at high energies.

The same model, which has been used for description of shadowing effects for nuclear structure functions, was used for prediction of inclusive particle densities in heavy ion collisions [24]. In this approach the expression (4) for densities of particles in $A_1 A_2$ collisions is modified as follows [24].

$$\frac{dn_{A_1 A_2}}{dy} = n_{A_1 A_2}(b) \frac{dn_{NN}}{dy} \gamma_{A_1} \gamma_{A_2} \quad (8)$$

where

$$\gamma_A = \frac{1}{A} \int d^2b \frac{T_A(b)}{1 + F(x, Q^2) T_A(b)} \quad (9)$$

For LHC eqs.(8),(9) predict a decrease of particle densities by a factor ~ 4 compared to the Glauber model [24], while for RHIC the suppression is ≈ 2 . Detailed predictions for shadowing suppressions are given in ref. [19]. This approach agrees with the results of experiments at RHIC [25, 26]. Dependence of number of produced particles on number of participant nucleons is also in agreement with data [27].

The kinematic borders for shadowing discussed above correspond also to an essential change in the space-time picture of nuclear interactions and change [28] in AGK cutting rules. For example for $x_{A_2} \ll \frac{1}{m_N R_{A_2}}$ the lifetime for the initial state configuration of a nucleus A_1 is larger than the size of a nucleus A_2 . In this case conditions for coherence are satisfied and usual AGK cutting rules [2] are valid. For $x_{A_2} \geq \frac{1}{m_N R_A}$ space-time picture is close to final state reinteractions of produced particles with formation time [28]. The last situation corresponds to a picture used in most of existing models of heavy ion collisions. Note that it is valid only in the nonshadowing region. This situation is very general. For J/ψ production in hadron-nucleus

interactions it was discussed in details in ref. [29]. It has important implications for production of particles and jets with large p_{\perp} at RHIC. For $x_F = 0$ and $p_{\perp} \geq 1 \div 2 \text{ GeV}$ the shadowing effects at $\sqrt{s} = 200 \text{ GeV}$ are small as was emphasized above and is demonstrated by the data on D-Au-collisions [30]. However in this region of $x_{A_i} \geq \frac{1}{mR_A}$ the final state interaction effects are important. In particular an account of Cronin effect and interaction of a particle (jet) with comovers allowed to describe [31] a suppression of particle production at large p_{\perp} observed at RHIC [26] for Au-Au collisions. The data in D-Au collisions [30] show that in the fragmentation region of D there is a suppression for production of particles with large p_{\perp} . This can be explained in present approach: due to small values of $x_{Au} \sim 10^{-3}$ in this region the shadowing of partons becomes important. It was shown recently [23], that shadowing of gluons, calculated in Gribov's approach, allows to describe experimental data on D-Au collisions in the forward rapidity region.

7. Conclusions

The Gribov theory of high-energy interactions is able to describe a large class of physical processes including small- x DIS and nuclear interactions. In this theory the Glauber approximation to nuclear dynamics is valid in the region of not too high energies and is modified already starting from RHIC energies.

The problem of “saturation” of parton densities is related in the Gribov theory to interactions between Pomerons. These effects are especially important for heavy ions collisions. The shadowing effects are clearly seen in the RHIC data, but the “saturation” is not achieved at RHIC energies in the central rapidity region..

Acknowledgements

This work was supported in part by grants:CRDF RUP2-MO-03, RFBR 04-02-17263, SS-1774.2003.

References

- 1 V.N. Gribov, *JETP* **56**, 892 (1969);
V.N. Gribov, *JETP* **57**, 1306 (1969).
- 2 V.A. Abramovsky, V.N. Gribov and O.V. Kancheli, *Sov. J. Nucl. Phys.* **18**, 308 (1974).

- 3 R.J. Glauber, Lectures in Theoretical Physics. Ed. Britten W.E. N.Y.: Int.Publ. 1959,v.1,p.315.
- 4 T. Ahmed *et al.* (H1 Collaboration), *Phys. Lett.* **299B**, 374 (1992).
M. Derrick *et al.* (ZEUS Collaboration), *Phys. Lett.* **293B**, 465 (1992).
- 5 L. Mc Lerran and R. Venugopalan, *Phys. Rev.* **D49**, 2233 (1994);
D50, 2225 (1994) ; **D53**, 458 (1996).
A. Kovner, L. Mc Lerran and H. Weigert, *Phys. Rev.* **D52**, 3809, 6231 (1995).
Yu.V. Kovchegov and A.H. Mueller, *Nucl. Phys.* **B529**, 451 (1998).
A.H. Mueller, *Nucl. Phys.* **B558**, 285 (1999).
- 6 L. Mc Lerran, *Nucl. Phys.* **A702**, 49 (2002).
- 7 A. Capella, E. Ferreiro, A.B. Kaidalov and C.A. Salgado, *Nucl. Phys.* **B593**, 336 (2001), *Phys. Rev.* **D63**, 054010 (2001).
- 8 V.N. Gribov, Lectures at VII LIYAF Winter School of Physics, 1973,v.II,p.5.
- 9 A.B. Kaidalov, Proc Quark Matter 90, *Nucl. Phys.* **A552**, 39c (1991).
- 10 E.A. Kuraev, L.N. Lipatov, V.S. Fadin, *Sov. Phys. JETP* **44**, 433 (1976); **45**, 199 (1977); Ya.Ya. Balitsky, L.N.Lipatov, *Sov. J. Nucl. Phys.* **28**, 822 (1979).
- 11 V.S. Fadin, L.N. Lipatov, *Phys. Lett.* **429B**, 127 (1998).
G. Camici, M. Ciafaloni, *Phys. Lett.* **430B**, 349 (1998).
S.J.Brodsky *et al.*, *JETP Lett.* **70**, 155 (1999).
- 12 L.P.A. Haakman, O.V. Kancheli, J.H. Koch, *Nucl. Phys.* **B518**, 275 (1998).
- 13 A.B. Kaidalov, Yu.A. Simonov, *Phys. Lett.* **477B**, 163 (2000);
A.B. Kaidalov, Yu.A. Simonov, *Yad. Fiz.* **63**, 1507 (2000).
- 14 Yu.A. Simonov, *Phys. Lett.* **249B**, 514 (1990)
- 15 A.B. Kaidalov, L.A. Ponomarev and K.A. Ter-Martirosyan, *Sov. J. Nucl. Phys.* **44**, 468 (1986).
- 16 A. Capella, A. Kaidalov, C. Merino, J. Tran Thanh Van, *Phys. Lett.* **337B**, 358 (1994).
- 17 K. Golec-Biernat and M. Wüsthoff, *Phys. Rev.* **D59**, 014017 (1999); **D60**, 114023 (1999).
- 18 A. Capella, A. Kaidalov, C. Merino, D. Pertermann, J. Tran Thanh Van, *Eur. Phys. J.* **C5**, 111 (1998).
- 19 J.L. Albacete, N. Armesto, A. Capella, A.B. Kaidalov, C. Salgado, *Eur. Phys. J.* **C29**, 531 (2003).
- 20 A. Schwimmer, *Nucl. Phys.*, **B94**, 445 (1975).
- 21 L. Frankfurt, V. Guzey, M.M. McDermott and M. Strikman, *JHEP* **0202**, 027 (2002); L. Frankfurt, V. Guzey and M. Strikman, hep-ph/0303022.
- 22 C. Adloff *et al.* (H1 Collaboration), abstract 980 presented at ICHEP02, amsterdam, July 2002.
- 23 I.C. Arsene, A.B. Kaidalov, K. Tywoniuk, paper submitted to the Conference QM2005.
- 24 A. Capella, A. Kaidalov, J. Tran Thanh Van, *Heavy Ion Phys.* **9**, 169 (1999).
- 25 B.B. Back *et al.* (PHOBOS Collaboration), *Phys. Rev. Lett.* **87**, 102303 (2001)

- 26 Phenix Collaboration, S.S. Adler *et al.*, *Phys. Rev. Lett.* **91**, 072301 (2003).
- 27 A. Capella and D. Sousa, *Phys. Lett.* **511B**, 185 (2001) .
- 28 K.G. Borekov *et al.*, *Yad. Fiz.* **53**, 569 (1991).
- 29 K. Borekov, A. Capella, A. Kaidalov and J. Tran Thanh Van, *Phys. Rev.* **D47**, 919 (1993).
- 30 Brahms Collaboration, I. Arsene *et al.*, *Phys. Rev. Lett.* **93**, 242303 (2004).
- 31 A. Capella, E.G. Ferreiro, A.B. Kaidalov, D. Sousa, *Eur. Phys. J.* **C40**, 129 (2005).

AN EXPERIMENTAL PROPOSAL TO MEASURE $K^+ \rightarrow \pi^+ \nu \bar{\nu}$

Venelin Kozhuharov (venelin.kozhuharov@cern.ch) *
University of Sofia “St. Kliment Ohridski”, Bulgaria
JINR Dubna, Russia

Abstract. An experimental proposal to measure $\text{Br}(K^+ \rightarrow \pi^+ \nu \bar{\nu})$ is described. The goal is to collect about 80 $K^+ \rightarrow \pi^+ \nu \bar{\nu}$ events with signal to background ratio of 10:1 in two years of data taking. This will allow determination of the CKM parameter V_{td} with approximately 10% accuracy. The proposed detector setup together with the analysis technique are reviewed.

Key words: flavour physics, kaon physics, rare decays

1. Introduction

Within the Standard Model the weak interactions of quarks are described by the Cabbibbo-Kobayashi-Maskawa matrix. The understanding of this mechanism is one of the most important goals in the particle physics.

The discovery of direct CP violation in $K^0 - \bar{K}^0$ system by NA31 experiment (Barr et al., 1993) and the consequent precise measurement of the CP violating parameter $\text{Re}(\epsilon'/\epsilon) = (1.67 \pm 0.26) \times 10^{-3}$ in $K^0 - \bar{K}^0$ system by (Batley et al., 2002) and (Alavi-Harati et al., 2003) and the CP violating parameter $\sin 2\beta = 0.726 \pm 0.037$ (H. F. A. Group, 2005) in B-meson system by BABAR and BELLE collaborations has been a triumph of the CKM theory of the quark mixing.

The rare decays of hadrons are also of great interest as they appear through loop processes and therefore are sensitive to short distance phenomena. They can be used to probe the physics at the TeV scale.

2. $K \rightarrow \pi \nu \bar{\nu}$ decays

Among the many kaon decays, the rare decays $K \rightarrow \pi \nu \bar{\nu}$ are extremely attractive as their branching ratios are theoretically very clean. The reason is that the hadronic matrix element can be determined experimentally, using isospin symmetry of the strong interactions, from the leading semileptonic decay

* On behalf of the P326 collaboration.

$K^+ \rightarrow \pi^0 e^+ \nu$ (Marciano and Parsa, 1996). At the quark level $K \rightarrow \pi \nu \bar{\nu}$ decays arise from the $s \rightarrow d \nu \bar{\nu}$ transitions via Z^0 penguin and W box diagrams.

The branching ratio for $K^+ \rightarrow \pi^+ \nu \bar{\nu}$ can be written as (Buchalla and Buras, 1999)

$$Br(K^+ \rightarrow \pi^+ \nu \bar{\nu}) = k_+ \left[\left(\frac{Im \lambda_t}{\lambda^5} X(x_t) \right)^2 + \left(\frac{Re \lambda_t}{\lambda^5} X(x_t) + \frac{Re \lambda_c}{\lambda^5} P_c \right)^2 \right] \quad (1)$$

$$k_+ = r_{K^+} \frac{3\alpha Br(K^+ \rightarrow \pi^0 e^+ \nu)}{2\pi^2 \sin^4 \theta_W} \lambda^8 = (5.04 \pm 0.17) \times 10^{-11} \left(\frac{\lambda}{0.2248} \right)^8 \quad (2)$$

where $\lambda = V_{us}$, $\lambda_c = V_{cs}^* V_{cd}$, $\lambda_t = V_{ts}^* V_{td}$, $x_t = m_t^2/m_W^2$ and the $r_{K^+} = 0.901$ is the isospin breaking correction. The coefficients X and P_c are being computed numerically and the most recent Next-to-Next-to-Leading Order χPT calculation predicts $Br(K^+ \rightarrow \pi^+ \nu \bar{\nu}) = (8.0 \pm 1.1) \times 10^{-11}$ (Buras et al., 2005b) where the error is almost entirely due to uncertainties in m_c and the CKM matrix elements.

The present three events of this decay observed by E787 and E949 collaborations (Adler et al., 2002) lead to

$$Br(K^+ \rightarrow \pi^+ \nu \bar{\nu}) = (14.7_{-8.3}^{+13.0}) \times 10^{-11} \quad (3)$$

Investigation of both $K^+ \rightarrow \pi^+ \nu \bar{\nu}$ and $K^0 \rightarrow \pi^0 \nu \bar{\nu}$ provides an alternative way for determination of the apex of the unitarity triangle. The comparison between this apex and the one obtained from the B -mesons gives possibly the cleanest test of the Standard Model.

$Br(K^+ \rightarrow \pi^+ \nu \bar{\nu})$ has been calculated also in several extensions of the Standard Model. The predictions vary one order of magnitude depending on the particular model and some of them, together with the SM prediction, are given in Table I. Measuring $Br(K^+ \rightarrow \pi^+ \nu \bar{\nu})$ could help to distinguish between the different types of new physics (Buras et al., 2004b) once it is discovered on the future collides.

3. Measurement strategy

In $K^+ \rightarrow \pi^+ \nu \bar{\nu}$ decay there is only one observable particle in the final state, the π^+ . In order to reconstruct the kinematic properties of the event we need to use two spectrometers to measure the kaon momentum as well as the pion momentum. Under the hypothesis that the observed charged particle in the final state is pion and that the decaying particle is kaon the missing mass squared is given by

$$m_{miss}^2 \simeq m_K^2 \left(1 - \frac{|P_\pi^2|}{|P_K^2|} \right) + m_\pi^2 \left(1 - \frac{|P_K^2|}{|P_\pi^2|} \right) - |P_K| |P_\pi| \theta_{\pi K}^2 \quad (4)$$

TABLE I. Predictions for $Br(K^+ \rightarrow \pi^+ \nu \bar{\nu})$

Model	Prediction	
SM	8.0	(Buras et al., 2005b)
MFV	19.1	(Buras, 2003)
EEWP	7.5	(Buras et al., 2004a)
EDSQ	15	(Deshpande et al., 2004)
MSSM	40	(Buras et al., 2005a)

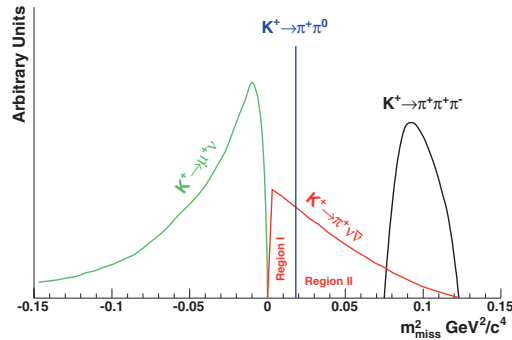


Figure 1. Distribution of the missing mass squared for $K^+ \rightarrow \pi^+ \nu \bar{\nu}$, $K^+ \rightarrow \mu^+ \nu$, $K^+ \rightarrow \pi^+ \pi^0$ and $K^+ \rightarrow \pi^+ \pi^+ \pi^-$ decays

On Figure 1 the missing mass squared distribution for the three most frequent K^+ decays together with $K^+ \rightarrow \pi^+ \nu \bar{\nu}$ is shown. Since the peak of $K^+ \rightarrow \pi^+ \pi^0$ decays lies in the signal region we are forced to separate the signal into two different regions

- Region I: $0 \text{ GeV}^2/c^4 < m_{\text{miss}}^2 < 0.01 \text{ GeV}^2/c^4$
- Region II: $0.026 \text{ GeV}^2/c^4 < m_{\text{miss}}^2 < 0.068 \text{ GeV}^2/c^4$

with borders defined by the resolution on the m_{miss}^2 .

In order to suppress the background in the defined kinematic regions particle identification and a system of veto detectors will be used. The detector should be made hermetic for photons originating from π^0 in the decay region. A cut on the maximum π^+ momentum of 35 GeV will be made to assure that the energy deposited in the photon veto system will be at least 35 GeV. The overall photon veto system has to provide an inefficiency less than 10^{-8} for a π^0 coming from $K^+ \rightarrow \pi^+ \pi^0$ decay. Decays with muons in the final state (like

TABLE II. Branching fractions for charged kaon decay modes (PDG, 2004) normalized to the Standard Model prediction for $Br(K^+ \rightarrow \pi^+ \nu \bar{\nu})$. The technique to suppress the background from the corresponding decay is also given

Decay Mode	$Br(K^+ \rightarrow X) / Br(K^+ \rightarrow \pi^+ \nu \bar{\nu})$	Rejection
$K^+ \rightarrow \mu^+ \nu$	7.93×10^9	Muon identification
$K^+ \rightarrow \pi^+ \pi^0$	2.64×10^9	Photon vetoes
$K^+ \rightarrow \pi^+ \pi^+ \pi^-$	0.7×10^9	Charged vetoes
$K^+ \rightarrow \pi^0 e^+ \nu$	0.61×10^9	Photon vetoes, Electron identification
$K^+ \rightarrow \pi^0 \mu^+ \nu$	0.41×10^9	Photon vetoes, Muon identification
$K^+ \rightarrow \pi^+ \pi^0 \pi^0$	0.22×10^9	Photon vetoes
$K^+ \rightarrow \mu^+ \nu \gamma$	0.07×10^9	Muon identification, Photon vetoes

$K^+ \rightarrow \mu^+ \nu$, $K^+ \rightarrow \pi^+ \pi^- \mu^+ \nu$) will be suppressed using a muon veto system for which the total inefficiency should be less than 5×10^{-6} .

The main kaon decay modes together with the way to suppress the background from them after applying the kinematic cuts are listed in table II.

4. Proposed experimental setup

The most appropriate place to construct the experiment has been identified to be CERN using as primary proton accelerator the Super Proton Synchrotron. It was decided to build the experiment profiting from the existing NA48 cavern and use part of NA48 detectors. However, P326 experiment is not a continuation of the very successful NA48, NA48/1 and NA48/2 series of experiments. It uses a novel technique and most of the detectors are completely new.

The overall beam and detector layout is designed to meet all the requirements defined in the previous section and is shown on Figure 2. Kaon decays in flight technique is considered. All mentioned angles are with respect to the Z-axis of the experiment (also used as a beam axis shown with dashed line on the Figure 2) if not specified explicitly.

4.1. FORMATION OF THE BEAM

The beam of positive charged particles is produced by 400 GeV primary proton beam with an intensity of 3×10^{12} protons per 5 s pulse hitting a beryllium target of 2 mm diameter and 40 cm length at a zero incidence angle. The particles with central momentum of 75 GeV and a momentum bite of 1% are selected by an achromat and transported through a differential Cherenkov counter - CEDAR. This counter will be able to tag only K^+ which represent

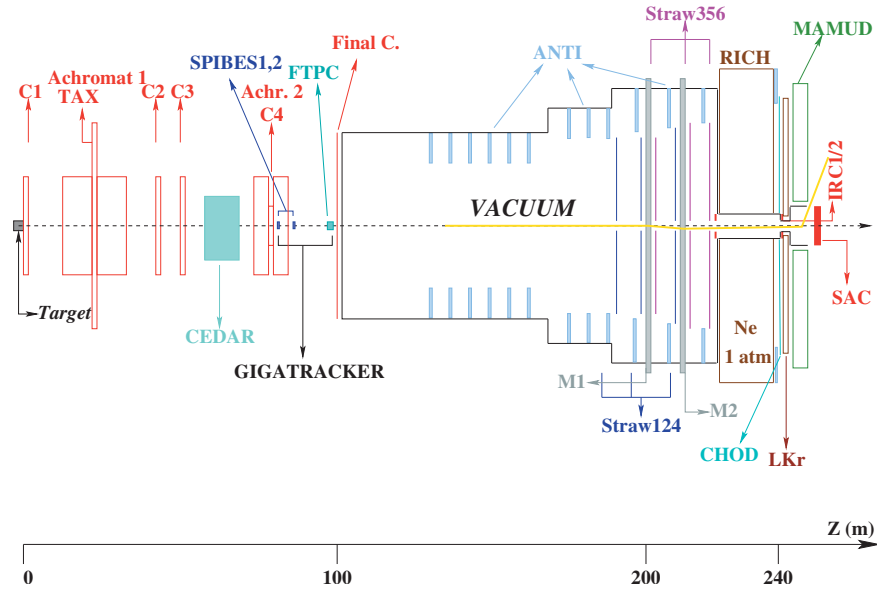


Figure 2. P326 detector layout

$\approx 6\%$ of the beam content. A second achromat which serves also as a beam spectrometer (GIGATRACKER) is placed in the next 30 m before the final collimator.

The selected particles enter the decay region which is housed in a ≈ 120 m long evacuated tank closed by a thin aluminium window. The center of this window is traversed by a beam tube allowing the beam to be transported in vacuum through the detectors downstream of the tank.

Within the detectors following the decay region the beam is deflected by two large-aperture dipole magnets of a double spectrometer. The beam is centered again on the axis at the place where a combined magnetized-iron hadron calorimeter and muon detector (MAMUD) is located. The MAMUD is designed to produce a $+1500$ MeV/c p_T -kick on the beam thus clearing a 100 mm radius photon veto calorimeter located 8 m further downstream.

Some of the beam properties are listed in table III.

One of the important aspects of the experiment is the quality of the vacuum in the decaying tank. The residual gas is dangerous because of the interactions with the beam particles. In order to have background of less than one fake event per year the vacuum should be better than 6×10^{-7} mbar assuming the positive kaon identification by CEDAR.

TABLE III. P326 Beam properties

Beam parameter	Value	Comment
Duty cycle	16.8 s with 4.8 s flat top	Current SPS duty cycle
Pulses per year	3×10^5	Requested in the proposal
Protons per pulse	3×10^{12}	Requested in the proposal
Beam acceptance	$16 \mu sr$	
Beam flux per pulse	250×10^7	
Kaon momentum (GeV/c)	75 GeV	
K decays per year	48×10^{11}	Assuming 60m fiducial region

4.2. DETECTOR COMPONENTS

The P326 detector system is designed to measure both the properties of the products of the decay and of the decaying particle. Here are the detector components as they appear if we are moving together with the beam.

- CEDAR

Positive K^+ tagging helps to reduce the background from the beam pions interacting in the residual gas of the vacuum tank (without it the vacuum should be better than $6 \times 10^{-8} mbar$). It is planned to use an upgraded version of one of the existing differential Cherenkov counters at CERN SPS - CEDAR West. This instrument will function well for our purposes if filled with hydrogen thus minimizing the scattering of the beam in the gas.

- GIGATRACKER

The beam spectrometer should perform measurement of the beam parameters at a rate of 1 GHz. The beam size will be 3.2×4.4 cm which leads to an average particle rate of $60 MHz/cm^2$. A hybrid detector is considered consisting of two stations of thin fast silicon micro-pixel detectors (SPIBES) for redundant momentum measurement of the beam and a micromegas-based Time Projection Chamber (FTPC) to measure the direction of the incoming particles with minimum amount of material in order to diminish the multiple scattering of the beam. The SPIBES will provide also time resolution of the order of 100 ps which will simplify the pattern recognition in the FTPC. The ultimate requirements for SPIBES can be achieved with $300 \mu m$ thick detector coupled to $100 \mu m$ readout chip for a total of $\approx 0.4\% X_0$ material per station. The FTPC will be an improved version of the gaseous beam detector developed for NA48/2 experiment equipped with FADC read-out. The precision of the beam momentum measurement is expected to be at the level of 0.3%.

- ANTI
ANTI is a set of ring shaped anti-counters surrounding the decay region. The tank will be equipped with 13 counters, each composed of 80 layers of 5 mm scintillator and 1 mm lead ($16 X_0$). The signal will be taken by wave-length shifting (WLS) fibers to photo-multipliers read-out. ANTI will provide full coverage for photons originating from the decay volume with angles up to 50 mrad.
- STRAW SPECTROMETER
In order to provide redundant measurements of the outgoing pion momentum and angle a double magnetic spectrometer is considered. It will consist of two dipole magnets with two chambers between them, two chambers before the first magnet and two chambers after the second magnet. Chambers of straw tubes with gas mixture of $Ar + CO_2$ (80%+20%) will be used because of their ability to operate in vacuum thus minimizing the multiple scattering. Each chamber consists of four views - horizontal, vertical and two tilted on angles of +45 and -45 degrees and each view consists of two layers of straws glued together. The central region of 10 cm width is not covered by the straws allowing the beam to go through in vacuum. The amount of material for each four-view chamber crossed by a track corresponds to a 0.4% of a radiation length. The momentum resolution of such spectrometer is expected to be better than 1% for 30 GeV/c pion.
- CHOD
The charged hodoscope is intended to be used in the event trigger and therefore must possess a very good efficiency for detecting charged particles. The hodoscope signal will be used offline to guarantee that the charged track is properly associated with the incoming particle. For this reason it should provide an intrinsic time resolution better than 100 ps. We will use multi-gap glass RPCs (Akindonov et al., 2000) which have shown time resolution down to 50 ps with rates up to 1 kHz/cm^2 and efficiency above 99.9% during tests (Akindonov et al., 2004).
- RICH
A gas Ring Imaging Cherenkov counter is placed after the charged hodoscope. It will measure the velocity of the charged particle. Together with the information for the mass of the particle the measurement from RICH turns into a precise momentum measurement. In our case the RICH will be used in the reverse way - using the momentum information from the straw spectrometer the RICH will serve the purpose of particle identification. It will provide muon/pion separation more than three sigma for momentum up to 35 GeV/c. The design chosen is similar to the KPLUS (Cooper, 2005) one adapted to our layout.

- LKR
The existing NA48 Liquid Krypton calorimeter will be exploited as a photon veto detecting photons from the decay volume with angles between 1.0 mrad and 15.0 mrad. The excellent performance of the calorimeter (Unal, 2000) will also help to reject the background from $K^+ \rightarrow \pi^0 e^+ \nu$ decays. An upgrade of the read-out electronics is considered in order to achieve single photon inefficiency of 10^{-5} for photons with energy above 5 GeV.
- MAMUD
The detector is designed as a an iron scintillator sandwich and consists of 150 iron plates, 2cm thick and $2.8m \times 2.6m$ size, interspersed with extruded scintillators. It will be equipped with two coils which will produce about 1 T magnetic field on the axis. Such a detector is capable of identifying muons with inefficiency of the order of 10^{-5} . It also serves the purpose of deflecting the charged beam away from the photon detector (SAC) at the end of the hall.
- IRC1/2, SAC
The two sets of small angle vetoes covering the regions around and in the beam will be $17 X_0$ deep in order to keep the photon punch through probability bellow 10^{-7} . An appropriate solution is based on shashlyk technique (Atoian et al., 2004) of 100 layers of 1 mm lead and 2 mm scintillator with longitudinal WLS fibers. The signal will be read-out with photo-multipliers on the back.

Assuming the main purpose of the different detector components several subsystems can be identified.

- The tagging subsystem consisting of CEDAR and CHOD will be intensively used in the trigger to perform the online selection of the events.
- The tracking subsystem based on GIGATRACKER and the straw spectrometer will be used to reconstruct the kinematics of the event. Together they provide measurement of the relative angle between the kaon and the pion with precision of 50-60 μrad . Taking into account also the momentum resolution of the two spectrometers a resolution on the missing mass squared of $0.008 GeV^2/c^4$ is achievable.
- LKR, ANTIs, SAC and IRCs form the photon veto subsystem which will be used to reject the events with photons in the final state. These detectors provide a completely hermetic coverage for photons originating from the decay volume with angles between 0 (SAC) and 50 mrad (ANTIs).
- The muon veto system is formed by the MAMUD and the RICH.

- The charged veto subsystem is based on the information from the CHOD and the straw spectrometer. They will be used to reject high multiplicity events.

5. Summary

With the presented detector setup the acceptance for the signal is approximately 10%. The analysis technique ensures signal to background ratio of about 10:1. Assuming two years of data taking with total of 4.8×10^{12} kaon decays per year in the fiducial volume and the Standard Model prediction for $K^+ \rightarrow \pi^+ \nu \bar{\nu}$ branching ratio 80 signal events are expected to be observed. This provides $\approx 10\%$ measurement of the CKM-matrix parameter V_{td} .

6. Conclusion

A measurement of the $BR(K^+ \rightarrow \pi^+ \nu \bar{\nu})$ is very challenging not only because of the theoretical interest to it but also due to the fact that it is very difficult experimentally. The P326 experiment gives an impressive opportunity to perform this measurement. The collaboration has been established and a proposal has been submitted to SPSC (Anelli et al., 2005). The experiment is planned to take data in 2009 and 2010.

Acknowledgements

I would like to thank the organizers of the NATO Advanced Research Workshop - Tomas Cechak and Laszlo Jenkovszky for the hospitality. I would like also to thank the Joint Institute for Nuclear Research - Dubna for the sponsorship and last but not least I would like to thank the members of P326 collaboration for the working atmosphere.

References

- Adler, S. *et al.* [E787 Collaboration], Phys. Rev. Lett. **88** (2002) 041803 [arXiv:hep-ex/0111091].
- Akindonov, A. *et al.*, Nucl. Instrum. Meth. A **456** (2000) 16.
- Akindonov, A. *et al.*, Nucl. Instrum. Meth. A **533** (2004) 74.
- Alavi-Harati, A. *et al.* [KTeV Collaboration], Phys. Rev. D **67** (2003) 012005 [Erratum-ibid. D **70** (2004) 079904] [arXiv:hep-ex/0208007].
- Anelli, G. *et al.*, CERN-SPSC-2005-013
- Anisimovsky, V. V. *et al.* [E949 Collaboration], Phys. Rev. Lett. **93** (2004) 031801 [arXiv:hep-ex/0403036].
- Atoian, G. S. *et al.*, Nucl. Instrum. Meth. A **531** (2004) 467. [arXiv:physics/0310047]
- Barr, G. D. *et al.* [NA31 Collaboration], Phys. Lett. B **317** (1993) 233.

- Batley, J. R. *et al.* [NA48 Collaboration], Phys. Lett. B **544** (2002) 97 [arXiv:hep-ex/0208009].
- Buchalla, G., and Buras, A. J., Nucl. Phys. B **548** (1999) 309 [arXiv:hep-ph/9901288].
- Buras, A. J., [arXiv:hep-ph/0310208].
- Buras, A. J., Fleischer, R., Recksiegel, S., Schwab, F., 2004a, Nucl. Phys. B **697**, 133
- Buras, A. J., Schwab, F., and Uhlig, S. 2004b, [arXiv:hep-ph/0405132].
- Buras, A. J., Ewerth, T., Jager, S., and Rosiek, J., 2005a, Nucl. Phys. B **714**, 103 [arXiv:hep-ph/0408142].
- Buras, A. J., Gorbahn, M., Haisch, U., and Nierste, U., 2005b, [arXiv:hep-ph/0508165].
- Cooper, P. S. [the CKM Collaboration], FERMILAB-CONF-05-015-CD
- Deshpande, N. J., Dilip Kumar Ghosh, Xiao-Gang He, [arXiv:hep-ph/0407021].
- H. F. A. Group(HFAG), arXiv:hep-ex/0505100.
- Marciano, W. J., and Parsa, Z., Phys. Rev. D **53**, 1 (1996).
- NA48 Collaboration, <http://na48.web.cern.ch/NA48/>
- NA48/2 Collaboration, http://na48.web.cern.ch/NA48/NA48-2/NA48_2.html
- P326 Collaboration, <http://na48.web.cern.ch/NA48/NA48-3/>
- Eidelman, S. *et al.*, Phys. Lett. B **592**, 1 (2004)
- Unal, G., Proceedings of the 9th International Conference on Calorimetry in High Energy Physics, Annecy, Oct. 2000, p. 355.

LOW-ENERGY PHOTON SCATTERING ON A POLARIZABLE PARTICLE

S.A. Lukashevich, N.V. Maksimenko
Gomel State University, Gomel, Belarus

Abstract. In the present paper a covariant Lagrangian constructed on the bases of the correspondence principle between the relativistic moving medium electrodynamics and relativistic quantum field theory requirements is used. The contribution and physical interpretation of the Lagrangian coefficients to invariant Compton scattering structures have been obtained. We have analyzed the phenomenological tensor constant quantities as well.

1. Introduction

By virtue of the low-energy theorem in $\mathcal{O}(\omega^2)$ the amplitude for spin-0 and -1/2 hadrons depends on their internal degrees of freedom, which are determined by the fundamental parameters such as the electric (α) and magnetic (β) polarizabilities [1, 2]. In turn, at $\mathcal{O}(\omega^3)$ the effective Lagrangian describing the photon-nucleon interaction and, as a result the amplitude for Compton scattering are determined by spin polarizabilities [3]-[9]. These characteristics are immediately connected to the spin properties of hadrons as a composite particles.

The classical process for the investigation of these features of the photon-hadron interaction is Compton scattering of photons, whose energies are below the resonance region. Nevertheless, data about spin polarizabilities can be extracted from other electrodynamic processes (see, for example Ref. [10]).

The determination of the hadron polarizability contributions to the amplitudes of QED processes is sequentially carried out by the effective Lagrangians of interaction of the electromagnetic field with the hadron as a composite particle. In the nonrelativistic electrodynamics such a Lagrangian is rather well determined. On the other hand, in the relativistic QED when hadrons look like bound states, due to the kinematic relativistic effects, the interpretation of polarizabilities is ambiguous [2, 9].

In the present report the correspondence principle between relativistically moving medium electrodynamics and relativistic quantum field theory will be sequentially used for the covariant Lagrangian construction of interaction of the electromagnetic field with polarized spin hadrons. Then we determine the contribution of the Lagrangian structures to the invariant Compton scattering amplitudes. The field-theoretical properties of the energy-momentum tensor and the Hamiltonian in the static limit have been determined.

2. The covariant Lagrangian

First we define the Lagrangian of the photon-hadron interaction taking into account the electric and magnetic polarizabilities.

In the nonrelativistic case, the interaction Hamiltonian of the isotropically-gyrotropic medium is [11, 12]:

$$H_I = -2\pi (\mathbf{PE} + \mathbf{MH}), \quad (1)$$

The polarization vectors \mathbf{P} and magnetization \mathbf{M} look like [11]

$$\mathbf{P} = \hat{\alpha}\mathbf{E}, \quad \mathbf{M} = \hat{\beta}\mathbf{H}, \quad (2)$$

where $\hat{\alpha}$ and $\hat{\beta}$ are the tensors of electric and magnetic polarizabilities, \mathbf{E} and \mathbf{H} are the strengths vectors of electric and magnetic fields.

Let us now define the effective Lagrangian in the relativistic QED for spin-0 and -1/2 hadrons taking into consideration their usual electric and magnetic polarizabilities.

According to the relativistic electrodynamics of the moving mediums the effective Lagrange function is [12, 8]:

$$L_{eff}^{pol} = 2\pi \{e^\mu \alpha_{\mu\nu} e^\nu + h^\mu \beta_{\mu\nu} h^\nu\}. \quad (3)$$

In this expression $e_\mu = F_{\mu\nu}U^\nu$, $h_\mu = \tilde{F}_{\mu\nu}U^\nu$, $\tilde{F}_{\mu\nu} = \frac{i}{2}\varepsilon_{\mu\nu\rho\sigma}F^{\rho\sigma}$, where $F_{\mu\nu}$ and $\tilde{F}_{\mu\nu}$ are the tensors of the electromagnetic field, $\alpha_{\mu\nu}$ and $\beta_{\mu\nu}$ are tensors determined by the polarizabilities in a medium at rest, U_μ is the 4-dimensional velocity of the medium, $\varepsilon_{\mu\nu\rho\sigma}$ - Levi-Chevita antisymmetric tensor ($\varepsilon^{0123} = 1$).

If we move from the Lagrangian (3) to the field-theoretical Lagrangian on the basis of the correspondence principle, then we obtain [8, 13]:

$$L_{eff}^{pol\ spin-0} = \frac{\pi}{m^2} \left(\varphi^* \overset{\leftrightarrow}{\partial}^\mu \overset{\leftrightarrow}{\partial}_\nu \varphi \right) K_\mu^\nu, \quad (4)$$

$$L_{eff}^{pol}{}_{spin-1/2} = -\frac{i\pi}{m} \left(\bar{\psi} \gamma^\mu \overleftrightarrow{\partial}_\nu \psi \right) K_\mu^\nu, \quad (5)$$

for spin-0 and spin-1/2 particles respectively, where $K_\mu^\nu = \alpha_0 F_{\mu\rho} F^{\rho\nu} + \beta_0 \tilde{F}_{\mu\rho} \tilde{F}^{\rho\nu}$, $\overleftrightarrow{\partial}_\nu = \overleftarrow{\partial}_\nu - \overrightarrow{\partial}_\nu$, φ and ψ are the wave functions of spin-0 and spin-1/2 particles.

In order to define the effective Lagrangian with account for the nucleon spin polarizabilities, Eq. (1) is used, where the polarization and magnetization vectors (\mathbf{P} and \mathbf{M}) are determined as follows [11]

$$\mathbf{P} = \hat{\alpha} \mathbf{E} + \hat{\gamma}'_{\mathbf{E}} [\nabla \mathbf{E}], \quad \mathbf{M} = \hat{\beta} \mathbf{H} + \hat{\gamma}'_{\mathbf{M}} [\nabla \mathbf{H}]. \quad (6)$$

Then the following Lagrangian of the electromagnetic field interacting with the moving medium is obtained [15] :

$$L_I^{eff} = 2\pi \{ [e_\mu \alpha^{\mu\nu} e_\nu + h_\mu \beta^{\mu\nu} h_\nu] - [(\gamma'_{\mathbf{E}})_{\mu\nu} e^\mu (U\partial) h^\nu + (\gamma'_{\mathbf{M}})_{\mu\nu} h^\mu (U\partial) e^\nu] \}, \quad (7)$$

where $(\gamma'_{\mathbf{E}})_{\mu\nu\rho}$ and $(\gamma'_{\mathbf{M}})_{\mu\nu\rho}$ are the gyration pseudotensors, $(U\partial) = U_\rho \partial^\rho$.

If the pseudotensors $(\gamma'_{\mathbf{E}})_{\mu\nu}$ and $(\gamma'_{\mathbf{M}})_{\mu\nu}$ are determined via $g_{\mu\nu}$ as $(\gamma'_{\mathbf{E},\mathbf{M}})_{\mu\nu} = (\gamma'_{\mathbf{E},\mathbf{M}}) g_{\mu\nu}$, then it violates the spatial parity conservation law (*i.e.* spin of a composite particle is not taken into account).

From expression (7) it follows that the usual polarizabilities (α , β) in a rest medium and the gyration give non-zero contributions to the Lagrangian, starting with the second and the third order in powers of frequency of an external electromagnetic field respectively.

Due to the correspondence principles [8, 13] and the expression (7), the field theory effective Lagrangian of interaction of the electromagnetic field with spinless hadrons will not satisfy the parity conservation law when the components of pseudotensors $(\gamma'_{\mathbf{E}})_{\mu\nu}$ and $(\gamma'_{\mathbf{M}})_{\mu\nu}$ are not equal to zero. However, in the case of spin particles, it is easy to determine the dependence of γ -structures from $(\bar{\psi} (\overleftrightarrow{\partial}_\alpha \overleftrightarrow{\partial}_\beta) \gamma^\mu \gamma^5 \psi)$ and $(F^{\alpha\nu} \overleftrightarrow{\partial}^\nu \tilde{F}_{\sigma\mu})$.

Hence, the effective field Lagrangian describing the electromagnetic field and the spin-1/2 hadron interaction is defined as follows:

$$L_{eff} = L_{eff}^{pol} + L_{eff}^{Sp}, \quad (8)$$

where L_{eff}^{pol} is determined by the expression (5) and L_{eff}^{Sp} is [15] :

$$L_{eff}^{Sp} = -\frac{\pi}{2m^2} (\bar{\psi} \overleftrightarrow{\partial}_\alpha \overleftrightarrow{\partial}_\beta \gamma^\mu \gamma^5 \psi) \left\{ -\frac{1}{2} \gamma_{E_1} \cdot F^{\alpha\nu} \overleftrightarrow{\partial}^\beta \tilde{F}_{\mu\nu} \frac{1}{2} \gamma_{M_1} \cdot \tilde{F}^{\alpha\nu} \overleftrightarrow{\partial}^\beta F_{\mu\nu} \right. \\ \left. - \gamma_{E_2} \cdot (F^{\alpha\nu} \overleftarrow{\partial}_\mu \tilde{F}_\nu^\beta - \tilde{F}^{\alpha\nu} \overrightarrow{\partial}_\nu F_\mu^\beta) \gamma_{M_2} \cdot (\tilde{F}^{\alpha\nu} \overleftarrow{\partial}_\mu F_\nu^\beta - F^{\alpha\nu} \overrightarrow{\partial}_\nu \tilde{F}_\mu^\beta) \right\}. \quad (9)$$

3. Invariant amplitudes

The amplitude T_{fi} for Compton scattering on the nucleon is defined by

$$\langle f | S - 1 | i \rangle = i(2\pi)^4 \delta^4(k + p - k' - p') T_{fi}. \quad (10)$$

The photon momenta are denoted by k, k' and the nucleon momenta by p, p' . Assuming invariance under parity, charge conjugation and time reversal symmetry the general amplitude for Compton scattering can be written in terms of six invariant amplitudes T_i as [1, 9, 14]

$$T_{fi} = \bar{u}'(p') e'^{* \mu} \left\{ -\frac{P'_\mu P'_\nu}{P'^2} (T_1 + \gamma \cdot K T_2) - \frac{N_\mu N_\nu}{N^2} (T_3 + \gamma \cdot K T_4) \right. \\ \left. + i \frac{P'_\mu N_\nu - P'_\nu N_\mu}{P'^2 K^2} \gamma_5 T_5 + i \frac{P'_\mu N_\nu + P'_\nu N_\mu}{P'^2 K^2} \gamma_5 \gamma \cdot K T_6 \right\} e^\nu u(p), \quad (11)$$

where $\bar{u}'(p')$ and $u(p)$ are spin wave functions of particles, \vec{e} and \vec{e}'^* – polarization vectors of incident and scattered photons. The system of units $c = \hbar = 1$ in this case is chosen. The orthogonal 4-vectors P', K, N and Q are defined as $P'_\mu = P_\mu - K_\mu \frac{P \cdot K}{K^2}$, $P = \frac{1}{2}(p + p')$, $K = \frac{1}{2}(k + k')$, $N_\mu = \varepsilon_{\mu\nu\lambda\sigma} P'^\nu K^\lambda Q^\sigma$, $Q = \frac{1}{2}(p - p') = \frac{1}{2}(k' - k)$.

The Lagrangian (8) allows us to get the covariant amplitude for Compton scattering on nucleons taking into account electric, magnetic and spin polarizabilities. By the decomposition of the covariant amplitude on invariant spin structures of expression (11) we obtain the relations

$$\begin{aligned} T_1 &= (-2\pi)\alpha_0 \cdot (-4K^2) + \left(-\frac{2\pi}{m}\right) (\gamma_{E_1} - \gamma_{M_2}) \cdot 4(PK)^2; \\ T_2 &= -\frac{2\pi}{m}(\alpha_0 + \beta_0) \cdot 2(PK) - \frac{2\pi}{m^2}(-\gamma_{E_1} + \gamma_{M_2}) \cdot 4(PK)(m^2 + K^2); \\ T_3 &= (-2\pi)\beta_0 \cdot (4K^2) + \left(-\frac{2\pi}{m}\right) (-\gamma_{M_1} + \gamma_{E_2}) \cdot 4(PK)^2; \\ T_4 &= -\frac{2\pi}{m}(-\alpha_0 - \beta_0) \cdot 2(PK) - \frac{2\pi}{m^2}(\gamma_{M_1} - \gamma_{E_2}) \cdot 4(PK)(m^2 + K^2); \\ T_5 &= \left(-\frac{2\pi}{m}\right) \cdot \left[2(PK)^2(\gamma_{E_1} - \gamma_{M_1} - \gamma_{E_2} + \gamma_{M_2}) + 4P'^2 K^2(-\gamma_{E_2} + \gamma_{M_2})\right]; \\ T_6 &= \left(-\frac{2\pi}{m^2}\right) \cdot \left[2(PK)^2(\gamma_{E_1} + \gamma_{M_1} - \gamma_{E_2} - \gamma_{M_2}) + 4P'^2 K^2(-\gamma_{E_2} - \gamma_{M_2})\right]; \end{aligned} \quad (12)$$

where combinations of orthogonal momenta are expressed via generally accepted kinematic variables ν and t as follows $P'^2 = \left(\frac{4m^2}{t}\right) \left(\nu^2 + \frac{t}{4} - \frac{t^2}{16m^2}\right)$, $N^2 = \left(\frac{m^2 t}{4}\right) \left(\nu^2 + \frac{t}{4} - \frac{t^2}{16m^2}\right)$, $K^2 P'^2 = -m^2 \left(\nu^2 + \frac{t}{4} - \frac{t^2}{16m^2}\right)$, $4K^2 P'^2 = -m^2 \eta$, $PK = m\nu$, $-4K^2 = t$.

If we realize amplitude (11) in the Lab frame, then the scalar functions A_i of spin structures [9] look like

$$\begin{aligned}
A_1 &= (-2\pi)(\alpha_0 - \beta_0) + \left(-\frac{2\pi}{m}\right)\nu^2 \cdot (\gamma_{E_1} - \gamma_{M_1} + \gamma_{E_2} - \gamma_{M_2}); \\
A_3 &= (-2\pi)m \cdot (\gamma_{E_1} + \gamma_{M_1} - \gamma_{E_2} - \gamma_{M_2}); \\
A_5 &= \left(-\frac{2\pi}{m}\right)\left(m^2 - \frac{t}{4}\right) \cdot (-\gamma_{E_1} + \gamma_{M_1} - \gamma_{E_2} + \gamma_{M_2}); \\
A_6 &= (-2\pi)(\alpha_0 + \beta_0) + \left(-\frac{2\pi}{m}\right)\left(m^2 - \frac{t}{4}\right) \cdot (-\gamma_{E_1} - \gamma_{M_1} + \gamma_{E_2} + \gamma_{M_2}); \\
A_2 &= \left(-\frac{2\pi}{m}\right) \left[\left(-2m^2 + \frac{t}{2}\right) \cdot (-\gamma_{E_2} + \gamma_{M_2}) - \nu^2(-\gamma_{E_1} + \gamma_{M_1} - \gamma_{E_2} + \gamma_{M_2}) \right]; \\
A_4 &= (-2\pi)m \cdot (+\gamma_{E_1} + \gamma_{M_1} + \gamma_{E_2} + \gamma_{M_2}), \tag{13}
\end{aligned}$$

where $\eta = \frac{1}{m^2}(m^4 - su) = 4\nu^2 + t - \frac{t^2}{4m^2}$ (s, u, t are the usual Mandelstam variables). The invariant amplitudes A_i are even functions of ν and are free of both kinematic singularities and zeros.

In the Lab system the kinematic invariants ν, t and η read: $\nu = \frac{1}{2}(\omega + \omega')$, $t = -2\omega\omega'(1 - z)$, $\eta = 2\omega\omega'(1 + z)$.

In the scattering amplitude (11) within the second order in the photon energy we have got the contribution for electric and magnetic polarizabilities in the form

$$T_{fi}^{pol} = \frac{8\pi m\omega\omega'}{N(t)} \left[\mathbf{e}'^* \cdot \mathbf{e}\alpha_0 + \mathbf{s}'^* \cdot \mathbf{s}\beta_0 \right], \tag{14}$$

and within the third order – the contribution for spin polarizabilities as

$$\begin{aligned}
T_{fi}^{Sp} &= -\frac{8i\pi m}{N(t)} \left[-\nu\omega\omega'\sigma \cdot \mathbf{e}'^* \times \mathbf{e}(\gamma_{E_1} - \gamma_{M_2}) + \nu\omega\omega'\sigma \cdot \mathbf{s}'^* \times \mathbf{s}(-\gamma_{M_1} - \gamma_{E_2}) \right. \\
&\quad \left. + (\sigma \cdot \widehat{\mathbf{k}}\mathbf{s}'^* \cdot \mathbf{e}\omega^2\omega' - \sigma \cdot \widehat{\mathbf{k}}'\mathbf{e}'^* \cdot \mathbf{s}\omega\omega'^2)(-\gamma_{E_2}) \right. \\
&\quad \left. + (-\sigma \cdot \widehat{\mathbf{k}}\mathbf{e}'^* \cdot \mathbf{s}\omega^2\omega' + \sigma \cdot \widehat{\mathbf{k}}'\mathbf{s}'^* \cdot \mathbf{e}\omega\omega'^2)(-\gamma_{M_2}) \right] \tag{15}
\end{aligned}$$

4. The energy-momentum tensor for interaction of the electromagnetic field with spinor particle

In the case of the spinor and electromagnetic fields the expression for energy-momentum tensor has the form [13]

$$T_\nu^\mu = \frac{\partial L}{\partial(\partial_\mu\psi)}(\partial_\nu\psi) + (\partial_\nu\bar{\psi})\frac{\partial L}{\partial(\partial_\mu\bar{\psi})} + (\partial_\nu A_\rho)\frac{\partial L}{\partial(\partial_\mu A_\rho)} - L\delta_\nu^\mu. \tag{16}$$

The total interaction Lagrangian for spin-1/2 particles with the electromagnetic field will consist of the Lagrangian for free electromagnetic field L_{e-m} , the spinor or Dirac's field L_D , the interaction Lagrangian of the free electromagnetic field with the Dirac's field L_{int-D} , the Pauli term L_P and the Lagrangian which considers electric and magnetic polarizabilities of particles $L_{\alpha_0\beta_0-D}$:

$$L_{total-D} = L_{e-m} + L_D + L_{int-D} + L_P + L_{\alpha_0\beta_0-D}. \quad (17)$$

All parts of the Lagrangian (17) are known. The last term $L_{\alpha_0\beta_0-D}$ will be equal to (5). So the total Lagrangian (17) has the form

$$L_{total-D} = -\frac{1}{4}F_{\alpha\beta}F^{\alpha\beta} - \bar{\psi}\left(\frac{1}{2}i\gamma_\alpha \overleftrightarrow{\partial}^\alpha + m\right)\psi - e(\bar{\psi}\gamma_\alpha\psi)A^\alpha - \mu\bar{\psi}\sigma^{\alpha\beta}\psi F_{\alpha\beta} - \frac{i\pi}{m}K_\mu^\nu(\bar{\psi}\gamma^\alpha \overleftrightarrow{\partial}_\nu\psi), \quad (18)$$

Then we substitute the Lagrangian $L_{total} = L_{e-m} + L_D + L_{int-D} + L_P + L_{\alpha_0\beta_0-D}$ into the expression for the energy-momentum tensor (16). By simplifying the total energy-momentum tensor we have

$$\begin{aligned} T_\xi^\gamma = & -(\partial^\gamma A^\mu)\partial_\xi A_\mu - (2\mu\bar{\psi}\sigma^{\gamma\mu}\psi)\partial_\xi A_\mu + \frac{1}{2}i\bar{\psi}\gamma^\gamma(\partial_\xi\psi) - \frac{1}{2}i(\partial_\xi\bar{\psi})\gamma^\gamma\psi \\ & - \left(-\frac{1}{2}\partial_\alpha A_\beta\partial^\alpha A^\beta - \bar{\psi}\psi m\right)\delta_\xi^\gamma + \left\{\left(-\frac{i\pi}{m}\right)\bar{\psi}\left[(\alpha_0 - \beta_0)\left(F^{\mu\nu}(\gamma^\gamma \overleftrightarrow{\partial}_\nu)\right.\right.\right. \\ & \left.\left.\left.- F^{\gamma\nu}(\gamma^\mu \overleftrightarrow{\partial}_\nu) + F^{\alpha\gamma}(\gamma_\alpha \overleftrightarrow{\partial}^\mu) - F^{\alpha\mu}(\gamma_\alpha \overleftrightarrow{\partial}^\gamma)\right] - 2\beta_0 F^{\gamma\mu}(\gamma^\nu \overleftrightarrow{\partial}_\nu)\right]\psi\right\}\partial_\xi A_\mu \\ & + [(\partial_\xi\bar{\psi})(\delta_\nu^\gamma\gamma^\alpha\psi) - (\delta_\nu^\gamma\bar{\psi}\gamma^\alpha)(\partial_\xi\psi)]\left(-\frac{i\pi}{m}\right)K_\alpha^\nu. \end{aligned} \quad (19)$$

The energy-momentum conservation law is fulfilled for the expression (19), i.e. $\partial_\gamma T_{\xi(I)}^\gamma = 0$.

Now we determine $T_{0(\alpha_0,\beta_0-D)}^0$, i.e. the Hamiltonian. The following expression was obtained [9]

$$T_{0(\alpha_0,\beta_0-D)}^0 = H_{(\alpha_0,\beta_0)} = -2\pi(\alpha_0 E^2 + \beta_0 H^2). \quad (20)$$

Thus, we have got the well known in the electrodynamic of continuous media [11] and elementary-particle physics [9] Hamiltonian for the case of interaction of the electromagnetic field with a polarizable particle.

5. Conclusion

The covariant Lagrangian of interaction of the electromagnetic field with a polarizable spin particles have been obtained. This Lagrangian

satisfies the main relativistic quantum field theory requirements (cross-invariance, P-, T- and gauge invariance). The Lagrangian can be used for the description of spin polarizabilities in two-photon electromagnetic processes. Besides, the Lagrangian gives relevant contribution of the electric, magnetic and spin polarizabilities to scattering amplitude. This contribution is in a good agreement with spin structures of the scattering amplitude of paper [9]. The correlations between the covariant Lagrangian and canonical energy-momentum tensor have been determined. This fact on the basis of the correspondence principle has given a proper definition of the low-energy presentation of the Lagrangian function.

References

- 1 V.A. Petrun'kin, Phys At. Nucl. 12 (1981) 692
- 2 A.J. L'vov, FIAN preprint N344 (1987)
- 3 S. Ragusa, Phys. Rev. D47 (1993) 3757
- 4 S. Ragusa, Phys. Rev. D47 (1994) 3157
- 5 K.Y. Lin, Nuovo Cimento A2 (1971) 695
- 6 K.Y. Lin, Phys. Rev. D24 (1981) 1014
- 7 M.I. Levchuk, L.G. Moroz, Vesti AN BSSR Ser.: fiz.-mat. nauk 1. (1985)
- 8 N.V. Maksimenko, L.G. Moroz, In Proc. 11 Intern. School on High Energy Physics and Relativistic Nucl. Phys. Dubna JINR D2-11707 (1979) 533
- 9 D. Babusci, J. Jiordano, A.J. L'vov, J. Matone, A.N. Nathan, Phys. Rev. C58 (1998) 1013
- 10 S. Scherer, A. Yu Korchin, J.H. Koch, Phys. Rev. C54 (1996) 904
- 11 F.I. Fedorov Gyrotropy theory. Minsk: Nauka i tehnika, (1973)
- 12 B.V. Bokut', A.N. Serdyukov, Journal of Applied Spectroscopy, 11 (1969)
- 13 A.A. Bogush, L.G. Moroz, Introduction in classic fields theory.- Nauka i tehnika.- Minsk. (1968).
- 14 A.C. Hearn and E. Leader, Phys.Rev 126,789 (1962)
- 15 S.A. Belousova, N.V. Maksimenko Proc. Of "OFTHEP'2000". Tver, Russia, 2000 305-308, hep-ph/0009334

FLUCTUATIONS NEAR THE DECONFINEMENT PHASE TRANSITION BOUNDARY

I.N. Mishustin

Frankfurt Institute for Advanced Studies, J.-W. Goethe University, Max von Laue Str. 1, D-60438 Frankfurt am Main, Germany The Kurchatov Institute, Russian Research Center, 123182 Moscow, Russia

Abstract. In this talk I discuss how a first order phase transition may proceed in rapidly expanding partonic matter produced in a relativistic heavy-ion collision. The resulting picture is that a strong collective flow of matter will lead to the fragmentation of a metastable phase into droplets. If the transition from quark-gluon plasma to hadron gas is of the first order, it will manifest itself by strong nonstatistical fluctuations in observable hadron distributions. I discuss shortly existing experimental data on the multiplicity fluctuations.

1. Introduction

A general goal of present and future experiments with heavy-ion beams is to study the properties of strongly interacting matter away from the nuclear ground state. The main interest is focussed on searching for possible phase transitions. Several phase transitions are predicted in different domains of temperature T and baryon density ρ_B . As well known, strongly interacting matter has at least one multi-baryon bound state at $\rho_B = \rho_0 \approx 0.16 \text{ fm}^{-3}$ corresponding to normal nuclei. It follows from the very existence of this bound state that there should be a first order phase transition of the liquid-gas type in normal nuclear matter at subsaturation densities, $\rho_B < \rho_0$, and low temperatures, $T \leq 10 \text{ MeV}$. This phase transition manifests itself in a remarkable phenomenon known as nuclear multifragmentation.

The situation at high T and nonzero baryon chemical potential μ_B ($\rho_B > 0$) is not so clear, although everybody is sure that the deconfinement and chiral transitions should occur somewhere. Reliable lattice calculations exist only for $\mu = 0$ i.e. $\rho_B = 0$ where they predict a smooth deconfinement transition (crossover) at $T \approx 170 \text{ MeV}$. As model calculations show, the phase diagram in the (T, μ_B) plane may contain a first order transition line (below called the critical line) which ends at a (tri)critical point [1, 2, 3]. Possible signatures of this point in heavy-ion collisions are discussed in ref. [4]. However, it is unclear at present whether critical fluctuations associated

with the second order phase transition can develop in a rapidly expanding system produced in a relativistic heavy-ion collision because of the critical slowing down effect [5]. In my opinion, more promising strategy would be to search for a first order phase transition which should have much more spectacular manifestations [6] discussed below. It is interesting to note that, under certain non-equilibrium conditions, a first order transition is also predicted for symmetric quark-antiquark matter with zero net baryon density [7].

A striking feature of central heavy-ion collisions at high energies, confirmed in many experiments (see e.g. [8, 9]), is a very strong collective expansion of matter at later stages of the reaction. This process looks like an explosion with the matter flow velocities comparable with the speed of light. The applicability of equilibrium concepts for describing phase transitions under such conditions becomes questionable and one should expect strong non-equilibrium effects [10, 11, 12]. In this talk I demonstrate that non-equilibrium phase transitions in rapidly expanding matter can lead to interesting phenomena which, in a certain sense, are even easier to observe.

2. Effective thermodynamic potential

To make the discussion more concrete, in this talk I adopt a picture of the chiral phase transition predicted by the linear sigma-model with constituent quarks [3, 13]. Then the mean chiral field $\Phi = (\sigma, \pi)$ serves as an order parameter. The constituent quark mass is generated by interaction with the sigma field, $m = g\sigma$, where g is a corresponding coupling constant. The effective thermodynamic potential $\Omega(\Phi; T, \mu)$ depends, besides Φ , on temperature T and quark chemical potential $\mu = \mu_B/3$. This model respects chiral symmetry which is spontaneously broken in the vacuum, where the sigma field has a nonzero expectation value, $\langle \sigma \rangle = f_\pi$, $\langle \pi \rangle = 0$. It is important for our discussion below that the model predicts a phase diagram on the (T, μ) plane with a critical point at $(T=100 \text{ MeV}, \mu=207 \text{ MeV})$ and a first order phase transition line at lower T and μ . A schematic behaviour of $\Omega(T, \mu; \Phi)$ as a function of the order parameter field σ at $\pi = 0$ is shown in Fig. 1. The minima of Ω determine the stable or metastable states of matter under the condition of thermodynamical equilibrium, where the pressure is $P = -\Omega_{min}/V$. The curves from bottom to top correspond to homogeneous matter at different quark chemical potentials and fixed temperature $T = 0$. The dash-dotted curve corresponds to the first order phase transition point (two equal minima separated by a potential barrier). Two dashed curves show the thermodynamic potential at upper and lower spinodal points, where one of the minima disappears. The range of thermodynamic parameters where two phases, one stable and one metastable, may exist simultaneously is constrained by these two curves. The critical point would correspond to the situation when two minima

fuse and the barrier disappears. This situation is illustrated in Fig. 2 showing the thermodynamic potential at different temperatures and fixed chemical potential $\mu_c = 207$ MeV. This model reveals a rather weak first order phase transition, although some other models [1, 2] predict a stronger transition. The discussion below is quite general.

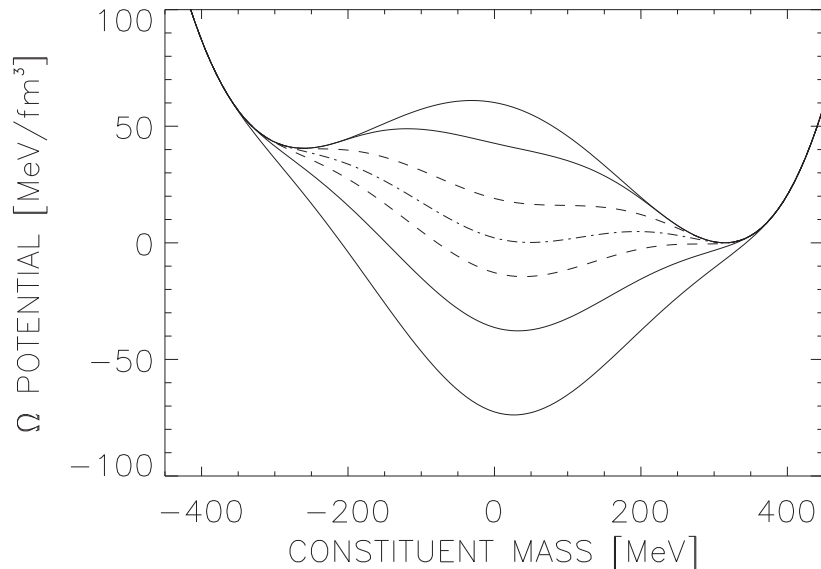


Figure 1. The thermodynamical potential Ω for the sigma model at $T = 0$ and quark chemical potentials (starting from the top): $\mu = [0, 225, 279, 306, 322, 345, 375]$ MeV.

One can plot a family of curves for the (T, μ) values corresponding to an isentropic expansion of matter. Qualitatively the potential curves look similar to the ones depicted in Fig. 1. Assume that at some early stage of the reaction the thermal equilibrium is established, and partonic matter is in a “high energy density” phase Q (lowest curve). This state corresponds to the absolute minimum of Ω with the order parameter close to zero, $\sigma \approx 0$, $\pi = 0$, and chiral symmetry restored. Due to a very high internal pressure, Q matter will expand and cool down. At some stage a metastable minimum appears in Ω at a finite value of σ corresponding to a “low energy density” phase H (lower dashed curve), in which chiral symmetry is spontaneously broken. At some later time, the critical line in the (T, μ) plane is crossed where the Q and H minima have equal depths, i.e. $P_H = P_Q$ (dot-dashed curve). At later times the H phase becomes more favorable, but the two phases are still separated by a potential barrier. At certain stage the minimum corresponding to the Q phase disappears (upper dashed curve). The dashed curves separate the regions in the phase diagram where one of the phases is unstable (spinodal points). If the expansion of the Q phase continues until the barrier vanishes,

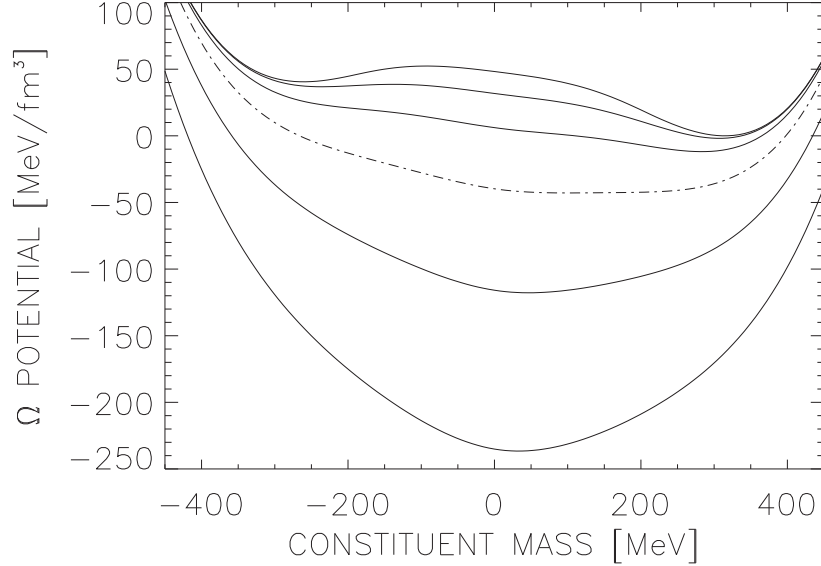


Figure 2. The thermodynamical potential Ω for the sigma model for the sigma model at μ fixed to 207 MeV and temperatures (starting from the top): $T = [0, 50, 75, 100, 125, 150]$ MeV.

the system will find itself in an absolutely unstable state at a maximum of the thermodynamic potential. Therefore, it will freely roll down into the lower energy state corresponding to the H phase. This situation is known as spinodal instability. As shown e.g. in ref. [14], the characteristic time of the “rolling down” process is relatively short, of about 1 fm/c.

As well known, a first order phase transition proceeds through the nucleation process. According to the standard theory of homogeneous nucleation [15], supercritical bubbles of the H phase can appear only below the critical line, when $P_H > P_Q$. Then the critical radius for growing bubbles is $R_c = 2\gamma/(P_H - P_Q)$, where γ is the interface energy per unit area (surface tension). In rapidly expanding matter the nucleation picture might be very different. As argued in ref. [6], the phase separation in this case can begin as early as the metastable H state appears in the thermodynamic potential, and a stable interface between the two phases may exist. An appreciable amount of nucleation bubbles and even empty cavities may be created already above the critical line. They are stabilized by the collective expansion of matter.

The bubble formation and growth will also continue below the critical line. Previously formed bubbles will now grow faster due to increasing pressure difference, $P_H - P_Q > 0$, between the two phases. It is most likely that the conversion of Q matter on the bubble boundary is not fast enough to saturate the H phase. Therefore, a fast expansion may lead to a deeper cooling of the

H phase inside the bubbles compared to the surrounding Q matter. Strictly speaking, such a system cannot be characterized by the unique temperature. At some stage the H bubbles will percolate, and the topology of the system will change to isolated regions of the Q phase (Q droplets) surrounded by the undersaturated vapor of the H phase.

3. Fragmentation of a metastable phase

The characteristic droplet size can be estimated by applying the energy balance consideration, proposed by Grady [16, 17] in the study of dynamical fragmentation of fluids. The idea is that the fragmentation of expanding matter is a local process minimizing the sum of surface and kinetic (dilational) energies per fragment volume. As shown in ref. [21], this prescription works fairly well for the multifragmentation of expanding nuclear systems produced in intermediate-energy heavy-ion reactions, where the standard statistical approach fails.

Let us consider first an isotropically expanding system where the collective velocity field follows locally the Hubble law

$$v(r) = H \cdot r, \quad (1)$$

where H is a Hubble constant. Since there is no preferred direction, the droplets of the Q phase will have a more or less spherical shape. The characteristic radius of the droplet, R , can be estimated as follows [16]. The energy ΔE associated with a Q droplet embedded in a background of the H phase is represented as the sum of three terms,

$$\Delta E = E_{bulk} + E_{kin} + E_{sur}. \quad (2)$$

The bulk term is simply equal to $\Delta \mathcal{E} V$ where $\Delta \mathcal{E} = \mathcal{E}_Q - \mathcal{E}_H$ is the energy density difference between the two bulk phases and $V \propto R^3$ is the volume of the droplet. The second term is the collective kinetic energy of the droplet expansion with respect to its center of mass,

$$E_{kin} = \frac{1}{2} \int \mathcal{E} v^2(r) dV = \frac{3}{10} \Delta \mathcal{E} V H^2 R^2. \quad (3)$$

The last term in eq. (2) is the interface energy, $E_{sur} = \gamma S$, which is parametrized in terms of the effective surface tension γ and the surface area $S \propto R^2$. Grady's argument is that the redistribution of matter is a local process minimizing the energy per droplet volume, $\Delta E/V$. Then the bulk contribution does not depend on R , and the minimization condition constitutes the balance between the collective kinetic energy and interface energy. This leads to the

optimum radius of a droplet

$$R^* = \left(\frac{5\gamma}{\Delta\mathcal{E}H^2} \right)^{1/3}. \quad (4)$$

It is worth noting that the collective kinetic energy acts here as an effective long-range potential similar to the Coulomb potential in nuclei.

At ultrarelativistic collision energies associated with RHIC and LHC experiments, the expansion of partonic matter will be very anisotropic with its strongest component along the beam direction [18]. Clear indications of such an anisotropy are seen already at SPS energies (see [9]). It is natural to think that in this case the inhomogeneities associated with the phase transition will rearrange into pancake-like slabs of Q matter embedded in a dilute H phase. The characteristic width of the slab, $2L$, can be estimated in a similar way and the resulting expression for L^* differs from Eq. (4) only by a geometrical factor (3 instead of 5 in parentheses). Generally, the faster is the expansion, the smaller are the fractures. Of course, at a later time the Q droplets will further fragment in the transverse direction due to the standard nucleation process.

As Eq. (4) indicates, the droplet size depends strongly on H . When expansion is slow (small H) the droplets are big. Ultimately, the process may look like a fission of a cloud of plasma. But fast expansion should lead to very small droplets. This state of matter is very far from thermodynamical equilibrium, particularly because the H phase is very dilute. One can say that the metastable Q matter is torn apart by a mechanical strain associated with the collective expansion. This has a direct analogy with the fragmentation of pressurized fluids leaving nozzles. In a similar way, splashed water makes droplets which have nothing to do with the liquid-gas phase transition.

The driving force for expansion is the pressure gradient, $\nabla P \equiv c_s^2 \nabla \mathcal{E}$, which depends crucially on the sound velocity in the matter, c_s . Here we are interested in the expansion rate of the partonic phase which is not directly observable. In the vicinity of the phase transition, one may expect a ‘‘soft point’’ [19, 20] where the sound velocity is smallest and the ability of matter to generate the collective expansion is minimal. If the initial state of the Q phase is close to this point, its subsequent expansion will be slow. Accordingly, the droplets produced in this case will be big. When moving away from the soft point, one would see smaller and smaller droplets. For numerical estimates we choose two values of the Hubble constant: $H^{-1}=20$ fm/c to represent the slow expansion from the soft point and $H^{-1}=6$ fm/c for the fast expansion.

One should also specify two other parameters, γ and $\Delta\mathcal{E}$. The surface tension γ is a subject of debate at present. Lattice simulations indicate that at the critical point it could be as low as a few MeV/fm². However, for our non-equilibrium scenario, more appropriate values are closer to 10-20 MeV/fm²

which follow from effective chiral models. As a compromise, the value $\gamma = 10 \text{ MeV/fm}^2$ is used below. Bearing in mind that nucleons and heavy mesons are the smallest droplets of the Q phase, one can take $\Delta\mathcal{E} = 0.5 \text{ GeV/fm}^3$, i.e. the energy density inside the nucleon. Then one gets $R^* = 3.4 \text{ fm}$ for $H^{-1} = 20 \text{ fm/c}$ and $R^* = 1.5 \text{ fm}$ for $H^{-1} = 6 \text{ fm/c}$. As follows from eq. (4), for a spherical droplet $V \propto 1/\Delta\mathcal{E}$, and in the first approximation its mass,

$$M^* \approx \Delta\mathcal{E}V = \frac{20\pi}{3} \frac{\gamma}{H^2}, \quad (5)$$

is independent of $\Delta\mathcal{E}$. For two values of R^* given above the mass is $\sim 100 \text{ GeV}$ and $\sim 10 \text{ GeV}$, respectively. The pancake-like droplets could be heavier due to their larger transverse size. Using the minimum information principle one can show [17, 21] that the distribution of droplets should follow an exponential law, $\exp\left(-\frac{M}{M^*}\right)$. Thus, about 2/3 of droplets have masses smaller than M^* , but with 1% probability one can find droplets as heavy as $5M^*$.

4. Observable manifestations of quark droplets

After separation, the droplets recede from each other according to the Hubble law, like galaxies in expanding Universe. Therefore, their c.m. rapidities are in one-to-one correspondence with their spatial positions. One may expect that they are distributed more or less uniformly between the target and the projectile rapidities. On this late stage it is unlikely that the thermodynamical equilibrium is re-established between the Q and H phases or within the H phase alone. If this were to happen, the final H phase would be uniform, and thus there would be no traces of the droplet phase in the final state.

The final fate of individual droplets depends on their sizes and on details of the equation of state. Due to the additional Laplace pressure, $2\gamma/R$, the residual expansion of individual droplets will slow down. The smaller droplets may even reverse their expansion and cooling to shrinking and reheating. Then, the conversion of Q matter into H phase may proceed through the formation of the imploding deflagration front [20, 22]. Bigger droplets may expand further until they enter the region of spinodal instability. At this stage the difference between 1-st and 2-nd order phase transitions or a crossover is insignificant. Since the characteristic “rolling down” time is rather short, $\sim 1 \text{ fm/c}$, the Q droplets will be rapidly converted into the non-equilibrium H phase. In refs. [10, 12] the evolution of individual droplets was studied numerically within a hydrodynamical approach including dynamical chiral fields (Chiral Fluid Dynamics). It has been demonstrated that the energy released at the spinodal decomposition can be transferred directly into the collective oscillations of the (σ, π) fields which give rise to the soft pion radiation. One can also expect the formation of Disoriented Chiral Condensates (DCC) in the voids between the Q droplets.

An interesting possibility arises if the metastable Q phase has a point of zero pressure. In particular, this is the case for the MIT bag model equation of state at temperatures only slightly below T_c [23]. In this case the droplets might be in mechanical equilibrium with the surrounding vacuum ($P_H \approx 0$), like atomic nuclei or water droplets. The equilibrium condition is

$$P_Q = \frac{\nu_Q}{2\pi^2} \left[\frac{7\pi^4}{180} T^4 + \frac{\pi^2}{6} T^2 \mu^2 + \frac{1}{12} \mu^4 \right] - B = \frac{2\gamma}{R}, \quad (6)$$

where $\nu_Q = 12$ is the degeneracy factor for massless u and d quarks (the gluon contribution is omitted here), and B is a bag constant. The evolution is then governed by the evaporation of hadrons from the surface (see also the discussion in Ref. [24]). One can speculate about all kinds of exotic objects, like e.g. strangelets, glueballs, formed in this way. The possibility of forming “vacuum bubbles”, i.e. regions with depleted quark and gluon condensates, was discussed in ref. [10]. All these interesting possibilities deserve further study and numerical simulations.

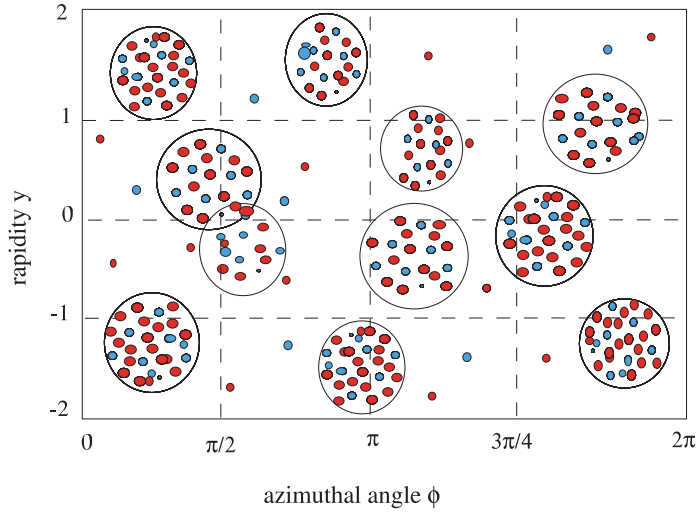


Figure 3. Schematic view of the momentum space distribution of secondary hadrons produced from an ensemble of droplets. Each droplet emits hadrons (mostly pions) within a rapidity interval $\delta y \sim 1$ and azimuthal angle spreading of $\delta\phi \sim 1$.

After separation the QGP droplets recede from each other according to the global expansion, predominantly along the beam direction. Hence their center-of-mass rapidities y_i are in one-to-one correspondence with their spatial positions. Presumably y_i will be distributed more or less evenly between the target and projectile rapidities. Since rescatterings in the dilute H phase

are rare, most hadrons produced from individual droplets will go directly into detectors. This may explain why freeze-out parameters extracted from the hadronic yields are always very close to the phase transition boundary [25].

In the droplet phase the mean number of produced hadrons in a given rapidity interval is

$$\langle N \rangle = \sum_i^{N_D} \bar{n}_i = \langle n \rangle \langle N_D \rangle, \quad (7)$$

where \bar{n}_i is the mean multiplicity of hadrons emitted from a droplet i , $\langle n \rangle$ is the average multiplicity per droplet and $\langle N_D \rangle$ is the mean number of droplets produced in this interval. If droplets do not overlap in the rapidity space, each droplet will give a bump in the hadron rapidity distribution around its center-of-mass rapidity y_i [14]. In case of a Boltzmann spectrum the width of the bump will be $\delta\eta \sim \sqrt{T/m}$, where T is the droplet temperature and m is the particle mass. At $T \sim 100$ MeV this gives $\delta\eta \approx 0.8$ for pions and $\delta\eta \approx 0.3$ for nucleons. These spectra might be slightly modified by the residual expansion of droplets. Due to the radial expansion of the fireball the droplets should also be well separated in the azimuthal angle. The characteristic angular spreading of pions produced by an individual droplet is determined by the ratio of the thermal momentum of emitted pions to their mean transverse momentum, $\delta\phi \approx 3T/\langle p_\perp \rangle \sim 1$. The resulting phase-space distribution of hadrons in a single event will be a superposition of contributions from different Q droplets superimposed on a more or less uniform background from the H phase. Such a distribution is shown schemmatically in Fig. 3. It is obvious that such inhomogeneities (clusterization) in the momentum space will reveal strong non-statistical fluctuations. The fluctuations will be more pronounced if primordial droplets are big, as expected in the vicinity of the soft point. If droplets as heavy as 100 GeV are formed, each of them will emit up to ~ 200 pions within a narrow rapidity and angular intervals, $\delta\eta \sim 1$, $\delta\phi \sim 1$. If only a few droplets are produced in average per unit rapidity, $N_D \gtrsim 1$, they will be easily resolved and analyzed. On the other hand, the fluctuations will be suppressed by factor $\sqrt{N_D}$ if many small droplets shine in the same rapidity interval.

5. Anomalous multiplicity fluctuations

For our discussion below we consider a more general case of the droplet mass distribution when masses follow a gamma-distribution

$$w_k(M) = \frac{b}{\Gamma(k)} (bM)^{k-1} \exp(-bM), \quad (8)$$

which is normalized for $0 \leq M \leq \infty$. The mean mass and its standard deviation are expressed through the parameters k and b as

$$\langle M \rangle = \frac{k}{b}, \quad \sigma_M = \frac{\sqrt{k}}{b} = \frac{\langle M \rangle}{\sqrt{k}}. \quad (9)$$

These expressions show that quantity $1/\sqrt{k}$ gives the relative scale of fluctuations of M around $\langle M \rangle$. It should be stressed that the gamma-distribution (8) drops at large M less rapidly than a corresponding gaussian distribution.

One can easily calculate the combined multiplicity distribution produced by the ensemble of many droplets. Let us assume that the normalized mass distribution of droplets is $w_k(M)$ and that each droplet emits hadrons according to the Poisson law, $p_{\bar{n}}(n)$, with the mean multiplicity proportional to the droplet mass, $\bar{n} = M/\langle E_\pi \rangle$ (for pions $\langle E_\pi \rangle \approx 3T \sim 0.5$ GeV). Then the combined distribution is given by the convolution of the two,

$$P_k(N) = \int_0^M dM w_k(M) p_{\bar{n}}(N). \quad (10)$$

For the gamma-distribution (8) one can perform explicit analytical calculations. It is remarkable that the resulting distribution is a famous Negative Binomial Distribution (NBD)

$$P_k(N) = \frac{(N+k-1)!}{N!(k-1)!} \frac{\left(\frac{\langle N \rangle}{k}\right)^N}{\left(1 + \frac{\langle N \rangle}{k}\right)^{N+k}}. \quad (11)$$

In a limiting case of the exponential mass distribution ($k=1$) the combined distribution is simply given by

$$P_1(N) = \frac{1}{\langle N \rangle} \left(\frac{\langle N \rangle}{1 + \langle N \rangle} \right)^{N+1}, \quad (12)$$

where $\langle N \rangle = \langle \bar{n} \rangle = \alpha \langle M \rangle$ is the mean total multiplicity.

It is convenient to characterize the fluctuations by the scaled variance

$$\omega_N \equiv \frac{\langle N^2 \rangle - \langle N \rangle^2}{\langle N \rangle}. \quad (13)$$

Its important property is that $\omega_N = 1$ for the Poisson distribution, and therefore any deviation from unity will signal a non-statistical emission mechanism. For the NBD, eq. (11), one easily finds $\omega_N = 1 + \langle N \rangle/k$. As shown in ref. [26], for an ensemble of emitting sources (droplets) ω_N can be expressed in a simple form, $\omega_N = \omega_n + \langle n \rangle \omega_D$, where ω_n is an average multiplicity

fluctuation in a single droplet, ω_D is the fluctuation in the droplet size distribution and $\langle n \rangle$ is the mean multiplicity from a single droplet. Since ω_n and ω_D are typically of order of unity, the fluctuations from the multi-droplet emission are enhanced by the factor $\langle n \rangle$. According to the picture of a first order phase transition advocated above, this enhancement factor could be as large as 10^2 . It is clear that the nontrivial structure of the hadronic spectra will be washed out to a great extent when averaging over many events. Therefore, more sophisticated methods of the event sample analysis should be applied. As demonstrated below, the simplest one is to search for non-statistical fluctuations in the hadron multiplicity distributions measured in a varied rapidity bin.

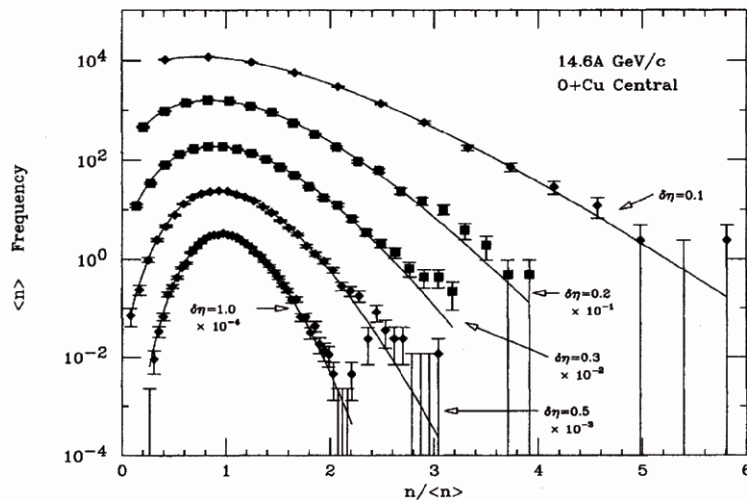


Figure 4. Event-by-event multiplicity distributions in $\delta\eta$ intervals 0.1, 0.2, 0.3, 0.5, 1.0 measured by E-802 Collaboration for central $^{16}\text{O}+\text{Cu}$ collisions at lab energy 14.6 AGeV [27]. The data for each interval are plotted as a function of $n/\langle n \rangle$ and scaled by $\langle n \rangle$, the mean multiplicity in the interval. Each successive distribution has been normalized by the factor indicated in the figure. The shape evolves from almost Gaussian ($\delta\eta = 1.0$) to nearly exponential ($\delta\eta=0.1$).

The event-by-event multiplicity fluctuations observed so far in heavy-ion experiments do not reveal any anomalous enhancement. Fig. 4 shows an example of the multiplicity distributions in varying pseudorapidity intervals measured for O+Cu central collisions at AGS [27]. These distributions can very well be fitted by the NBD where parameters $k(\delta\eta)$ and $\langle N(\delta\eta) \rangle$ follow a linear relationship with nonzero intercept $k(0)$. The data show an increase in scaled variances of about 15÷30% over 1. Apparently such moderate deviations can be explained by ordinary reasons, not related to a phase transition. An interesting observation has been made by the NA49 collaboration [28],

which has found non-monotonic behaviour of ω_N as a function of the projectile participant number N_p . But in this case too the actual values of ω_N are only of about 2, and most likely they can be explained by the fluctuations in the number of target participants [29].

It should be noted that the NBD fits were first used to describe the multiplicity distributions in high-energy pp and $p\bar{p}$ collisions (see e.g. ref.[30]). They are consistent with the so called KNO scaling [31].

6. Conclusions

- A first order phase transition in rapidly expanding matter should proceed through the nonequilibrium stage when a metastable phase splits into droplets whose size is inversely proportional to the expansion rate. The primordial droplets should be biggest in the vicinity of a soft point when the expansion is slowest.
- Hadron emission from droplets of the quark-gluon plasma should lead to large nonstatistical fluctuations in their rapidity and azimuthal spectra, as well as in multiplicity distributions in a given rapidity window. The hadron abundances may reflect directly the chemical composition in the plasma phase.
- To identify the phase transition threshold the measurements should be done at different collision energies. The predicted dependence on the expansion rate and the reaction geometry can be checked in collisions with different ion masses and impact parameters.
- If the first order deconfinement/chiral phase transition is only possible at finite baryon densities, one should try to identify it by searching for the anomalous fluctuations in the regions of phase space characterized by a large baryon chemical potential. These could be the nuclear fragmentation regions in collisions with very high energies (high-energy SPS, RHIC, LHC) or the central rapidity region (AGS, low-energy SPS, future GSI facility FAIR).

The author is grateful to L.M. Satarov, M.I. Gorenstein and M. Gazdzicki for many fruitful discussions. This work was supported partly by the RFBR grant 05-02-04013 (Russia).

References

- 1 M.A. Halasz, A.D. Jackson, R.E. Shrock, M.A. Stephanov and J.J.M. Verbarshot, *Phys. Rev. D* **58**, 096007 (1998).
- 2 J. Berges and K. Rajagopal, *Nucl. Phys.* **B538**, 215 (1999).

- 3 O. Scavenius, A. Mocsy, I.N. Mishustin, D. Rischke, *Phys. Rev. C* **64**, 045202 (2001).
- 4 M. Stephanov, K. Rajagopal and E. Shuryak, *Phys. Rev. Lett.* **81**, 4816 (1998).
- 5 Boris Berdnikov and Krishna Rajagopal, *Phys. Rev.* **D61**, 105017 (2000).
- 6 I.N. Mishustin, *Phys. Rev. Lett.* **82**, 4779 (1999).
- 7 I.N. Mishustin, L.M. Satarov, H. Stoecker and W. Greiner, *Phys. Rev.* **C59**, 3243 (1999).
- 8 W. Reisdorf and FOPI Collaboration, *Nucl. Phys.* **A612**, 493 (1997).
- 9 Nu Xu, *Prog. Part. Nucl. Phys.* **53**, 165 (2004).
- 10 I.N. Mishustin, O. Scavenius, *Phys. Rev. Lett.* **83**, 3134 (1999).
- 11 O. Scavenius, A. Dumitru, E. S. Fraga, J. T. Lenaghan and A. D. Jackson, *Phys. Rev. D* **63**, 116003 (2001).
- 12 K. Paech, H. Stoecker and A. Dumitru, *Phys. Rev. C* **68**, 044907 (2003).
- 13 L.P. Csernai, I.N. Mishustin and A. Mocsy, *Heavy Ion Phys.*, **3**, 151 (1996);
A. Mocsy, M.Sc. thesis, University of Bergen, 1996.
- 14 L.P. Csernai, I.N. Mishustin, *Phys. Rev. Lett.* **74**, 5005 (1995).
- 15 L.P. Csernai, J.I. Kapusta, *Phys. Rev. Lett.* **69**, 737 (1992); *Phys. Rev.* **D46**, 1379 (1992).
- 16 D.E. Grady, *J. Appl. Phys.* **53**(1), 322 (1981).
- 17 B.L. Holian and D.E. Grady, *Phys. Rev. Lett.* **60**, 1355 (1988).
- 18 J. Bjorken, *Phys. Rev.* **D27**, 140 (1983).
- 19 C.M. Huang and E.V. Shuryak, *Phys. Rev. Lett.* **75**, 4003 (1995); *Phys. Rev.* **C57**, 1891 (1998).
- 20 D. Rischke, M. Gyulassy, *Nucl. Phys.* **A597**, 701 (1996); **A608**, 479 (1996).
- 21 I.N. Mishustin, *Nucl. Phys.* **A630**, 111c (1998).
- 22 S. Digal, A.M. Srivastava, *Phys. Rev. Lett.* **80**, 1841 (1998).
- 23 J.I. Kapusta, *Phys. Rev.* **D23**, 2444 (1981).
- 24 M. Alford, K. Rajagopal and F. Wilczek, *Phys. Lett.* **B422**, 247 (1998).
- 25 P. Braun-Münzinger, D. Magestro, K. Redlich, and J. Stachel, *Phys. Lett.* **B518**, 41 (2001);
P. Braun-Münzinger, J. Stachel, *J. Phys. G: Part. Nucl. Phys.* **28**, 1971 (2002).
- 26 G. Baym, H. Heiselberg, *Phys. Lett.* **B469**, 7 (1999).
- 27 T. Abbot and E-802 Collaboration, *Phys. Rev.* **C52**, 2663 (1995).
- 28 M. Rybczynski and NA49 Collaboration, *J. Phys. Conf. Ser.* **5**, 74 (2005).
- 29 V.P. Konchakovski, S. Haussler, M.I. Gorenstein, E.L. Bratkovskaya, M. Bleicher, and H. Stöcker, nucl-th/0511083.
- 30 P. Curruthers and C.C. Shih, *Phys. Lett.* **127B**, 242 (1983).
- 31 Z. Koba, H.B. Nielsen and P. Olesen, *Nucl. Phys.* **B40**, 317 (1972).

RESULTS FROM K2K AND STATUS OF T2K*

Yuichi Oyama[‡]

High Energy Accelerator Research Organization (KEK)

Abstract. Results from the K2K experiment and status of the T2K experiment are reported.

1. Results from the K2K experiment

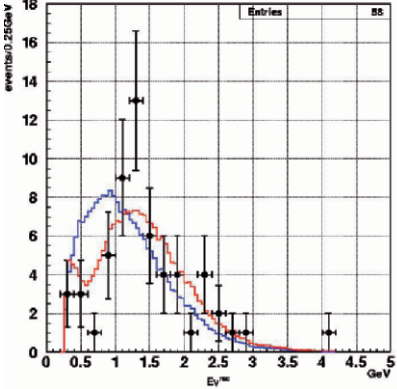
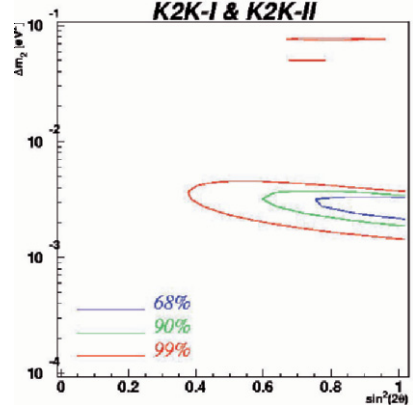
The K2K experiment[1] is the first long-baseline neutrino oscillation experiment with a distance of hundred kilometers and using an accelerator-based neutrino beam. It started in 1999 and ended in November, 2004. The main purpose of K2K is to confirm muon neutrino oscillation claimed by the Super-Kamiokande experiment[2] using an artificial neutrino beam. Because the details of the experiment are already described in other articles[1, 3], only updated numbers and figures are presented in Table 1. Some comments that were not covered in my previous articles[3] are itemized below:

- After the accident of Super-Kamiokande in November, 2001, the total number of PMTs in Super-Kamiokande was reduced to be about one half. The K2K experiment of this period was named K2K-II. In this period, the lead-glass counters of the front detector were replaced by a SciBar detector[1], a fully active fine-grained detector made of 14848 strips of extruded scintillator read out by wavelength-shifting fibers. There is no essential change in the oscillation analysis.
- A possible ν_e appearance signal from $\nu_e \leftrightarrow \nu_\mu$ oscillation was also searched[4]. From tight e -like event selection, only one candidate remains, where the expected background is 1.63. The expected signal is $1 \sim 2$ events if the parameter region around the CHOOZ limit[5] is assumed. The 90% C.L. upper limit on $\sin^2 2\theta_{e\mu}$ ($=\frac{1}{2} \sin^2 2\theta_{13}$) is 0.18 for $\Delta m^2 = 2.8 \times 10^{-3} \text{eV}^2$. This limit has no impact on our present knowledge on the oscillation parameters because of the poor statistics (see Section 3.1).

[‡] E-mail address: yuichi.oyama@kek.jp; URL: <http://www-nu.kek.jp/~oyama>

* Talk at International Conference on New Trends in High-Energy Physics (Crimea2005), Yalta, Ukraine, September 10-17, 2005

TABLE I. Summary of the K2K results. For explanations of the numbers and figures, see [3]

• Beam period	Jun 4, 1999 - Jul 12, 2001 (K2K-I) Jan 17, 2003 - Nov 6, 2004 (K2K-II)	
• Total beam time	442.8 days (233.7 for K2K-I + 209.1 for K2K-II)	
• Total spill numbers	17.4×10^6 spills	
• Total POT for analysis	92.2×10^{18}	
• Total event (data/expectation)	112 /	$155.9^{+13.6}_{-15.6}$
Single ring events	67 /	99.0
μ -like	58 /	90.8
e -like	9 /	8.2
(tight e -like cut)	(1) /	(1.63)
Multi ring events	45 /	56.8
• Null oscillation probability	0.003%	
• Best fit parameters in physical region	$(\Delta m^2, \sin^2 2\theta) = (2.76 \times 10^{-3} \text{eV}^2, 1.0)$	
• 90% C.L. Δm^2 for $\sin^2 2\theta = 1$	$(1.88 \sim 3.48) \times 10^{-3} \text{eV}^2$	
• Reconstructed neutrino energy spectrum		
• Allowed region in Δm^2 - $\sin^2 2\theta$ plane		

2. The T2K project: beamline and detectors

T2K (Tokai to Kamioka)[6] is the next long-baseline neutrino-oscillation experiment in Japan. A high-intensity neutrino beam from the J-PARC 50GeV Proton Synchrotron in JAEA, Tokai is shot toward Super-Kamiokande, 295 km away. Since all of these facilities, except Super-Kamiokande, are not familiar in the high-energy physics society, they are summarized in Table 2. A bird's eye view illustration of the entire J-PARC is shown in Fig. 1.

J-PARC has been under construction since 2001. The T2K experiment was officially approved in December, 2003, except for the 2-km detector discussed below. Construction of the neutrino beamline started in April, 2004. The experiment will start in early 2009.

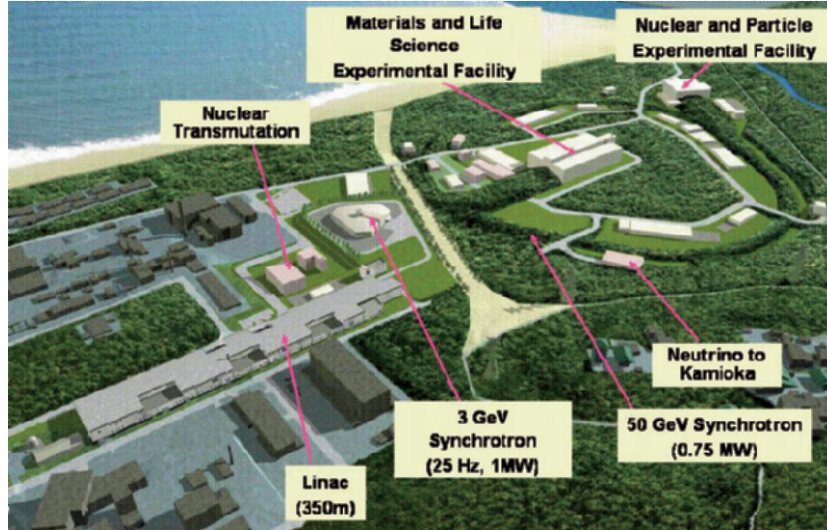


Figure 1. Bird's eye view of the entire J-PARC project.

Schematic configurations of the T2K beamline and detectors are illustrated in Fig. 2. They consist of the proton beamline, target station, decay volume, beam dump, muon monitors at 140 m downstream from the target, first front detectors at 280 m, second front detectors at 2 km, and Super-Kamiokande as a far detector at 295 km. The main differences from the K2K experiment are: (1) very high beam intensity, (2) off-axis beam and (3) 2 km detector. In the following, these three main differences are focused on one by one.

TABLE II. Summary of the facilities and nicknames related to the T2K experiment.

J-PARC	Japan <u>P</u> roton <u>A</u> ccelerator <u>R</u> esearch <u>C</u> omplex. The name of the entire project. It includes high energy physics, nuclear physics, life science, material science and nuclear technology. The Accelerators consist of 400MeV Linac, 3 GeV Proton Synchrotron and 50GeV proton Synchrotron.
JAEA	Japan <u>A</u> tom ic <u>E</u> nergy <u>A</u> gency. Host institute of J-PARC. KEK is the second host institute. Renamed from JAERI (Japan <u>A</u> tom ic <u>E</u> nergy <u>R</u> esearch <u>I</u> nstitute) on October 1, 2005.
Tokai	Name of the village where JAEA is located. About 110km north-east from Tokyo
JHF	Japan <u>H</u> adron <u>F</u> acility. Name of the 50GeV Proton Synchrotron project.
T2K	<u>T</u> okai to <u>K</u> amioka. Name of the long-baseline neutrino-oscillation experiment. It was also called JHF- ν or J-PARC ν

TABLE III. Comparisons of the beam parameters between K2K and T2K. For the neutrino events in Super-Kamiokande, 22.5kton is the fiducial mass and one year is taken as 100 days. The absence of neutrino oscillation is assumed, and the number for K2K was calculated from 155.9events/442.8days (see Table 1). For T2K, a 2° off-axis angle is assumed. Some of the parameters in the T2K upgrade are still being designed.

	K2K	T2K	T2K upgrade
Proton Energy (GeV)	12	50	50
Beam power (kW)	5.2	750	4000
Proton per second	3×10^{12}	1×10^{14}	5×10^{14}
Accelerator cycle (sec)	2.2	3.64	
Beam duration (μ sec)	1.2	4.2	
Neutrino events in SK (/22.5kton/year)	35	3900	

2.1. HIGH-INTENSITY PROTON BEAM

The most significant upgrade from the K2K experiment is the beam intensity. The beam power of T2K in the first stage is 0.75 MW. It is more than 2 orders of magnitude larger than that of K2K. A further upgrade of the beam intensity after several years of 0.75 MW operation is also under consideration. Comparisons of the beam parameters between the K2K, T2K and T2K upgrade are summarized in Table III.

The number of neutrino events in T2K is about 110-times larger than that of K2K. This high-statistics observation enables searches for unknown oscillation channels as well as precise determinations of the oscillation parameters in $\nu_\mu \leftrightarrow \nu_\tau$.

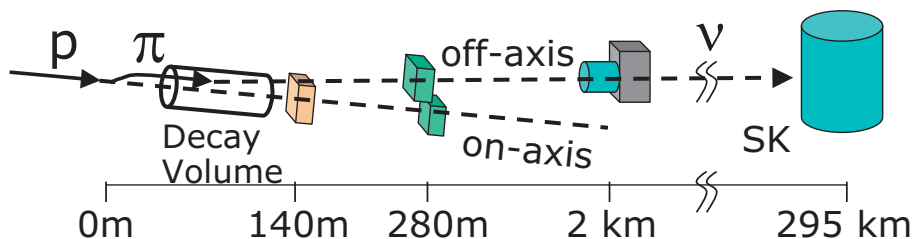


Figure 2. Schematic configuration of the T2K beamline and detectors.

2.2. OFF-AXIS BEAM

Off-axis beam[7] means that the center of the beam direction is adjusted to be $2^\circ \sim 3^\circ$ off from the Super-Kamiokande direction, as shown in Fig. 2. Although the neutrino beam intensity at Super-Kamiokande is lower than that of the beam center (on-axis) direction, the peak energy is low and high-energy neutrinos are strongly suppressed. The neutrino energy spectra for several off-axis angles are shown in Fig. 3. An off-axis beam is favored because a neutrino energy lower than ~ 1 GeV is preferable in the T2K experiment for the following three reasons:

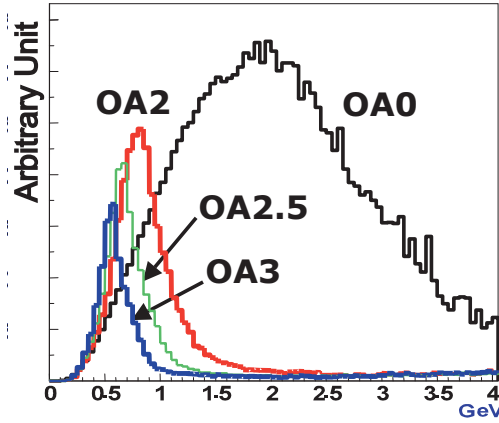


Figure 3. Neutrino energy spectrum for several off-axis angles.

The first reason is the neutrino oscillation probability. The probability that ν_μ remains as ν_μ is written as

$$P(\nu_\mu \rightarrow \nu_\mu) = 1 - \sin^2 2\theta_{23} \sin^2 \left(\frac{1.27 \Delta m_{23}^2 L}{E_\nu} \right), \quad (1)$$

where L is the neutrino travel distance ($L = 295\text{km}$) and E_ν is the neutrino energy. $P(\nu_\mu \rightarrow \nu_\mu)$ as a function of E_ν is also shown in Fig. 4. The neutrino energy, which corresponds to the first oscillation maximum, E_{oscmax} , is obtained from

$$\frac{1.27 \Delta m_{23}^2 L}{E_{oscmax}} = \frac{\pi}{2} \quad (2)$$

or

$$E_{oscmax} = \frac{2.54 \Delta m^2 L}{\pi}. \quad (3)$$

$E_{oscmax} = 0.596\text{GeV}$ for $\Delta m^2 = 2.5 \times 10^{-3}\text{eV}^2$ and $E_{oscmax} = 0.834\text{GeV}$ for $\Delta m^2 = 3.5 \times 10^{-3}\text{eV}^2$. If the neutrino beam energy agrees with

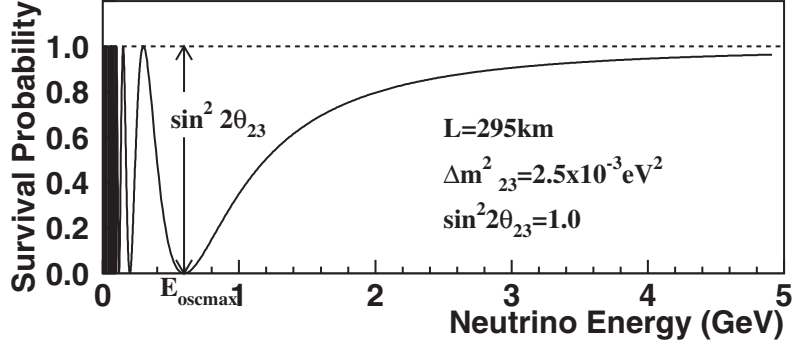


Figure 4. Survival probability of muon neutrinos as a function of the neutrino energy. The neutrino travel distance is 295 km and oscillation parameters are assumed to be $(\Delta m_{23}^2, \sin^2 2\theta_{23}) = (2.5 \times 10^{-3} \text{eV}^2, 1.0)$.

E_{oscmax} , the oscillation occurs effectively, and a study of neutrino oscillation is also efficient.

The second reason is the fraction of the charged-current quasi-elastic scattering (CCQE) in the neutrino interactions. As reported in K2K[1], the neutrino energy spectrum is obtained from CCQE interactions,

$$\nu_{\mu} + n \rightarrow \mu^{-} + p, \quad (4)$$

calculated by simple 2-body kinematics

$$E_{\nu} = \frac{m_N E_{\mu} - m_{\mu}^2/2}{m_N - E_{\mu} + p_{\mu} \cos \theta_{\mu}}, \quad (5)$$

where m_N and m_{μ} are the masses of the nucleon and the muon, respectively, and $E_{\mu} = \sqrt{p_{\mu}^2 + m_{\mu}^2}$. Other neutrino interactions cannot be used for this purpose because of complex kinematics. Moreover they constitute serious background when CCQE events are selected. The neutrino cross section and the contribution of CCQE interactions are shown in Fig. 5. Although neutrinos of energy larger than ~ 1 GeV have larger total cross sections, most of the interactions are non-CCQE and disturb the determination of neutrino energy spectrum.

The third reason is related to the second reason, but concerns the nature of water Cherenkov detectors. Water Cherenkov detectors show excellent performance for single ring events or multiple ring events in which particles forward to opposite directions and the Cherenkov rings

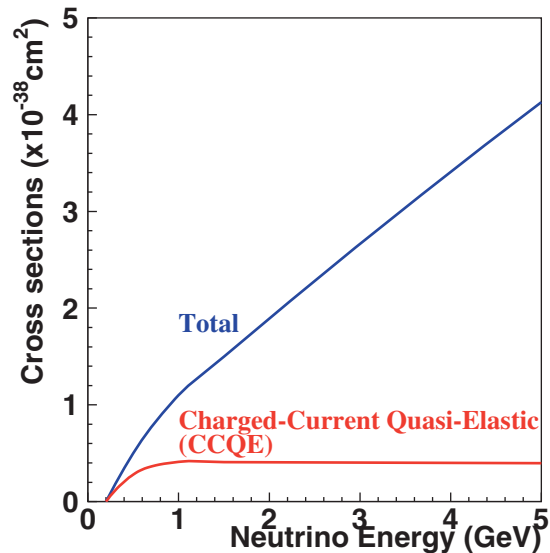


Figure 5. Neutrino cross section and the fraction of CCQE as a function of the neutrino energy.

do not overlap with each other. On the other hand, it does not have good performance for events with heavy ring overlapping. High-energy ($E_\nu \gtrsim 1$ GeV) neutrinos that produce multiple rings are not preferable in water Cherenkov detectors.

The best off-axis angle implies that the peak of the neutrino energy spectrum is exactly in accordance with the oscillation maximum. See Table 4 for the relation between the off-axis angle, the peak of the neutrino energy and the corresponding Δm_{23}^2 . Unfortunately, the Δm_{23}^2 values reported by other experiments[1, 2] have large ambiguity, and the best off-axis angle is still unknown. For this reason, we must maintain the tunability of the off-axis angle until just before the commissioning of the neutrino beam.

We are constructing a decay volume having a special shape, as shown in Fig. 6. The cross section of the decay volume is rectangular and the height of the volume is becoming larger downstream. The cross section in the most downstream part is 3 m (width) \times 5.43 m (height). If the position of the beam center is adjusted to 1.50 m (3.93 m) below the top of the decay volume, the direction of the Super-Kamiokande and Hyper-Kamiokande[6, 8] is 2.0° (3.0°) off-axis, as shown in Fig. 6. The direction of the beam center can be adjusted by arranging the magnets

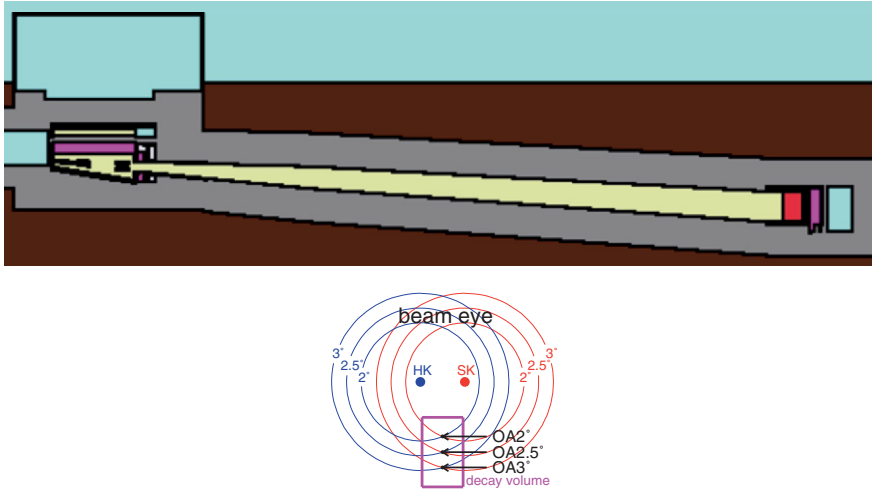


Figure 6. (left) Schematic view of the target station, decay volume and beam dump. The height of the decay volume is becoming larger in the downstream region in order to change the direction of the beam center. (right) Cross section view of the decay volume and the directional correlation with Super-Kamiokande and Hyper-Kamiokande.

in the final focusing section and target/horn in the target station. Civil construction is not required. We can determine the beam direction about a half year before the beam commissioning which is scheduled for early 2009. Hopefully, we can decide the exact beam direction in the summer of 2008, after hearing about the latest result from the MINOS[9] experiment, reported at the 2008 summer conferences.

TABLE IV. Off-axis angle, peak of the neutrino energy spectrum and the corresponding Δm^2 for a neutrino travel distance of 295 km, which were calculated from $E_{oscmax} = E_{peak}$.

Off axis angle	2.0°	2.1°	2.4°	3.0°
E_{peak} (GeV)	0.782	0.756	0.656	0.520
$\Delta m_{23}^2 (\times 10^{-3} \text{eV}^2)$	3.28	3.17	2.75	2.18

2.3. THE 2 KM DETECTOR

We have proposed to construct second front detectors at about 2 km from the proton target for the following two reasons.

The first reason is related to the off-axis beam. For reliable neutrino flux extrapolation from the front detectors to the far detector, the 110 m of the neutrino production point (i.e. decay volume) must be viewed as “point like” from the front detectors. At the 280 m detector with a 2.5° off-axis position, the angular difference between the neutrino from the most upstream part of the decay volume and the most downstream part is about 1.6° . Obviously, this angular difference is not negligible. The 280 m detector site is too near to the neutrino production point.

The other reason is the water Cherenkov detector as a front detector. A water Cherenkov detector is definitely needed as a front detector because the detection technique is exactly the same as the far detector, and most of the systematic errors inherent to the detector can be canceled out. However, we have a serious difficulty with the event rate. If a 1 kt water Cherenkov detector (the same size as K2K) is constructed at the 280 m site, the event rate will be about 60 events per one spill, which is a $4.2 \mu\text{sec}$ beam duration. This event rate is much larger than the capacity of the water Cherenkov detector.

Because of these reasons, we decided to construct second front detectors, whose main component is a water Cherenkov detector outside of the JAEA campus. From physics constraints as well as a problem concerning estate ownership, we proposed them to be located at about 2 km away from the target. This 2 km detector was not included in the first proposal, and has not yet been approved.

3. Physics goal of T2K

If neutrinos have mass, the flavor eigenstates are a mixture of the mass eigenstates:

$$\begin{pmatrix} \nu_e \\ \nu_\mu \\ \nu_\tau \end{pmatrix} = \mathbf{U} \begin{pmatrix} \nu_1 \\ \nu_2 \\ \nu_3 \end{pmatrix}. \quad (6)$$

The neutrino mass matrix, \mathbf{U} , has 6 independent parameters. They are 2 square mass differences (Δm_{12}^2 and Δm_{23}^2), 3 mixing angles (θ_{12} , θ_{23} and θ_{13}) and 1 CP-violation phase (δ).

Among 6 parameters, Δm_{12}^2 and θ_{12} were determined by solar neutrino experiments[10, 11] and a reactor experiment[12]. At present, their values are

$$\Delta m_{12}^2 = (6 \sim 8) \times 10^{-5} \text{eV}^2 \quad \text{and} \quad \sin^2 2\theta_{12} \approx 0.8. \quad (7)$$

On the other hand, Δm_{23}^2 and θ_{23} were studied by using atmospheric neutrinos[2] and long-baseline accelerator neutrinos[1]. The present values are

$$\Delta m_{23}^2 = (2 \sim 3) \times 10^{-3} \text{eV}^2 \quad \text{and} \quad \sin^2 2\theta_{23} \gtrsim 0.9. \quad (8)$$

Accordingly, unknown oscillation parameters are θ_{13} and δ .

The physics goal of the T2K experiment is a complete understanding of the neutrino-oscillation parameters. It includes: (1) the first observation of finite θ_{13} ; (2) precise measurements of Δm_{23}^2 and θ_{23} ; (3) observation of the CP violation phase δ after a beam-intensity upgrade from 0.75 MW to 4MW and construction of Hyper-Kamiokande. The third topic will not occur within the next decade, and is thus beyond the scope of this document. Only the first and second items are discussed below.

3.1. $\nu_e \leftrightarrow \nu_\mu$ OSCILLATION

Within the framework of 3-flavor oscillation, the oscillation probability of ν_μ to ν_e with the θ_{13} channel is written as

$$P(\nu_\mu \rightarrow \nu_e) \approx \sin^2 \theta_{23} \sin^2 2\theta_{13} \sin^2 \left(\frac{1.27 \Delta m_{23}^2 L}{E_\nu} \right). \quad (9)$$

In past neutrino oscillation searches, Δm^2 and $\sin^2 2\theta$ were simultaneously searched for in the Δm^2 - $\sin^2 2\theta$ plane. On the contrary, in the θ_{13} search, other parameters in the oscillation probability have almost been determined from the $\nu_\mu \leftrightarrow \nu_\tau$ oscillation, as given in Eq.(8).

From a theoretical point of view, θ_{13} is expected to be small because it is the mixing angle between the first and third generation. In fact, the present upper limit reported by the CHOOZ experiment[5] is $\sin^2 2\theta_{13} \sim 0.1$. Even though the energy of the neutrino beam is adjusted to E_{oscmax} based on knowledge of the $\nu_\mu \leftrightarrow \nu_\tau$ oscillation,

$$P(\nu_\mu \rightarrow \nu_e) \approx \frac{1}{2} \sin^2 2\theta_{13} \sin^2 \left(\frac{1.27 \Delta m_{23}^2 L}{E_\nu} \right) < 0.05, \quad (10)$$

where $\sin^2 \theta_{13}$ is taken as $\sim 1/2$ from Eq.(8). Therefore, an appearance search of electron neutrinos with a probability of less than a few percent is necessary to find a finite θ_{13} . Obviously, the statistics of K2K was too poor to examine such a small oscillation probability (see [4] and the first section).

More than 100-times larger statistics in T2K makes a search for such a small oscillation probability possible. Furthermore, in addition

to the analysis procedure in K2K, constraints on the electron neutrino energy can be applied in selecting the ν_e appearance signal, because the parent neutrino energy calculated from Eq.(5) (by replacing muon by electron) has a quasi-monochromatic energy spectrum, as discussed in Section 2.2.

From a careful Monte-Carlo study, about ~ 100 ν_e signals are expected, whereas the background from the neutral current and the beam-originated ν_e are less than 15, if the oscillation parameter is assumed to be $\sin^2 2\theta_{13} = 0.1$ with 5×10^{21} POT. The nominal sensitive region is

$$\sin^2 2\theta_{13} > 0.006. \quad (11)$$

This improves the sensitive region from the CHOOZ experiment by a factor of ~ 20 .

3.2. $\nu_\mu \leftrightarrow \nu_\tau$ OSCILLATION

Precise determinations of Δm_{23}^2 and $\sin^2 2\theta_{23}$ were attained by precise measurements of the neutrino survival probability as a function of the neutrino energy given in Fig. 4.

Δm_{23}^2 is directly determined from the position of the oscillation maximum (E_{oscmax}) from Eq.(3). From $\sim 5\%$ accuracy of the E_{oscmax} measurement, Δm_{23}^2 is also determined with $\sim 5\%$ accuracy. Since $\Delta m_{23}^2 = (2 \sim 3) \times 10^{-3} \text{eV}^2$,

$$\delta(\Delta m_{23}^2) \sim 0.1 \times 10^{-3} \text{eV}^2 \quad (12)$$

is possible.

On the other hand, $\sin^2 2\theta_{23}$ is determined from the depth of the dip at E_{oscmax} in the neutrino survival probability (see Fig. 4) and/or the absolute reduction rate of muon neutrino events. Because more than 10000 neutrino events are expected within 5 years of operation, the statistical error for the event rate is reduced to be about 1%. Therefore,

$$\delta(\sin^2 2\theta_{23}) \sim 0.01 \quad (13)$$

is expected.

The author is grateful to the members of K2K and T2K collaborations for fruitful discussions.

References

- 1 K.Nishikawa *et al.*, KEK-PS proposal, Nucl.Phys.B (Proc. Suppl.) 59,289 (1997).
- S.H.Ahn *et al.*, Phys.Lett.B511,178 (2001).

- M.H.PAhn *et al.*, Phys. Rev. Lett. 90,041801 (2003).
M.H.PAhn *et al.*, Phys. Rev. Lett. 93,051801 (2004).
E.PAliu *et al.*, Phys. Rev. Lett. 94,081802 (2005).
- 2 Y.Fukuda *et al.*, Phys.Lett.B 433,9 (1998).
Y.Fukuda *et al.*, Phys.Lett.B 436,33 (1998).
Y.Fukuda *et al.*, Phys.Rev.Lett. 81,1562 (1998).
Y.Fukuda *et al.*, Phys.Rev.Lett. 82,2644 (1999).
Y.Fukuda *et al.*, Phys.Lett.B 467,185 (1999).
S.Fukuda *et al.*, Phys.Rev.Lett. 85,3999 (2000).
Y.Pashie *et al.*, Phys.Rev.Lett. 93,101801 (2004).
Y.Pashie *et al.*, Phys.Rev.D 71, 112005 (2005).
- 3 Y.Oyama, hep-ex/9803014 (1998).
Y.Oyama, hep-ex/0004015 (2000).
Y.Oyama, hep-ex/0104014 (2001).
Y.Oyama, hep-ex/0210030 (2002).
- 4 K2K collaboration, in preparation.
- 5 M.Papollonio *et al.*, Phys.Lett.B 466,415 (1999).
- 6 Y.Htow *et al.*, hep-ex/0106019 (2001).
- 7 D.PBeavis *et al.*, BNL AGS E-889(1995).
- 8 An one mega ton water Cherenkov detector, Hyper-Kamiokande, is under preparation for proposal. The location is also in Kamioka area, but is about 10km south from the Super-Kamiokande site. To provide the same off-axis beam both toward Super-Kamiokande and Hyper-Kamiokande, the beam center must be moved in vertical.
- 9 E.Pables *et al.*, Fermilab-Proposal-P875.
- 10 Y.Fukuda *et al.*, Phys.Rev.Lett. 81,1158 (1998).
Y.Fukuda *et al.*, Phys.Rev.Lett. 82,1810 (1999).
Y.Fukuda *et al.*, Phys.Rev.Lett. 82,2430 (1999).
S.Fukuda *et al.*, Phys.Rev.Lett. 86,5651 (2001).
S.Fukuda *et al.*, Phys.Rev.Lett. 86,5656 (2001).
S.Fukuda *et al.*, Phys.Lett.B 539,179 (2002).
M.B.Smy *et al.*, Phys.Rev.D 69, 011104 (2004).
- 11 Q.R.PAhmad *et al.*, Phys.Rev.Lett. 89, 011301 (2002).
- 12 K.Eguchi *et al.*, Phys.Rev.Lett. 90, 021802 (2003).

HAMILTONIAN APPROACH TO COSMOLOGICAL PERTURBATIONS IN GENERAL RELATIVITY

B.M. Barbashov

Bogoliubov Laboratory of Theoretical Physics, JINR, 141980 Dubna

V.N. Pervushin

Bogoliubov Laboratory of Theoretical Physics, JINR, 141980 Dubna

A.F. Zakharov

*National Astronomical Observatories of Chinese Academy of Sciences, 20A
Datun Road, Chaoyang District, Beijing, 100012, China*

Institute of Theoretical and Experimental Physics, 25, 117259, Moscow

Astro Space Center of Lebedev Physics Institute of RAS, Moscow

Bogoliubov Laboratory of Theoretical Physics, JINR, 141980 Dubna

V.A. Zinchuk

Bogoliubov Laboratory of Theoretical Physics, JINR, 141980 Dubna

Abstract. The Hamiltonian approach to cosmological perturbations in general relativity (GR) in finite space-time is considered, where a cosmological scale factor is identified with spatial averaging the metric determinant logarithm. This identification keeps the number of variables and energy constraint in GR. It leads to a cosmological perturbation theory with the scalar potential perturbations in contrast to the kinetic ones in the Lifshitz version of 1946.

The “CMBR primordial power spectrum” and other problems of modern cosmology are described in terms of scale-invariant variables by quantization of the energy constraint and cosmological creation of both a universe and its matter with the assumption that the initial data of this quantum creation can be determined by the uncertainty principle.

1. Introduction

The cosmological perturbation theory in general relativity (GR) (Lifshits, 1946; Bardeen, 1980; V. F. Mukhanov and Brandenberger, 1992) based on the separation of the cosmological scale factor by the transformation $g_{\mu\nu} = a^2 \tilde{g}_{\mu\nu}$ is one of the basic tools applied for analysis of modern observational data including Cosmic Microwave Background Radiation (CMBR).

In the present paper we discuss the problem of the relation between the cosmological perturbation theory and the Hamiltonian approach (Dirac, 1958;

R. Arnowitt and Misner, 1960) to GR, where a similar scale factor was considered in (Pawlowski and Pervushin,) as the homogeneous invariant evolution parameter in accordance with the Hamiltonian diffeomorphism subgroup $x^0 \rightarrow \tilde{x}^0 = \tilde{x}^0(x^0)$ (Zelmanov, 1973) meaning in fact that the coordinate evolution parameter x^0 is not observable.

The content of the paper is the following. In Section 2, the status of the cosmological perturbation theory in GR is described. In Section 3, it is shown that the separation of the scale factor can lead to exact resolution of the energy constraint and to the Hamiltonian reduction. Sections 4 and 5 are devoted to a cosmological model of a quantum universe that follows from the reduced theory. The Hamiltonian perturbation theory and its comparison with Lifshitz's one are given in Section 6.

2. Status of cosmological perturbation theory

GR is given in terms of metric components and fields f by the Hilbert action

$$S = \int d^4x \sqrt{-g} \left[-\frac{\varphi_0^2}{6} R(g) + \mathcal{L}_{(M)}(\varphi_0|g, f) \right] \quad (1)$$

and the space-time geometric interval $ds^2 = g_{\mu\nu} dx^\mu dx^\nu$, where the parameter

$$\varphi_0 = \sqrt{3/8\pi G_0} = \sqrt{3M_{\text{Planck}}^2/8\pi} \quad (2)$$

scales all masses, and G_0 is the Newton coupling constant in units $\hbar = c = 1$.

The Hamiltonian approach is formulated by means of a geometric interval

$$ds^2 = g_{\mu\nu} dx^\mu dx^\nu \equiv \omega_{(0)}\omega_{(0)} - \omega_{(1)}\omega_{(1)} - \omega_{(2)}\omega_{(2)} - \omega_{(3)}\omega_{(3)}, \quad (3)$$

where $\omega_{(a)}$ are linear differential forms (Fock, 1929) in terms of the Dirac variables (Dirac, 1958)

$$\omega_{(0)} = \psi^6 N_d dx^0, \quad \omega_{(b)} = \psi^2 \mathbf{e}_{(b)i} (dx^i + N^i dx^0); \quad (4)$$

here ψ is the spatial metrics determinant, $\mathbf{e}_{(a)i}$ are triads with $\det|\mathbf{e}| = 1$, N_d is the Dirac lapse function, and N^i is the shift vector. The comparison of this interval with the one

$$ds^2 = a^2(\eta) \left[(1 + 2\Phi)d\eta^2 - 2N_k dx^k d\eta - (1 - 2\Psi)(dx^k)^2 - dx^i dx^j (h_{ij}) \right] \quad (5)$$

used in the cosmological perturbation theory (Lifshits, 1946) raises to the following questions: What is the difference between the coordinate parameter x^0 in the Hamiltonian approach (4) and the conformal time η in the theory (5)? What is number of variables (in particular, homogeneous ones) in GR?

3. Separation of cosmological scale factor and Hamiltonian reduction

There is a set of arguments (Pawlowski and Pervushin,; Zelmanov, 1973; York, 1971) to identify an “evolution parameter” in GR with the cosmological scale factor $a(x_0)$ introduced by the scale transformation: $g_{\mu\nu} = a^2(x_0)\tilde{g}_{\mu\nu}$, where $\tilde{g}_{\mu\nu}$ is defined by (3) and (4), where $\tilde{N}_d = a^2 N_d$ and $\tilde{\psi}^2 = a^{-1}\psi^2$. In order to keep the number of variables of GR, the scale factor can be defined using the spatial averaging $\log \sqrt{a} \equiv \langle \log \psi \rangle \equiv V_0^{-1} \int d^3x \log \psi$, so that there is the identity

$$\langle \log \tilde{\psi} \rangle \equiv V_0^{-1} \int d^3x \log \tilde{\psi} = V_0^{-1} \int d^3x [\log \psi - \langle \log \psi \rangle] \equiv 0, \quad (6)$$

where $V_0 = \int d^3x$ is finite volume. The similar scale transformation of a curvature

$$\sqrt{-g}R(g) = a^2 \sqrt{-\tilde{g}}R(\tilde{g}) - 6a\partial_0 \left[\partial_0 a \sqrt{-\tilde{g}} \tilde{g}^{00} \right]$$

converts action (1) into

$$S = \tilde{S} - \int_{V_0} dx^0 (\partial_0 \varphi)^2 \int \frac{d^3x}{\tilde{N}_d}, \quad (7)$$

where \tilde{S} is the action (1) in terms of metrics \tilde{g} and the running scale of all masses $\varphi(x^0) = \varphi_0 a(x^0)$ and $(\tilde{N}_d)^{-1} = \sqrt{-\tilde{g}} \tilde{g}^{00}$.

One can construct the Hamiltonian function using the definition of a set of canonical momenta:

$$P_\varphi = \frac{\partial \mathcal{L}}{\partial(\partial_0 \varphi)} = -2V_0 \partial_0 \varphi \langle (\tilde{N}_d)^{-1} \rangle = -2V_0 \frac{d\varphi}{d\zeta} \equiv -2V_0 \varphi', \quad (8)$$

$$p_\psi = \frac{\partial \mathcal{L}}{\partial(\partial_0 \log \tilde{\psi})} \equiv -\frac{4\varphi^2}{3} \cdot \frac{\partial_l(\tilde{\psi}^6 N^l) - \partial_0(\tilde{\psi}^6)}{\tilde{\psi}^6 \tilde{N}_d}, \quad (9)$$

where $d\zeta = \langle (\tilde{N}_d)^{-1} \rangle^{-1} dx^0$ is a time-interval invariant with respect to reparametrizations of the coordinate parameter x^0 . One can construct the Hamiltonian form of the action in terms of momenta P_φ and $P_F = [p_\psi, p_{(b)}^i, p_f]$ including (8), (9)

$$S = \int dx^0 \left[\int d^3x \left(\sum_F P_F \partial_0 F + C - \tilde{N}_d \tilde{T}_0^0 \right) - P_\varphi \partial_0 \varphi + \frac{P_\varphi^2}{4 \int d^3x (\tilde{N}_d)^{-1}} \right], \quad (10)$$

where $C = N^i T_i^0 + C_0 p_\psi + C_{(b)} \partial_k \mathbf{e}_{(b)}^k$ is the sum of constraints with the Lagrangian multipliers $N^i, C_0, C_{(b)}$ and the energy–momentum tensor components T_i^0 ; these constraints include the transversality $\partial_i \mathbf{e}_{(b)}^i \simeq 0$ and the

Dirac minimal surface (Dirac, 1958):

$$p_\psi \simeq 0 \quad \Rightarrow \quad \partial_j(\tilde{\psi}^6 \mathcal{N}^j) = (\tilde{\psi}^6)' \quad (\mathcal{N}^j = N^j \langle \tilde{N}_d^{-1} \rangle). \quad (11)$$

The explicit dependence of \tilde{T}_0^0 on $\tilde{\psi}$ was given in terms of the scale invariant Lichnerowicz variables (York, 1971) $\omega_{(\mu)}^{(L)} = \psi^{-2} \omega_{(\mu)}$ in (A. F. Zakharov and Pervushin, 2006):

$$\tilde{T}_0^0 = \tilde{\psi}^7 \hat{\Delta} \tilde{\psi} + \sum_I \tilde{\psi}^I a^{I/2-2} \tau_I, \quad (12)$$

where $\hat{\Delta} F \equiv (4\varphi^2/3)\partial_{(b)}\partial_{(b)}F$ is the Laplace operator and τ_I is partial energy density marked by the index I running a set of values $I = 0$ (stiff), 4 (radiation), 6 (mass), 8 (curvature), 12 (Λ -term) in accordance with a type of matter field contributions, and a is the scale factor.

The energy constraint $\delta S[\varphi_0]/\delta \tilde{N}_d = 0$ takes the algebraic form

$$-\frac{\delta \tilde{S}[\varphi]}{\delta \tilde{N}_d} \equiv \tilde{T}_0^0 = \frac{(\partial_0 \varphi)^2}{\tilde{N}_d^2} = \frac{P_\varphi^2}{4V_0^2[\langle (\tilde{N}_d)^{-1} \rangle \tilde{N}_d]^2}, \quad (13)$$

where T_0^0 is the local energy density by definition. The spatial averaging of this equation multiplied by \tilde{N}_d looks like the energy constraint

$$P_\varphi^2 = E_\varphi^2, \quad (14)$$

where the Hamiltonian functional

$$E_\varphi = 2 \int d^3x \sqrt{\tilde{T}_0^0} = 2V_0 \left\langle \sqrt{\tilde{T}_0^0} \right\rangle \quad (15)$$

can be treated as the ‘‘universe energy’’ by analogy with the ‘‘particle energy’’ in special relativity (SR). Eqs. (8) and (14) have the exact solution

$$\zeta(\varphi_0|\varphi) \equiv \int dx^0 \langle (\tilde{N}_d)^{-1} \rangle^{-1} = \pm \int_\varphi^{\varphi_0} \frac{d\tilde{\varphi}}{\langle \sqrt{\tilde{T}_0^0(\tilde{\varphi})} \rangle} \quad (16)$$

well known as the Hubble-type evolution. The local part of Eq. (13) determines a part of the Dirac lapse function invariant with respect to diffeomorphisms of the Hamiltonian formulation $x^0 \rightarrow \tilde{x}^0 = \tilde{x}^0(x^0)$ (Zelmanov, 1973):

$$N_{\text{inv}} = \langle (\tilde{N}_d)^{-1} \rangle \tilde{N}_d = \left\langle \sqrt{\tilde{T}_0^0} \right\rangle \left(\sqrt{\tilde{T}_0^0} \right)^{-1}. \quad (17)$$

One can find evolution of all field variables $F(\varphi, x^i)$ with respect to φ by the variation of the ‘‘reduced’’ action obtained as values of the Hamiltonian

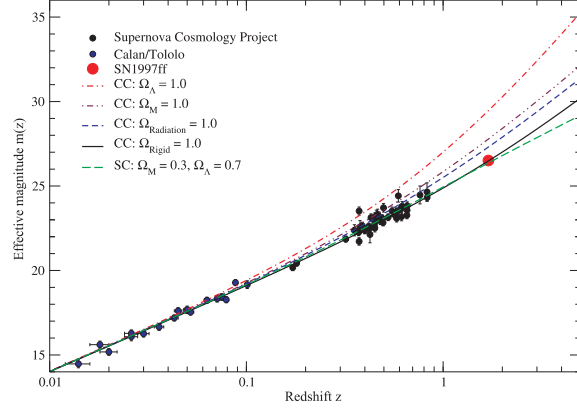


Figure 1. The Hubble diagram (D. B. Behnke, 2004) in cases of the “scale-variant” units of standard cosmology (SC) and the “scale-invariant” ones of conformal cosmology (CC). The points include 42 high-redshift Type Ia supernovae (A. G. R., 1998; S. P., 1999) and the reported farthest supernova SN1997ff (A. G. R., 2001). The best fit to these data requires a cosmological constant $\Omega_\Lambda = 0.7$ $\Omega_{\text{CDM}} = 0.3$ in the case of SC, whereas in CC these data are consistent with the dominance of the rigid (stiff) state.

form of the initial action (10) onto the energy constraint (14) (Pawlowski and Pervushin,):

$$S[\varphi_0]|_{P_\varphi=\pm E_\varphi} = \int_{\varphi}^{\varphi_0} d\bar{\varphi} \left\{ \int d^3x \left[\sum_F P_F \partial_\varphi F + \bar{C} \mp 2\sqrt{\bar{T}_0(\bar{\varphi})} \right] \right\}, \quad (18)$$

where $\bar{C} = C/\partial_0\bar{\varphi}$. The reduced Hamiltonian $\sqrt{\bar{T}_0}$ is Hermitian, if the minimal surface constraint (11) removes a negative contribution of p_ψ from the energy density. Thus, the Hamiltonian reduction as the solution of the energy constraint converts two basic quantities of the theory (the initial action (10) and interval (4)) into the reduced action (18) (with the nonzero energy (15) as the generator of evolution with respect to the scale factor φ) and the Hubble-type geometric relations (16) and (17) with the diffeo-invariant homogeneous time, respectively.

4. Observational data in terms of scale-invariant variables

Let us assume that the local density $T_0^0 = \rho_{(0)}(\varphi) + T_f$ contains a tremendous cosmological background $\rho_{(0)}(\varphi)$.

In this case, one can apply the low-energy decomposition of “reduced” action (18) $2d\varphi \sqrt{\bar{T}_0^0} = 2d\varphi \sqrt{\rho_{(0)} + T_f} = d\varphi \left[2\sqrt{\rho_{(0)}} + T_f/\sqrt{\rho_{(0)}} \right] + \dots$ over field density T_f . The first term of this sum $S^{(\pm)}|_{P_\varphi=\pm E_\varphi} = S_{\text{cosmic}}^{(\pm)} + S_{\text{field}}^{(\pm)} + \dots$

is the reduced cosmological action $S_{\text{cosmic}}^{(\pm)} = \mp 2V_0 \int_{\varphi_1}^{\varphi_0} d\varphi \sqrt{\rho_{(0)}(\varphi)}$, whereas the second one is the standard field action of GR and SM

$$S_{\text{field}}^{(\pm)} = \int_{\zeta_1}^{\zeta_0} d\zeta \int d^3x \left[\sum_F P_F \partial_\eta F + \bar{C} - T_f \right] \quad (19)$$

in the space determined by the interval

$$ds^2 = d\zeta^2 - [e_{(a)i}(dx^i + \mathcal{N}^i d\zeta)]^2; \quad \partial_i e_{(a)}^i = 0, \quad \partial_i \mathcal{N}^i = 0 \quad (20)$$

with conformal time $d\eta = d\zeta = d\varphi/\rho_{(0)}^{1/2}$, coordinate distance $r = |x|$, and running masses $m(\zeta) = a(\zeta)m_0$.

We see that the correspondence principle leads to the theory (19), where the scale-invariant conformal variables and coordinates are identified with observable ones and the cosmic evolution with the evolution of masses:

$$\frac{E_{\text{emission}}}{E_0} = \frac{m_{\text{atom}}(\eta_0 - r)}{m_{\text{atom}}(\eta_0)} = \frac{\varphi(\eta_0 - r)}{\varphi_0} = a(\eta_0 - r) = \frac{1}{1+z}.$$

The best fit to the data including cosmological SN observations (A. G. R., 1998; S. P., 1999; A. G. R., 2001) requires a cosmological constant $\Omega_\Lambda = 0.7$, $\Omega_{\text{CDM}} = 0.3$ in the case of the Friedmann “scale-variant quantities” of standard cosmology, whereas for the “scale-invariant conformal quantities” these data are consistent with the dominance of the stiff state of free scalar field $[z+1]^{-1}(\eta) = \sqrt{1+2H_0(\eta-\eta_0)}$: $\Omega_{\text{Stiff}} = 0.85 \pm 0.15$, $\Omega_{\text{CDM}} = 0.15 \pm 0.10$ (D. Behnke and Proskurin, 2002) (see Fig. 1). Thus the stiff state can describe all epochs including the creation of a quantum universe.

5. The quantum universe

In the lowest order of the cosmological perturbation theory $\tilde{T}_0^0 \simeq \rho_0(\varphi)$, $\tilde{N}_d = N_0(x^0)$, the Hilbert action (1) and the invariant interval ζ (16) take the form

$$S_{\text{cosmic}} = V_0 \int dx^0 N_0 \left[- \left(\frac{d\varphi}{N_0 dx^0} \right)^2 + \rho_0(\varphi) \right], \quad \zeta = \int N_0 dx^0 \quad (21)$$

keeping the symmetry of GR in the homogeneous approximation $x^0 \rightarrow \tilde{x}^0 = \tilde{x}^0(x^0)$, where the time ζ coincides with the conformal one η .

In the Hamiltonian approach, the action (21) takes the form

$$S = \int dx^0 \left[-P_\varphi \partial_0 \varphi + \frac{N_0}{4V_0} (P_\varphi^2 - E_\varphi^2) \right],$$

where $E_\varphi \equiv 2V_0 \sqrt{\rho_0}$ is treated as the reduced energy, since the scale factor φ plays the role of an evolution parameter; whereas the canonical momentum P_φ is considered as a generator of the evolution with respect to the scale factor φ forward or backward in the Wheeler – DeWitt field space of events depending on a sign of resolution of the energy constraint $P_\varphi^2 - E_\varphi^2 = 0 \rightarrow P_{\varphi_\pm} = \pm E_\varphi$. The problem of the negative reduced energy (defined as values of the reduced Hamiltonian onto equations of motion) is solved by the primary and secondary quantizations of the energy constraint in accordance with QFT.

The primary quantization is known as the Wheeler – DeWitt equation (Wheeler, ; DeWitt, 1967) $[\hat{P}_\varphi^2 - E_\varphi^2]\Psi_{\text{wdw}} = 0$, here $\hat{P}_\varphi = -id/d\varphi$. In order to diagonalize the WDW field Hamiltonian, this equation is rewritten in terms of holomorphic variables A^+, A^- : $\Psi_{\text{wdw}} = (1/\sqrt{2E_\varphi})[A^+ + A^-]$ (Pervushin and Smirichinski, 1999). After the secondary quantization of the WDW field A^+ and A^- are the operators of creation and annihilation of a quantum of a universe.

Bogoliubov’s transformation: $A^+ = \alpha B^+ + \beta^* B^-$ diagonalizes the equations of motion by the condensation of “universes” $\langle 0|(i/2)[A^+A^+ - A^-A^-]|0 \rangle = R$ and describes creation of a “number” of universes $\langle 0|A^+A^-|0 \rangle = N$ from the stable Bogoliubov vacuum $B^-|0 \rangle = 0$ (Bogoliubov, 1947). The vacuum postulate $B^-|0 \rangle = 0$ leads to an arrow of the conformal time $\eta \geq 0$ and its absolute point of reference $\eta = 0$ at the moment of creation $\varphi = \varphi_I$ (Pawlowski and Pervushin,).

The cosmological creation of the “universes” is described by the Bogoliubov equations

$$\frac{dN(\varphi)}{d\varphi} = \frac{1}{2E_\varphi} \frac{dE_\varphi}{d\varphi} \sqrt{4N(N+1) - R^2}, \quad (22)$$

$$\frac{dR(\varphi)}{d\varphi} = -2E_\varphi \sqrt{4N(N+1) - R^2}. \quad (23)$$

In the model of the stiff (rigid) state $\rho = p$, where $E_\varphi = Q/\varphi$, the equations (22) and (23) have an exact solution (Pervushin and Zinchuk,)

$$N(\varphi) = \frac{1}{4Q} R(\varphi) = \frac{1}{4Q^2 - 1} \sin^2 \left[\sqrt{Q^2 - \frac{1}{4}} \ln \frac{\varphi}{\varphi_I} \right] \neq 0, \quad (24)$$

where $\varphi = \varphi_I \sqrt{1 + 2H_I \eta}$. The initial data $\varphi_I = \varphi(\eta = 0)$, $H_I = \varphi'_I/\varphi_I = Q/(2V_0\varphi_I^2)$ are considered as a point of creation or annihilation of a universe; whereas the Planck value of the running mass scale $\varphi_0 = \varphi(\eta = \eta_0)$ belongs to the present day moment η_0 .

These initial data φ_I and H_I are determined by parameters of matter cosmologically created from the Bogoliubov vacuum at the beginning of a universe $\eta \simeq 0$. In the Standard Model (SM), W-, Z- vector bosons have

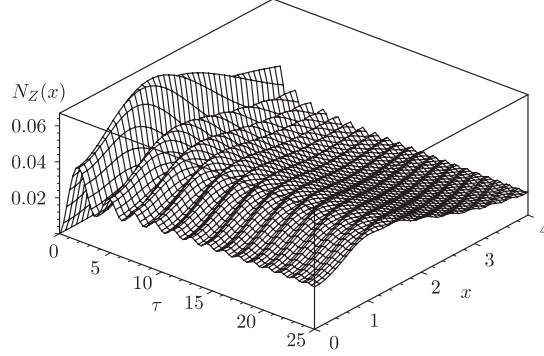


Figure 2. Longitudinal ($N_Z(x)$) components of the boson distribution versus the dimensionless time $\tau = 2\eta H_I$ and the dimensionless momentum $x = q/M_I$ at the initial data $M_I = H_I$ (D. B. Blaschke and Proskurin, 2004; A.G., 2004a).

maximal probability of this cosmological creation due to their mass singularity (D. B. Blaschke and Proskurin, 2004) (see Fig. 2). The uncertainty principle $\Delta E \cdot \Delta \eta \geq 1$ (where $\Delta E = 2M_I$, $\Delta \eta = 1/2H_I$) shows that at the moment of creation of vector bosons their Compton length defined by its inverse mass $M_I^{-1} = (a_I M_W)^{-1}$ is close to the universe horizon defined in the stiff state as $H_I^{-1} = a_I^2 (H_0)^{-1}$. Equating these quantities $M_I = H_I$ one can estimate the initial data of the scale factor $a_I^2 = (H_0/M_W)^{2/3} = 10^{-29}$ and the Hubble parameter $H_I = 10^{29} H_0 \sim 1 \text{ mm}^{-1} \sim 3K$. Just at this moment there is an effect of intensive cosmological creation of the vector bosons described in (D. B. Blaschke and Proskurin, 2004); in particular, the distribution functions of the longitudinal vector bosons demonstrate a large contribution of relativistic momenta. Their temperature T_c can be estimated from the equation in the kinetic theory for the time of establishment of this temperature $\eta_{relaxation}^{-1} \sim n(T_c) \times \sigma \sim H$, where $n(T_c) \sim T_c^3$ and $\sigma \sim 1/M_I^2$ is the cross-section. This kinetic equation and values of the initial data $M_I = H_I$ give the temperature of relativistic bosons $T_c \sim (M_I^2 H_I)^{1/3} = (M_0^2 H_0)^{1/3} \sim 3K$ as a conserved number of cosmic evolution compatible with the SN data (D. Behnke and Proskurin, 2002). We can see that this value is surprisingly close to the observed temperature of the CMB radiation $T_c = T_{\text{CMB}} = 2.73 \text{ K}$. The primordial mesons before their decays polarize the Dirac fermion vacuum and give the baryon asymmetry frozen by the CP – violation so that $n_b/n_\gamma \sim X_{CP} \sim 10^{-9}$, $\Omega_b \sim \alpha_{\text{QED}}/\sin^2 \theta_{\text{Weinberg}} \sim 0.03$, and $\Omega_R \sim 10^{-5} \div 10^{-4}$ (D. B. Blaschke and Proskurin, 2004). The equations describing the longitudinal vector bosons in SM, in this case, are close to the equations that follow from the Lifshitz perturbation theory and are used, in the inflationary model (V. F. Mukhanov and Brandenberger, 1992), for description of the “power primordial spectrum” of the CMB radiation.

6. The potential perturbations and shift vector

In order to simplify equations of the scalar potentials $N_{\text{inv}}, \tilde{\psi}$, one can introduce a new table of symbols:

$$N_s = \psi^7 N_{\text{inv}}, \quad \tilde{T} = \sum_I \tilde{\psi}^{(I-7)} a^{\frac{I}{2}-2} \tau_I, \quad \rho_{(0)} = \left\langle \sqrt{\tilde{T}_0^0} \right\rangle^2 = \varphi'^2. \quad (25)$$

The variations of the action (10) with respect to $N_s, \log \tilde{\psi}$ lead to equations

$$\hat{\Delta} \tilde{\psi} + \tilde{T} = \frac{\tilde{\psi}^7 \rho_{(0)}}{N_s^2}, \quad (26)$$

$$\tilde{\psi} \hat{\Delta} N_s + N_s \frac{d\tilde{T}}{d \log \tilde{\psi}} + 7 \frac{\tilde{\psi}^7 \rho_{(0)}}{N_s} = \rho_{(1)}, \quad (27)$$

respectively, where $\rho_{(1)} = \langle \tilde{\psi} \hat{\Delta} N_s + N_s \tilde{\psi} \partial_{\tilde{\psi}} \tilde{T} + 7 \tilde{\psi}^7 \rho_{(0)} / N_s \rangle$.

For $N_s = 1 - \nu_1$ and $\tilde{\psi} = 1 + \mu_1$ and the small deviations $\mu_1, \nu_1 \ll 1$ the first orders of Eqs. (26) and (27) take the form

$$[-\hat{\Delta} + 14\rho_{(0)} - \rho_{(1)}]\mu_1 + 2\rho_{(0)}\nu_1 = \bar{\tau}_{(0)}, \quad (28)$$

$$[7 \cdot 14\rho_{(0)} - 14\rho_{(1)} + \rho_{(2)}]\mu_1 + [-\hat{\Delta} + 14\rho_{(0)} - \rho_{(1)}]\nu_1 = 7\bar{\tau}_{(0)} - \bar{\tau}_{(1)}, \quad (29)$$

where

$$\rho_{(n)} = \langle \tau_{(n)} \rangle \equiv \sum_I I^n a^{\frac{I}{2}-2} \langle \tau_I \rangle. \quad (30)$$

This choice of variables determines $\tilde{\psi} = 1 + \mu_1$ and $N_s = 1 - \nu_1$ in the form of a sum

$$\tilde{\psi} = 1 + \frac{1}{2} \int d^3y \left[D_{(+)}(x, y) \bar{T}_{(+)}^{(\mu)}(y) + D_{(-)}(x, y) \bar{T}_{(-)}^{(\mu)}(y) \right], \quad (31)$$

$$N_s = 1 - \frac{1}{2} \int d^3y \left[D_{(+)}(x, y) \bar{T}_{(+)}^{(\nu)}(y) + D_{(-)}(x, y) \bar{T}_{(-)}^{(\nu)}(y) \right], \quad (32)$$

where β is given by

$$\beta = \sqrt{1 + [\langle \tau_{(2)} \rangle - 14\langle \tau_{(1)} \rangle] / (98\langle \tau_{(0)} \rangle)}, \quad (33)$$

$$\bar{T}_{(\pm)}^{(\mu)} = \bar{\tau}_{(0)} \mp 7\beta[7\bar{\tau}_{(0)} - \bar{\tau}_{(1)}], \quad \bar{T}_{(\pm)}^{(\nu)} = [7\bar{\tau}_{(0)} - \bar{\tau}_{(1)}] \pm (14\beta)^{-1} \bar{\tau}_{(0)} \quad (34)$$

are the local currents, $D_{(\pm)}(x, y)$ are the Green functions satisfying the equations

$$[\pm \hat{m}_{(\pm)}^2 - \hat{\Delta}] D_{(\pm)}(x, y) = \delta^3(x - y), \quad (35)$$

where $\hat{m}_{(\pm)}^2 = 14(\beta \pm 1)\langle \tau_{(0)} \rangle \mp \langle \tau_{(1)} \rangle$.

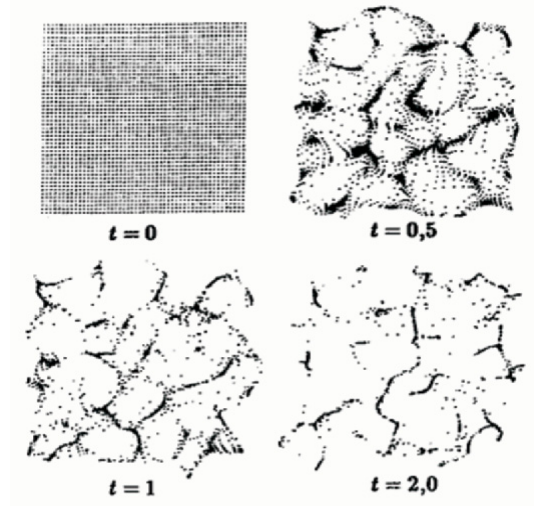


Figure 3. The diffusion of a system of particles moving in the space $ds^2 = d\eta^2 - (dx^i + N^i d\eta)^2$ with periodic shift vector N^i and zero momenta could be understood from analysis of O.D.E. $dx^i/d\eta = N^i$ considered in the two-dimensional case by Klyatskin (2001), if we substitute $t = m_{(-)}\eta$ and $N^i \sim \frac{x^i}{r} \sin m_{(-)}r$ in the equations, where $m_{(-)}$ is defined by Eq. (37).

In the case of point mass distribution in a finite volume V_0 with the zero pressure and the density $\overline{\tau}_{(0)}(x) = \overline{\tau}_{(1)}(x)/6 \equiv M [\delta^3(x-y) - 1/V_0]$, solutions (31), (32) take a form

$$\widetilde{\psi} = 1 + \mu_1 = 1 + \frac{r_g}{4r} \left[\gamma_1 e^{-m_{(+)}(z)r} + (1 - \gamma_1) \cos m_{(-)}(z)r \right], \quad (36)$$

$$N_s = 1 - \nu_1 = 1 - \frac{r_g}{4r} \left[(1 - \gamma_2) e^{-m_{(+)}(z)r} + \gamma_2 \cos m_{(-)}(z)r \right], \quad (37)$$

where $\gamma_1 = \frac{1+7\beta}{2}$, $\gamma_2 = \frac{14\beta-1}{28\beta}$, $r_g = \frac{3M}{4\pi\varphi^2}$, $r = |x-y|$, $m_{(\pm)}^2 = \hat{m}_{(\pm)}^2 3/(4\varphi^2)$.

The minimal surface (10) $\partial_i[\widetilde{\psi}^6 N^i] - (\widetilde{\psi}^6)' = 0$ gives the shift of the coordinate origin in the process of evolution

$$N^i = \left(\frac{x^i}{r} \right) \left(\frac{\partial_\zeta V}{\partial_r V} \right), \quad V(\zeta, r) = \int^r d\bar{r} \bar{r}^2 \widetilde{\psi}^6(\zeta, \bar{r}). \quad (38)$$

Solutions (36), (37) have spatial oscillations and the nonzero shift of the coordinate origin of the type of (38). In the infinite volume limit $\langle \tau_{(n)} \rangle = 0$, $a = 1$ solutions (36) and (37) coincide with the isotropic version of the Schwarzschild solutions: $\widetilde{\psi} = 1 + \frac{r_g}{4r}$, $N_s = 1 - \frac{r_g}{4r}$, $N^k = 0$.

Now one can compare the Hamiltonian perturbation theory with the standard cosmological perturbation theory (5) (Lifshits, 1946) where $\overline{\Phi} = \nu_1 + \mu_1$, $\overline{\Psi} = 2\mu_1$, $N^i = 0$. We note that the zero-Fourier harmonics of the spatial determinant is taken into account by V. F. Mukhanov and Brandenberger (1992)

twice that is an obstruction to the Hamiltonian method. The Hamiltonian approach shows us that if this double counting is removed, the equations of scalar potentials (28), and (29) will not contain time derivatives that are responsible for the CMB “primordial power spectrum” in the inflationary model (V. F. Mukhanov and Brandenberger, 1992). However, these equations of the Lifshits perturbation theory are close to ones of the primordial vector bosons considered in Section 6. We have seen above that the Hamiltonian approach to GR gives us another possibility to explain the CMBR “spectrum” by cosmological creation of vector W-, Z- bosons.

The next differences are a nonzero shift vector and the spatial oscillations of the scalar potentials determined by $\hat{m}_{(-)}^2$ (see Fig. 3). In the diffeo-invariant version of cosmology (D. Behnke and Proskurin, 2002), the SN data dominance of stiff state determines the parameter of spatial oscillations $\hat{m}_{(-)}^2 = \frac{6}{7}H_0^2[\Omega_R(z+1)^2 + \frac{9}{2}\Omega_{\text{Mass}}(z+1)]$. The values of red shift in the recombination epoch $z_r \sim 1100$ and the clustering parameter $r_{\text{clustering}} = \pi/\hat{m}_{(-)} \sim \pi/[H_0\Omega_R^{1/2}(1+z_r)] \sim 130$ Mpc recently discovered in the researches of large scale periodicity in redshift distribution (K. B., 2004b) lead to a reasonable value of the radiation-type density $10^{-4} < \Omega_R \sim 3 \cdot 10^{-3}$ at the time of this epoch.

7. Conclusion

Now one can reply the questions given in Section 2 about the difference between the coordinate parameter x^0 in the Hamiltonian approach (4) and the conformal time η , and a number of variables (in particular, homogeneous ones) in GR. The coordinate parameter x^0 in GR is an object of diffeomorphisms $x^0 \rightarrow \tilde{x}^0 = \tilde{x}^0(x^0)$ (which means that the parameter of evolution is a variable of the type of the scale factor), whereas the conformal time η is the diffeo-invariant geometric interval. The identification of x^0 and η on the level of the initial action in (V. F. Mukhanov and Brandenberger, 1992) converts GR into the Newton-type classical theory with a negative energy removing the energy constraint and the possibility to solve the energy-time problem using the experience of quantum field theory formulation. The conservation of the number of variables in GR leads to the potential perturbations describing the “primordial power spectrum” provided that the above-mentioned quantization of energy constraint is fulfilled in terms of scale-invariant variables.

Acknowledgements

The authors are grateful to D. Blaschke, A. Gusev, A. Efremov, E. Kuraev, V. Priezzhev, and S. Vinitsky for fruitful discussions. AFZ is grateful to the National Natural Science Foundation of China (NNSFC) (Grant # 10233050) for a partial financial support.

References

- A. F. Zakharov, V. A. Z. and Pervushin, V. N. (2006) Tetrad Formalism and Frames of References in General Relativity, *Physics of Particles and Nuclei* **37**, to be published.
- Bardeen, J. M. (1980) Gauge-invariant cosmological perturbations, *Phys. Rev. D* **22**, 1882–1905.
- Behnke, D. (2004) Conformal Cosmology Approach to the Problem of Dark Energy, Cosmology PhD, University of Rostock, Germany, Rostock Report MPG-VT-UR 248/04.
- Bogoliubov, N. N. (1947) On the theory of superfluidity, *J. Phys. (USSR)* **11**, 23–32.
- D. B. Blaschke, S. I. Vinitsky, A. A. G. V. N. P. and Proskurin, D. V. (2004) cosmological Production of Vector Bosons and Cosmic Microwave Background Radiation, *Physics of Atomic Nuclei* **67**, 1050–1062, hep-ph/0504225.
- D. Behnke, D. B. Blaschke, V. N. P. and Proskurin, D. V. (2002) Description of supernova data in conformal cosmology without cosmological constant, *Phys. Lett. B* **530**, 20–26, gr-qc/0102039.
- DeWitt, B. C. (1967) Quantum Theory of Gravity. I. The Canonical Theory, *Phys. Rev.* **160**, 1113–1148.
- Dirac, P. A. M. (1958) Generalized Hamiltonian Dynamics, *Proc. Roy. Soc. (London)* **A 246**, 326–332.
- A. G. (2004)a Cosmological Creation of W-, Z-Bosons and the Large-Scale Structure of the Universe, In *Problems of Gauge Theories*, Dubna, Russia, , JINR D2-2004-66, pp. 127–130.
- A. G. R. (1998) Observational Evidence from Supernovae for an Accelerating Universe and a Cosmological Constant, *Astron. J.* **116**, 1009–1038, astro-ph/9805201.
- A. G. R. (2001) The Farthest Known Supernova: Support for an Accelerating Universe and a Glimpse of the Epoch of Deceleration, *Astrophys. J.* **560**, 49–71, astro-ph/0104455.
- D. B., On the Nature of Dark Energy, In *Proceeding of the XVIII IAP Colloquium*, Paris.
- K. B. (2004)b Search For Quasar Redshift Periodicity, *Fizika Elementarnykh Chastits i Atomnogo Yadra* **35**, 178–186.
- S. P. (1999) Measurements of Omega and Lambda from 42 High-Redshift Supernovae, *Astrophys. J.* **517**, 565–586, astro-ph/9812133.
- Fock, V. A. (1929) Geometrisierung der Diracschen Theorie des Electrons. (Geometrization of the Dirac electron theory), *Zs. Phys.* **57**, 261–277.
- Klyatskin, V. I. (2001) *Stochastic Equations from Physicist Point of View*, Moscow, Russia, Fizmatlit.
- Lifshits, E. M. (1946) On the gravitational stability of the expanding universe, *ZhETF* **16**, 587–602.
- Pawlowski, M. and Pervushin, V. N., Reparametrization-Invariant Path Integral in GR and.
- Pervushin, V. and Smirichinski, V. (1999) Bogoliubov quasiparticles in constrained systems, *J. Phys. A: Math. Gen.* **32**, 6191–6201.
- Pervushin, V. and Zinchuk, V., Quantum Cosmological Origin of Universes, gr-qc/0504123.
- R. Arnowitt, S. D. and Misner, C. W. (1960) Canonical Variables for General Relativity, *Phys. Rev.* **117**, 1595–1602.
- V. F. Mukhanov, H. A. F. and Brandenberger, R. H. (1992) Theory of cosmological perturbations, *Phys. Rep.* **215**, 203–333.
- Wheeler, J. A., *Superspace and the nature of quantum geometrodynamics*.
- York, J. W. (1971) Gravitational Degrees of Freedom and the Initial-Value Problem, *Phys. Rev. Lett.* **26**, 1656–1658.
- Zelmanov, A. L. (1973) Kinematic invariants and their relation to chronometric ones in Einstein's gravitation theory, *Dokl. AN USSR* **209**, 822–825.

RECENT RESULTS FROM EP INTERACTIONS AT HERA

Alessandro Polini (alessandro.polini@bo.infn.it)
INFN Bologna

Abstract. In this writeup a selection of recent results from the experiments H1 and ZEUS with electron-proton collisions at HERA is presented. After a brief introduction, the review covers structure functions, QCD fits and the determination of α_s , heavy flavor production, determination of electroweak parameters, spectroscopy and search for new physics. The results described use mostly the full HERA I luminosity but first measurements from HERA II data using collisions with polarised e^\pm beam are also presented. Prospects for future measurements with HERA II and their relevance for future high energy physics experiments are addressed.

Key words: HERA, Deep Inelastic Scattering

1. Introduction

HERA is the first and only high energy electron-proton collider. After being commissioned in 1992, during the years 1994-2000 the accelerator delivered a total of about 120 pb^{-1} to each of the two colliding experiments, H1 and ZEUS. The HERA II upgrade, started in 2001 and finalized in year 2003, aiming at an increase of the luminosity and at the use of a polarised electron beam, will provide by mid of 2007 a fivefold increase of the total luminosity.

Collisions at HERA of 27.5 GeV electrons (or positrons) with 920 GeV protons, corresponding to a center-of-mass energy of 319 GeV, are equivalent to a fixed target experiment with a 54 TeV electron beam. At the lowest order the scattering process is described by the e^\pm emitting a boson (γ, Z^0, W^\pm), of virtuality Q^2 , that interacts with the proton or one of its constituents. At low Q^2 (photoproduction regime) the emitted photon can be considered quasi-real and the scattering process can be written in terms of a photon-proton cross section convoluted with a photon flux at the electron vertex. As Q^2 increases, deep inelastic scattering (DIS) takes place and the emitted photon becomes sensitive to the proton structure tested up to the unprecedented scale of 10^{-18} m. The Bjorken x scaling variable, corresponding to the momentum fraction carried by the struck parton of the proton, together with Q^2 , give a complete description of the inclusive process. Fig. 1 summarizes the inclusive $e^\pm p$ cross sections as measured by H1 and ZEUS for neutral current (NC, γ, Z^0 exchange) and charged current (CC, W^\pm exchange) processes. For $Q^2 \sim M_{W^\pm, Z}^2$

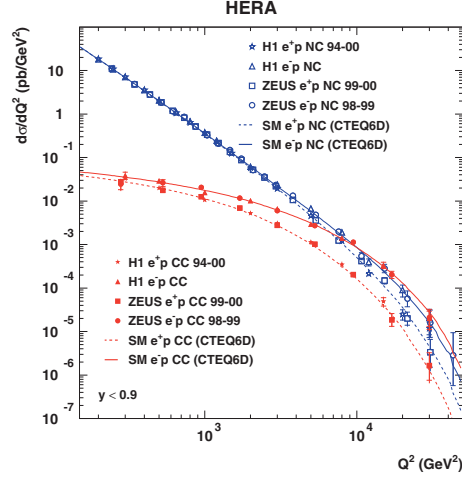


Figure 1. The NC and CC $e^\pm p$ cross sections as a function of Q^2 . At $Q^2 \sim M_{W,Z}^2$ the electromagnetic and weak contribution become comparable as expected from the electroweak unification.

and above, contributions from weak processes, with W, Z^0 exchange, become comparable to γ exchange as expected by the electroweak unification. When a W^\pm is exchanged the incoming e^\pm lepton converts into a neutrino tagged by the experiments via missing momentum/energy. Fig. 2a shows the kinematic region investigated by HERA as a function of Q^2 and x , together with fixed target experiments, the Tevatron and the LHC. The measurement of the inclusive $e^\pm p$ cross section over several orders of magnitude, from photoproduction up to Q^2 of 10^5 GeV^2 , and very small x down to 10^{-4} , has been the major contribution of HERA. In Fig. 2b the proton structure function F_2 is presented as a function of Q^2 for different values of x . The measurement by H1 and ZEUS is shown together with results from fixed target experiments. Scaling violations are clearly visible: F_2 increases with Q^2 at low x due to the dominance of the gluon and the sea quarks; F_2 decreases at high x where the valence quarks dominate. These measurements provide a solid reference for future experiments like LHC, where processes like top or Z production are expected to originate in similar regions of x .

2. QCD fits, PDFs and α_s extraction

ZEUS has recently performed next to leading order (NLO) QCD fits, based on the DGLAP evolution, to determine parton distributions functions (PDFs), using minimum input from external experiments [1]. Uncertainties from heavy-target corrections, present in global analyses which include also fixed-target data, are therefore avoided. While the low Q^2 NC data determine the low- x

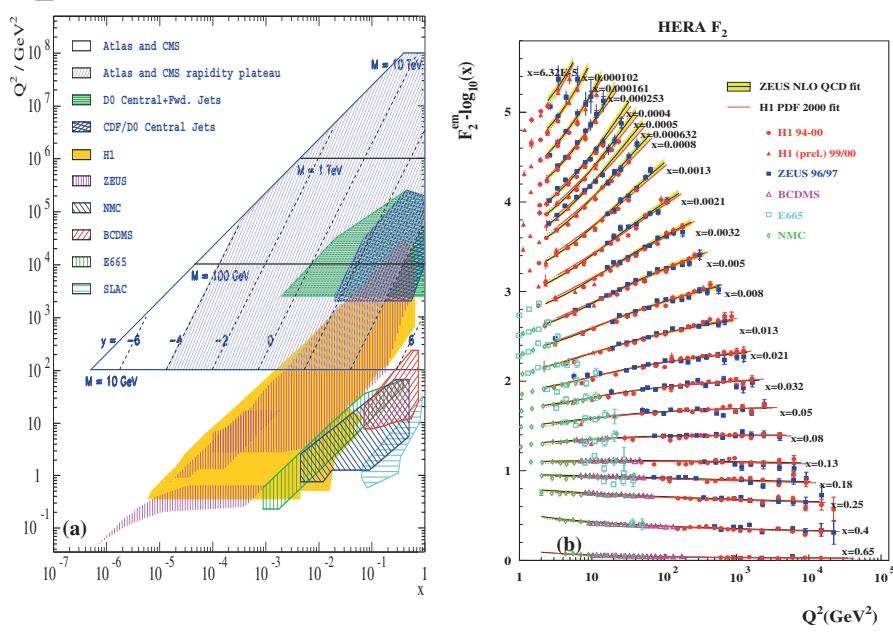


Figure 2. (a) The kinematic plane of DIS as function of x and Q^2 , for HERA and fixed target experiments. The kinematics of pp scattering in jet production for the Tevatron and LHC is also presented. (b) The structure function F_2 as measured by H1 and ZEUS as a function of Q^2 for several values of x . A pointlike proton structure would not show any Q^2 dependence; the scaling violations at small and large x demonstrate the dynamic structure of the proton and the interaction of its constituents (quarks and gluons).

sea and gluon distributions, the high Q^2 NC and CC cross sections constrain the valence distributions. In addition, published jet cross sections from the 96-97 data were used to constrain the gluon density in the mid-to-high- x region ($x \approx 0.01 - 0.5$). The predictions for the cross sections used in the fit were calculated to NLO. The resulting PDFs, called ZEUS-JETS fit, give a very good description of both inclusive and jet cross sections, in agreement with QCD factorization. Fig. 3 shows the parton densities, separately for valence, sea quark and gluons, at $Q^2 = 10 \text{ GeV}^2$. The new fits are in good agreement with the fits from H1 [2]. The advantage of using the jets is shown in the right part of Fig. 3. As an example, in the bin at $Q^2 = 7 \text{ GeV}^2$ and $x \approx 0.06$, the uncertainty on the gluon density is reduced from 17% to 10% using the jets. A similar decrease of approximately a factor two is visible in the whole Q^2 range in the mid-to-high- x region. By leaving the strong coupling constant, α_s , as a free parameter, a new value of α_s has been extracted.

H1 and ZEUS have performed a variety of measurements of α_s from events with jets using different methods (inclusive jet cross sections, event shapes, dijet to three-jet ratio etc.). Fig. 4 summarizes the latest measurements of α_s together with the world average [3]. Although each of the measurements

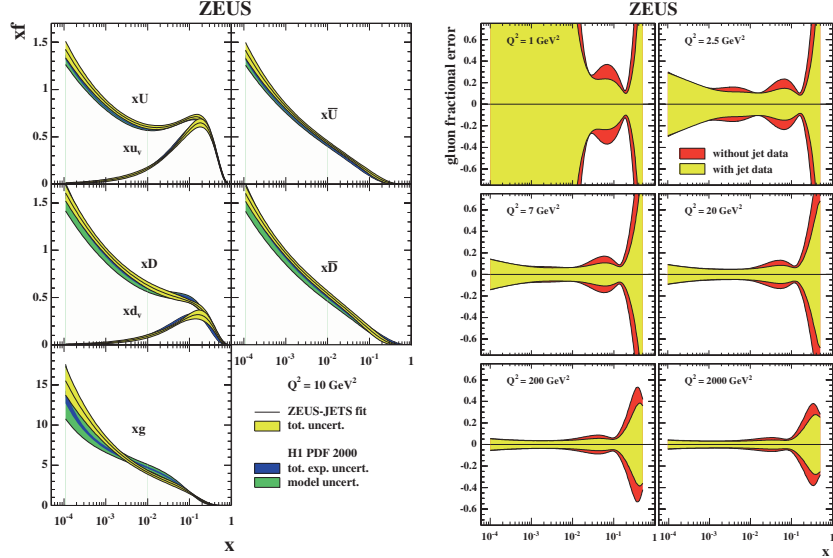


Figure 3. On the left: parton distribution functions for the u -valence, d -valence, sea and gluon density obtained from the ZEUS-JETS fit, and the H1 PDF2000 fit for a Q^2 value of 10 GeV^2 . On the right side: the uncertainty on the gluon density for different values of Q^2 and for the two cases in which the jets are included or not in the fit.

has a precise experimental determination (typically 3%), competitive with the world average, the error is dominated by the theoretical uncertainties (typically 4%). NNLO (next-to-NLO) calculations for jet based variables and for PDFs are therefore needed.

3. $F_2^{c\bar{c}}$ and $F_2^{b\bar{b}}$

H1 has recently reported on the measurement of inclusive charm and beauty cross section over a wide range of momentum transfer: $3.5 \leq Q^2 \leq 650 \text{ GeV}^2$ [4]. The fraction of events containing charm and beauty quarks was determined using a method based on tracks impact parameter, in the transverse plane, as measured by the H1 Vertex detector. Values of the structure functions $F_2^{c\bar{c}}$ and (for the first time at HERA) $F_2^{b\bar{b}}$ were extracted. The results are shown in Fig. 5 as a function of Q^2 in bins of the Bjorken scaling variable x . The measurements show positive scaling violations which increase with decreasing x . The charm measurements are in good agreement with the previous results extracted from D^* meson measurements by H1 and ZEUS. The new measurements have the advantage of a high acceptance which exceeds 70% in each Q^2 and x bin, both for charm and beauty. The data are compared to several QCD model predictions. The charm contribution to the total ep cross section, i.e. the ratio of $F_2^{c\bar{c}}/F_2$, is found to be around 20%-30%, and

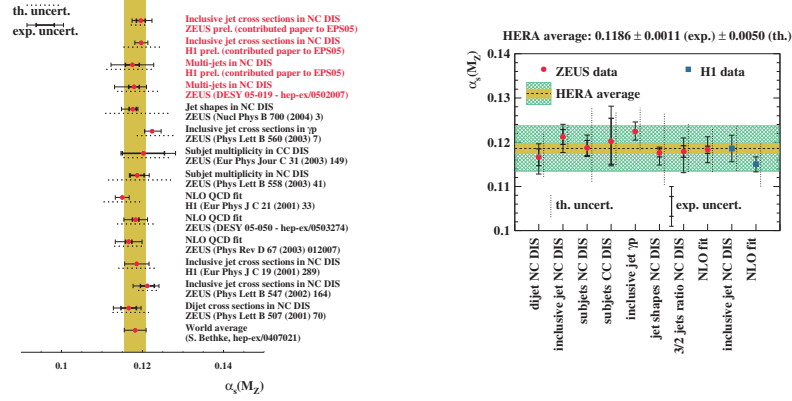


Figure 4. On the left: summary of $\alpha_s(M_Z)$ determinations at HERA together with the world average; on the right: $\alpha_s(M_Z)$ determinations at HERA compared with HERA (H1+ZEUS) average. The theoretical uncertainties are shown by the dashed lines.

increases slightly with increasing Q^2 and decreasing x . The beauty contribution increases rapidly from below 0.4 % at $Q^2 = 12 \text{ GeV}^2$ to about 5% at $Q^2 = 650 \text{ GeV}^2$.

4. Very high- x at HERA

While HERA has provided precision results on structure functions at low- x , the high- x region has still to be explored, because of both limited statistics and difficulty in reconstructing the kinematic variables. ZEUS has developed a new method to select events at very high- x and in the middle Q^2 region ($Q^2 > 576 \text{ GeV}^2$) [5]. These events are characterized by a well measured scattered electron or positron in the central part of the detector and by a very forward (i.e. close to the proton beam pipe) jet. As x increases, the jet is boosted towards the forward direction and eventually disappears in the beam pipe; the value of x at which this occurs is Q^2 dependent. The kinematics of the event was reconstructed as follows. First the Q^2 of the event is determined from the electron variables E_e and θ_e , which are measured with good resolution. The events are then separated into those with exactly one good reconstructed jet and those without any jet. For the 1-jet events, the jet information is used to calculate the Bjorken x variable from E_{jet} and θ_{jet} and the double differential cross section $d^2\sigma/dx dQ^2$ is calculated in each x, Q^2 bin. For the 0-jet sample, it is assumed that the events come from very high- x , with a lower value x_{edge} which can be evaluated for each Q^2 bin based on kinematic constraints. In this case the events are collected in

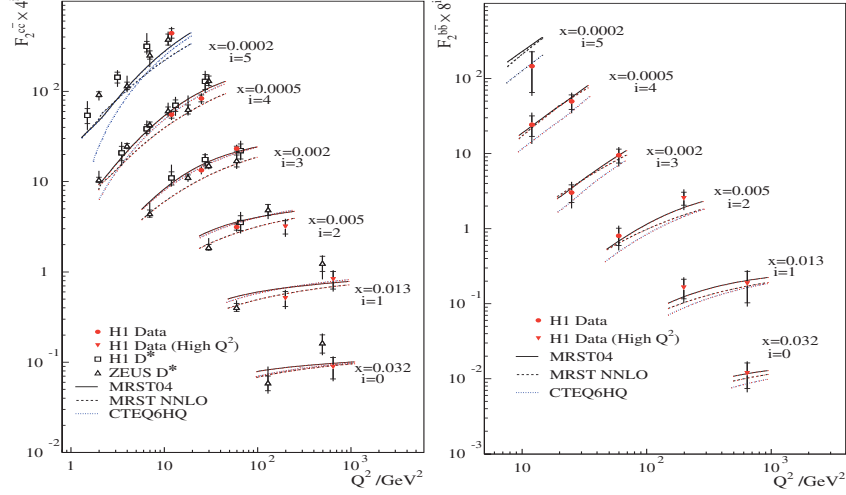


Figure 5. The measured $F_2^{c\bar{c}}$ (left) and $F_2^{b\bar{b}}$ (right) shown as a function of Q^2 for various x values. The inner error bars show the statistical error, the outer errors represent the statistical and systematic errors added in quadrature. The $F_2^{c\bar{c}}$ measurements from D^* mesons by H1 and ZEUS and the predictions of different QCD calculations are also shown.

a bin $x_{\text{edge}} < x < 1$ and an integrated cross section $\int_{x_{\text{edge}}}^1 (d^2\sigma/dxdQ^2)dx$ is measured.

The result is shown in Fig. 6, where, for each Q^2 , the open squares in the last bin are the integrated cross sections up to $x = 1$ and the closed squares show the double differential cross section in x, Q^2 . The precision in the last bin is comparable to the other bins. For most of these highest x -bins, where there was no previous measurement, the data tend to lie above the expectations from CTEQ6D. Precision measurements at high- x at HERA will allow to constrain the valence parton distributions in a region where measurements have come, up to now, only from fixed target experiments.

5. Search for pentaquarks resonances

Hadron spectroscopy has experienced a revival as several experiments reported evidence of new baryonic states consisting of five quarks. A number of experiments have observed a narrow resonance decaying either to nK^+ or to pK_S^0 , and with a mass around 1530 MeV, which could correspond to the pentaquark state $\Theta^+ = uud\bar{d}\bar{s}$.

ZEUS is at the moment the only high energy experiment to have observed a Θ^+ candidate as a pK_S^0 resonance at 1522 MeV with a statistical significance of 4.6σ [6] using the whole HERA I data sample of 121 pb^{-1} . A recent update [7] has focused in trying to understand the production mechanism

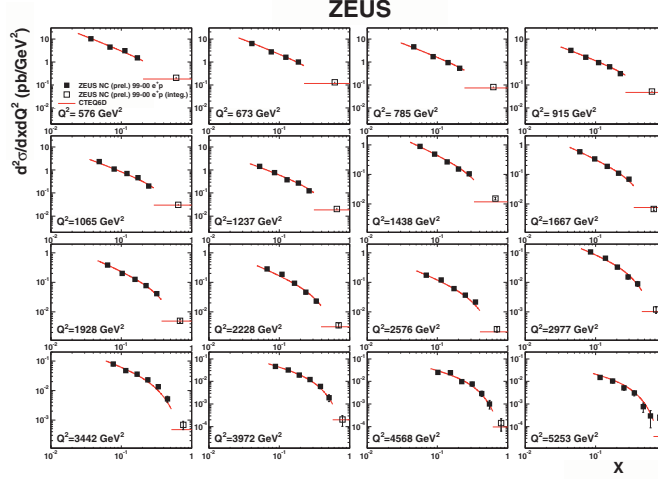


Figure 6. Double differential cross sections (solid squares) for the 99-00 e^+p data, as a function of x in Q^2 bins, compared to the CTEQ6D parton distributions. The last bin (open symbol) shows the integrated cross section over x divided by the bin width, i.e. $1/(1 - x_{edge}) \cdot \int_{x_{edge}}^1 (d^2\sigma/dxdQ^2) dx$; the symbol is shown at the center of the bin. In this bin the prediction is drawn as a horizontal line. The error bars represent the quadratic sum of the statistical and systematic uncertainties.

of this state. The $K_S^0 p(\bar{p})$ spectrum was studied for $Q^2 > 20 \text{ GeV}^2$ separately in the forward proton region, selecting events with $\eta > 0$, and in the rear region, $\eta < 0$. The resulting spectra are shown in Fig. 7: the fitted number of events under the peak is higher in the region closer to the proton remnant, compared to the rear region. This is not what is observed in the production of the $\Lambda(1520) \rightarrow K^+ p$, as shown in the same figure. This fact suggests that the production mechanism for the Θ^+ could be different from pure fragmentation in the central rapidity region and could be related to proton-remnant fragmentation. H1 has performed a similar search [8]. With the assumption that pentaquarks are produced by fragmentation, mass dependent upper limits on the visible Θ^+ production cross section were obtained in the range of $5 < Q^2 < 100 \text{ GeV}^2$. Although the limits set by H1 are not incompatible, when repeating the analysis with similar cuts as applied by ZEUS, no signal was observed.

H1 reported evidence [9] for a narrow resonance in the $D^{*\pm} p^\mp$ mass spectrum around 3.1 GeV, explained as the charmed pentaquark $\theta_C = uudd\bar{c}$. This evidence was not confirmed by ZEUS [10]. The HERA II program will allow to shed some light on this topic.

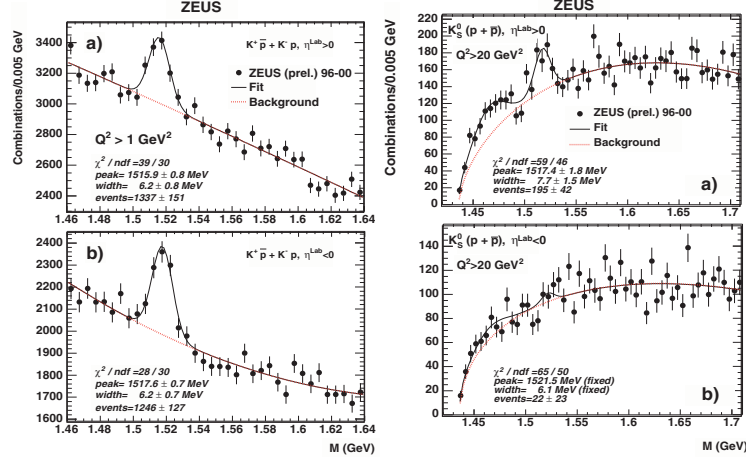


Figure 7. Invariant mass spectra for the $\Lambda(1520)$ (left) and for the Θ^+ (right), for $Q^2 > 20 \text{ GeV}^2$ and divided into forward pseudorapidity region (top) and rear region (bottom).

6. Fit of electroweak parameters

Using NC and CC cross section data recently published by H1, combined electroweak and QCD fits have been performed. The NC measurements were used to determine, for the first time at HERA, the vector and axial coupling constants of the Z boson to the u and d quarks [11]. The results are shown in Fig. 8. The obtained parameters are in good agreement with the expected Standard Model values. The observed Q^2 shape of the CC data was exploited to determine a W propagator mass with the result $M_{prop} = 82.87 \pm 1.82_{exp} +0.30_{model} -0.16_{model} \text{ GeV}$. When analysing the data in the framework of the Standard Model, in the on mass shell scheme, the Fermi constant G_F can be expressed in terms of M_Z and M_W and, hence, also the global normalisation of the data becomes sensitive to M_W . The corresponding fit result for M_W was translated into an indirect determination of $\sin^2 \theta_W$, yielding $\sin^2 \theta_W = 0.2151 \pm 0.0040_{exp} +0.0019_{model} -0.0011_{model}$. The W exchange is also sensitive to the top mass through loop corrections. This fact was exploited to determine, for the first time at HERA, the top mass with the result of $m_t = 108 \pm 44 \text{ GeV}$, where the error covers only the experimental uncertainty.

7. HERA II

7.1. CROSS SECTIONS AT HIGH Q^2

The HERA II running phase has started, e^+p collisions with longitudinally polarised positrons have been collected in 2003-2004 and in 2004-2005 the machine has switched to polarised electron beams.

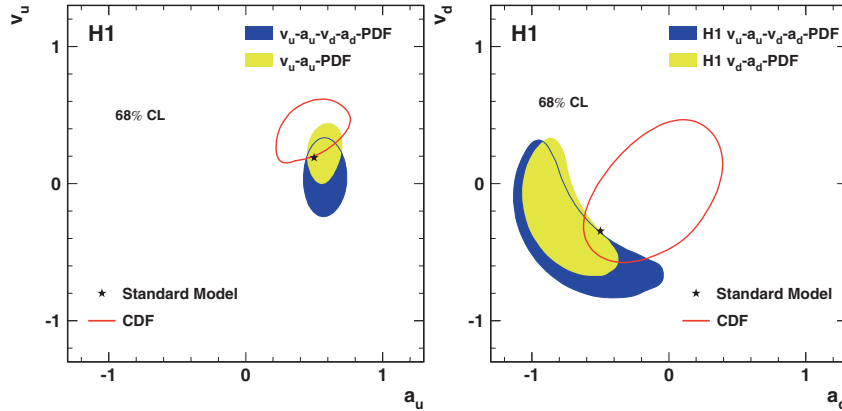


Figure 8. Results at 68% confidence level on the weak NC couplings of u and d quarks to the Z^0 boson as determined by H1. (shaded contours). The dark-shaded contours correspond to results of a simultaneous fit of all four couplings and can be compared with those determined by the CDF experiment (open contours). The light-shaded contours correspond to results of fits where either d or u quark couplings are fixed to their SM values. The stars show the expected SM values.

ZEUS recently reported on DIS cross sections at high Q^2 with positive and negative values of electron beam longitudinal polarisation [12]. The measurements were based on data samples of integrated luminosities of 41.7 pb^{-1} and 53.5 pb^{-1} , for CC and NC, respectively. In the Standard Model the total CC cross section is predicted to have a linear dependence on the polarisation, becoming zero for right-handed electrons (or left-handed positrons). The measured CC cross sections for the two luminosity-weighted polarisation values are shown together with previous measurements with polarised positrons and measurements from H1 [13] in Fig. 9(left). The linear dependence on P is clearly visible and the points are in good agreement with the Standard Model prediction.

Figure 9(right) shows the cross section $d\sigma/dQ^2$ for NC DIS for positive and negative longitudinal polarisations and the ratio of the two cross sections. The measurements are well described by the Standard Model. The statistical precision of the current data set does not allow the effect of polarisation to be conclusively observed.

7.2. ISOLATED LEPTON EVENTS WITH LARGE MISSING TRANSVERSE MOMENTUM

One exciting result from HERA I is an excess observed in the H1 data of events with an isolated lepton and large missing transverse momentum [14], as this might be a hint for new physics beyond the Standard Model. The main contribution from the Standard Model to these events is the production of a

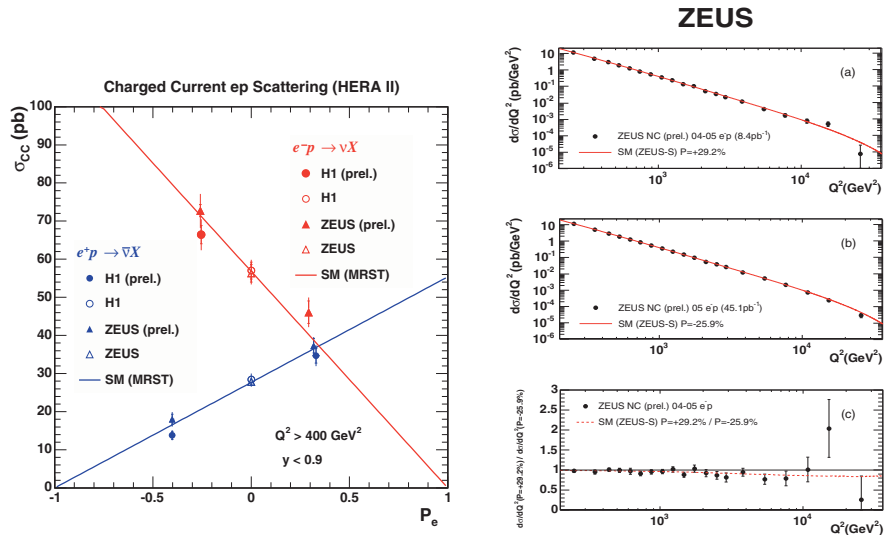


Figure 9. On the left: the total cross sections for $e^\pm p$ CC DIS as a function of the longitudinal polarisation of the lepton beam as measured by H1 and ZEUS; on the right: the $e^- p$ cross section $d\sigma/dQ^2$ for (a) positive polarisation data and (b) negative polarisation data and (c) the ratio of the two. The lines show the Standard Model predictions.

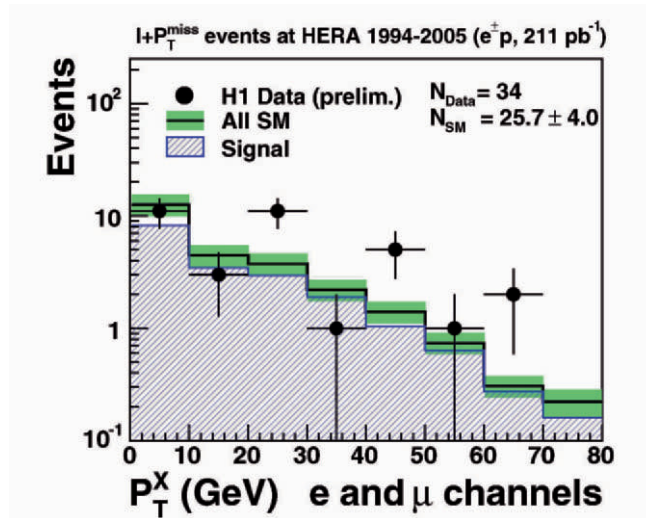


Figure 10. The hadronic transverse momentum distribution for isolated leptons in the electron and muon channels combined: data is compared to the Standard Model expectation (open histogram). The signal component of the SM expectation, dominated by real W production, is given by the hatched histogram N_{Data} is the total number of data events observed while N_{SM} is the total SM expectation. The total error on the SM expectation is given by the shaded band.

real W boson (radiated from a quark) and the subsequent decay into lepton and neutrino. An excess over the predicted cross sections was observed both for the electron and muon channel, for large hadronic transverse momenta $p_T^X > 25$ GeV. H1 has recently updated the measurement with the available HERA II data. Six new electron events were found in these data but no new muon event. The yield of isolated electrons is still in excess over the Standard Model prediction. Fig. 7.1 shows the observed event yield, when combining the electron and muon channel and exploiting the full HERA data set of e^+p and e^-p collisions from 1994 to 2005 as a function of p_T^X . In the region of $p_T^X > 25$ GeV, 17 events are observed while the Standard Model predicts only 6.4.

8. Conclusion

A limited selection of recent results from the rich physics program of HERA has been presented here. H1 and ZEUS, while completing the analyses of HERA I, are starting to obtain the first promising results from the HERA II data. The improved luminosity and the polarisation will help to clarify many open questions.

Acknowledgments

I would like to thank Prof. Laszlo Jenkovszky for the excellent organization of this workshop.

References

- 1 ZEUS Collab., S. Chekanov et al., Eur. Phys. J. C42 (2005) 1
- 2 H1 Collab., A. Aktas et al., Eur. Phys. J. C30 1 (2003)
- 3 C. Glasman, arXiv:hep-ex/0506035 and references therein.
- 4 H1 Collab., A. Aktas et al., DESY 05-110 accepted by Eur. Phys. J. H1 Collab., A. Aktas et al., Eur. Phys. J. C40 (2005) 349.
- 5 ZEUS Collab., Conference Paper, Abs. 261, LP 2005, Summer 2005.
- 6 ZEUS Collab., S. Chekanov et al., Phys. Lett. B591 (2004) 7.
- 7 ZEUS Collab., Conference Paper, Abs. 369, EPS 2005, Summer 2005.
- 8 H1 Collab., Conference Paper abs. 400 submitted to LP2005, Summer 2005.
- 9 H1 Collab., A. Aktas et al., Phys. Lett., B588, (2004) 17. H1 Collab., Conference Paper abs. 401 submitted to LP2005, Summer 2005.
- 10 ZEUS Collab., S. Chekanov et al., Eur. Phys. J. C38 (2004) 29.
- 11 H1 Collab., A. Aktas et al., DESY 05-93, accepted by Phys. Lett. B
- 12 ZEUS Collab., Conference Paper abs. 255 submitted to LP2005, Summer 2005.
- 13 H1 Collab., Conference Paper abs. 388 submitted to LP2005, Summer 2005.
- 14 H1 Collab., Conference Paper abs. 637 submitted to EPS2005, Summer 2005.

TOP QUARK PHYSICS FROM TEVATRON TO LHC

V. Šimák

*Faculty of Nuclear Sciences and Physical Engineering, CTU
Institute of Physics ASCR, Prague*

Abstract. Brief summary of top quark physics from discovery to LHC.

1. Introduction

After discovery of b quark the prediction of top quark, which with b quark create doublet in Standard Model (SM), was obvious. Its properties could be similar to the quarks u , c , spin $1/2$ and charge $+2/3$. However, the mass of the top quark could not be predicted. It was considered only that it is much greater than the mass of the b quark. First attempt to see top quark was made in experiment UA1 on SPS antiproton-proton collider at CERN. [1]. The evidence, however, of this observation of particle with mass around 40 GeV was not confirmed by experiment UA2 nor at the LEP. In SM one of the mechanisms of $b\bar{b}$ production may be due to virtual exchange of possible t quark as addition to u and c quark. Indeed it was observed that heavier virtual particle than u and c contribute to the cross section [2].

In 1995 the top quark was really discovered at Tevatron in Fermilab in antiproton-proton collider (cms energy of 1.8 TeV) [3] in both experiments CDF and DO. However, even after ten years from this discovery the reason for such high mass for elementary constituent, which may be compared with mass of atom of gold, is not known. Also the details knowledge of top quark interactions would need large statistics of observations. This will be possible in the new proton-proton collider LHC at CERN.

2. Top quark in standard model [4]

Possibility existence of top quark followed from theoretical consideration. The realizability of the SM demands the absence of triangle anomalies. Triangular fermion loops, built up by an axial vector charge $I_{3A} = -I_{3L}$ combined with two electric vector charges Q , would spoil the realizability of the gauge

theory. Since the anomalies do not depend on the masses of the fermions circulating in the loops, it is sufficient to demand that the sum

$$\sim \sum_L I_{3A} Q^2 = - \sum_L I_3 \left[I_3 + \frac{1}{2} Y \right]^2 \sim \sum_L Y \sim \sum_L Q$$

of all contributions be zero. (Where I_3 is the third component of isospin, for b quark $I_3 = -\frac{1}{2}$). Such a requirement can be translated into a condition on the electric charges of all the left-handed fermions

$$\sum_L Q = 0$$

This condition is met in complete standard family in which the electric charges of the lepton plus those of all color components of the up and down quarks add up to zero,

$$\sum_L Q = -1 + 3 \times \left[\left(+\frac{2}{3} \right) + \left(-\frac{1}{3} \right) \right] = 0$$

If the top quark were absent from the third family, the condition would be violated and the SM would be theoretically inconsistent.

Defining the Yukawa coupling in the SM through

$$\mathcal{L}_Y = g_Y \left(\frac{v + H}{\sqrt{2}} \right) (\bar{t}_L t_R + h.c.),$$

the coupling constant g_Y is related to the top mass by

$$g_Y(ttH) = m_t \sqrt{2} \sqrt{2} G_F.$$

Demanding the effective expansion parameter $g_Y^2/4\pi$ to be smaller than 1, the top mass is bounded to

$$m_t = \sqrt{\frac{\sqrt{2}\pi}{G_F}} \approx 620 \text{ GeV}.$$

For a top mass of 180 GeV , the coupling $g_Y^2/4\pi \approx 0.085$ is comfortably small so that perturbation theory can safely be applied in this region.

At asymptotic energies, the amplitude of the zeroth partial wave for elastic $t\bar{t}$ scattering in the color singlet same-helicity channel.

$$a_0(t\bar{t} \rightarrow t\bar{t}) = -\frac{3g_Y^2}{8\pi} = -\frac{3G_F m_t^2}{4\sqrt{2}\pi}$$

grows quadratically with the top mass. Unitarity, however, demands this real amplitude to be bounded by $|Re a_0| \leq 1/2$. This condition translates to

$$m_t < \sqrt{\frac{2\sqrt{2}\pi}{3G_F}} \approx 500 GeV.$$

The bound improves by taking into account the running of the Yukawa coupling.

First indications of high top quark mass were derived from the rapid $(B - \bar{B})$ oscillations observed by ARGUS[2]. Combining the high-precision measurement of the Z mass with $\sin^2 \theta_W$ from the Z -decay rate, from the forward-backward asymmetry and from LR polarization measurements, the top quark mass has been determined:

$$m_t = 178 \pm 8_{-20}^{+17} GeV.$$

The close agreement between direct and indirect top mass determination can be considered as a triumph of SM.

For such mass of top quark the most obvious decay mode was via b quark and W , which is governed by amplitude

$$\mathcal{M} = (t \rightarrow bW) = \frac{ig}{\sqrt{2}} \bar{b} \not{\epsilon}^W \frac{1 - \gamma_5}{2} t.$$

The longitudinal or transversal W is produced in conjunction with a left-handed b quark. The production of W 's with helicity $h^W = +1$ is thus forbidden by angular momentum conservation.

In total one finds

$$(h^W = -1) : (h^W = -0) : (h^W = +1) = 1 : \frac{m_t^2}{2M_W^2} : 0$$

The implications for the angular distributions of the decay products is demonstrated in Fig. 1.

The decay rate

$$\Gamma = \frac{G_F m_t^3}{8\sqrt{2}\pi} \left(1 - \frac{M_W^2}{m_t^2}\right) \left(1 + 2\frac{M_W^2}{m_t^2}\right) \approx 175 MeV \left(\frac{m_t}{M_W}\right)^3$$

increases with the third power of the quark mass, and for top mass around $180 GeV$ which amounts to more than $1.5 GeV$. In the three generations of quarks in SM there are possibilities of top quark decays via W and b or s or d quark. The corresponding ratios in unitary CKM matrix are

$$\begin{aligned} V_{tb} &= 0.9990 \pm 0.0004 \Rightarrow BR(b) \approx 1 \\ V_{ts} &= 0.044 \pm 0.010 \Rightarrow BR(b) \approx 0.2\% \\ V_{td} &= 0.011 \pm 0.009 \Rightarrow BR(b) \approx 0.01\%. \end{aligned}$$

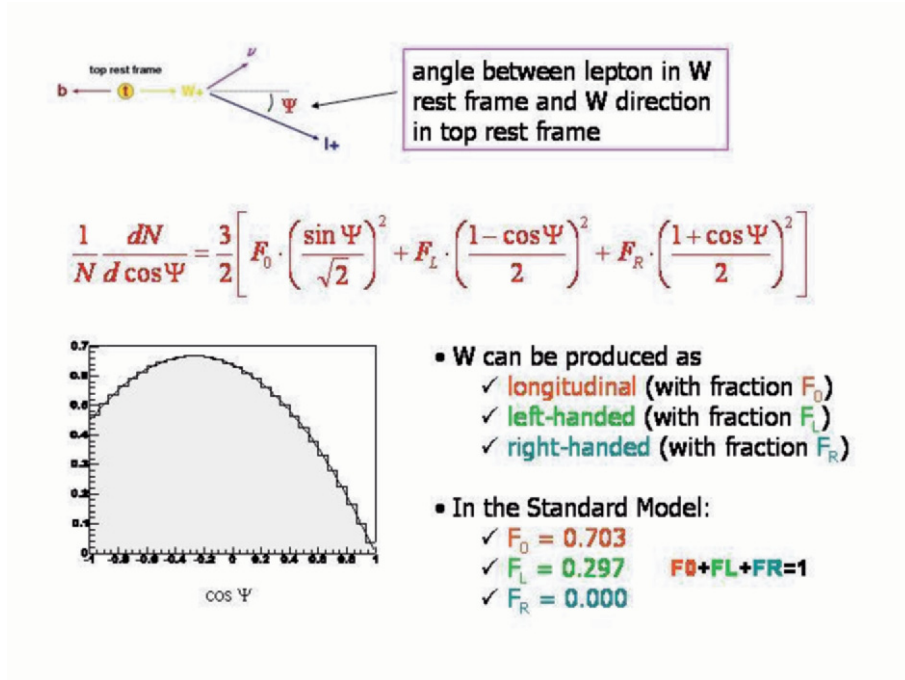


Figure 1. Polarization of W from top decay. The helicity angle distribution of lepton from W decay[9].

Dominated decay mode into W and b thus give relative final states as show in Fig. 2.

The narrow width of the top quark corresponding to fast decay reveals the formation of the bound states. Individual toponium state would give a decay rate 1.5 GeV . The formation time of hadron from a locally produced t quark is governed by its size which is significantly larger than its lifetime:

$$\tau_{\text{formation}} \approx \text{size} \approx 1/0.5 \text{ GeV} \gg \tau_{\text{decay}} \approx 1/\Gamma_t.$$

Top quarks decay before they have time to communicate hadronically with light quarks and dilute their spin orientation.

3. Top quark at Tevatron

In experiments CDF and D0 only few hundreds of top quark pairs are being observed. Resent results concerning the cross sections and masses from various final state have been published. There are summarized in Fig. 3. and in Fig. 4.

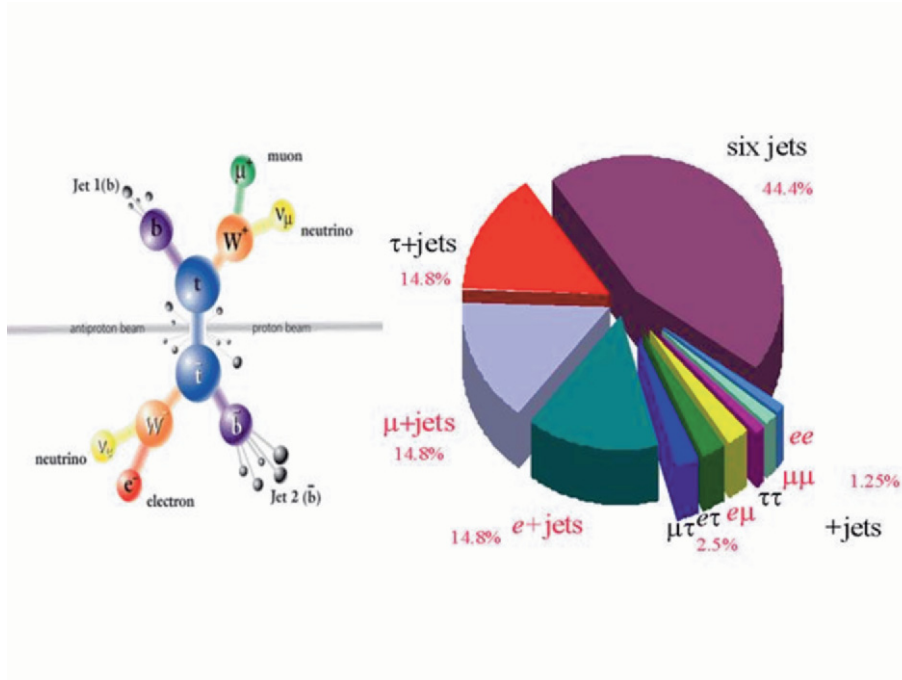


Figure 2. Schema $t\bar{t}$ decay into two leptons and two jets from $b\bar{b}$ quarks. The branching ratios of different final states from $t\bar{t}$ production.

The masses of top quark, W give constrain on mass of the Higgs boson. From the recent Tevatron results the upper limit for Higgs mass is: $m_H \leq 186 GeV$.

4. Top Quark at LHC

In LHC at CERN, the 8×10^6 pairs of $t\bar{t}$ a year will be observed at low luminosity runs. The LHC collider will be true top factory, which brings new study of top quark physics. At Tevatron the main production of $t\bar{t}$ is due to quark annihilations, Fig. 3. At the LHC the situation ($14 TeV$) is quite opposite. Dominant top production (87%) is due to gg interaction and only 13% via quark annihilations. Total cross section of top production in proton-proton interaction predicted for LHC is $825 \pm 150, pb$ at NLO from SM.

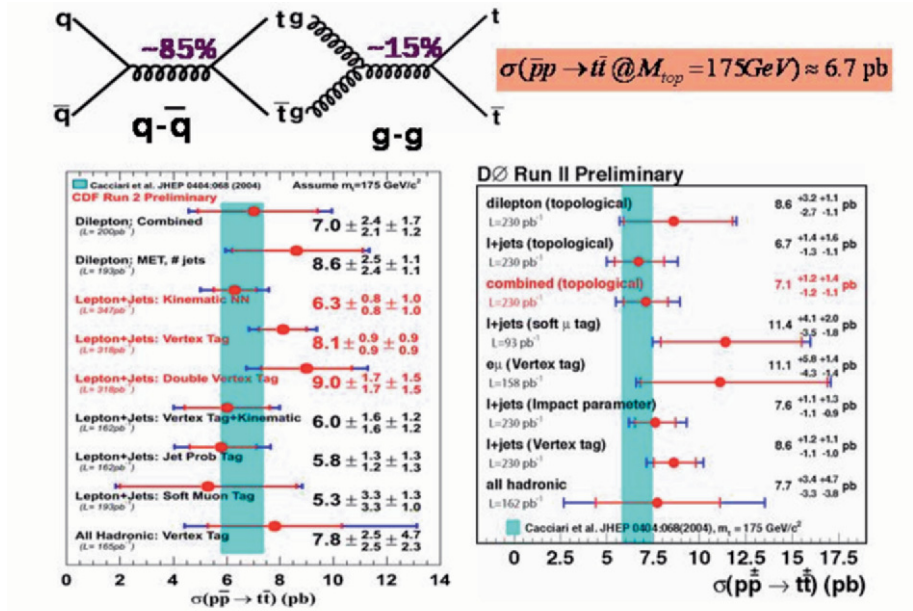


Figure 3. Recent results of cross section measurement of $t\bar{t}$ production from different final states at Tevatron. Above the production mechanism and theoretical prediction[5].

4.1. CHARGE

From the SM is obvious that the charge of the top quark is $+2/3$. However, there are other models, suggesting charge different of heavy quarks. There are two methods for top charge measurement:

- The photon production from the fermions is coupled by α_e and therefore cross section for photons produced on top line is sensitive to his charge. Measuring the prompt photon production in appropriate phase space region could indicate, compared with MC calculations, the value of the electric charge of the top quark
- Jet produced by the quark could remember the charge of the quark via charges of produced particle weighted by longitudinal component along the quark.

4.2. MASS OF THE TOP

As the top quark ,like the other quarks, is color object, his mass cannot be determined exactly as it is subject of the strong color interaction with typical

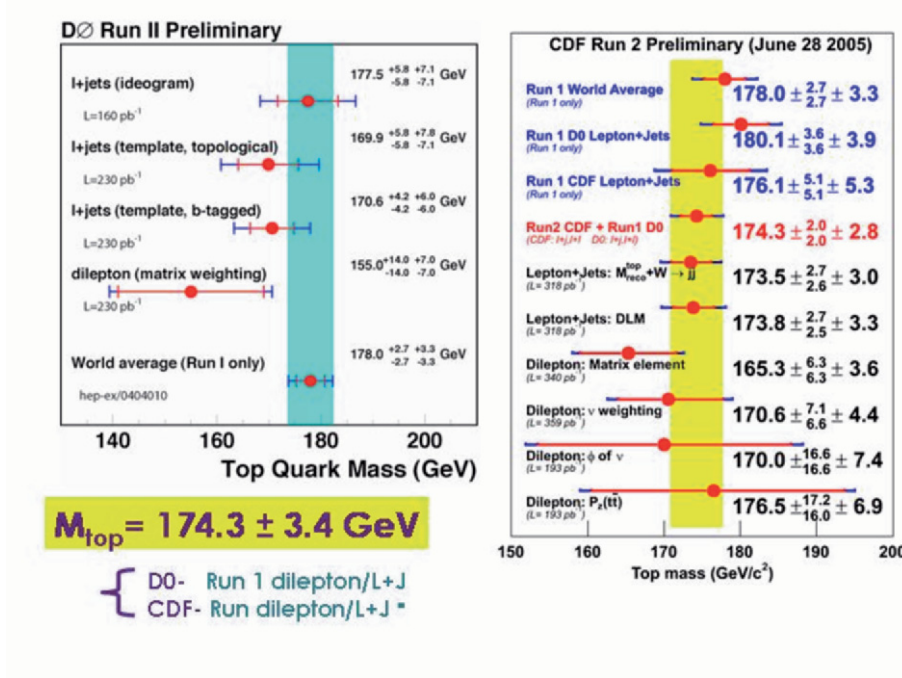


Figure 4. Recent results of top mass measurement from different final states at Tevatron[5].

error of Λ scale which is around 1 GeV in LHC energies. However, there are possibility to estimate the effective mass from reconstructed topology of interactions. The real measurement of mass is splitting according to final states of interactions[7].

- Mass Measurement in single lepton channel Most promising channel for the precise mass measurements seems to be single lepton final state, where goes 45% of whole production cross section.
- Mass Measurement in double lepton channel Several methods has also be developed for determination of top quark mass in double lepton final sates. Leptons are usually well measured comparing to hadronic jets and therefore this channel is most promising. However the neutrino and anti-neutrino final sates complicate the reconstruction of topology of events. For LHC energies the full reconstruction of events has been suggested. The six equations with known mass of W and top give solution to three vectors for neutrino and antineutrino.
- Mass measurement in multi-jet final state In mutlijet final state, where at least six jets are produced, the measurement is very difficult. The maximum likelihood method is used to select combination by looking of

W masses from different combinations of two jets. The neural network method has been also applied to determined the mass and topology in this channel.

4.3. DYNAMICS OF $T\bar{T}$ PAIRS PRODUCTION AND SPIN CORRELATIONS

Due to fast decay of top quark the spin properties of produced top remember the dynamics of his origin. Study of the spin correlations of top and antitop pair can show the dynamics of top quark creation. In the following picture, the orientations of spins of top and antitop are shown. The percentage of different orientations of spin of course depends on the dynamics of productions[8].

$$\frac{1}{\sigma} \frac{d^2\sigma}{d \cos \theta_{l+} d \cos \theta_{l-}} = \frac{1}{4} (1 - \mathcal{A} \kappa_{l+} \kappa_{l-} \cos \theta_{l+} \cos \theta_{l-})$$

$$\mathcal{A} = \frac{\sigma(t_{\uparrow}\bar{t}_{\uparrow}) + \sigma(t_{\downarrow}\bar{t}_{\downarrow}) - \sigma(t_{\uparrow}\bar{t}_{\downarrow}) - \sigma(t_{\downarrow}\bar{t}_{\uparrow})}{\sigma(t_{\uparrow}\bar{t}_{\uparrow}) + \sigma(t_{\downarrow}\bar{t}_{\downarrow})} + \sigma(t_{\uparrow}\bar{t}_{\downarrow}) + \sigma(t_{\downarrow}\bar{t}_{\uparrow})$$

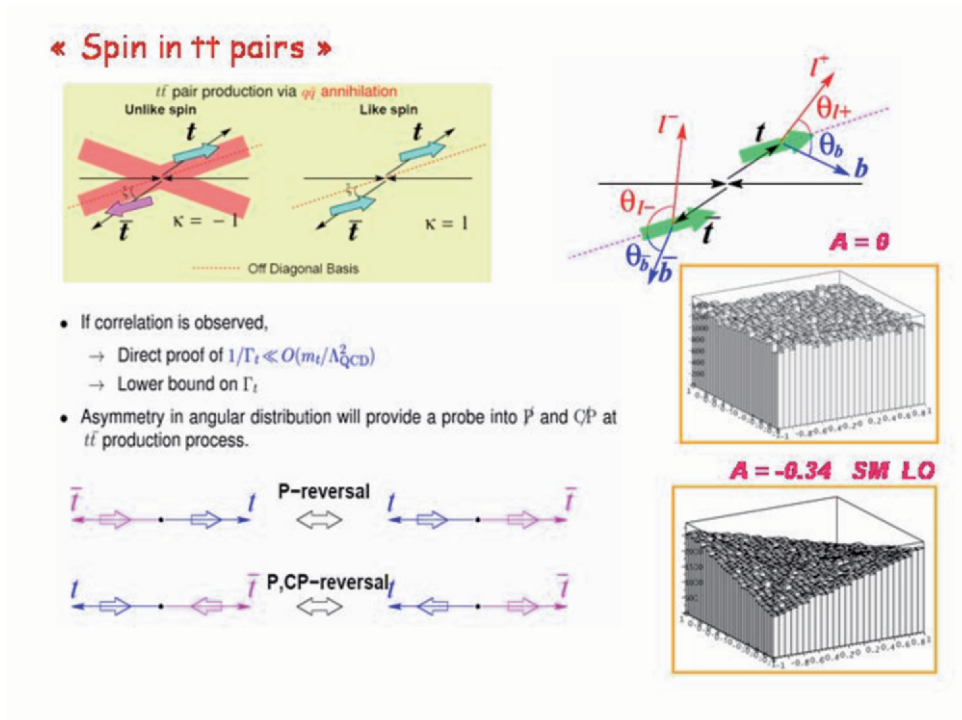


Figure 5. Spin orientations of $t\bar{t}$ indicating the symmetry properties and helicity angles correlation for MC generated events (Lego plots for no correlated spins, $A=0$ and for SM prediction).

For the lepton/antilepton the $\kappa_i = 1$. Therefore the final state for $t\bar{t}$ pair is most sensitive to the spin orientation and dynamics of its production. The correlation between lepton and antilepton (e, μ) are displayed for MC events in Lego plots for different dynamics $A = 0$ (no correlations), $A = -0.34$ (SM) in Fig. 5. At Tevatron in Run I this spin correlations has been studied [10] and limit for the coefficient A was estimated to $A > -0.25$ (SM $A = 0.88$).

The LHC events, however (about 10^6 events produced in one year with two leptons in final state), may enable to study different production mechanism of the top quark[9].

4.4. SINGLE TOP PRODUCTION

Electroweak interactions in SM also predict the reactions in which only one top or antitop is produced. There are three mechanism of such production Fig. 6. Interesting feature in those reactions is that the W produced from top/antitop is longitudinal polarized. Such events have not been yet observed, but predicted cross sections may indicate the possibility of such observation at Tevatron.

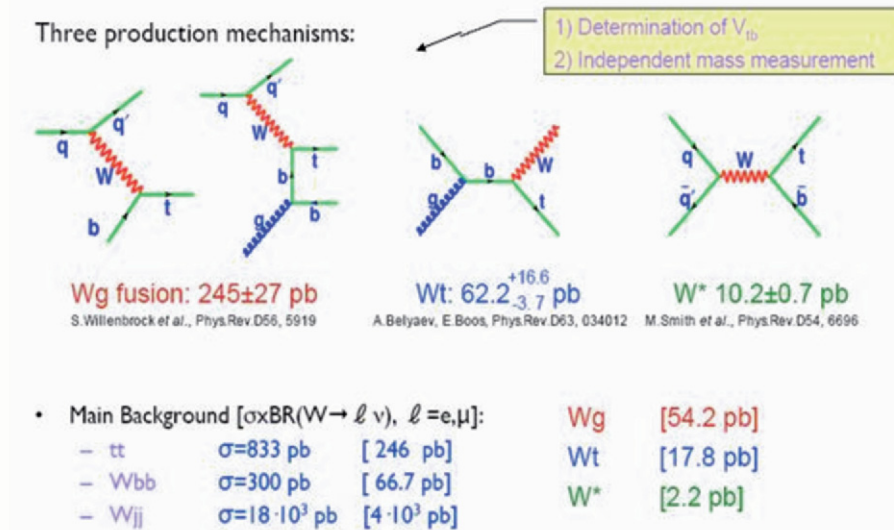


Figure 6. Single top production at LHC.

5. Top quark beyond the standard model

5.1. BOUND STATE OF $T\bar{T}$

The observation of bound state of $t\bar{t}$ pair with width around 2 GeV is improbable due to fast decay of the top. The situation could be different in extension of the SM. Decays of the fourth generation $b' \rightarrow t + W$ are suppressed by small mixing angles. Alternatively, if $m_{b'} < m_t + m_W$, the $b' \rightarrow c + W$ mode would have to compete with loop-induced FCNC decays-leaving ample room for narrow quarkonium states. [12].

5.2. TOP IN SUSY ENVIRONMENT

In several extensions of the SM the Higgs sector can, apart from breaking the electroweak gauge symmetry, also violate CP. The neutral Higgs bosons ϕ which are predicted by these models then act also as messengers of the latter phenomenon.

In general we consider an neutral Higgs boson ϕ with unspecified CP parity. Its coupling to the top quark reads [6]

$$\mathcal{L} = -(\sqrt{2}G_F)^{1/2}m_t(a\bar{t}t + \tilde{a}\bar{t}i\gamma_5t)\phi,$$

where G_F is Fermi's constant, m_t is the top mass, and a, \tilde{a} are reduced scalar and pseudoscalar couplings, respectively. (For the SM Higgs boson $a = 1, \tilde{a} = 1$.) If $a\tilde{a} \neq 0$ then ϕ has undefined CP parity, signaling CP violation in the Higgs sector. This can occur, for instance, in two-Higgs doublet extension of the MSSM and could be seen in spin correlation study.

5.3. RARE TOP DECAY

The rare t quark decays $t \rightarrow cl_j^+l_k^-$, $t \rightarrow c\tilde{\nu}_j\nu_k$ via the scalar leptoquark doublets are investigated in the minimal four-color symmetry model with Higgs mechanism of the quark-lepton mass splitting. The partial widths of these decays are calculated and the total width of the charged lepton mode $\Gamma(t \rightarrow cl^+l^-) = \sum_{j,k} \Gamma(t \rightarrow cl_j^+l_k^-)$ and the total width of the neutrino mode $\Gamma(t \rightarrow c\tilde{\nu}'\nu) = \sum_{j,k} \Gamma(t \rightarrow c\tilde{\nu}_j\nu_k)$ are found. The corresponding branching ratios are shown to be [11]

$$\begin{aligned} Br(t \rightarrow cl^+l^-) &\approx (3.5 - 0.4) \times 10^{-5} \\ Br(t \rightarrow c\tilde{\nu}'\nu) &\approx (7.1 - 0.8) \times 10^{-5} \end{aligned}$$

for the scalar leptoquark masses $m_S = 180 - 250\text{ GeV}$.

5.4. GRAVITON WITH $t\bar{t}$ PRODUCTION

Recently, new theories have been developed to solve the hierarchy problem using a higher dimensional spacetime. The motivation for this comes from string theory, where all particles are described as vibrational modes of one-dimensional objects known as strings.

In the ADD model there is a new contribution to the $t\bar{t}$ pair production process through the virtual KK graviton exchange in the s -channel. The spin asymmetry can be altered from the SM one. As the graviton has spin of 2, the influence of its virtual exchange in s -channel to spin correlations of $t\bar{t}$ is obvious. The matrix elements corresponding to such processes has been calculated and spin correlations at LHC due to graviton exchange have been considered [13].

6. Conclusions and perspectives

In Run II at Tevatron the data from integrated luminosity 300 fb^{-1} will be taken. New phenomena, especially of single top production could be seen. Several standard predictions will be measured with good accuracy up few percent.

The LHC could be considered as a top factory. Already in one year of running at low luminosity about 10^7 events with $t\bar{t}$ could be obtained. Therefore, we may expect many new features indicating new physics beyond SM and of course very good precision of measurements of standard physics.

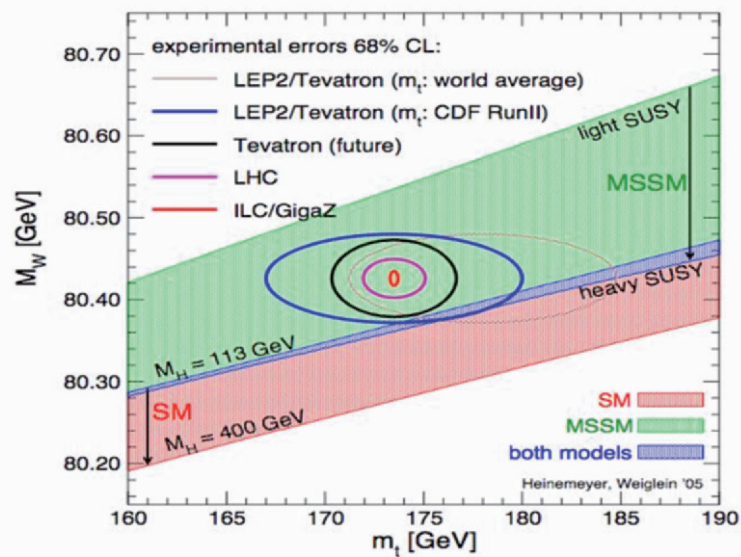


Figure 7. Constraints on Higgs mass from Collider experiments.

In the future linear collider (ICL) the study of top physics will be in advance compared to LHC. There, the new physics could be seen more explicitly as the top and antitop are polarized. The constrains for mass of Higgs boson from experiments in colliders are given in Fig. 7.

References

- 1 C. Albajar et al. (UA1) Phys.Lett. B256, 121 (1991).
- 2 H. Albrecht et al. (ARGUS), Phys. Lett.B192, 245 (1987), M. Artuso et al. (CLEO) Phys. Rev. Lett. 62, 2233 (1989).
- 3 F. Abe et al. (CDF) Phys Rev. Lett. 74, 3636 (1995), S. Abachi et al.(D0)Phys. Rev.Lett. 74, 2632 (1995).
- 4 J.H. Kühm: Theory of Top Quark Production and Decay, XXIII. Summer School of Particle Physics, July 1995.
- 5 R.D. Erbacher (CDF): Top Physics at TEVATRON, Conference XXV Physics in Collisions, Prague, June 2005.
- 6 W. Bernreuther et al., CERN-TH/98-390, Phys. Rev. D V58; 114031, Phys. Rev. D V49 1994, 4481; Phys. Letters B 314 (1993) 104-11
- 7 I. Bojanovic et al., Eur.Phys.J.C39S2:63-90,2005, heh-ex/043021.
- 8 G. Nahlon and S. Parke: Phys. Rev. D V53 4886 (1996); Phys. Letters B411 (1997) 173-179; hep-ph/9706304, Fermilab-Pub-97/185-T
- 9 F. Hubart et al., Eur.Phys.J.C44S2:13-33,2005, heh-ex/0508061 43021.
- 10 B. Abott et al. (D0) Phys.Rev.Lett. 85, 256 (2000).
- 11 P. Yu. Popov at al.: Modern Phys. Letters A V20, No. 10 (2005) 755-767
- 12 Zurab Berezhiani and Gia Dvaldi: Flavor violation in theories with TeV scale quantum gravity, Phys. Letters B 450 (1999) 24-33
- 13 M. Arai et al., Phys Rev. D70:115015 (2004).

THE QCD ANALYTIC PERTURBATION THEORY DESCRIPTION OF HADRONIC CONTRIBUTIONS INTO FEW IMPORTANT EFFECTS

I.L. Solovtsov^{1,2}, O.P. Solovtsova²

¹ *BLTP, JINR, Dubna, 141980 Russia*

² *ICAS, GSTU, Gomel, 246746 Belarus*

Abstract. A method based on analytic approach in QCD, involving a summation of threshold singularities and taking into account a nonperturbative character of the light quark masses, is applied to find hadronic contributions to different physical quantities.

1. Introduction

A comparison of QCD theoretical results with experimental data is often based on the conception of the quark-hadron duality [1]. The idea of quark-hadron duality formulated in [2] is as follows: inclusive hadronic cross sections, being appropriately average over an energy interval, had to approximately coincide with the corresponding quantities derived by using quark-gluon description. For many physical quantities the corresponding interval of integration involves a nonperturbative region and nonperturbative effects may play an important role for their description. We consider the following quantities and functions, which cannot be calculated reliably within the framework of perturbative QCD:

the ratio of hadronic to leptonic τ -decay widths in the non-strange vector channel

$$R_\tau^V = R^{(0)} \int_0^{M_\tau^2} \frac{ds}{M_\tau^2} \left(1 - \frac{s}{M_\tau^2}\right)^2 \left(1 + \frac{2s}{M_\tau^2}\right) R(s); \quad (1)$$

the Adler function [3], which can be constructed from τ -decays data [4],

$$D_V(Q^2) = Q^2 \int_0^\infty ds \frac{R(s)}{(s+Q^2)^2}; \quad (2)$$

the smeared R_Δ function [2]

$$R_\Delta(s) = \frac{\Delta}{\pi} \int_0^\infty ds' \frac{R(s')}{(s-s')^2 + \Delta^2}; \quad (3)$$

the hadronic contribution to the anomalous magnetic moment of the muon

$$a_\mu^{\text{had}} = \frac{1}{3} \left(\frac{\alpha}{\pi} \right)^2 \int_0^\infty \frac{ds}{s} K(s) R(s); \quad (4)$$

the hadronic contribution to the electromagnetic coupling

$$\Delta\alpha_{\text{had}}^{(5)}(M_Z^2) = -\frac{\alpha(0)}{3\pi} M_Z^2 \mathcal{P} \int_0^\infty \frac{ds}{s} \frac{R(s)}{s-M_Z^2}. \quad (5)$$

A method, which we use here for description of these quantities and functions, is based on the analytic approach in QCD [5, 6]. The analytic approach allows us to describe self-consistently the timelike region [7, 8] that is used in the integrals in Eqs. (1) - (5). This method also involves into consideration a summation of threshold singularities and takes into account nonperturbative character of the light quark masses.

2. R -function

To incorporate the quark mass effects one usually uses the approximate expression proposed in [2, 9] above the quark-antiquark threshold

$$R(s) = T(v) [1 + g(v)r(s)], \quad (6)$$

where

$$T(v) = v \frac{3-v^2}{2}, \quad g(v) = \frac{4\pi}{3} \left[\frac{\pi}{2v} - \frac{3+v}{4} \left(\frac{\pi}{2} - \frac{3}{4\pi} \right) \right]. \quad (7)$$

In Eq. (6) one cannot directly use the perturbative expression for $r(s)$, which contains unphysical singularities, to calculate, say, the Adler

D -function (2). Instead of that one can use the analytic perturbation theory for $r(s)$. The explicit three-loop form for $r_{\text{an}}(s)$ is given in [4].

In describing a charged particle-antiparticle system near threshold, it is well known from QED that the so-called Coulomb resummation factor plays an important role. For a systematic relativistic analysis of quark-antiquark systems, it is essential from the very beginning to have a relativistic generalization of the S -factor. A new form for this relativistic factor in the case of QCD has been proposed in [10]¹

$$S(\chi) = \frac{X(\chi)}{1 - \exp[-X(\chi)]}, \quad X(\chi) = \frac{4}{3} \frac{\pi \alpha_s}{\sinh \chi}, \quad (8)$$

where χ is the rapidity which related to s by $2m \cosh \chi = \sqrt{s}$. The relativistic resummation factor (8) reproduces both the expected non-relativistic and ultrarelativistic limits and corresponds to a QCD-like Coulomb potential.

The modified expression for R -function is [4, 12]

$$\begin{aligned} R(s) &= [R_0(s) + R_1(s)] \Theta(s - 4m^2), \\ R_0(s) &= T(v) S(\chi), \quad R_1(s) = T(v) \left[r_{\text{an}}(s) g(v) - \frac{1}{2} X(\chi) \right]. \end{aligned} \quad (9)$$

The function $r_{\text{an}}(s)$ is taken within the analytic approach as in [4]. To avoid a double counting the function R_1 contains subtracted term with $X(\chi)$. The term R_0 gives a principle contribution to $R(s)$, the correction R_1 is less than twenty percent for whole energy interval.

3. Quark masses

A solution of the Schwinger-Dyson equations performed in [13–17] demonstrates a fined infrared behavior of the invariant charge and quark mass function. This behavior can be understood by using a conception of the dynamical quark mass. This mass has an essentially nonperturbative nature. Its connection with the quark condensate has been established in [18]. By using the analysis based on the Schwinger-Dyson equations the similar relation has been found in [19]. It has been demonstrated in [20] that on the mass-shell one has a gauge-independent result: $m^3 = -4/3\pi\alpha_s < 0|\bar{q}q|0 >$. An analysis performed in [21] leads to a step-like behavior of the quark mass function.

According to these results one can assume that at small p^2 the function $m(p^2)$ is rather smooth (nearly constant). In the region $p^2 >$

¹ Here we consider the vector channel for which a threshold resummation S -factor for the s -wave states is used. For the axial-vector channel the P -factor is required. The corresponding relativistic factor has recently been found in [11].

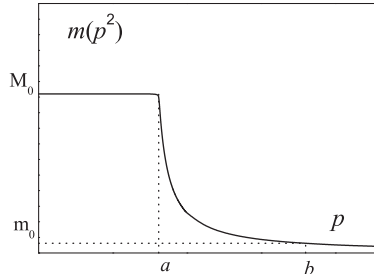


Figure 1. Effective quark mass.

1 \div 2 GeV the principle behavior of the function $m(p^2)$ is defined by perturbation theory.

We perform our analysis by using constant quark masses and the mass function $m(p^2)$ which is shown in Fig. 1. We take the line that connects the points a and b in the form $A^3/(p^2 - B^2)$. The parameter m_0 are taken from the known value of the running (current) mass at $b = 2.0$ GeV [22], the parameter a is taken as $a = 0.8$ GeV. The quantities considering here are not too sensitive to parameters of heavy quarks and we take for c , b and t quarks $m^f(p^2) = m_0^f = M_0^f$. We have a consistent description of all mentioned quantities, if the light quark parameter $M_0^{u,d} = 260 \pm 10$ MeV and the mass parameters M_0^s is varied in the limits from 400 to 550 MeV. The masses of the heavy quarks are $M_0^c = 1.3$ GeV, $M_0^b = 4.4$ GeV and $M_0^t = 174.0$ GeV.

4. Physical quantities and functions

Let us apply the formulated model to describe mentioned in Introduction physical quantities and functions connected with $R(s)$.

Inclusive decay of the τ -lepton. The experimental data presented by the ALEPH, $R_{\tau,V}^{\text{expt}} = 1.775 \pm 0.017$ [23], and the OPAL, $R_{\tau,V}^{\text{expt}} = 1.764 \pm 0.016$ [24], collaborations. In our analysis we use the non-strange vector channel spectral function obtained by the ALEPH collaboration and keep in all further calculations the value $R_\tau^V = 1.78$ as the normalization point.

D_V -function. In order to construct the Euclidean D -function we use for $R(s)$ the following expression $R(s) = R^{\text{expt}}(s)\theta(s_0 - s) + R^{\text{theor}}(s)\theta(s - s_0)$. The continuum threshold $s_0 \simeq 1.6$ GeV² has been found from the duality relation [25].

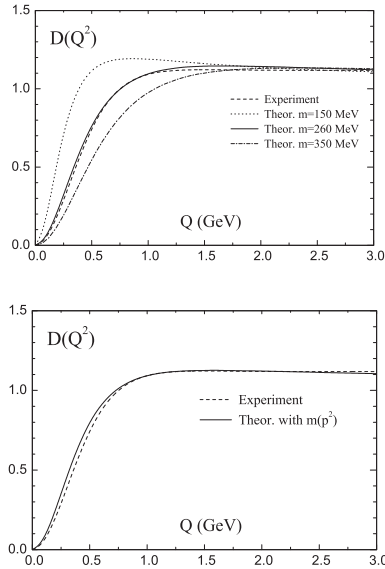


Figure 3. D -function for $m = m(p^2)$.

In Fig. 2 we plot curves corresponding to different values of the quark masses. A result for the D -function that obtained by using the mass function $m(p^2)$ with $M_0^{u,d} = 260$ MeV is shown in Fig. 3. Thus we obtained the result that is rather close to the result obtained for $m(p^2) = \text{const.}$

‘Light’ smeared R_Δ -function. By using the ALEPH data [23], we construct the ‘light’ experimental function $R_\Delta(s)$.

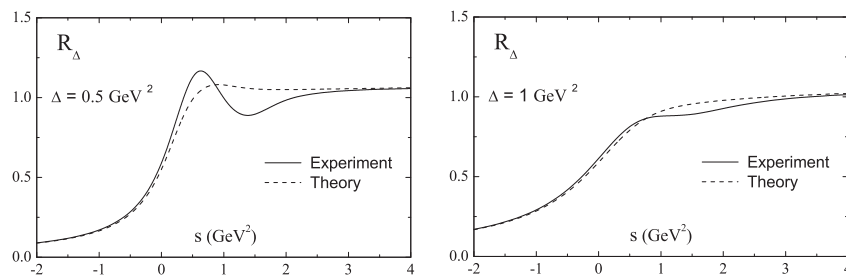


Figure 5. Smeared function for $\Delta = 1.0$ GeV².

Figures 4 and 5 demonstrate behavior of experimental and theoretical smeared functions for $\Delta = 0.5$ GeV² and $\Delta = 1.0$ GeV². Let us

emphasize, in the spacelike region ($s < 0$) there is a good agreement between data and theory starting from $s = 0$.

Hadronic contribution to a_μ . The hadronic contribution to the anomalous magnetic moment of the muon in the leading order of the electromagnetic coupling constant is defined by Eq. (4). In our calculations we take into account the matching conditions at quark thresholds according to procedure described in [8]. The strong interaction contribution to a_μ we estimate as

$$a_\mu^{\text{had}} = (693 \pm 34) \times 10^{-10}. \quad (10)$$

The experimental value of a_μ^{had} is extracted from e^+e^- annihilation and τ decay data: $(696.3 \pm 6.2_{\text{exp}} \pm 3.6_{\text{rad}}) \times 10^{-10}$ (e^+e^- - based), $(711.0 \pm 5.0_{\text{exp}} \pm 0.8_{\text{rad}} \pm 2.8_{SU(2)}) \times 10^{-10}$ (τ - based) [26].

Hadronic contributions to $\Delta\alpha$. Consider the hadronic correction to electromagnetic fine structure constant α at the Z -boson scale defined by Eq. (5). For $\Delta\alpha_{\text{had}}^{(5)}(M_Z^2)$ we obtain

$$\Delta\alpha_{\text{had}}^{(5)}(M_Z^2) = (278.2 \pm 3.5) \times 10^{-4}. \quad (11)$$

The experimental average value is $\Delta\alpha_{\text{had}}^{(5)}(M_Z^2) = (275.5 \pm 1.9_{\text{expt}} \pm 1.3_{\text{rad}}) \times 10^{-4}$ [27].

5. Conclusions

Nonperturbative method of performing QCD calculations has been developed. The method based on analytic approach, takes into account a summation of infinite numbers of threshold singularities and involves non-perturbative light quark masses. The following quantities and functions have been analysed: R_τ^V , $D_V(Q^2)$, $R_\Delta(s)$, a_μ^{had} , and $\Delta\alpha_{\text{had}}^{(5)}(M_Z^2)$. It has been demonstrated that the method proposed allows us to describe well these objects.

Acknowledgments

It is a pleasure to thank Academician D.V. Shirkov for interest in the work, support and useful discussion. We also express our gratitude to A.E. Dorokhov, S.B. Gerasimov, A.V. Efremov, O.V. Teryaev, and A.V. Nesterenko for valuable discussions and helpful remarks.

This work was supported in part by the International Program of Cooperation between Republic of Belarus and JINR, the Belarus State

Program of Basic Research “Physics of Interactions”, the RFBR grant No. 05-01-00992, and NSh-2339.2003.2.

References

- 1 E.D. Bloom, F.J. Gilman, Phys. Rev. Lett. **25** (1970) 1140.
- 2 E.C. Poggio, H.R. Quinn, S. Weinberg, Phys. Rev. D **13** (1976) 1958.
- 3 S.L. Adler, Phys. Rev. D **10** (1974) 3714.
- 4 K.A. Milton, I.L. Solovtsov, O.P. Solovtsova, Phys. Rev. D **64** (2001) 016005.
- 5 D.V. Shirkov, I.L. Solovtsov, JINR Rap. Comm. **2** [76] (1996) 5.
- 6 D.V. Shirkov, I.L. Solovtsov, Phys. Rev. Lett. **79** (1997) 1209.
- 7 K.A. Milton, I.L. Solovtsov, Phys. Rev. D **55** (1997) 5295.
- 8 K.A. Milton, O.P. Solovtsova, Phys. Rev. D **57** (1998) 5402.
- 9 T. Appelquist, H.D. Politzer, Phys. Rev. Lett. **34** (1975) 43.
- 10 K.A. Milton, I.L. Solovtsov, Mod. Phys. Lett. A **16** (2001) 2213.
- 11 I.L. Solovtsov, O.P. Solovtsova, Yu.D. Chernichenko, Phys. Part. Nuclei Lett. **2** (2005) 199.
- 12 A.N. Sissakian, I.L. Solovtsov, O.P. Solovtsova, JETP Lett. **73** (2001) 166.
- 13 C.D. Roberts, Phys. Part. Nuclei **30** (1999) 537.
- 14 C.S. Fisher, R. Alkofer, Phys. Lett. B **536** (2002) 177.
- 15 J.C. Bloch, Phys. Rev. D **64** (2001) 116011.
- 16 C.S. Fisher, R. Alkofer, Phys. Rev. D **67** (2003) 094020.
- 17 R. Alkofer, L. Smekal, Phys. Rept. **353** (2001) 281.
- 18 H.D. Politzer, Nucl. Phys. B **117** (1976) 397.
- 19 N.V. Krasnikov, A.A. Pivovarov, Sov. Phys. J. **25** (1982) 55.
- 20 V. Elias, M.D. Scadron, Phys. Rev. D **30** (1984) 647.
- 21 L.J. Reinders, K. Stam, Phys. Lett. B **195** (1987) 465.
- 22 Particle Data Group, S. Eidelman *et al.*, Phys. Lett. B **592** (2004) 1.
- 23 ALEPH Collab., R. Barate *et al.*, Eur. Phys. J. C **4** (1998) 409.
- 24 OPAL Collab., K. Ackerstaff *et al.*, Eur. Phys. J. C **7** (1999) 571.
- 25 S. Peris, M. Perrottet, E. de Rafael, JHEP **05** (1998) 011.
- 26 M. Davier, S. Eidelman, A. Hocker, Z. Zhang, Eur. Phys. J. C **31** (2003) 503.
- 27 K. Hagiwara, A.D. Martin, D. Nomura, T. Teubner, Phys. Rev. D **69** (2004) 093003.

**ON NATURE OF SCALAR AND TENSOR MESONS FROM
THE ANALYSIS OF PROCESSES $\pi\pi \rightarrow \pi\pi, K\bar{K}, \eta\eta$**

Yu.S. Surovtsev¹, R. Kamiński², D. Krupa³ and M. Nagy³

² *Institute of Nuclear Physics PAS PL 31 342, Cracow, Poland*

³ *Institute of Physics SAS, Dúbravská cesta 9, 842 28 Bratislava, Slovakia*

Abstract. Analysis of the isoscalar S - and D -waves of processes $\pi\pi \rightarrow \pi\pi, K\bar{K}, \eta\eta$ is carried out aimed at studying the status and QCD nature of scalar and tensor mesons below 2 GeV and 2.3 GeV, respectively. Assignment of these mesons to lower scalar and tensor nonets is proposed.

1. An assignment of the scalar mesons to quark-model configurations is problematic up to now. When studying this sector, we have applied our model-independent method [1]. We analyzed the S -waves of $\pi\pi \rightarrow \pi\pi, K\bar{K}, \eta\eta$ in the 3-channel approach. The relevant S -matrix is determined on the 8-sheeted Riemann surface. The elements $S_{\alpha\beta}$ ($\alpha, \beta = 1(\pi\pi), 2(K\bar{K}), 3(\eta\eta)$) have the right-hand cuts on the s -plane, starting with $4m_\pi^2$, $4m_K^2$ and $4m_\eta^2$, and the left-hand cuts. The sheets of surface are numbered according to the signs of analytic continuations of the 3-momenta $k_1 = (s/4 - m_\pi^2)^{1/2}$, $k_2 = (s/4 - m_K^2)^{1/2}$, $k_3 = (s/4 - m_\eta^2)^{1/2}$ as follows: signs $(\text{Im}k_1, \text{Im}k_2, \text{Im}k_3) = + + +, - + +, - - +, + - +, + - -, - - -, - + -, + + -$ correspond to sheets I, II, ..., VIII.

The Le Couteur-Newton relations[3] are used which express the S -matrix elements of all coupled processes in terms of the Jost matrix determinant $d(k_1, k_2, k_3)$ that is a real analytic function with the only square-root branch-points at $k_i = 0$. Resonances are represented by pole clusters (of poles and zeros on the Riemann surface) [1]. In the 3-channel case we have 7 types of resonance clusters corresponding to 7 possible standard situations when there are conjugate resonance zeros on sheet I only in **(a)** S_{11} ; **(b)** S_{22} ; **(c)** S_{33} ; **(d)** S_{11} and S_{22} ; **(e)** S_{22} and S_{33} ; **(f)** S_{11} and S_{33} ; and **(g)** S_{11} , S_{22} , and S_{33} . The cluster type is related to the state nature. The branch points are taken into account in a uniformizing variable. Here we neglect the influence of the $\pi\pi$ threshold. Then the variable $w = (k_2 + k_3) / \sqrt{m_\eta^2 - m_K^2}$ uniformizes our S -matrix [1]. The $d(w)$ -function is taken as $d(w) = d_B d_{res}$ where the resonance part is $d_{res}(w) = w^{-\frac{M}{2}} \prod_{r=1}^M (w + w_r^*)$ with M the number of resonance zeros. The background, is $d_B = \exp[-i \sum_{n=1}^3 (k_n/m_n)(\alpha_n + i\beta_n)]$, where

$$\alpha_n = a_{n1} + a_{n\sigma}(s - s_\sigma)/s_\sigma \theta(s - s_\sigma) + a_{nv}(s - s_v)/s_v \theta(s - s_v),$$

$$\beta_n = b_{n1} + b_{n\sigma}(s - s_\sigma)/s_\sigma \theta(s - s_\sigma) + b_{nv}(s - s_v)/s_v \theta(s - s_v).$$

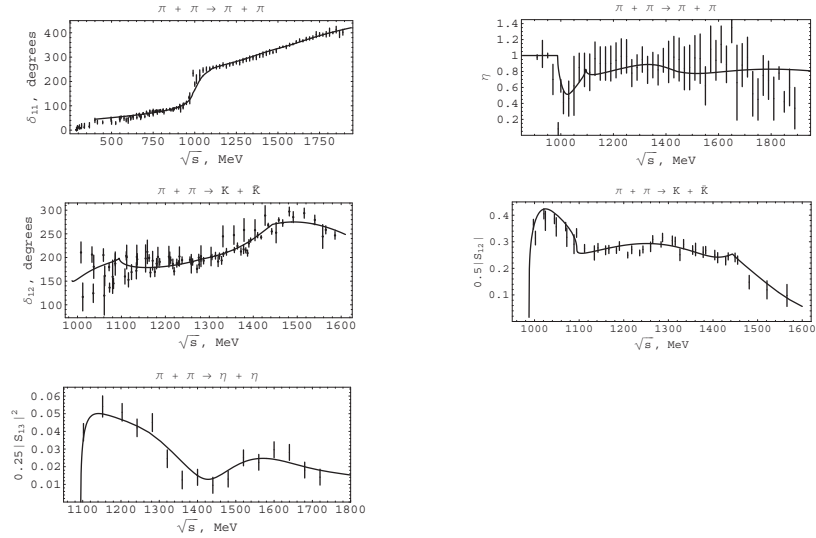


Figure 1. Comparison of obtained energy dependences for the S-waves with exp. data.

We obtained a satisfactory description (the total $\chi^2/\text{ndf} \approx 380.22/(301 - 43) \approx 1.47$, see Fig. 1). Data on $\pi\pi \rightarrow \pi\pi, K\bar{K}$ are taken from [4]; on $\pi\pi \rightarrow \eta\eta$, from [5]. The background parameters are $a_{11} = 0.183$, $a_{1\sigma} = 0.0252$, $a_{1v} = 0.0155$, $b_{11} = 0$, $b_{1\sigma} = -0.00743$, $b_{1v} = 0.04122$, $a_{21} = -0.6973$, $a_{2\sigma} = -1.427$, $a_{2v} = -5.935$, $b_{21} = 0.0451$, $b_{2\sigma} = 0$, $b_{2v} = 6.3594$, $b_{31} = 0.6337$, $b_{3\sigma} = 0.332$, $b_{3v} = 0$; $s_\sigma = 1.6384 \text{ GeV}^2$, $s_v = 2.084 \text{ GeV}^2$.

Analysis selects the case when the $f_0(600)$ is described the cluster of type **(a)** and has properties the σ -meson; $f_0(1370)$ and $f_0(1710)$, types **(c)** and **(b)** that tells us about their mainly $s\bar{s}$ nature; $f_0(1500)$, type **(g)** that points to its dominant glueball component [1]. In Table I, the obtained pole clusters are shown on the \sqrt{s} -plane. Note the surprising conclusion about the $f_0(980)$ nature. It turns out that this state lies slightly above the $K\bar{K}$ threshold and under the $\eta\eta$ threshold. It is described by a pole on sheet II and by a shifted pole on sheet III without an accompaniment of the corresponding poles on sheets VI and VII, as it was expected for standard clusters. This corresponds to the description of the $\eta\eta$ bound state [1].

The resonance masses and widths, calculated from pole positions, are respectively (in the MeV units): for $f_0(600)$, 868 and 1212; for $f_0(980)$, 1015.5 and 64; for $f_0(1370)$, 1407.5 and 344; for $f_0(1500)$, 1546 and 716; for $f_0(1710)$, 1709.6 and 276.

TABLE I.

Sheet		II	III	IV	V	VI	VII	VIII
$f_0(600)$	E_r	682±14	687±16			622±17	617±15	
	Γ_r	606±22	606±9			606±28	606±26	
$f_0(980)$	E_r	1015±5	987±18					
	Γ_r	32.5±8	57.5±16					
$f_0(1370)$	E_r				1397±21	1397±20	1397±20	1397±20
	Γ_r				288±13	270±15	154±6	172±9
$f_0(1500)$	E_r	1504±22	1479±30	1504±19	1499±20	1494±27	1487±25	1504±20
	Γ_r	358±23	140±21	238±29	139±21	194±27	87.8±15	357.6±30
$f_0(1710)$	E_r		1704±18	1704±21	1704±32	1704±30		
	Γ_r		138±14	155±17	327±26	310±45		

2. We propose a following assignment of scalar mesons to lower nonets, excluding from this consideration the $f_0(980)$ as the $\eta\eta$ bound state. The ground nonet: $a_0(980)$, $K_0^*(900)$ [6], $f_0(600)$ and $f_0(1370)$ as mixtures of the eighth component of octet and the SU(3) singlet. Then the Gell-Mann–Okubo formula $3m_{f_8}^2 = 4m_{K^*}^2 - m_{a_0}^2$ gives $m_{f_8} = 0.87$ GeV. Our result for the σ -meson mass is $m_\sigma \approx 0.868 \pm 0.02$ GeV. In the relation for masses of nonet $m_\sigma + m_{f_0(1370)} = 2m_{K_0^*(900)}$, the left-hand side is about 26 % bigger than the right-hand one.

The nonet of radial excitations: the $a_0(1450)$, $K_0^*(1430 - 1450)$, and the $f_0(1500)$ and $f_0(1710)$ as mixtures of the eighth component of octet (mixed with a glueball) and the SU(3) singlet. From the Gell-Mann–Okubo formula we obtain $m_{f_8} \approx 1.45$ GeV. In second formula $m_{f_0(1500)} + m_{f_0(1710)} = 2m_{K^*(1450)}$, the left-hand side is about 12 % bigger than the right-hand one. This assignment moves a number of questions and does not put the new ones.

3. Further we analyzed the isoscalar D-waves of the same processes for studying the f_2 mesons below 2.3 GeV. Here from thirteen discussed resonances, the nine ones ($f_2(1430)$, $f_2(1565)$, $f_2(1640)$, $f_2(1810)$, $f_2(1910)$, $f_2(2000)$, $f_2(2020)$, $f_2(2150)$, $f_2(2220)$) must be confirmed in various experiments and analyses. We applied the 4-channel approach with the explicit account of the channel $(2\pi)(2\pi)$ ($i=4$), too. In the Jost matrix determinant $d(k_1, k_2, k_3, k_4) = d_B d_{res}$, the resonance part is taken as $(\rho_{rj} = 2k_i / \sqrt{M_r^2 - 4m_j^2})$: $d_{res}(s) = \prod_r [M_r^2 - s - i \sum_{j=1}^4 \rho_{rj}^5 R_{rj} f_{rj}^2]$, where f_{rj}^2/M_r is the partial width, R_{rj} is a Blatt-Weisskopf barrier factor [7] with radii of 0.957 Fm for all resonances,

except for $f_2(1270)$, $f'_2(1525)$ and $f_2(1963)$ for which they are 1.492, 0.708 and 0.608 Fm for $f_2(1270)$, 0.957, 0.576 and 0.58 for $f'_2(1525)$ and 0.957, 0.178 and 0.651 for $f_2(1963)$ respectively in the channels $\pi\pi$, $K\bar{K}$ and $\eta\eta$.

The background is $d_B = \exp\left[-i \sum_{n=1}^3 (2k_n/\sqrt{s})^5 (a_n + ib_n)\right]$ where

$$a_1 = \alpha_{11} + (s - 4m_K^2)/s\alpha_{12}\theta(s - 4m_K^2) + (s - 4m_0^2)/s\alpha_{10}\theta(s - 4m_0^2),$$

$$b_n = \beta_n + (s - 4m_0^2)/s\gamma_n\theta(s - 4m_0^2) \quad (n = 1, 2, 3).$$

The data are taken from Ref. [8]. We obtain a reasonable description (the total $\chi^2/\text{ndf} = 167.506/(168 - 68) \approx 1.675$, see also Fig. 2) with ten resonances (see Table II, all parameters in the MeV units). The background parameters: $\alpha_{11} = -0.0828$, $\alpha_{12} = 0.0474$, $\alpha_{10} = -0.23422$, $\beta_1 = -0.065$,

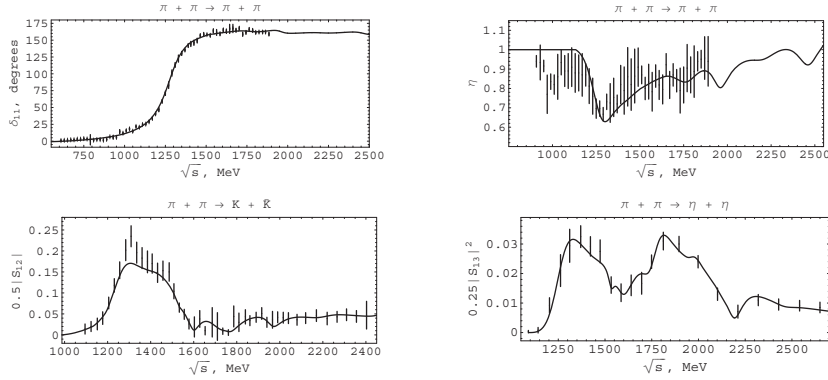


Figure 2. Comparison of obtained energy dependences for the D-waves with exp. data.

TABLE II.

State	M	f_{r1}	f_{r2}	f_{r3}	f_{r4}
$f_2(1270)$	1274.7±1.8	470.9±5.4	201.4±11.4	88.8±4.76	24.2±4.6
$f_2(1430)$	1450.5±18.7	127.9±45.9	562.5±142	26.3±18.4	18.3±65
$f'_2(1525)$	1535±8.6	28.6±8.3	253.8±78	92.9±11.5	41.4±160
$f_2(1565)$	1601.8±27.5	75.5±19.4	315±48.6	388.9±27.7	127±199
$f_2(1730)$	1726.4±5.7	78.8±43	289.5±62.4	460.3±76.2	108.6±76.7
$f_2(1810)$	1775.6±15.3	129.5±14.4	259±30.7	469.7±22.5	90.3±100
$f_2(1950)$	1963±29.3	132.6±22.4	333±61.3	319±42.6	65.4±94
$f_2(2000)$	2015±21.6	143.5±23.3	614±92.6	57.4±24	457.4±221
$f_2(2240)$	2207±44.8	136.4±32.2	551±149	375±114	166.8±104
$f_2(2464)$	2464±31.6	177±47.2	411±196.9	4.5±70.8	460.8±209

$\gamma_1 = -0.039$, $\beta_2 = -0.9809$, $\gamma_2 = 0.744$, $\beta_3 = -0.531$, $\gamma_3 = 0.8222$, $m_0 = 0.759$ GeV.

4. In the isoscalar-tensor sector, we did not obtain $f_2(1640)$, $f_2(1910)$, $f_2(2150)$, $f_2(2220)$, however, see $f_2(1450)$ and $f_2(1726)$ that are related to the statistically-valued experimental points.

Usually one assigns to the ground nonet the $f_2(1270)$ and $f_2'(1525)$. To the second nonet, one could assign $f_2(1602)$ and $f_2(1776)$.

The $f_2(1963)$ and $f_2(2207)$ together with $K_2^*(1980)$ could be placed into the third nonet. Then in the relation $M_{f_2(1963)} + M_{f_2(2207)} = 2M_{K^*(1980)}$, the left-hand side is only 5.3 % bigger than the right-hand one.

If one consider $f_2(1963)$ as the eighth component of octet, then the Gell-Mann–Okubo formula $M_{a_2} = 4M_{K^*(1980)} - 3M_{f_2(1963)}$ gives $M_{a_2} = 2.031$. In [2] one predicts the mass about 2.03 for the second radial excitation of the 1^-2^{++} state on the basis of consideration of the a_2 trajectory on the (n, M^2) plane (n is the radial quantum number of the $q\bar{q}$ state). Note that at our assignment to the $q\bar{q}$ nonets the masses of resonances lie down well on the corresponding trajectories on the (n, M^2) plane.

As to $f_2(2015)$, the ratio of the $\pi\pi$ and $\eta\eta$ partial widths is in the range obtained in [2]) for the glueball. However, the $K\bar{K}$ partial width is too large to correspond to the glueball.

Finally we have $f_2(1450)$ and $f_2(1726)$ with the rather unusual properties. These are non- $q\bar{q}$ states and non-glueball. Since one predicts that hybrids are above glueballs, maybe, these states are the 4-quark ones.

5. Yu.S. and R.K. acknowledge support provided by the Bogoliubov – Infeld Program. M.N. were supported in part by the Slovak Scientific Grant Agency, Grant VEGA No. 2/3105/23; and D.K., by Grant VEGA No. 2/5085/99.

References

- 1 D. Krupa et al., Nuovo Cim. **A109** (1996) 281.
- 2 V.V. Anisovich et al., hep-ph/0506133.
- 3 K.J. Le Couteur, Proc. Roy. Soc. **A256** (1960) 115; R.G. Newton, J. Math. Phys. **2** (1961) 188.
- 4 Yu.S. Surovtsev et al., Eur. Phys. J. **A15** (2002) 409.
- 5 F. Binon et al., Nuovo Cim. **A78** (1983) 313.
- 6 S. Ishida et al., Prog. Theor. Phys. **98** (1997) 621.
- 7 J. Blatt, V. Weisskopf, *Theoretical nuclear physics*, Wiley, N.Y., 1952.
- 8 B. Hyams et al., Nucl. Phys. **B64** (1973) 134; S. Lindenbaum, R. Longacre, Phys. Lett. **B274** (1992) 492 .

**NEW PROPOSAL OF NUMERICAL MODELLING
OF BOSE-EINSTEIN CORRELATIONS: BOSE-EINSTEIN
CORRELATIONS FROM “WITHIN”***

Oleg V. Utyuzh (utyuzh@fuw.edu.pl)

*The Andrzej Sołtan Institute for Nuclear Studies; Hoża 69; 00-681 Warsaw,
Poland*

Grzegorz Wilk (wilk@fuw.edu.pl)

*The Andrzej Sołtan Institute for Nuclear Studies; Hoża 69; 00-681 Warsaw,
Poland*

Zbigniew Włodarczyk (wlod@pu.kielce.pl)

*Institute of Physics, Świętokrzyska Academy, Świętokrzyska 15; 25-406 Kielce,
Poland*

Abstract. We describe an attempt to numerically model Bose-Einstein correlations (BEC) from “within”, i.e., by using them as the most fundamental ingredient of a Monte Carlo event generator (MC) rather than considering them as a kind of (more or less important, depending on the actual situation) “afterburner”, which inevitably changes the original physical content of the MC code used to model multiparticle production process.

Key words: Bose-Einstein correlations; Statistical models; Fluctuations

1. Introduction

In all multiparticle production processes one observes specific correlations caused by quantum statistics satisfied by the produced secondaries. Because majority of them are boson (pions, kaons,...) subjected to Bose-Einstein statistics, one usually observes enhancements in the yields of pairs of identical boson produced with small relative momenta. They are called Bose-Einstein correlations [1, 2, 3, 4]. The corresponding depletion observed for fermionic identical particles (like nucleons or lambdas) satisfying Fermi-Dirac statistics is also observed but we shall not discuss it here. There is already extraordinary vast literature (see, for example, [2, 3, 4], and references therein), to which we refer, in what concerns measurements, formulations and

* Invited talk delivered by G.Wilk at the International Conference *NEW TRENDS IN HIGH-ENERGY PHYSICS (experiment, phenomenology, theory)*, Yalta, Crimea, Ukraine, September 10-17, 2005.

interpretation of BEC as well as expectations they cause for our understanding of spatio-temporal details of the multiparticle production processes (or hadronization processes). Here we shall concentrate only on one particular field, namely on the numerical modelling of BEC and we shall propose new approach to this problem, which we call *BEC from within* [5].

The need for numerical modelling of the BEC phenomenon arises because the only effective way to investigate multiparticle production processes is by using one out of many of Monte Carlo (MC) numerical codes developed so far, each based on different physical picture of hadronization process [6]. However, such codes do not contain BEC because they are based on classical probabilistic schemes whereas BEC is of the purely quantum mechanical origin. Modelling BEC is therefore equivalent to modelling quantum mechanical part of hadronization process and by definition can only be some, better or worse, approximation. Actually, so far there is only one attempt in the literature of proper modelling of BEC using them as input of the numerical code. Namely in [7], using information theory approach based on the maximalization of the information (Shannon) entropy, identical particles were allocated in separated cells in the (longitudinal in this case) momentum space. In this way one is at the same time obtaining proper multiplicity distributions and bunching of particles in momentum space mimicking bunching of bosons in energy states, i.e., effect of the Bose-Einstein statistics. The method we shall propose here develops this idea further. However, before continuing along these lines let us first mention other attempts of introducing effects of BEC, which are widely used nowadays and let us point out why they cannot be regarded as satisfactory.

2. Numerical modelling of BEC

Among methods of numerical modelling of BEC using, in one or another way, some known numerical MC codes one can distinguish two approaches. One, represented by [8] (working with plane waves) and [9] (working with wave packets) starts with some distribution of momenta of particles in selected event and then, using a kind of Metropolis rejection method, changes step-by-step their momenta until multiparticle distribution containing effect of BEC is reached. This is now regarded as a true event. The drawback of this method is that it is extremely time consuming and therefore can only be used to explain some fine details of how BEC works, not for comparison with real data.

The other approaches are tacitly assuming that, on the whole, BEC constitutes only a small effect and it is therefore justify to add it in some way to the already known outputs of the MC event generators widely used to model results of high energy collisions in the form of the so called *afterburner* [10]. There are two types of such afterburners.

- The first one modifies accordingly energy-momenta of identical secondaries, $\mathbf{p} \rightarrow \mathbf{p} + d\mathbf{p}$, where $d\mathbf{p}$ are selected from some function $f(d\mathbf{p})$ chosen in such way as to reproduce the observed correlation pattern [11]. The advantage of this approach is that it applies to a single event and does not change multiplicity of secondaries produced in this event. The obvious drawback is that it spoils energy-momentum conservation so afterwards one has to correct for it in some way.
- The second type of afterburners preserves the energy-momentum conservation but it changes multiplicity distribution pattern of given MC code and works only for the whole ensemble of events produced by MC. In it one weights each event depending on how big BEC effect it shows (because of inevitably fluctuations they can be events which already show quite substantial BEC effect - those are multiplied by bigger weight - together with events which show no BEC - they are multiplied by small weight). In practice it leads to distortion of physics because “suitable” events are counted many times more than the MC code used allows [12, 13]. Again, the weight function is some phenomenological input chosen in such way as to reproduce the observed BEC pattern of the whole ensemble of events considered.

However, even - as it is usually assumed - if the above afterburners do not change in a substantial way the *numerical* output of MC generators, which they are using, they surely do change their *physical basis* (i.e., the number and the type of the initial physical assumptions forming a basis of such MC code). This change, neglected in the assumption made above, has never been investigated in detail. We shall now demonstrate how dramatic this change can be by using as example simple MC cascade code (CAS) [14] proposed by us some time ago and endow it with some specific afterburner. The physical basis of CAS is very simple. It starts with decay of the original mass M into two objects of mass M_1 and M_2 such that $M_{i=1,2} = k_{i=1,2} \cdot M$ where $k_{i=1,2} < 1$ are parameters responsible for development of the cascade ($k_1 + k_2 < 1$). The masses $M_{i=1,2}$ fly then apart and after some time $t_{i=1,2}$ they decay (in their rest frame) again into two lighter masses according to the above scheme but now with different values of the new decay factors k . This branching process continues until the original mass M finally dissipates into a number of masses $M_{i=1,\dots,2^N}$ equal to masses of the lightest particles (N is the number of cascade generations). Values of “life-times” t and decay factors k are chosen from some assumed distribution. The charges in the vertices change in the simple possible way: $(0) \rightarrow (+) + (-)$, $(+) \rightarrow (0) + (+)$ and $(-) \rightarrow (0) + (-)$. (see left panel of Fig. 1). This code produces both the energy-momentum distributions of produced particles and spatial distributions of their production points (which show features of the truncated Lévy distributions). The example of the correlation function it leads to is shown in Fig. 3.

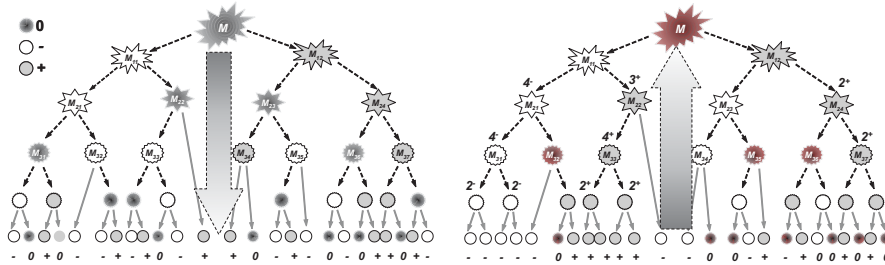


Figure 1. Example of charge flows in MC code using simple cascade model for hadronization [14]: left panel - no effect of BEC observed; right panel - after applying afterburner described in [15] (based on new assignment of charges to the produced particles) one has BEC present at the cost of appearance of multicharged vertices.

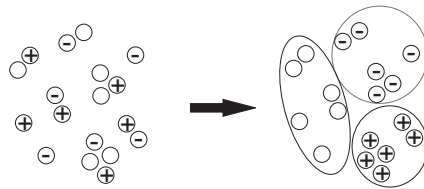


Figure 2. Charge reassignment method of generating effect of BEC in a single event without changing its energy-momentum and spatio-temporal characteristics [16].

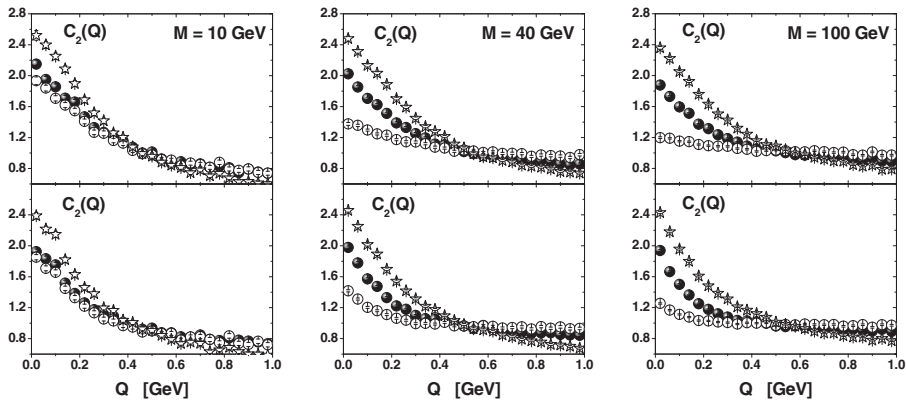


Figure 3. Examples of BEC patterns obtained for $M = 10, 40$ and 100 GeV for constant weights $P = 0.75$ (stars) and $P = 0.5$ (full symbols) and for the weight given by gaussian weights build on the information on momenta and positions of particles considered [16] (open symbols). Upper panels are for CAS, lower for simple statistical model (see [16] for details).

CAS being classical scheme produces no BEC effect by itself. However, as we have demonstrated in [15, 16] the effect of BEC can be introduced by special afterburner applicable to every separate event, but, contrary to afterburners mentioned before, working without changing the number of secondaries $N_{+/0/-}$ and without changing the energy-momentum and spatio-temporal structure of this event. It is based on the observation that effect of BEC can be visualized classically as phenomenon originating due to correlations of some specific fluctuations present in such stochastic systems as blob of the hadronizing matter [17, 8, 7]. It means that in phase space there occur bunches of identical particles and BEC arises as *correlation of fluctuations* effect. To get such effect in our case it is enough to forget about the initial charge assignment in the event under consideration (but keeping in mind the recorded multiplicities $N_{+/0/-}$ and both energy-momenta and spatio-temporal positions of particles emerging from NC code in event under consideration) and look for bunches of identical particles, both in energy-momentum and space-time. The procedure of selection of bunches of particles of the same charge, is therefore the crucial point of such algorithm [15, 16], cf. Fig. 2. It generally consists in selecting particles located nearby in the phase space, forming a kind of cell, and endowing them with the same charge. In what follows we shall call such cell *elementary emitting cell*, EEC. In this way we explore natural fluctuations of spatio-temporal and energy-momentum characteristic of produced particles resulting from CAS. Referring to [15, 16] for details let us only notice here that this methods works surprisingly well and is very effective. Unfortunately it was not yet developed to fully fledged MC code available for the common use but it allows to follow changes made in the original CAS by imposing on it requirements or reproducing also BEC patter. This is shown in Fig. 1 where CAS without BEC (left panel) is compared with CAS with BEC imposed. Whereas $N_{+/0/-}$ and positions of all secondaries in phase space remain the same the *charge flow pattern* changes considerably (see the right panel of Fig. 1). BEC in this case enforces occurrence of *multicharged vertices*, not present in the original CAS.

To summarize, the change in the original CAS required to observe BEC pattern amounts to introduction of bunching of particles of the same charge (in the form of EEC's). However, when done directly in the CAS it would lead to great problems with the proper ending of cascade (without producing spurious multicharged hadronic states, not observed in the nature) and from this point of view, once we know what is the physics behind BEC, the proposed afterburner algorithm occurs as a viable numerical short cut solution to this problem. No such knowledge is, however, provided for other afterburners used nowadays (although the idea of bunching origin of BEC can be spotted in the literature, cf., for example [18]). The problem, which is clearly visible in the CAS model, is not at all straightforward in other approaches. However,

at least in the string-type models of hadronization [13], one can imagine that it could proceed through the formation of charged (instead of neutral) color dipoles, i.e., by allowing formation of multi(like)charged systems of opposite signs out of vacuum when breaking the string. Because only a tiny fraction of such processes seems to be enough in getting BEC in the case of CAS model, it would probably be quite acceptable modification. It is worth to mention at this point that there is also another possibility in such models, namely when strings are nearby in the phase space one can imagine that production of given charge with one string enhances emission of the same charge from the string nearby - in this case one would have a kind of *stimulated emission* discussed already in [19, 20].

3. BEC from “within”

The above observations, especially notion of EEC’s, will be the cornerstone of our new proposition. Let us remind that the idea of bunching of particles as quantum statistical (QS) effect is not new and has been used in the phenomenology of multiparticle production already long time ago [21, 22, 23, 24, 25]. In connection with BEC it was mentioned for the first time in [19, 20] and later it formed a cornerstone of the so called *clan model* of multiparticle distributions $P(n)$ leading in natural way to their negative binomial (NB) form observed in experiment [26]. It was introduced in the realm of BEC again in [27], where the notion of EEC has been introduced for the first time, and in [7].

Because our motivation concerning viewing of BEC *from “within”* comes basically from the work [7] let us, for completeness, outline shortly its basic points. It was the first MC code which intended to provide as output distribution of particles containing already, among its physical assumptions, the effect of BEC with no need for any afterburner whatsoever. It deals with the problem of how to distribute in phase space (actually in longitudinal phase space given by rapidity variable) in a least biased way a given number of bosonic secondaries, $\langle n \rangle = \langle n^{(+)} \rangle + \langle n^{(-)} \rangle + \langle n^{(0)} \rangle$, $\langle n^{(+)} \rangle = \langle n^{(-)} \rangle = \langle n^{(0)} \rangle$. Using information theory approach (cf., [28]) their single particle rapidity distribution was obtained in the form of grand partition function with temperature T and with chemical potential μ . To obtain effect of BEC the rapidity space was divided into a number of *cells* of size δy (which was fitted parameter) each. Two very important observations are made there: (i) - whereas the very fact of existence of cells in rapidity space was enough to obtain reasonably good multiparticle distributions, $P(n)$, (actually, in the NB-like form) and (ii) their size, δy , was crucial for obtaining the characteristic form of the 2-body BEC function $C_2(Q = |p_i - p_j|)$ (peaked and greater than unity at $Q = 0$ and then decreasing in a characteristic way towards $C_2 = 1$ for large values of Q)

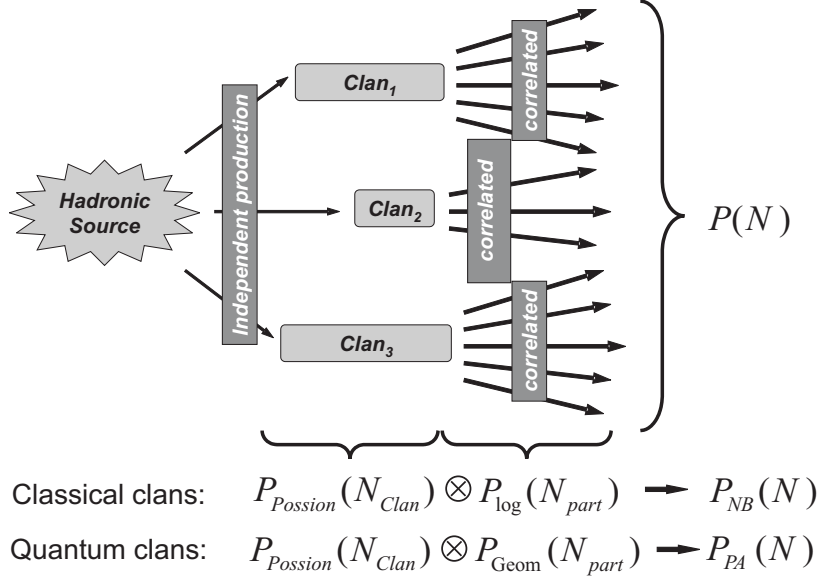


Figure 4. Schematic view of our algorithm, which leads to bunches of particles (*clans*). Whereas in [26] these clans could consist of any particles distributed logarithmically in our case they consist of particles of the same charge and (almost) the same energy and are distributed geometrically to comply with their bosonic character. We are therefore led to *Quantum Clan Model* [5].

out of which one usually deduces the spatio-temporal characteristics of the hadronization source [1] (see [7] for more details). The message delivered was obvious: to get correlation function [1]

$$C_2(Q = |p_1 - p_2|) = \frac{d\sigma(p_1, p_2)}{d\sigma(p_1) \cdot d\sigma(p_2)} \quad (1)$$

peaked and greater than unity at $Q = 0$ and then decreasing in a characteristic way towards $C_2 = 1$ for large values of Q , one must have particles located in cells in phase space which are of nonzero size. It means therefore that from C_2 one gets not the size of the hadronizing source, as it is frequently said, but only the size of the emitting cell, $R \sim 1/Q$ [30] (in [7] it is $R \sim 1/\delta y$).

It is worth to mention at this point that, as has been demonstrated in [31] in the quantum field theoretical formulation of BEC, the requirement to get nonzero width of $C_2(Q)$ function corresponds directly to the necessity of replacing delta functions of the type $\delta(Q)$ in some commutator relations by a well defined, peaked at $|Q| \rightarrow 0$ functions $f(Q)$ introducing in this way some dimensional scale to be obtained from the fits to data. This fact was known even before but without any phenomenological consequences [32].

Let us now proceed to our proposition of looking on the problem of BEC. As already mentioned, work [7] has been our inspiration but we would like

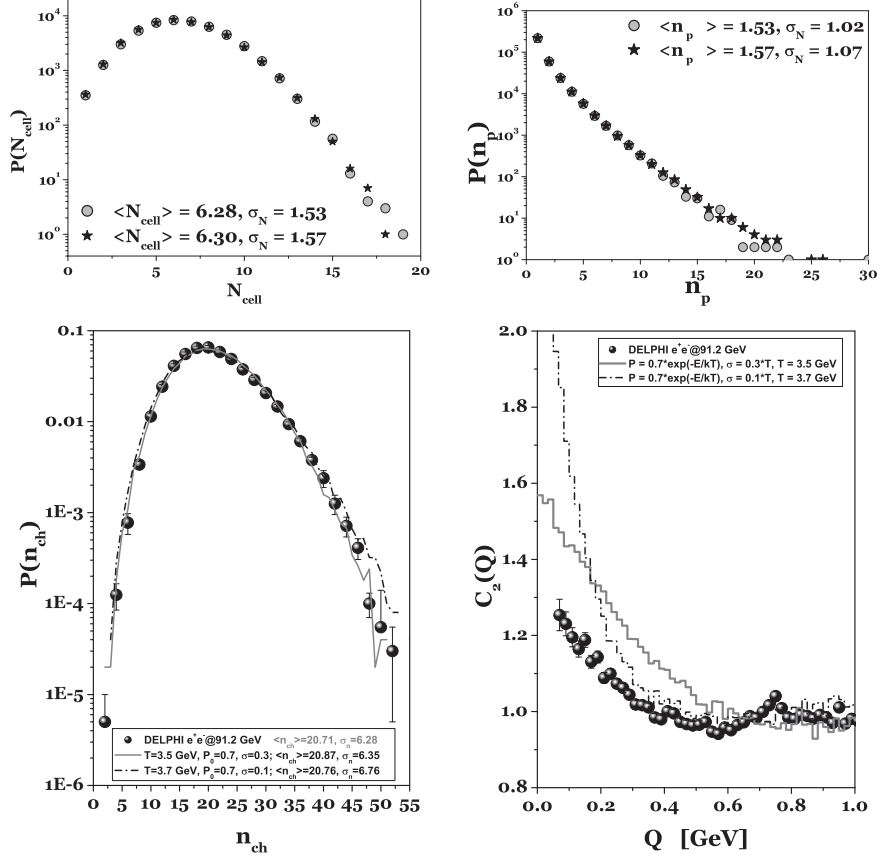


Figure 5. Upper panels: distribution of cells and particles in a given cell. Lower-left panel: the corresponding summary $P(n)$ which is convolution of both $P(n_{cell})$ and $P(n_p)$. Lower-right panel: examples of the corresponding corresponding correlation functions $C_2(Q)$. Two sets of parameters were used. Data are from [29].

to allow for dynamically defined EEC's and to assure energy-momentum conservation. This was only approximate in [7] and rapidity cells there were fixed in size and were consecutively filled with previously preselected number of particles. But already from our previously described afterburner we have learned that EEC's can be of different sizes (in fact, they even can overlap in phase-space) [16]. What counts most is the fact that distribution of particles in each EEC, $P(n_p)$, must follow geometrical distribution in order to get the characteristic energy spectra for bosonic particles,

$$\langle n(E) \rangle = [\exp(E - \mu) / T - 1]^{-1}. \quad (2)$$

To obtain such effect we proceed in the following way.

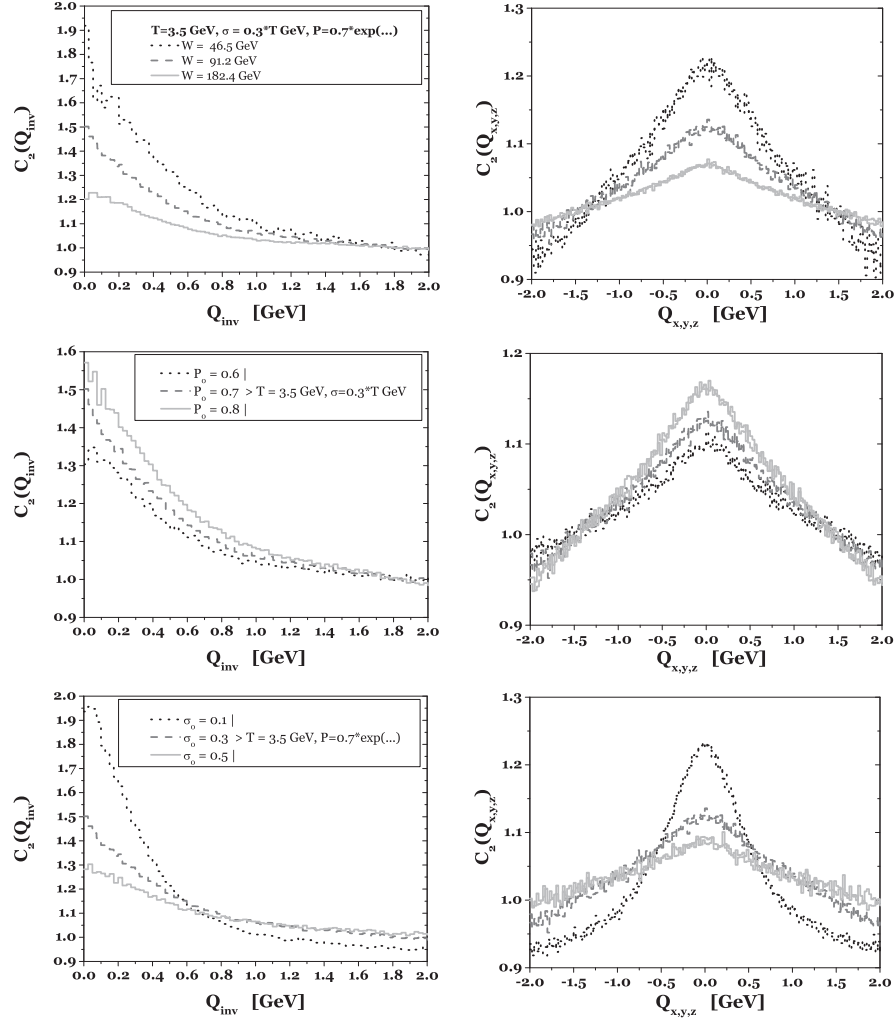


Figure 6. Example of results obtained for $C_2(Q_{inv})$ (left column) and corresponding $C_2(Q_{x,y,z})$ (right column, for parameters used here all $C_2(Q_{x,y,z})$ are the same). Calculations were performed assuming spherical source $\rho(r)$ of radius $R = 1$ fm (spontaneous decay was assumed, therefore there is no time dependence) and spherically symmetric distribution of $p_{x,y,z}$ components of momenta of secondaries p . Energies were selected from $f(E) \sim \exp(-E/T)$ distribution. The changes investigated are - from top to bottom: different energies of hadronizing sources, different values of parameter P_0 and different spreads σ of the energy in EEC.

- (1) Using some (assumed) function $f(E)$ we select a particle of energy $E_1^{(1)}$ and charge $Q^{(1)}$. The actual form of $f(E)$ should reflect our *a priori* knowledge of the particular collision process under consideration. In what follows we shall assume that $f(E) = \exp(-E/T)$, with T being parameter (playing in our example the role of “temperature”).
- (2) Treating this particle as seed of the first EEC we add to it, with probability $P(E) = P_0 \cdot \exp(-E/T)$, until the first failure, other particles of the same charge $Q^{(1)}$. Such procedure results in desired geometrical (or Bose-Einstein) distribution of particles in the cell, i.e., in

$$\langle n_p \rangle = P(E)/([1 + P(E)]), \quad (3)$$

accounting for their bosonic character. Together with exponential factor in probability $P(E)$, it assures that occupancy number of state with given energy will eventually follow characteristic bosonic form as given by eq. (2) (here P_0 is another parameter playing the role of “chemical potential” $\mu = T \cdot \ln P_0$). As result $C_2(Q) > 1$ but only *at one point*, namely for $Q = 0$.

- (3) Because process of emission of particles in a given EEC has finite duration, the resultant energies must be spread around the energy of the particle defining given EEC by some amount σ (which is another free parameter). It automatically leads to the experimentally observed widths of $C_2(Q)$.

Points (1)-(3) are repeated until all energy is used. Every event is then corrected for energy-momentum conservation caused by the selection procedure adopted and condition $N^{(+)} = N^{(-)}$ is imposed as well.

As result in each event we get a number of EEC with particles of the same charge and (almost) the same energy, i.e., picture closely resembling classical *clans* of [26] (with no effects of statistics imposed, see Fig. 4). Our clans (i.e., EECs containing identical bosonic particles subjected to quantum statistics and therefore named *quantum clans*) are distributed in the same way as the particles forming the seeds for EEC, i.e., according to Poisson distribution. With particles in each clan distributed according to geometrical distribution they lead therefore to the overall distribution being of the so called Pölya-Aeppli type [33]. This distribution strongly resembles the Negative Binomial distributions obtained in the classical clan model [26] where particles in each clans were assumed to follow *logarithmic* distribution instead (with differences occurring for small multiplicities [34]). The first preliminary results presented in Fig. 5 are quite encouraging (especially when one remembers that so far effects of resonances and all kind of final state interactions to which C_2 is sensitive were neglected here).

The main outcome so far is strong suggestion that EEC's are among the possible explanations of the BEC effect, in which case BEC provide us mainly with their characteristics, not with the characteristics of the whole hadronizing source. So far our method applies only to one-dimensional example of $C_2(Q)$. This is because process of formation of EEC's proposed here gives us energies of all particles in a given cell and therefore also $p_i = |\vec{p}_i|$, but says us nothing about their angular distributions (i.e., about their components $p_{ix, iy, iz}$). To extend it to three dimensional case of $C_2(Q_{x,y,z})$ one has to somehow build cells also in (p_x, p_y, p_z) components of the momenta of particles forming EEC. This can be done in many ways. Here we present as example approach using pairwise symmetrization of the wave functions of every $i > 1$ particle in a given EEC with the first particle ($i = 1$) defining it. As result one gets for each such pair (in the plane wave approximation [1] and assuming instantaneous hadronization) the known $1 + \cos [(\vec{p}_1 - \vec{p}_i) \cdot (\vec{r}_1 - \vec{r}_i)]$ term which connects the spatial extension of the hadronizing source $\rho(r)$ with its momentum space characteristics obtained before. In this way the assumed shape of $\rho(r)$ translates into the respective cells in momentum space. Preliminary results of this procedure are presented in Fig. 6.

4. Summary

We propose new numerical method of accounting for BEC phenomenon from the very beginning of the modelling process. Once the expected energy spectrum $f(E)$ of produced particles is chosen one constructs EEC's in energy. We regard this method as very promising but we are aware of the fact that our proposition is still far from being complete. To start with one should allow for time depending emission by including $\delta E \cdot \delta t$ term in the $\cos(\dots)$ above. The other is the problem of Coulomb and other final state interactions. Their inclusion is possible by using some distorted wave function instead of the plane waves used here. Finally, so far only two particle symmetrization effects have been accounted for: in a given EEC all particles are symmetrized with the particle number 1 being its seed, they are not symmetrized between themselves. To account for this one would have to add other terms in addition to the $\cos(\dots)$ used above - this, however, would result in dramatic increase of the calculational time.

We shall close with remark that there are also attempts in the literature to model numerically BE condensation effect [35, 36] (or to use notion of BE condensation in other branches of science as well [37, 38]) using ideas of bunching of some quantities in the respective phase spaces.

Acknowledgements

GW is grateful for the support and warm hospitality extended to him by organizers of the International Conference NEW TRENDS IN HIGH-ENERGY PHYSICS (experiment, phenomenology, theory), Yalta, Crimea, Ukraine, September 10-17, 2005, conference. Partial support of the Polish State Committee for Scientific Research (KBN) (grant 621/E-78/SPUB/CERN/P-03/DZ4/99 (GW)) is acknowledged.

References

- 1 R.M. Weiner, *Introduction to Bose-Einstein Correlations and Subatomic Interferometry*, J. Wiley, 1999.
- 2 T. Csörgő, in *Particle Production Spanning MeV and TeV Energies*, eds. W.Kittel et al., NATO Science Series C, Vol. 554, Kluwer Acad. Pub. (2000), p. 203
- 3 W. Kittel, *Acta Phys. Polon. B* **32**, 3927 (2001).
- 4 G. Alexander, *Rep. Prog. Phys.* **66** (2003) 481.
- 5 O.V. Utyuzh, G. Wilk, Z. Włodarczyk, *Quantum Clan Model description of Bose Einstein Correlations*, hep-ph/0503046, to be published in *Acta Phys. Hung. A - Heavy Ion Phys.* (2005).
- 6 K.J. Eskola, *Nucl. Phys. A* **698**, 78 (2002).
- 7 T. Osada, M. Maruyama and F. Takagi, *Phys. Rev. D* **59**, 014024 (1999).
- 8 W. Zajc, *Phys. Rev. D* **35**, 3396 (1987).
- 9 H. Merlitz and D. Pelte, *Z. Phys. A* **357**, 175 (1997).
- 10 K. Geiger, J. Ellis, U. Heinz and U.A. Wiedemann, *Phys. Rev. D* **61**, 054002 (2000).
- 11 L. Lönnblad and T. Sjöstrand, *Eur. Phys. J. C* **2**, 165 (1998).
- 12 K. Fiałkowski, R. Wit and J. Wosiek, *Phys. Rev. D* **58**, 094013 (1998).
- 13 B. Andersson, *Acta Phys. Polon. B* **29**, 1885 (1998).
- 14 O.V. Utyuzh, G. Wilk and Z. Włodarczyk, *Phys. Rev. D* **61**, 034007 (1999).
- 15 O.V. Utyuzh, G. Wilk and Z. Włodarczyk, *Phys. Lett. B* **522**, 273(2001).
- 16 O.V. Utyuzh, G. Wilk and Z. Włodarczyk, *Acta Phys. Polon. B* **33**, 2681 (2002).
- 17 J.W. Goodman, *Statistical Optics*, John Wiley & Sons, 1985.
- 18 B. Buschbeck and H.C. Eggers, *Nucl. Phys. B (Proc. Suppl.)* **92**, 235(2001).
- 19 E.E. Purcell, *Nature* **178**, 1449 (1956)
- 20 A. Giovannini and H.B. Nielsen, *Stimulated emission effect on multiplicity distribution in: Proc. of the IV Int. Symp. on Multip. Hadrodynamics*, Pavia 1973, Eds. F. Duimio, A. Giovannini and S. Rattii, p. 538.
- 21 W.J. Knox, *Phys. Rev. D* **10**, 65 (1974).
- 22 E.H. De Groot and H. Satz, *Nucl. Phys. B* **130**, 257 (1977).
- 23 J. Kripfganz, *Acta Phys. Polon. B* **8**, 945 (1977).

- 24 A.M. Cooper, O. Miyamura, A. Suzuki and K. Takahashi, *Phys. Lett. B* **87**, 393 (1979).
- 25 F. Takagi, *Prog. Theor. Phys. Suppl.* **120**, 201 (1995).
- 26 A. Giovannini and L. Van Hove, *Z. Phys. C* **30**, 391 (1986).
- 27 M. Biyajima, N. Suzuki, G. Wilk and Z. Włodarczyk, *Phys. Lett. B* **386**, 297 (1996).
- 28 F.S. Navarra, O.V. Utyuzh, G. Wilk and Z. Włodarczyk, *Phys. Rev. D* **67**, 114002 (2003).
- 29 P. Abreu et al. (DELPHI Collab.), *Phys. Lett. B* **286**, 201(1992).
- 30 W.A. Zajc, *A pedestrian's guide to interferometry*, in "Particle Production in Highly Excited Matter", eds. H.H.Gutbrod and J.Rafelski, Plenum Press, New York 1993, p. 435.
- 31 G.A. Kozlov, O.V. Utyuzh and G. Wilk, *Phys. Rev. C* **68**, 024901 (2003).
- 32 K. Zalewski, *Lecture Notes in Physics* **539**, 291 (2000).
- 33 J. Finkelstein, *Phys. Rev. D* **37**, 2446 (1988).
- 34 Ding-wei Huang, *Phys. Rev. D* **58**, 017501 (1998).
- 35 R. Kutner and M. Regulski, *Comp. Phys. Com.* **121-122**, 586 (1999).
- 36 R. Kutner, K.W. Kehr, W. Renz and R. Przeniosło, *J.Phys. A* **28**, 923 (1995).
- 37 A.E. Ezhov and A.Yu. Khrennikov, *Phys. Rev. E* **71**, 016138 (2005).
- 38 K. Stalinas, *Bose-Einstein condensation in classical systems* cond-mat/0001347.

DISSOCIATION OF RELATIVISTIC NUCLEI IN PERIPHERAL INTERACTIONS IN NUCLEAR TRACK EMULSION *

P. I. Zarubin^a, D. A. Artemenkov^a, G. I. Orlova^b
on behalf of the BECQUEREL Collaboration

^a *Joint Institute for Nuclear Research, Dubna, Russia*

^b *Lebedev Institute of Physics, Moscow, Russia*

Abstract. Possibilities of the nuclear emulsion technique for the study of the systems of several relativistic fragments produced in the peripheral interactions of relativistic nuclei are discussed. The interactions of the ^{10}B and ^9Be nuclei in emulsion are taken as an example to show the manifestation of the cluster degrees of freedom in relativistic fragmentation. For the case of the relativistic ^9Be nucleus dissociation it is shown that exact angular measurements play a crucial role in the restoration of the excitation spectrum of the alpha particle fragments. The energy calibration of the angular measurements by the ^9Be nucleus enables one to conclude reliably about the features of internal velocity distributions in more complicated systems of relativistic α particles.

Key words: nucleus, relativistic, peripheral, fragmentation, emulsion, clustering

1. Introduction

The peripheral collisions of nuclei proceeding at energy above 1 A GeV are collisions of a special type in which the breakup of the primary nuclei is provoked by electromagnetic and diffraction interactions, as well as by nucleon collisions for a minimal overlap of nuclear densities. Nuclear track emulsions exposed to beams of relativistic nuclei make it possible to obtain information about the charged products of such collisions which is unique as concerns details of observation of particle tracks and the accuracy of their spatial metrology (E.M. Friedlander et al., 1983; G. Baroni et al., 1990; G. Baroni et al., 1992).

* The work was supported by the Russian Foundation for Basic Research (Grants nos. 96-1596423, 02-02-164-12a, 03-02-16134, 03-02-17079, 04-02-16593, 04-02-17151), the Agency for Science of the Ministry for Education of the Slovak Republic and the Slovak Academy of Sciences (Grants VEGA 1/9036/02 and 1/2007/05) and Grants from the JINR Plenipotentiaries of Bulgaria, Czech Republic, Slovak Republic, and Romania during years 2002-5.

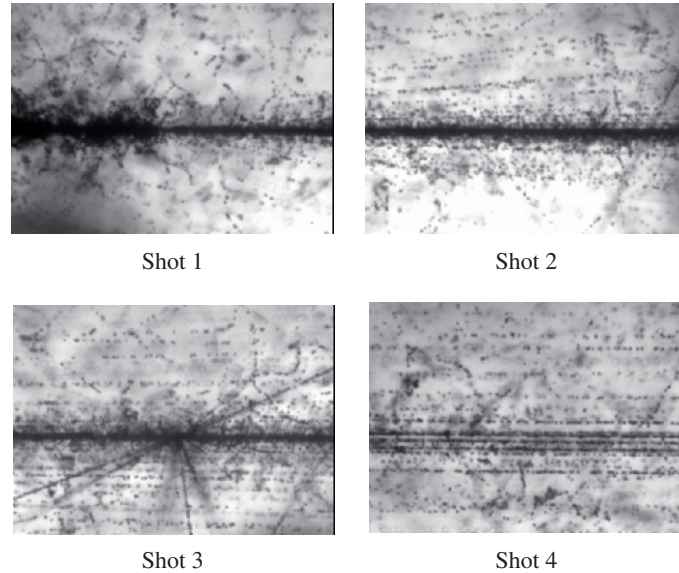


Figure 1. Subsequently photoed event of peripheral interaction of a 158 A GeV ^{207}Pb nucleus in a nuclear track emulsion in $\approx 100 \times 100 \mu\text{m}^2$ viewing fields: primary nucleus track and interaction vertex followed by projectile fragment jet (Shot 1); jet core with apparent tracks of singly and doubly charged particles (Shot 2); jet core with a secondary interaction star (Shot 3); completely recognizable jet core (Shot 4, 3 cm distance from the vertex).

2. Relativistic fragmentation

In peripheral interactions, nuclei are given an excitation spectrum near the energy dissociation thresholds. In the kinematical region of fragmentation of a relativistic nucleus, there arise systems consisting of nuclear fragments whose total charge is close to the parent nucleus charge. The opening angle of the relativistic fragmentation cone is defined by the Fermi nucleon motion. Thus, the fragments find themselves on the periphery of the particle rapidity distribution which is obtained by summing over all the channels of the reaction in question.

The values of the fragment momenta normalized to the mass numbers are distributed about the normalized momentum of the primary nucleus with a few-percent dispersion. Therefore the distribution of the velocities of fragments in their c.m.s. must be a non-relativistic one. In accordance with the established pattern of the nuclear limiting fragmentation the probabilities of population of the fragment final states reveal a very high degree of universality. They are found to be weakly dependent on the initial energy and target-nucleus properties.

The interactions of the above-mentioned type can serve as a “laboratory” for the generation of non-relativistic ensembles of several lighter

nuclei. The term “peripheral” does not reflect in full measure dramatic changes which occur at the microscopic level. The dissociation degree of a nucleus can reach its total destruction into separate nucleons and lightest nuclei having no excited states, that is, ${}^2,{}^3\text{H}$ and ${}^3,{}^4\text{He}$ nuclei. A relative intensity of their production permits one to reveal the importance of different cluster degrees of freedom.

For the experimental study of multi-particle systems, the choice of those of them which result from the dissociation of a relativistic projectile and not from the dissociation of the target-nucleus has special methodical advantages. Owing to the kinematical collimation and absence of the detection threshold, relativistic fragments can completely be observed in a small solid angle and the distortions due to energy ionization losses in the detector material are minimal.

When selecting events with the dissociation of a projectile into the fragmentation cone, the non-relativistic fragments are either absent (“white” stars), or their number is insignificantly small. These fragments are emitted over all the solid angle, therefore, their fraction in the relativistic fragmentation angular cone is negligible. The target-fragments have non-relativistic momenta which allow one to distinguish them from the projectile fragments in this cone.

Of course, in the relativistic approach to the fragmentation study, there also arise its own methodical troubles. For a primary nucleus with charge Z , it is very desirable to provide the detection up to singly-charged particles. The ionization produced by all fragments can be reduced down to a factor Z , while the ionization per one track - to a factor Z^2 as compared with that from the primary nucleus. Therefore the experimental method should provide the widest detection range taking the Z^2 value into account.

3. Capabilities of nuclear track emulsion

The full kinematical information about the secondary particles in the relativistic fragmentation cone is needed to reconstruct an invariant mass of a fragment system. The accuracy of invariant mass estimation drastically depends on the accuracy of the track angular resolution. Hence, to provide the best angular resolution the detection of fragments with the best spatial resolution is needed.

At the initial stage of investigations, the nuclear emulsion method well satisfies these requirements. The major task of it is to search for reliable proofs of the existence of different fragmentation channels for a statistical provision at the level of dozens of events. Emulsions provide a record spatial resolution (about $0.5\ \mu\text{m}$) which makes it possible to separate the charged particle tracks in the three-dimensional image of an event within one layer

thickness ($600\ \mu\text{m}$), as well as ensure a high accuracy of measurement of the angles. The emulsion technique allows one to measure the particle charges, starting with the single-charged particles up to the highest-charged ones, by combining the ionization means (counting the number of breaks and the number of δ electrons per track length unit). The tracks of relativistic H and He nuclei are distinguished by vision. In the peripheral fragmentation of a light nucleus its charge can often be established by the charge topology of the relativistic fragments. A collection of appropriate reaction images can be found in (V. Bradnova et al., 2004) and in the BECQUEREL project web site (BECQUEREL, 2005). Multiple scattering measurements on the light fragment tracks enable one to separate the $^2,^3\text{H}$ and $^3,^4\text{He}$ isotopes.

A vivid illustration of these assertions is the microphotograph of the event of a total disintegration of Pb nucleus of energy 158 A GeV in its peripheral interaction with an emulsion nucleus (see Fig. 1). The exposure was performed in beams from the SPS accelerator (CERN) in the framework of the EMU collaboration. Experiment details can be found in (EMU01 Collaboration, 1997; M.I. Adamovich et al., 1999). Shot 1 shows the primary nucleus track which is surrounded by a dense cloud of δ electrons. On Shot 1 the interaction vertex looks like a stepped lowering of the ionization density in which there are no tracks from the target-nucleus fragmentation. Shots 2-4 show a gradual separation of the tracks of singly and doubly charged particles from the shower trunk. At a given energy the He nucleus emission angles are restricted to a 0.1° value. A total separation of tracks is seen on Shot 4 corresponding to a distance of about 3 cm from the vertex. The observer does not see in this event an intense flux of dozens of relativistic neutrons that have not to be able to bind the lightest nuclei. The image of an event in emulsion is created by microscopic crystals about $1\ \mu\text{m}$ in thick, i.e. the latter are larger than the real sizes of nuclear fragments by about 9 orders of magnitude. Nevertheless this image reproduces rather well details of a “catastrophe” occurred at the micro-world scale.

The events of a total disintegration make up a small fraction of all the variety of the final states of heavy nuclei which embraces pairing fission, formation of single fragments accompanied by a great number of the lightest nuclei, formation of groups of light nuclei (E.M. Friedlander et al., 1983; P.L. Jain et al., 1984; EMU-01/012 Collaboration, 1997; M.I. Adamovich et al., 1998; M.L. Cherry et al., 1998). The excitation transferred to the nucleus is, to a large extent, defined by the energy threshold of the final-state mass. It grows with increasing fragment multiplicity. In this sense, the charge topology of the final state already defines the excitation. In a complicated process of the energy distribution over the multiplicity of the degrees of freedom, nuclear fragments go onto the mass surface and get some possibility to realize the Coulomb energy of mutual repulsion into the kinetic energy of each fragment. Some kind of a Coulomb “explosion” of a nucleus occurs.

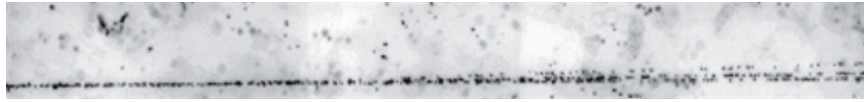
The example of a total disintegration of a Pb nucleus may be interpreted as an event of the phase transition of nuclear matter from the state of quantum liquid to the state of quantum dilute gas of nucleons and the lightest nuclei. The metrology of such events is laborious and requires a high level of skill. Nevertheless such events are of an undoubted scientific interest, therefore their accumulation continues by the BECQUEREL collaboration (BECQUEREL, 2005). The light nucleus fragmentation can be considered as a component of the heavy nucleus fragmentation picture. In what follows, some examples are given to consider the role of the cluster degrees of freedom in the light nucleus fragmentation, as well as the energy scale of inter-cluster interactions.

4. Clustering in light nuclei

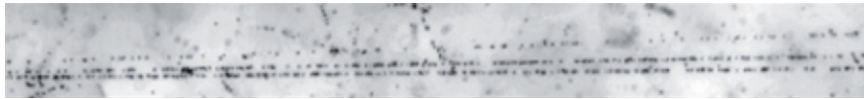
The charge topology of the relativistic fragmentation of N, O, Ne, Mg and Si nuclei in peripheral interactions in emulsion is presented in (A. El-Naghy et al., 1988; G. Baroni et al., 1990; G. Baroni et al., 1992; M.A. Jilany, 2004; N.P. Andreeva et al., 2005). A special feature of the excitation increase in this group of nuclei consists in the growth of the multiplicity of the He and H nuclei with decreasing charge of the only fragment with $Z > 3$. In light nuclei the pairing splitting channel is practically suppressed.

More specific correlation studies were performed for the leading fragmentation channels like $^{12}\text{C} \rightarrow 3\alpha$ (V.V. Belaga et al., 1995), $^{16}\text{O} \rightarrow 4\alpha$ (N.P. Andreeva et al., 1996; V.V. Glagolev et al., 2001), $^6\text{Li} \rightarrow d\alpha$ (F.G. Lepekhnin et al., 1998; M.I. Adamovich et al., 1999), $^7\text{Li} \rightarrow t\alpha$ (M.I. Adamovich et al., 2004), $^{10}\text{B} \rightarrow d\alpha\alpha$ (M.I. Adamovich et al., 2004), and $^7\text{Be} \rightarrow ^3\text{He}\alpha$ (V. Bradnova et al., 2004). In addition to the α clustering, a clustering of nucleons in the form of deuterons in ^6Li and ^{10}B decays, as well as of tritons in ^7Li decays has been revealed. Besides, the multiparticle dissociation is found to be important for these nuclei. Emulsions exposed to relativistic ^{14}N and ^{11}B isotopes are being analyzed with the aim to study clustering of these types. A ^3He clustering in ^7Be relativistic excitation is demonstrated (V. Bradnova et al., 2004; N.P. Andreeva et al., 2005). The next round of research, as to whether this kind of nuclear clustering is revealed in light neutron-deficient nuclei like ^8B and $^{9,10,11}\text{C}$ is in progress now at the JINR Nuclotron (A.I. Malakhov, 2004).

The decay of the excited states in the Be, B and C isotopes is of a clearly expressed α cluster character. In overcoming the mass threshold of a reaction their dissociation proceeds through the formation of an unstable ^8Be nucleus in the ground and excited states. Among the reaction channels, 3-particle decays into He and H nuclei are dominant. Fragments with $Z > 3$ do not play a crucial role.



Shot 1



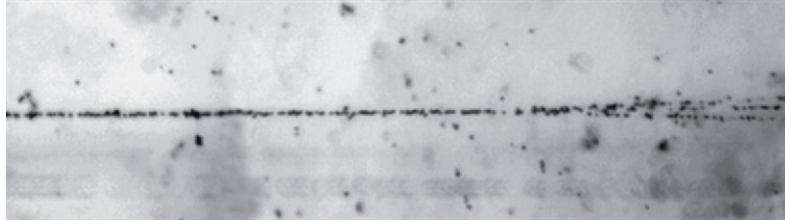
Shot 2

Figure 2. Subsequently reconstructed photo of dissociation of a 1 A GeV ^{10}B nucleus into 1 doubly and 2 singly charged fragments without production of target nucleus fragments and mesons (“white”star): interaction vertex (Shot 1); apparent tracks of 1 H and 2 He nuclei (from top to bottom, Shot 2).

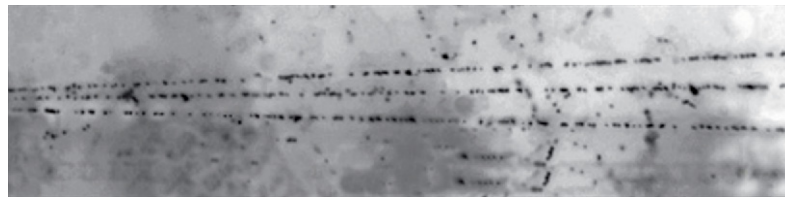
As an important application, this conclusion can affect the problems of cosmic-ray physics related to the element abundance in the region of a Li-Be “gap”. The fundamental problem of Li-Be-B abundance in galactical cosmic rays as compared with their abundance in the matter of the Solar system has not been solved yet. This pattern points out that the main chain of subsequent splitting of nuclei, when they are propagate in interstellar H and He gases, passes over the production of the Li, Be and B nuclei. This fact greatly stimulates the interest in the search for the sources of origin of the mentioned group of nuclei, especially the $^{6,7}\text{Li}$ isotopes.

The dissociation of the ^{10}B nucleus at an energy of 1 A GeV, studied in (M.I. Adamovich et al., 2004), may be an example which shows the dominance of the decay cluster channels. The microphotograph (see Fig. 2) gives an event corresponding to the decay $^{10}\text{B} \rightarrow 2^4\text{He} + \text{H}$. The fraction of these events is about 80% of the total number of the events of the peripheral type. By measuring the multiple particle scattering, it is established that the deuterons participate in 40% of the decay of such a type, in just the same way as in the ^6Li nucleus with a pronounced α -d structure. The decay $^{10}\text{B} \rightarrow ^6\text{Li} + ^4\text{He}$ amounts to 15% for a lower 4.5 MeV threshold. The decay $^{10}\text{B} \rightarrow ^9\text{Be} + \text{p}$ is only 3% for a 6 MeV threshold. Thus, for a giving type of the interaction of the ^{10}B nucleus one has revealed the role of the 3-particle excitations as well as the role of the deuteron as a cluster element of the structure of this nucleus.

The next microphotograph (see Fig. 3) shows the event of a three-particle decay of the ^{10}B nucleus in the charge-exchange reaction without the production of a charged meson. Its charge topology may unambiguously be interpreted as $^{10}\text{B} \rightarrow 2^3\text{He} + ^4\text{He}$. Because of a deep rearrangement of nucleons which results in the formation of a ^3He cluster, an essentially higher (18 MeV) threshold should have been overcome in this event. Thus, there proceeds the population of a strongly excited state in a mirror ^{10}C nucleus. This event



Shot 1



Shot 2

Figure 3. Subsequently reconstructed photo of dissociation of a 1 A GeV ^{10}B nucleus into 3 doubly charged fragments without production of target nucleus fragments and mesons (“white”star): interaction vertex (Shot 1); apparent tracks of 3 He nuclei (Shot 2).

points to the fact that in stellar media consisting of the $^{3,4}\text{He}$ mixture there can occur an inverse process which is similar to the 3α process $3^4\text{He} \rightarrow ^{12}\text{C}$. The fusion process $2^3\text{He} + ^4\text{He} \rightarrow ^{10}\text{C}$ results in a larger energy yield which is followed in the world of stable nuclei by the production of the ^{10}B nucleus as a final product.

This example illustrates the suggestion that the proof of the existence of the nuclear-physical process may become the basis for developing the ideas about the nucleosynthesis. However, in order to relate the relativistic fragmentation to thermonuclear synthesis it is necessary to establish an internal scale of kinetic energies in the c.m.s. of relativistic fragments.

5. The energy and velocity scales in $N\alpha$ -particle systems

The study of the ^9Be nucleus dissociation into two α particles allows one to restore their resonance states without a combinatorial background. Owing to a low-energy threshold (1.7 MeV) this process dominates the channel $^3\text{He} + ^4\text{He} + 2n$ (22 MeV threshold) which is similar to the latter by the image of the tracks. The separation of a neutron from the ^9Be nucleus can lead to the production of an unstable ^8Be nucleus with a decay through the ground state 0^+ (the decay energy is 92 keV, the width is 5.6 eV), as well as through the 1st 2^+ (3 MeV, 1.5 MeV width) and the 2nd 4^+ (11.4 MeV, 3.5 MeV width) excited states. On the basis of a reliable observation of these states in the excitation spectrum Q , i.e. of the invariant mass of a pair of relativistic

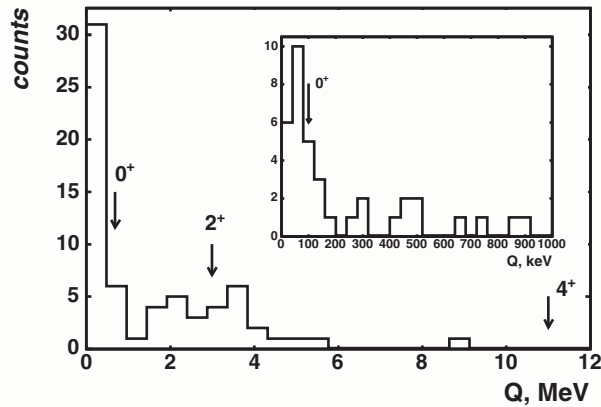


Figure 4. Distribution of α particle pairs vs Q for the fragmentation mode ${}^9\text{Be} \rightarrow 2\alpha$. Insertion: the distribution zoomed between 0-1000 keV.

α particles minus their masses, it is possible to verify the validity of the excitation estimate using only the angular measurements.

Emulsions are exposed to the secondary beam of ${}^9\text{Be}$ nuclei of energy 1.2 GeV which is formed on the basis of the fragmentation of the ${}^{10}\text{B}$ nuclei. At present, a total of 160 stars with a pair of relativistic He nuclei have been found in the exposed material. The directions of their tracks are within the forward cone with about a 3° opening angle. The emission angles have already been measured for 70 events which allow one to present the spectrum Q of their excitation energies (see Fig. 4).

The peaks correspond to the ${}^8\text{Be}$ decay from the 0^+ and 2^+ . The scale of the spectrum part 0–1 MeV, given on the insertion of Fig. 4, is increased by a factor of 10. On it one can see a good coincidence of the distribution center with the decay energy of the ${}^8\text{Be}$ ground state. The width of the peak makes it possible to define also the resolution of the method in this region of the spectrum. It is about 30 keV. On the right border of the distribution there are no events which would correspond to the second excited state 4^+ at 11.35 MeV energy. This spectrum area needs some additional statistics. Thus, in the system of two relativistic α particles there are reflections of two known resonances.

These excitations can be compared with those of more complicated $N\alpha$ particle systems. The comparison will be made for the events of the type of “white” stars, that is, the events which contain neither target-nucleus fragments, no produced mesons. In such events, there proceeds a more “delicate” excitation of the fragmenting nucleus. The excitation of the system is defined by the mean values of the transverse momenta of α particles. The α particle transverse momenta are calculated in the laboratory system by the formula

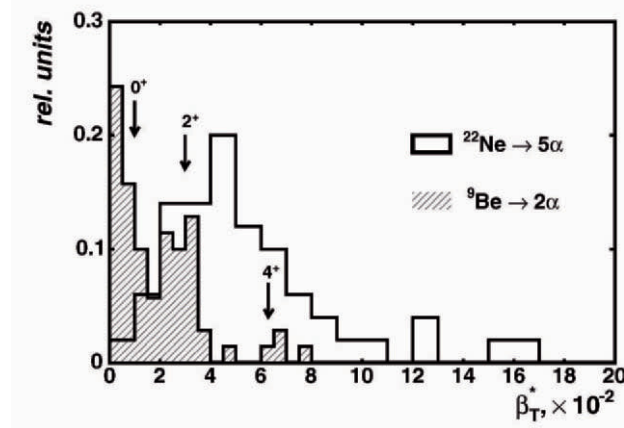


Figure 5. Distribution over the transverse velocities β_T in the c.m.s. for the α particles produced in ${}^9\text{Be} \rightarrow 2\alpha$ and ${}^{22}\text{Ne} \rightarrow 5\alpha$ processes.

$P_T = 4P_0 \sin\theta$, where P_0 is the momentum per nucleon of a primary nucleus, θ the polar angle. As suggested in (V.V. Belaga et al., 1995), the transition to the transverse momentum vectors in the c.m.s. is possible for small angles of scattering of the primary nucleus and is described by the following equation

$$\mathbf{P}_{Ti}^* \cong \mathbf{P}_{Ti} - \frac{\sum_{i=1}^n \mathbf{P}_{Ti}}{N_\alpha} \quad (1)$$

where, \mathbf{P}_T is the residual vector of the α particle momenta.

The mean values obtained for the alpha particle transverse momenta are as follows for ${}^9\text{Be} \rightarrow 2\alpha$ $\langle P_T^* \rangle = 103 \pm 2$ MeV/c (the present paper), for ${}^{16}\text{O} \rightarrow 4\alpha$ $\langle P_T^* \rangle = 121 \pm 2$ MeV/c ${}^{16}\text{O} \rightarrow 4\alpha$ (N.P. Andreeva et al., 1996), and for ${}^{22}\text{Ne} \rightarrow 5\alpha$ $\langle P_T^* \rangle = 200 \pm 2$ MeV/c (processing of the available data presented in (A. El-Naghy et al., 1988)). These values clearly demonstrate the tendency to an increase of the average momentum of the α particles with increasing their multiplicity and consequently an increase of the total Coulomb interaction of α clusters.

Figure 5 shows the distribution over the transverse velocities β_T in the c.m.s. for the α particles produced in ${}^9\text{Be} \rightarrow 2\alpha$ and ${}^{22}\text{Ne} \rightarrow 5\alpha$ processes. It can be concluded that the distribution over the velocities β_T , in spite of a broadening, is situated in a non-relativistic domain. In the ${}^9\text{Be}$ case, the distribution has peaks which are due to the decay of the 0^+ and 2^+ states. The distribution for the ${}^{22}\text{Ne}$ nucleus is essentially broader, its mean value reflects the growth of the α particle transverse momenta, and the possible contribution from the decay of the ${}^8\text{Be}$ 0^+ state is not significant. Thus, the energy calibration of the angular measurements by the ${}^9\text{Be}$ nucleus enables one to conclude

reliably about the features of internal velocity distributions in more complicated systems of relativistic α particles.

A nuclear state analogous to the dilute Bose gas can be revealed as the formation of $N\alpha$ particle ensembles possessing quantum coherence near the production threshold. Being originated from relativistic nuclei it can appear in a form of narrow $n\alpha$ particle jets in the forward cone. The predicted property of these systems is a narrow velocity distribution in the c. m. s. (P. Schuck et al., 2003). The detection of such “ultracold” $N\alpha$ states is a serious argument in favor of the reality of the phase transition of α clusterized nuclei to the dilute Bose gas of α particles. It gives a special motivation to explore lighter $N\alpha$ systems produced as potential “building blocks” of the dilute α particle Bose gas.

The behaviour of relativistic systems consisting of several H and He nuclei will be described in terms of invariant variables of a 4-velocity space as suggested in (A.M. Baldin and L.A. Didenko, 1990). The relativistic projectile fragmentation results in the production of a fragment jet which can be defined by invariant variables characterizing relative motion

$$b_{ik} = -\left(\frac{P_i}{m_i} - \frac{P_k}{m_k}\right)^2 ,$$

with $P_{i(k)}$ and $m_{i(k)}$ being the 4-momenta and the masses of the i or k fragments. Following (A.M. Baldin and L.A. Didenko, 1990), one can suggest that a jet is composed of the nuclear fragments having relative motion within the non-relativistic range $10^{-4} < b_{ik} < 10^{-2}$. The lower limit corresponds to the ground state decay ${}^8\text{Be} \rightarrow 2\alpha$, while the upper one - to the boundary of low-energy nuclear interactions. The expression of the data via the relativistic invariant variable b_{ik} makes it possible to compare the target and projectile fragmentation in a common form.

6. Conclusions

The degree of the dissociation of the relativistic nuclei in peripheral interactions can reach a total destruction into nucleons and singly and doubly charged fragments. In spite of the relativistic velocity of motion of the system of fragments as a whole, the relative motion of fragments is non-relativistic one. The invariant presentation makes it possible to extract qualitatively new information about few-cluster systems from fragmentation of relativistic nuclei in peripheral interactions. The emulsion technique allows one to observe these systems to the smallest details and gives the possibility of studying them experimentally

Investigations of the relativistic fragmentation of the nuclei ranging from Be to C can serve as some kind of “bricks” in the construction of a complete

picture of the phase transition of heavy nuclei to the lightest clusters. In solving such problems, the nuclear energy of the order of several GeV per nucleon is optimal as far as at these energies the relativistic fragmentation cone has the optimal value which can be measured by microscopes.

In the charge topology of the light nucleus fragments, the cluster character of their excitations is clearly manifested. The cluster degrees of freedom in nuclei are deeply associated with the process of their synthesis. The given event of the breakup with simultaneous charge-exchange of the ^{10}B nucleus into 3 He nuclei points to a possible population of the excited states of the ^{10}C nucleus with a deep rearrangement of the cluster structure of this nucleus. Observation of this process can point to the occurrence of an inverse fusion process $2^3\text{He}+^4\text{He}$ in stellar media.

For the particular case of the relativistic ^9Be nucleus dissociation it is shown that precise angular measurements play a crucial role in the restoration of the excitation spectrum of the alpha particle fragments. This nucleus is dissociated practically totally through the 0^+ and 2^+ states of the ^8Be nucleus.

A detailed study of the nuclear fragment ensembles makes it possible to go on to the search for complicated quasi-stationary states of fragments. In the nuclear scale of distances and excitations they can possess properties which make them analogous to dilute quantum gases in atomic physics at ultra-cold temperatures. The proof of the existence of such systems can find some important applications for the problems of nuclear astrophysics. In this respect, the fragment jets are a microscopic model of stellar media.

Acknowledgements

In conclusion, we would like to remember the names of our leaders in the domain of investigations with relativistic nuclei. Unfortunately, they are no more among the living. The foundations of the research along these lines had been laid by Academician A.M. Baldin. For many years, M.I. Adamovich, V.I. Ostroumov, Z.I. Solovieva, K.D. Tolstov, M.I. Tretiakova, and G.M. Chernov had been leaders of the investigations carried out by nuclear emulsion technique at the JINR synchrophasotron. We hope that this sketch will be a contribution to a thankful memory of the senior generation scientists in Russia.

References

- E.M. Friedlander et al. (1983) Nuclear collisions of uranium nuclei up to about 1 GeV/nucleon, *Physical Review* **C27**, 2436–2438.
- G. Baroni et al. (1990) Electromagnetic dissociation of 200 GeV/nucleon ^{16}O and ^{32}S in emulsion, *Nuclear Physics* **A516**, 673–714.

- G. Baroni et al. (1992) The electromagnetic and hadronic diffractive dissociation of ^{16}O ions, *Nuclear Physics* **A540**, 646–658.
- V. Bradnova et al. (2004) Studies of light nucleus clustering in relativistic multifragmentation processes, *Acta Phys. Slovaca* **54**, 351–365.
- Web site of the BECQUEREL Project: <http://becquerel.jinr.ru>.
- P.L. Jain et al. (1984) Fission of Uranium Nuclei in Flight at Relativistic Energies, *Physical Review Letters* **52**, 1763–1766.
- M.I. Adamovich et al. (1997) He production in 158 A GeV/c Pb on Pb interactions, *Physics Letters* **B 390**, 445–449.
- M.I. Adamovich et al. (1999) Angular distributions of light projectile fragments in deep inelastic Pb+Em interactions at 160 A GeV, *The European Physical Journal* **A 6**, 421–427.
- M.I. Adamovich et al. (1997) Multifragmentation of Gold nuclei in the interactions with photoemulsion at 10.7 GeV/nucleon, *Zeitschrift für Physik* **A 359**, 277–290.
- M.I. Adamovich et al. (1997) Critical behavior in Au fragmentation at 10.7A GeV, *The European Physical Journal* **A 1**, 77–83.
- M.L. Cherry et al. (1998) Fragmentation and particle production in interactions of 10.6 GeV/N gold nuclei with hydrogen, light and heavy targets, *The European Physical Journal* **C 5**, 641–645.
- A. El-Naghy et al. (1988) Fragmentation of ^{22}Ne in emulsion at 4.1 A GeV/c, *Journal of Physics* **G14**, 1125–1137.
- M.A. Jilany(2004) Nuclear fragmentation in interactions of 3.7A GeV ^{24}Mg projectiles with emulsion targets, *Physical Review* **C70**, 014901-01–014901-13.
- N.P. Andreeva et al. (2005) Topology of "white stars" in relativistic fragmentation of light nuclei, *Physics of Atomic Nuclei* **68**, 455–465.
- V.V. Belaga et al. (1995) Coherent dissociation $^{12}\text{C} \rightarrow 3\alpha$ in lead-enriched emulsion at 4.5 GeV/c per nucleon, *Physics of Atomic Nuclei* **58**, 1905–1910.
- N.P. Andreeva et al. (1996) Coherent dissociation $^{16}\text{O} \rightarrow 4\alpha$ in photoemulsion at an incident moment of 4.5 GeV/c per nucleon, *Physics of Atomic Nuclei* **58**, 1905–1910.
- V.V. Glagolev et al. (2001) Fragmentation of relativistic oxygen nuclei in interactions with a proton, *The European Physical Journal* **A11**, 285–296.
- F.G. Lepekhin et al. (1998) Yields and transverse momenta of the ^6Li fragments in the emulsion at 4.5 GeV/c per nucleon, *The European Physical Journal* **A1**, 137–141.
- M.I. Adamovich et al. (1999) Interactions of ^6Li with photoemulsion nuclei, *Physics of Atomic Nuclei* **62**, 1378–1387.
- M.I. Adamovich et al. (2004) Dissociation of relativistic ^7Li in emulsion and structure of ^7Li nucleus, *Journal of Physics* **G30**, 1479–1485.
- M.I. Adamovich et al. (2004) Investigations of clustering in light nuclei by means of relativistic-multifragmentation processes, *Physics of Atomic Nuclei* **62**, 514–517.
- V. Bradnova et al. (2004) Nuclear clustering in processes of relativistic multifragmentation, *Nuclear Physics* **A734**, E92–E95.
- A.I. Malakhov (2004) Research program for the Nuclotron, *Nuclear Physics* **A734**, 82–90.
- P. Schuck et al. (2003) Alpha-particle condensation in nuclei, *Comptes Rendus Physique* **4**, 537–540.
- A.M. Baldin and L.A. Didenko (1990) Asymptotic properties of hadron matter in relative four velocity space, *Fortschritte der Physik* **38**, 261–332.

COSMIC EVOLUTION AS “SUPERFLUID” MOTION IN GR

V.N. Pervushin

Bogoliubov Laboratory of Theoretical Physics, JINR, 141980 Dubna

A.F. Zakharov

*National Astronomical Observatories of Chinese Academy of Sciences, 20A
Datun Road, Chaoyang District, Beijing, 100012, China*

*Astro Space Center of Lebedev Physics Institute of RAS, Moscow
Institute of Theoretical and Experimental Physics, 25, 117259, Moscow*

V.A. Zinchuk

Bogoliubov Laboratory of Theoretical Physics, JINR, 141980 Dubna

Abstract. A set of arguments in favor of the concept of “superfluidity” of the cosmic evolution is discussed in the context of the topical problems of modern cosmology.

1. Landau’s superfluidity versus Lifshitz’s friction in GR

The cosmic evolution was given in the hands of Friedmann as the result of the homogeneous approximation of the interval in the Einstein general relativity (GR)

$$ds^2 = g_{\mu\nu} dx^\mu dx^\nu \rightarrow a^2(x^0)[(N_0 dx^0)^2 - (dx^i)^2] = dt^2 - a^2(dx^i)^2.$$

This approximation keeps in Einstein’s equations only dynamics of the cosmological scale factor a in form of the energy constraint $\varphi'^2 = \rho_0$, where $\varphi(\eta) = aM_{\text{Planck}} \sqrt{3/8\pi}$ is the running Planck mass, and $\eta_{(\pm)} = \int N_0 dx^0 = \pm \int d\varphi / \sqrt{\rho_0}$ is the conformal time of photons flying in the conformal flat space-time. This dependence of the conformal time on the scale factor is the main tool of analysis of observational data on the Supernova luminosity-distance – redshift relation (Behnke et al., 2002).

In GR, the cosmic evolution is extracted by a scale transformation $g_{\mu\nu} = a^2 \tilde{g}_{\mu\nu}$ well known as the cosmological perturbation theory (Mukhanov, Feldman and Brandenberger, 1992). This theory describes the “primordial power spectrum” of the Cosmic Microwave Background radiation (CMBR) without any constraint on the rest metrics $\tilde{g}_{\mu\nu}$ that contains one more homogeneous variable. In this case, the GR action contains the “velocity-velocity” interaction known as a “friction”.

As it was shown in (Barbashov et al., 2005; Pervushin and Zinchuk, 2005; Zakharov et al., 2006) that the conservation of the number of variables of GR by the identification of the scale factor $a(\eta)$ with averaging spatial metric determinant removes the “velocity-velocity” interaction from the GR action. Recall that the absence of the “friction” was defined by Landau (Landau, 1941) as a superfluid motion. When the rest metrics $\tilde{g}_{\mu\nu}$ is free from any homogeneous variables (Barbashov et al., 2005; Zakharov et al., 2006), it is just the case of the pure potential perturbations instead of the kinetic ones in the standard perturbation theory with the “friction” (Mukhanov, Feldman and Brandenberger, 1992). The superfluid version of the perturbation equations does not contain the time derivatives of the scalar potentials forming the “primordial power spectrum” in the inflationary model. This spectrum can be reproduced in terms of the scale-invariant and diffeo-invariant variables by the primary and secondary quantization of the energy constraint in the Hamiltonian formulation of GR in terms of the Dirac – ADM metric components in interval $ds^2 = a^2\tilde{\psi}^4[(\tilde{\psi}^4\tilde{N}_d dx^0)^2 - (\mathbf{e}_{(b)i}(dx^i + N^i dx^0))^2]$ and momenta P_φ and $P_F = [p_\psi, p_{(b)}, p_f]$

$$S = \int dx^0 \left[\int_{V_0} d^3x \left(\sum_F P_F \partial_0 F + C - \tilde{N}_d \tilde{T}_0^0 \right) - P_\varphi \partial_0 \varphi + \frac{P_\varphi^2}{4 \int_{V_0} dx^3 (\tilde{N}_d)^{-1}} \right], \quad (1)$$

where V_0 is finite volume and $C = N^i T_i^0 + C_0 p_\psi + C_{(b)} \partial_k \mathbf{e}_{(b)}^k$ is the sum of constraints with the Lagrangian multipliers $N^i, C_0, C_{(b)}$ and the energy-momentum tensor components T_i^0 ; these constraints include the transversality of triads $\partial_i \mathbf{e}_{(b)}^i \simeq 0$ and the Dirac minimal surface $p_\psi \simeq 0 \Rightarrow \partial_j (\tilde{\psi}^6 N^j) = (\tilde{\psi}^6)'$. Such the Hamiltonian formulation is possible only in the “superfluid” version of the cosmological perturbation theory (Barbashov et al., 2005; Zakharov et al., 2006).

2. London’s wave function versus Wheeler – DeWitt’s equation

The superfluid version of GR (1) is single one where the dimension of the group of diffeomorphisms of the Dirac – ADM metrics (which includes homogeneous transformations $x^0 \rightarrow \tilde{x}^0 = \tilde{x}^0(x^0)$) coincides with the dimension of the Gauss-type constraints $P_\varphi^2 - E_\varphi^2 = 0, T_i^0 = 0$, where $E_\varphi = 2 \int d^3x (\tilde{T}_0^0)^{1/2} \equiv 2V_0 \langle (\tilde{T}_0^0)^{1/2} \rangle$, which remove the scale factor momentum and three local triad momenta. The local part of the energy constraint $\delta S / \delta \tilde{N}_d = 0$ determines the lapse function $\tilde{N}_d^{-1} \langle \tilde{N}_d^{-1} \rangle^{-1} = (\tilde{T}_0^0)^{1/2} \langle (\tilde{T}_0^0)^{1/2} \rangle^{-1}$. The equation of P_φ ($P_\varphi = 2V_0 \varphi'$) leads to the Friedmann cosmological equation: $\varphi'^2 = \langle (\tilde{T}_0^0)^{1/2} \rangle^2$, where $\varphi' = d\varphi/d\zeta$ and $\zeta_{(\pm)} = \int dx^0 \langle N_d^{-1} \rangle^{-1} = \pm \int d\varphi / \langle (\tilde{T}_0^0)^{1/2} \rangle$ is

the diffeo-invariant homogeneous time coinciding with the conformal one η in homogeneous approximation.

In the superfluid version of GR (1) the primary quantization of the energy constraint $[\hat{P}_\varphi^2 - E_\varphi^2]\Psi_L = 0$ leads only to the unique London-type wave function Ψ_L (London, 1938) of the collective cosmic motion, in contrast with the complicated local Wheeler – DeWitt equation (Wheeler, 1968) in GR without the separation of the scale factor a .

3. Bogoliubov’s transformation versus Faddeev – Popov’s integral

The secondary quantization of the London-type function is given as its holomorphic representation in the form of the sum of the operators of creation and annihilation of the universe: $\Psi_L = [1/\sqrt{2E_\varphi}][A^+ + A^-]$, where the role of energy is played by the integral $E_\varphi = 2 \int d^3x (\bar{T}_0^0)^{1/2}$. In the case when this energy depends on the “time” φ , a stable vacuum is obtained by the Bogoliubov diagonalizing of the equations of motion and the nonzero condensation of quantum universes (Bogoliubov, 1947).

As the final result, the quantum superfluid cosmic evolution describes a cosmological creation of universes with the arrow of the conformal time $\eta \geq 0$ and its absolute reference point $\eta = 0$ at the creation moment $\varphi(\eta = 0) = \varphi_I$. The FP integral appears as a result of the low-energy decomposition identifying observables with the scale-invariant conformal quantities (Pervushin and Zinchuk, 2005).

4. Early Universe as W-,Z- Factory versus Planck’s epoch

In terms of the scale-invariant variables $ds_{s-i}^2 = ds^2/[a^2\psi^4]$ the Planck mass loses its status as the fundamental parameter of the equations of motion and becomes the present-day value of the running mass scale $\varphi_0 = \varphi(\eta = \eta_0)$. Conformal quantities describe both the SN data (Behnke et al., 2002) and the chemical evolution, if the rigid state $p = \rho$ dominates (Behnke et al., 2002). In this case, the Standard Model reveals the intensive creation of W-,Z- bosons at the beginning $\eta \sim 0$ when their Compton length $M_W^{-1}(\eta = 0) = M_I^{-1}$ coincides with the horizon H_I^{-1} and the initial data $\varphi_I = \varphi(\eta = 0)$, $H_I = \varphi'_I/\varphi_I$ are considered as a point of creation of universe (Blaschke et al., 2004).

In the Superfluid Scenario, CMBR is described as the product of decay of primordial W-,Z- bosons with the constant conformal temperature $T_c \sim (M_I^2 H_I)^{1/3} = (M_0^2 H_0)^{1/3} \sim 3K$ during the time-life $\eta_L \sim (2/\alpha_W)^{2/3} (T_c)^{-1}$ expressed in terms of the Weinberg coupling constant $\alpha_W = \alpha_{QED}/\sin^2 \theta_W$ (Blaschke et al., 2004).

The length of the semi-circle on the surface of the last emission of photons at the life-time of W-bosons in terms of the length of an emitter (i.e.

$M_W^{-1}(\eta_L) = (\alpha_W/2)^{1/3}(T_c)^{-1}$ is $\pi \cdot 2/\alpha_W$. It is close to $l_{min} \sim 210$ of CMBR, whereas $(\Delta T/T)$ is proportional to the inverse number of emitters $1/(\alpha_W)^3 \sim 3 \cdot 10^{-5}$. The observational data on CMBR reflect the SM parameters, and the equations of the primordial vector bosons are close to ones of the Lifshitz perturbation theory.

Acknowledgements

AFZ is grateful to National Natural Science Foundation of China (NNSFC) (Grant # 10233050) for a partial financial support.

References

- Barbashov, B.M., Pervushin, V.N., Zakharov, A.F., Zinchuk, V.A., Quantum Gravity as Theory of Superfluidity; gr-qc/0509006.
- Behnke, D. et al. (2002) Description of Supernova Data in Conformal Cosmology without Cosmological Constant, *Phys. Lett. B* **530**, 20–26; [gr-qc/0102039].
- Blaschke, D.B. et al. (2004) Cosmological Production of Vector Bosons and Cosmic Microwave Background Radiation, *Physics of Atomic Nuclei* **67**, 1050–1062; [hep-ph/0504225].
- Bogoliubov, N.N. (1947) On the Theory of Superfluidity, *J. Phys. (USSR)* **11**, 23–32.
- DeWitt, B.C. (1967) Quantum Theory of Gravity. I. The Canonical Theory, *Phys. Rev.* **160**, 1113–1148.
- Landau, L.D. (1941) Theory of Superfluid Helium II, *ZhETF* **11**, 592–611 (in Russian); *J. Phys. USSR*, **5**, 71–90; Theory of the Superfluidity of Helium II, *PR* **60**, 356–358.
- London, F., The λ -Phenomenon of Liquid Helium and the Bose-Einstein Degeneracy, *Nature* **141** (1938) 643–644.
- Mukhanov, V.F., Feldman H.A. and Brandenberger, R.H. (1992) Theory of Cosmological Perturbations, *Phys. Rep.* **215**, 203–333.
- Pervushin, V. and Zinchuk, V. (2005) Quantum Cosmological Origin of Universes, gr-qc/0504123.
- Wheeler, J.A. (1968) Superspace and the nature of quantum geometrodynamics, in *Batelle Recontres: 1967 Lectures in Mathematics and Physics*, edited by C. DeWitt and J.A. Wheeler, New York, 1968, 242-307.
- Zakharov, A.F., Zinchuk, V.A., and Pervushin, V.N. (2006), Tetrad Formalism and Frames of References in General Relativity *Physics of Particles and Nuclei* **37**, to be published.

II. Nuclear Safety

THE URANIUM MINING AND STORAGE OF NUCLEAR WASTE IN CZECH REPUBLIC

Tomáš Čechák and Jaroslav Klusoň
Czech Technical University in Prague
Faculty of Nuclear Sciences and Physical Engineering
Břehová 7, 115 19 Praha1, Czech republic

Abstract. The paper describes the situation in the uranium mining and spent fuel management in the Czech Republic. Uranium mining has a long history in the Jachymov area. By the 1960s Czech mines producing 3000 tons a year. After 1989 the uranium mine are mostly closed down and only one active mine in Rozna is active and it is being phased out.

The paper contains a list of NPP in the Czech Republic furthermore and brief descriptions of facilities used spent fuel management in this nuclear power and research facilities. The photon field analysis in the spent fuel storage is briefly described.

Key words: Uranium mining, uranium ore, nuclear power plant, spent fuel, spent fuel storage facility, scintillation detector, dose rates portable monitor

1. Introduction

The discovery of the Jachymov ore district dates back to 1516. After several years, the district became one of the most important producers of silver ores in central Europe. Together with the silver ore was mined uranium ore, at that time worthless. It was called pitchblende. In 17th to 19th century, the original interest in silver was substituted by mining of cobalt, nickel and bismuth. In the early 19th century, uranium ores were collected from old dumps and later mined for paints production and was used mainly in the glass industry. It was only the discovery by Pierre and Marie Curie that radium could be isolated from Jachymov uranium ore that gave the impulse to the using of pitchblende. After the discovery of radium, uranium ores were mined for radium. After World War II, large-scale production and export of uranium ore took place in the district. It is worth to note that radioactive waters of the district have been used for medical purposes since 1906 [1].

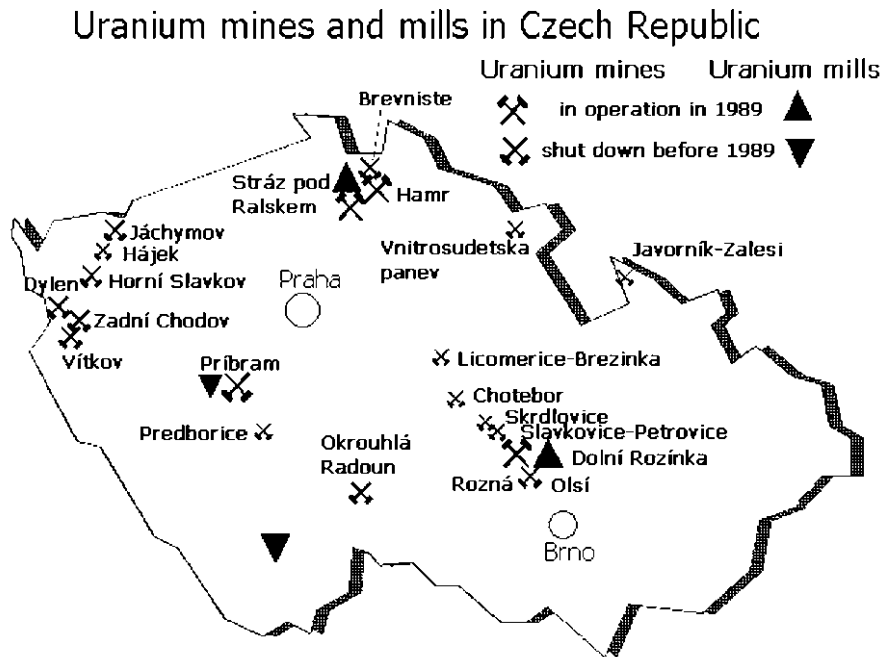


Figure 1. Uranium mines and mills in the Czech Republic (1945 – 1995)

2. Uranium mining in the Czechoslovakia

Uranium mining began immediately after the end of World War II in the historic mining province on the Czech side of the Krušné Mountains at Jáchymov and surroundings; these deposits were depleted in the sixties. Further deposits were discovered and mined in various areas of Bohemia and Moravia. See fig. 1. The annual production was in the range of 2500 - 3000 tonnes of uranium between 1955 and 1988. See fig. 2. The total production was 102,245 tonnes from 1946 to 1992. The uranium was shipped to the Soviet Union for further processing. The mining was performed by the state enterprise. The largest uranium province was Příbram; 38.9 % of the uranium was produced there, at an annual production of up to 2000 tonnes. Exploitation of uranium ore since 1946 in Czechoslovakia can be divided into four periods based on the exploration and exploitation strategies and methods.

- Period 1 (1946 – 1960) Re-assessment of the known Jáchymov deposit. Several new uranium deposits were discovered during this period: Příbram, Chodov, Rozinka.

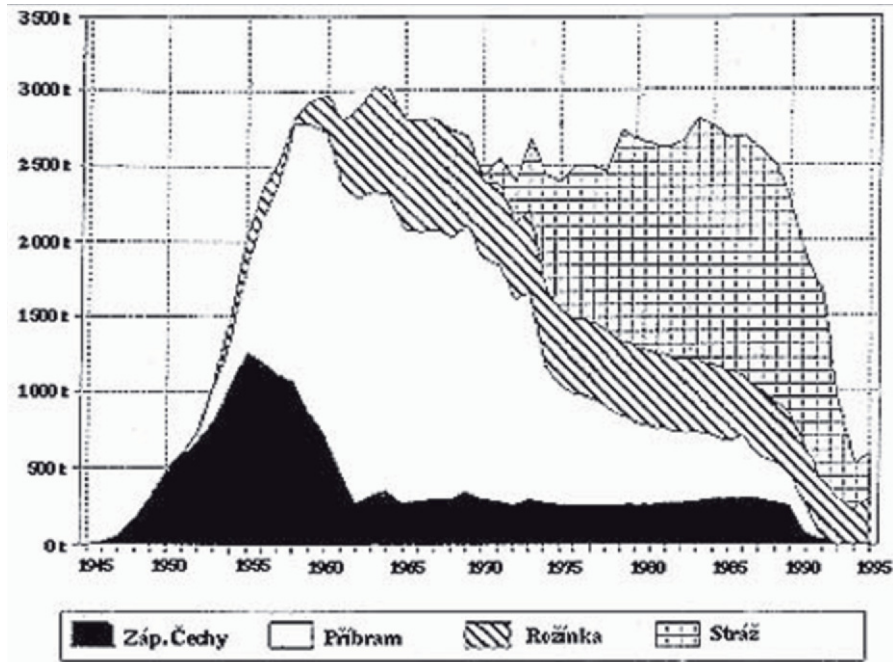


Figure 2. Uranium production in the main mining districts of the Czech Republic(1945 – 1995)

- Period 2 (1961 – 1975) Main exploitation of the Příbram deposit.
- Period 3 (1975 – 1992) Main exploitation of the Straz deposit.
- Period 4 (1992 -) Reduction of the uranium related activities in the Czech republic.

After the political changes, mining was discontinued at this site due to depletion of the deposit. The same happened at the West Bohemian site of Zadní Chodov and at the South Bohemian site Okrouhla Radouň. The North Bohemian Hamr na Jezerce mine with the Straz pod Ralskem mill is now being decommissioned.

At the South Bohemian site of Mydlovary near Budweis, a uranium mill was in operation, processing exclusively uranium ore that was supplied from other sites.

Uranium mining is still in operation at a reduced production rate at the West Moravian Rozna mine with the associated Dolní Rozinka mill.

In Straz pod Ralskem moreover, the in-situ leaching technology was used on a large scale: The ore deposit is located in Cretaceous

sandstones with grades of 0.08 - 0.15 % uranium. In an area of 5.6 km², 9340 wells were drilled from the surface into the deposit. Diluted sulfuric acid was injected as a leaching agent through some of the wells, while the uranium bearing liquid was pumped from the others. See Table I.

TABLE I. Uranium Mill Tailings in Czech Republic [3]

	Solids contents $10^6 m^3$	surface <i>ha</i>
Czech Republic	~ 45	~ 607
Mydlovary	18.8	264
Straz pod Ralskem	14.2	187
Dolni Rozinka	8	110
Pribram	?	46

3. Nuclear power plants and reactors in the Czech Republic

In 1958 the Czechoslovak government started building its first nuclear power plant - a gas-cooled heavy water reactor at Bohunice (now in Slovakia). This was completed in 1972 and ran until 1977. VVER 440 reactors were built at Bohunice in the 1970s and put into operation in the 1980s.

In 1978 construction of the Dukovany plant commenced, with four VVER 440 type 213 reactors designed by Russian organisations and Energoprojekt and built by Skoda. These came in to commercial operation 1985-87.

In 1982 work started on the Temelin plant, with two VVER-1000 type V-320 reactors, designed by Russian organisations and Energoprojekt and built by VSB with engineering by Skoda Praha. Construction was delayed and when it resumed in the mid 1990s, Westinghouse instrument and control systems were incorporated. The reactors started up in 2000 and 2002, with the upgrading having been financed by CEZ with a loan from the World Bank. A further two units were originally envisaged on the site.

The plants are owned and operated by the Czech Power Company (CEZ) which has been two thirds state-owned but will be privatised. CEZ has financed the upgrading of the Dukovany reactors.

TABLE II. Operating Czech power reactors

Reactors	Model PWR	Net MWe	First power
Dukovany 1	V-213	412	1985
Dukovany 2	V-213	412	1986
Dukovany 3	V-213	412	1986
Dukovany 4	V-213	412	1987
Temelin 1	V-320	912	2000
Temelin 2	V-320	912	2003
Total		3472	

After the political changes, it was planned to keep the uranium production at a level sufficient to supply the reactor related uranium needs of the country. The nuclear power plant Dukovany, needs 1632 tonnes per year; after the start of the Temelin plant, the demand is approximately double. But, due to the high production cost, uranium mining will now be further reduced.

The 2004 state energy policy envisages building two or more large reactors, probably at Temelin, eventually to replace Dukovany after 2020.

Two research reactors are operated by the Rez Nuclear Research Institute (one is a 10 MW unit) and another by the Czech Technical University in Prague. The main one was originally Russian but has been extensively rebuilt; the other two were designed locally [2].

4. Radioactive waste management

There is no state policy on reprocessing and the decision is left to CEZ, which does not perceive it as being economic. However, the question remains open. Fresh nuclear fuel was supplied to the former Czechoslovakia from the previous U.S.S.R and spent fuel was originally planned to be re-exported after 5 year cooling period. The transport of spent fuel from the Czechoslovak NPPs was suspended in 1988 and the spent fuel assemblies from the NPP Dukovany were after 3 year cooling period transported to the wet interim storage facility at Jaslovsk Bohunice in the Slovakia. These transports were halted in 1992. The necessity to

handle a growing number of spent fuel assemblies in the NPP Dukovany and need to transport the 1176 spent fuel assemblies stored at Jaslovsk Bohunice (Slovakia) back to the Czech republic, have led to the construction of an away from reactor spent fuel storage facility at Dukovany [5].

To assure safe storage of SF removed from reactors, SF pool is provided next to each reactor unit, its volume is 335 m^3 and the SF is stored in it for a period of time required to reduce the residual heat output. After that period the thermal output and radiation of SF assemblies drops to a level permitting their transport in CASTOR-440/84 type-approved casks for transport and storage in ISFSF Dukovany. The SF pools assure the following functions:

- Undercriticality of the stored SF,
- Removal of residual heat from FA,
- Protection against radioactive radiation.

In the pools the SF is stored in a compact grid with the capacity of 682 positions. SF pool also contains 17 positions for hermetic cases to store damaged SF. Depending on the number of removed FA in the annual reactor campaign; the pools enable to store SF for a period of at least 7 years. Only in the case of emergency removal of fuel from the core or during inspection of the reactor pressure vessel, a reserve grid is inserted into SF pool. As on 31 December 2002 all four pools contained 2288 FA with the total weight 491 920 kg, with the weight of heavy metals about 273 000 kg.

ISFSF Dukovany, situated inside the NPP Dukovany site, is designed for dry storage of SF in CASTOR-440/84 casks. A central building of ISFSF Dukovany is a ground-level hall with a combined structural system, with fixed poles from reinforced concrete and steel roof structure with a 6-meter module. The poles bear a crane runway and roof steel open-web girders supporting the roof structure. The building shell is mounted from panels made of reinforced concrete 100 mm thick. The storage part of the building is surrounded with a shielding concrete wall 5 m high and 500 mm thick. The floor is a slab of reinforced concrete with dust-free consolidating surface finish.

ISFSF Dukovany is an independently functioning unit linked by utility networks to the networks of NPP Dukovany. It has a railway siding and road links to the reactor units of NPP Dukovany.

The total capacity of ISFSF Dukovany is 60 casks, while on 31 December 2002 ISFSF Dukovany contained 46 CASTOR-440/84 casks and the 47th was being prepared by the said date in the reactor hall

of unit 3 of NPP Dukovany to be transported to ISFSF. 4-5 casks are transported to ISFSF Dukovany every year [5].

Similarly as in NPP Dukovany, the main production building in NPP Temelin has a storage pool for SF removed from the reactor with the volume 1440 m^3 , immediately next to the reactor well. The removed SF is stored here for a period of 12 years (in the course of NPP operation) or for at least 5 years (after NPP operation is closed) in a storage pool. SF pool is divided into 3 parts: two bigger parts have two grid sections each and the third has only one storage grid section. The entire SF pool enables to store 679 FA, 24 FA in hermetic cases and 2 cluster cases. In a standard storage regime, however, at least 163 positions shall remain free for potential emergency removal of FA from the entire reactor core. As on 31 December 2002 Unit I of NPP Temelin was in trial operation and Unit II in the stage of power start up and SF pools contained no SF by the said date. In connection with the commissioning of ETE units additional storage capacity will be required for SF in 2014, as the first fuel will be moved from the reactor to SF pool early in 2003. The most recent plan of CEZ, a. s. is to develop SFSF directly on the NPP Temelin site and thus eliminate the necessity to transport SF outside the NI site before the SF is handed over to DGR. As part of the plan a feasibility study was made in 2002 to find a suitable location for SFSF inside the NPP Temelin site. Based on the favourable experience with dry storage technology for SF in casks for transport and storage, which CEZ, a. s. acquired in NPP Dukovany, the technology used for SF storage at NPP Temelin will be similar. In agreement with the Policy the anticipated storage time of SF in the facility will be 60 years.

The implementation of SFSF will be performed in a standard manner. An international tender is expected to be opened for a contractor of storage technology. Individual steps leading to the storage facility implementation will start in near future so that SFSF is available as scheduled. If CEZ, a. s. encounters some fundamental problems which may endanger timely implementation of the storage facility at the NPP Temelin location the reserve location Skalka is ready to replace it. Investigations, including the drilling of exploration gallery, were performed in the Skalka location, which is situated about 160 km from the NPP Temelin (to develop an underground dry cask storage facility for SF). At the moment a valid decision for the construction sitting is not available for the location [4].

CEZ is fully responsible for storage and management of its spent fuel until it is handed over to the state organisation Radioactive Waste Repository Authority (RAWRA).



Figure 3. Inside view of the Interim Spent Fuel Storage Facility.

Spent fuel is stored at each power plant in dry spent fuel storage. The interim dry storage with capacity of 600 t is operated at Dukovany. Another new one with capacity of 1300 t is under construction also at Dukovany and a new project has been started for Temelin. CEZ creates an internal financial reserve for the long term spent fuel storage.

At Dukovany a low- and intermediate-level waste repository is operated by RAWRA, and designed for all such wastes from both plants.

At Rez there is an interim storage facility for spent research reactor fuel.

Eventual provision of a high-level waste repository is the responsibility of the state Radioactive Waste Repository Authority (RAWRA). Site selection is scheduled for 2015, with construction start after 2050.

5. The measurement of photon and neutron fields in Spent Fuel Storage Facility

The measurement of photon and neutron fields in the storage hall was made by the authors with the aim to assess the radiation risk inside the storage hall and the influence of the storage facility on the surrounding environment, as well as to evaluate and estimate the time dependence of the time factors, corresponding to the gradual storage filling [6]. A set of the periodical measurements was performed in order to get the

basic information on the time dependence of the photon fields spatial distribution and the spectral characteristic at the temporary storage facility and its vicinity. For the direct measurements, the high sensitive dose/dose rates portable monitor with special combined scintillation detector, compensated for the energy and directional dependence, was used. The deconvolution technique based on the detection system response matrix and the Scofield-Gold iterative method was used for the spectrometry data mathematical processing. This technique enables to calculate the spectral distributions of the required dosimetric quantities. The fig. 4 shows the example of the isolines in the storage hall in Dukovany. The performed photon field analysis in the vicinity of the temporary spend fuel storage facility and the inside storage hall respectively gives the basic view about the spectra of radiation and the trends of development and changes of this spectra and radiation hazards respectively.

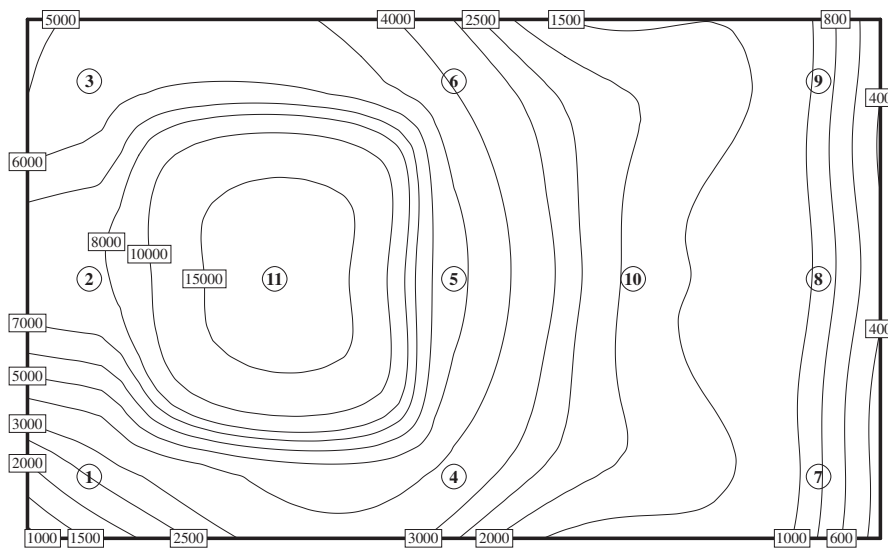


Figure 4. Isolines in the storage hall

6. Summary

Uranium mining has a long history in the Jachymov area. By the 1960s Czech mines producing 3000 tons a year and the Czech Republic was the second most important uranium producer in Europe. After 1989 the uranium mine are mostly closed down and only one active mine in Rozna is active and it is being phased out.

NPP in the Czech Republic produced more than one third of the electricity production. The safe operation of these NPPs will require new spent fuel storage facilities and the preparation and the building of the central storage facility.

References

- 1 D. Pittauerová & V. Goliáš, Weathering of mine wastes after historical silver mining in the Jáchymov ore district (Czech Republic) and migration of uranium in Uranium Deposits, B. Kribek & J. Zeman (eds.) Czech Geological Survey, Prague, ISBN 80-7075-583-0
- 2 National Report under the Joint Convention on Safety in Spent Fuel Management and Safety in Radioactive Waste Management State Office of Nuclear Safety, Prague, Czech Republic 2003
- 3 P. Diel: Uranium Mining in Europe The Impacts on Man and Environment, WISE Amsterdam P.O.Box 59636 1040 LC Amsterdam The Netherlands
- 4 <http://www.world-nuclear.org/info/inf04.htm>
- 5 V. Fajman et al. Czech interim spent fuel storage facility: operation experience, inspections and future plants, IAEA –TECDOC-1089, IAEA 1999
- 6 T. Čechák, T., J. Klusoň, Spent fuel Temporary Storage, Environmental Impact Assessment, IAEA –TECDOC-1089, IAEA 1999

CURRENT STATE AND THE FUTURE OF NUCLEAR ENERGY

D.P. Belozorov and L.N. Davydov (ldavydov@kipt.kharkov.ua)
*National Science Centre “Kharkov Institute of Physics and Technology”,
Kharkov 61108 Ukraine*

Abstract. The current status and prospects of the world nuclear energy are analyzed. It is shown that because of the fossil fuel shortage the future of the mankind is hardly possible without the nuclear energy. The scientific and technology challenges of the future Generation III and IV nuclear energy systems are outlined. It is stated that to meet the safety criteria they must be sustainable, economical, reliable, proliferation resistant, and physically protected.

Key words: nuclear energy, fuel shortage, global warming, nuclear reactors, Generation III reactors, Generation IV reactors

PACS: 28.41-i, 28.90+i

1. Introduction

The nuclear power industry born in the 20th century seemed to become a key solution of all continuously increasing energy problems of human civilization. But the years of operation opened some dangerous features of nuclear industry, which destroyed its image of unlimited safe source of cheap electricity. Reactor accidents at Three Mile Island (USA) and Chernobyl (Ukraine), fraught with fatal consequences, resulted in various extent of public disfavor towards the nuclear industry and even in its prohibition in some countries.

Now, however, nuclear power has again attracted an active interest. The most important reasons for this are the forthcoming shortage of fossil fuels and growing concern about global warming, together with the world growing demand for energy and electricity, in particular.

First we dwell short on these, favoring nuclear energy conditions. After that we consider the main problems it faces.

2. The reasons to revive the nuclear power

2.1. GROWING DEMAND FOR ENERGY

The Energy Information Administration (IAE) forecasts (EIA, 2004) that the world's total energy consumption will rise by 54% between 2001 and 2025,

from 404 to 623 quads (Fig. 1 (EIA, 2004)). (A quad is one quadrillion, or 10^{15} Btu¹, about 10^{18} joules, approximately 3×10^{11} kilowatt hours.) The same IAE report predicts a 25-year increase of carbon dioxide emissions by a similar 55%, from 23.9 to 37.1 billion metric tons, and a population increase from 6.14 to 7.84 billion people. Most of the growth in all three areas will take place in rapidly developing parts of the world. The evolution of the energy production through 1970-2000 by fuel can be seen from Fig. 2 (IEA, 2002).

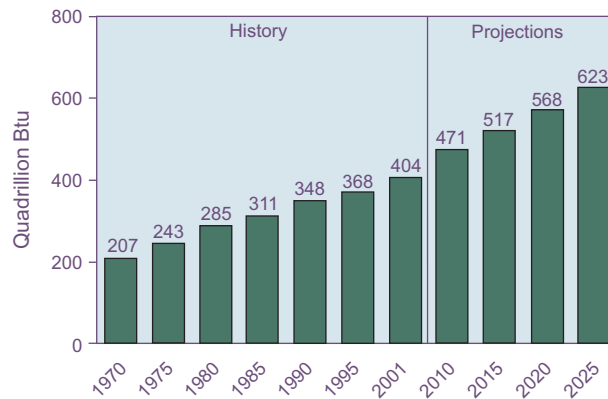


Figure 1. World Marketed Energy Consumption, 1970-2025 (Energy Information Administration, 2004).

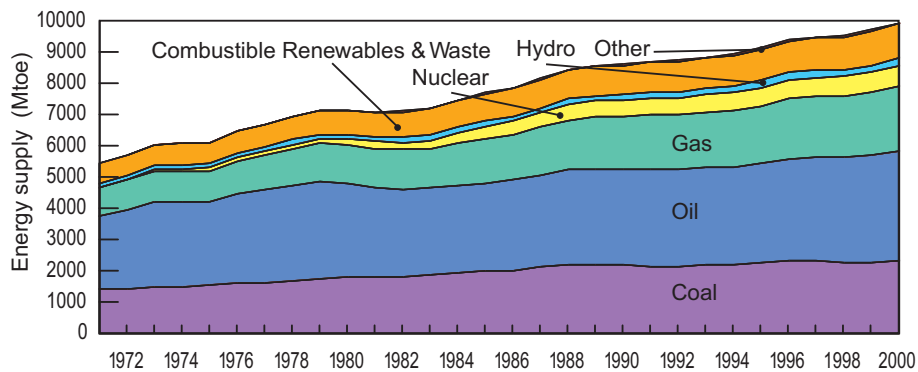


Figure 2. Evolution from 1971 to 2000 of world total primary energy supply by fuel (in Mtoe; 1 Mtoe = 11.6 TWh; Source: International Energy Agency, 2002).

The United Nations compiles annual statistics about human development and the environment in 174 countries. Three of the indicators (life expectancy; educational attainment, and standard of living) are combined to calculate a Human Development Index (HDI). There is a correlation between electricity consumption and the HDI (Benka, 2002; MIT, 2003) (Fig. 3). The HDI

¹ British Thermal Unit, i.e., heat required to increase 1 lb. of water by 1 degree Fahrenheit

reaches a high plateau when a nation's people consumed about 4000 kWh of electricity annually per capita, a value unchanged between 1980 and these 1997 data.

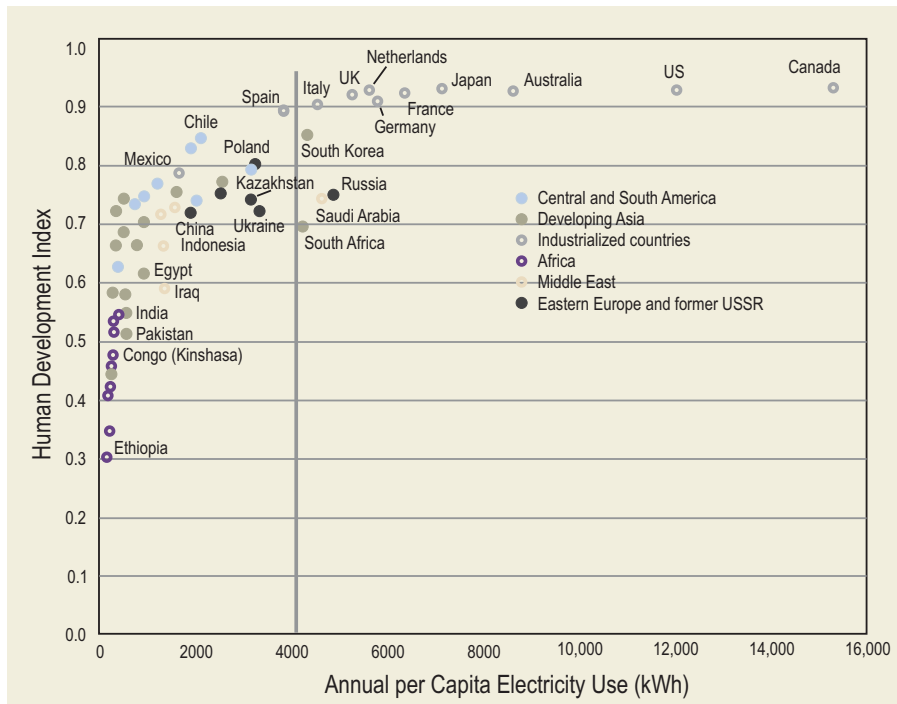


Figure 3. Correlation between HDI and per capita electricity consumption (MIT, 2003).

Now it is clear that reaching the goal of basic human well-being in poor countries will require significantly greater global consumption of electricity and primary energy than do projections for 2020 by the DOE and others. This circumstance is reflected in the currently growing demand for oil in developing East Asia.

- With the increase in population and human well-being the world's total energy consumption will rise and the mankind will need greater amount of energy reserves

2.2. SHORTAGE IN ENERGY RESOURCES

The World Energy Council (WEC) survey on energy resources stated in 2003 that conventional commercial fossil fuels on the whole, encompassing coal, oil and natural gas, remained in adequate supply, with a substantial resource base (Yokobori, 2003). However, the resources differ for constituent fuels.

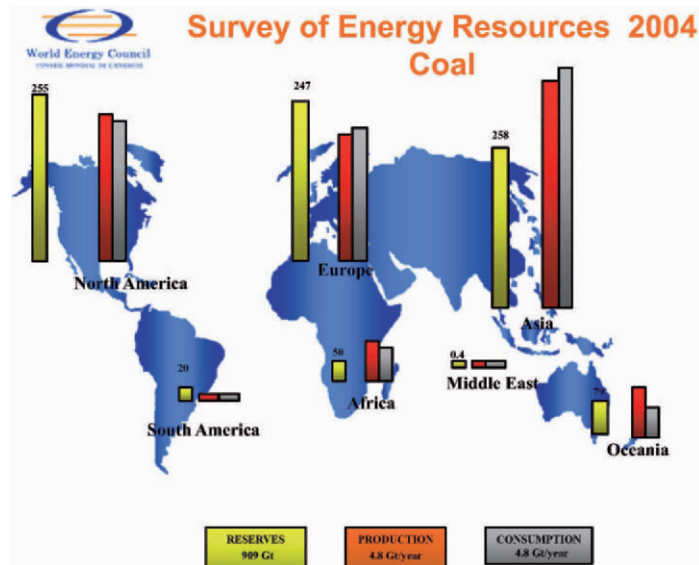


Figure 4. 2004 Survey of world coal resources (Clerici, 2004).

Coal. The rough and ready estimation of the coal reserves shows that exploitation can continue at current levels in excess of 200 years (Fig. 4 (Clerici, 2004)). The world is not going to run out of physically-available supplies of coal in nearest future. However, coal use in future will largely depend on the impact of deregulation of electricity markets, policies to reduce greenhouse gases, and technological advances (Knapp, 2004).

Oil and gas. While coal supply in the medium and long term is assured, the commentaries on oil and gas appear to incline towards less optimistic reserve assessments (Figs. 5 and 6 (Clerici, 2004)).

Between the 1998 and 2001 proved recoverable reserves of hydrocarbons (as reported by WEC Member Committees and other sources) remained fairly stable overall: oil reserves fell by 2.7% while gas reserves went up by 2.8% (Alazard-Toux and Bensaid, 2004; Storm, 2004).

At the current rate of production, the industry could continue to produce oil for 40 more years, gas for over 55 years. The geographic breakdown of hydrocarbon resources remains basically unchanged, with a high concentration in the Middle East (65%) and in the OPEC countries for oil, and a more equitable distribution between the FSU (37%) and the Middle East (35%) for gas. Therefore, we can conclude:

- At the current rate of production, the industry could continue to produce oil for 40 more years, gas for over 55 years, and coal for more than 200 years.

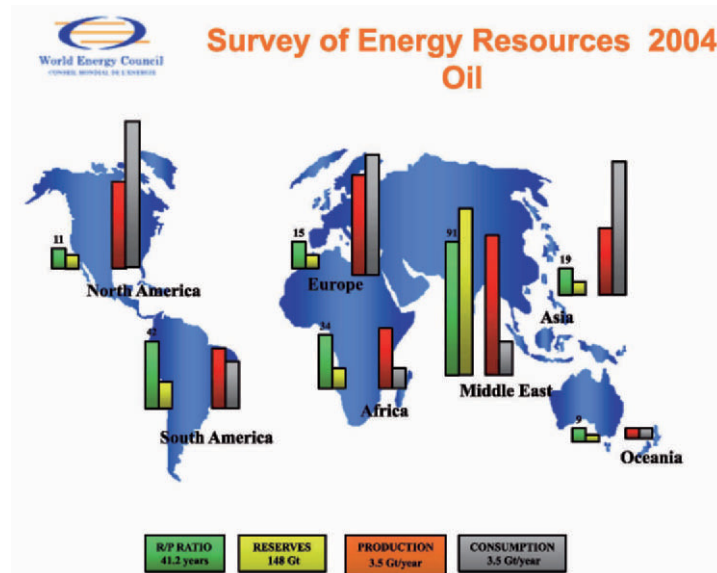


Figure 5. 2004 Survey of world oil resources (Clerici, 2004).

Uranium Now 21 countries produce uranium and nearly all of them provide official reports (China, India and Pakistan are the exception) (Underhill, 2004; WNA, 2004). In 1999 over 90% of world production came from the 10 major producing countries (Australia, Canada, Kazakhstan, Namibia, Niger, the Russian Federation, South Africa, Ukraine, USA and Uzbekistan), each of them producing over 1000 tU (Fig. 7). Canada continued to be the largest producer, with a 2003 output of 10 457 tU, or 29.2% of the world total; Australia retained the second place, with production of 7 572 tU and a share of 21.2%, while the third largest producer was Kazakhstan, with 3 300 tU (9.2%) (WNA, 2004).

According to this data the current rate of production of the uranium industry could be maintained for 100 more years (Fig. 8, (WNA, 2004a)). However, the situation is more complicated, because the current production is much below the consumption.

To understand the outlook for uranium it is necessary to consider recent history (Underhill, 2004). Uranium is an unusual commodity because a major portion of market demand is met now from sources other than new mine production. From 1991 through 1999 about 215 000 tU, or over 40% of the total world requirements, were met from non-mine supplies. During the early part of this period a major contribution came from drawdown of the commercial inventory held by nuclear utilities. However, with each year, the importance of other sources has been increasing. For example, during the period 1992 to 1999 a total of 96 700 tU was delivered to the European Union from the NIS, with the bulk of this material coming from Russia.

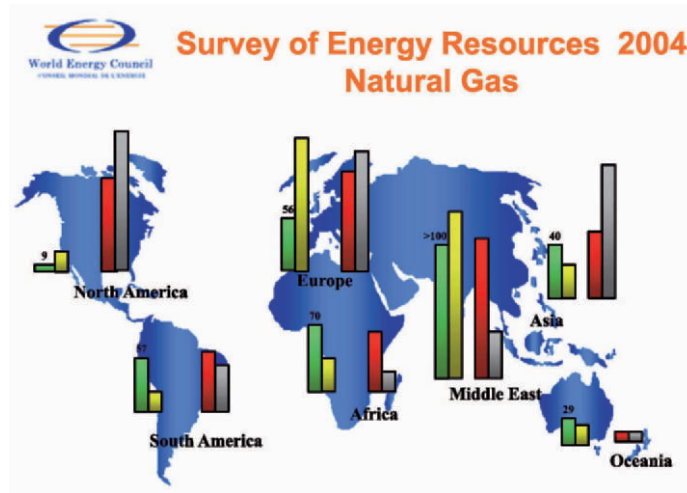


Figure 6. 2004 Survey of world gas resources (Clerici, 2004).

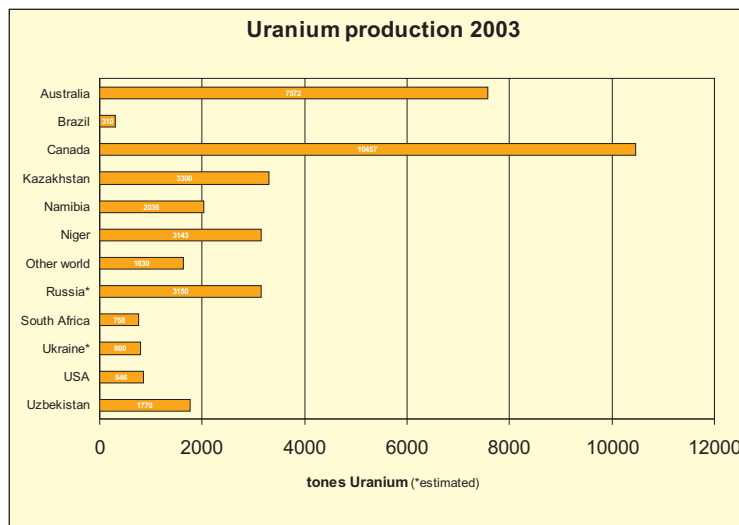


Figure 7. Uranium production 2003 (Source: WNA (WNA, 2004)).

Another major source of uranium supply developed starting in 1995. This supply is based on a government-to-government agreement signed in February 1993 between the United States and the Russian Federation concerning the disposition and purchase of 500 t highly enriched uranium (HEU) from dismantled nuclear weapons (Megatons to Megawatts). It is equivalent to

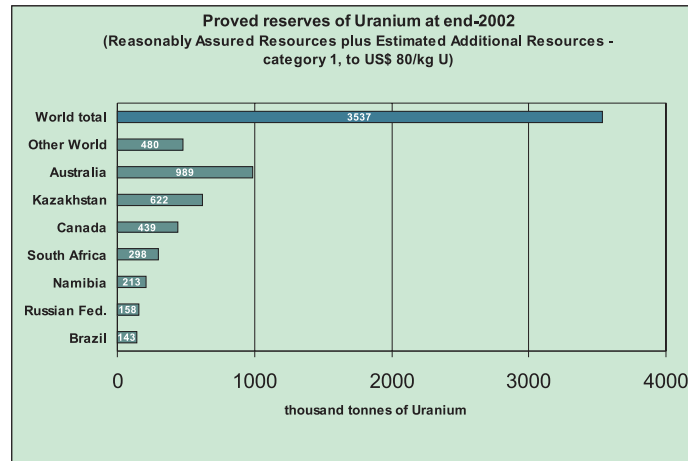


Figure 8. Proved reserves of uranium at end-2002 (Source: NEA & IAEA; WNA (WNA, 2004a)).

150 000 tU natural uranium. Other supplies that are being used in place of new mine production include re-enrichment of tails from the enrichment of uranium, use of mixed oxide (MOX) fuel and re-processed uranium. It is anticipated that most of these supplies will continue to be available over the next 10 years or so.

Figure 9 (WNA, 2004b) is a supposition of how these various sources of supply might look in the decade ahead and the next graph, Fig. 10 (WNA, 2004b), gives an historical perspective, showing how early production went first into military inventories and then, in the early 1980s, into civil stockpiles. This early production is now being released to the market.

Therefore, the above prognosis of 100 years for uranium reserves should be shortened for the currently used once-through fuel cycle to 50-70 years.

The following conclusion can be formulated:

- Production from world uranium mines now supplies only 55% of the requirements of power utilities.
- Mine production is increasingly supplemented by ex-military material.
- World mine production will need to expand significantly post 2005.
- For the currently used once-through fuel cycle uranium reserves will last for 50-70 years. Breeder technology could prolong this term hundredfold.

However, there are more optimistic views on fossil reserves. The authors of Interdisciplinary MIT study on the future of nuclear power (MIT, 2003) assert that with the increase in the uranium prices, presently uneconomic

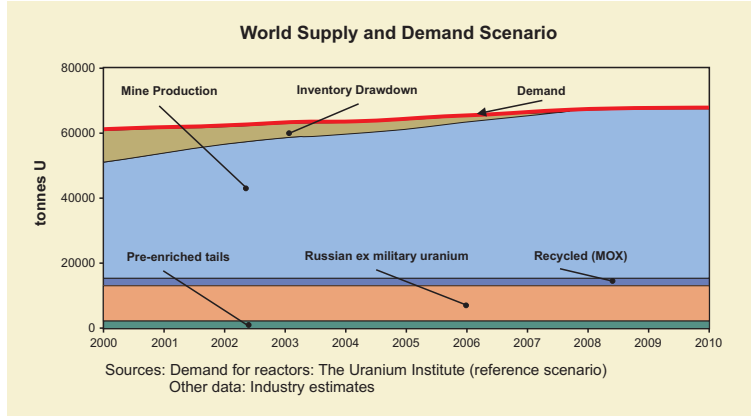


Figure 9. World supply and demand scenario (tonnes U) (WNA, 2004b).

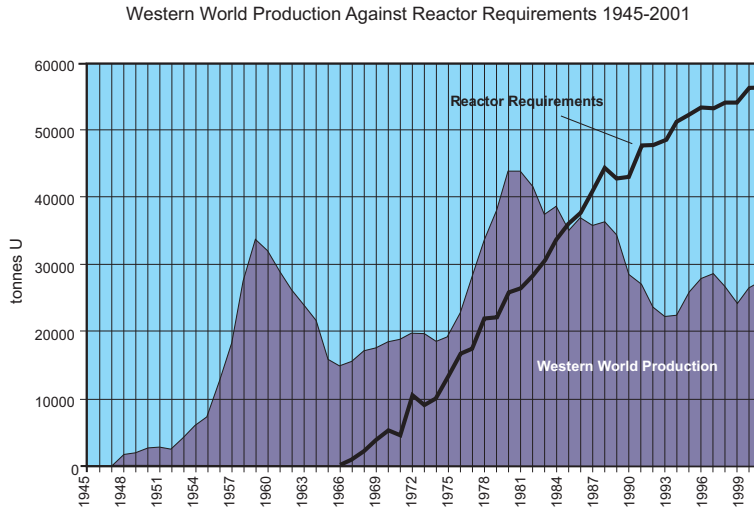


Figure 10. Western world production against reactor requirements 1945-2001 (WNA, 2004b).

resources will become economic to recover. A doubling of the uranium price could be expected to create about a tenfold increase in measured resources (Hore-Lacy, 2003). The non-traditional resources, for example, phosphates (22 million tonnes) are not taken also into account, as well as marine water (up to 4000 million tonnes), which can be used for uranium production at the cost from two to six times more expensive, than now.

Despite of so optimistic assertions, it is impossible to get rid of the feeling, that all these reserves of uranium, oil, gas, and even coal are not illimitable, and the years of their exhaustion are comparable to the life-span of one or two human generations, Fig. 11 (Hore-Lacy, 2003a).

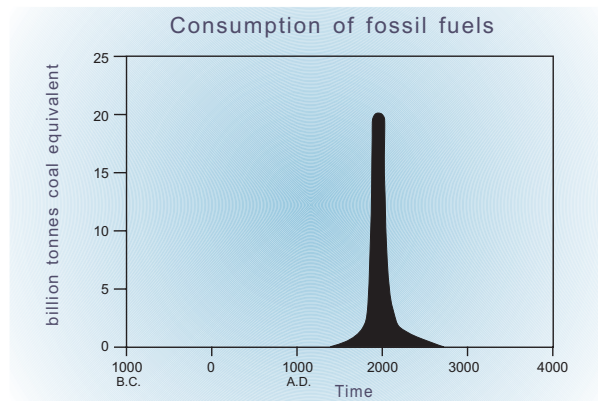


Figure 11. Consumption of fossil fuels (Hore-Lacy, 2003a).

2.3. GLOBAL ECOLOGICAL PROBLEMS OF ENERGY PRODUCTION AND CONSUMPTION

In the coming decades, two major environmental issues, global climate change and local or regional air pollution, could affect energy use throughout the world. Current and future policies and regulations designed to limit energy-related emissions of anthropogenic carbon dioxide have already implemented the Kyoto protocol in 2005. These efforts could also have significant implications on a structure and growth of world energy consumption, including nuclear energy.

World carbon dioxide emissions are expected to increase from 23,899 million metric tons in 2001 to 37,124 million metric tons in 2025 – growing by 1.9 percent per year – if world energy consumption reaches the levels projected in the International Energy Outlook (IEO) 2004 reference case (Fig. 12) (EIA, 2004). According to this projection, world carbon dioxide emissions in 2025 would exceed 1990 levels by 72%. Combustion of petroleum products contributes 5,733 million metric tons (43%) to the projected increase from 2001, coal 4,120 million metric tons (31%), and natural gas the remaining 3,374 million metric tons (26%).

- Carbon taxes could make nuclear energy more favorable as carbon-free option.

In 1998 due to the decline in production level and living standards, Ukraine has moved to the tenth place in the list of the carbon emitting states after USA, Russia, Japan, Germany, Canada, Great Britain, France, Italy and Australia. Nevertheless, the combined share of Russia and Ukraine adds up to about 20%. It means that if Russia and Ukraine had not ratified the Protocol, it basically could not come into force.

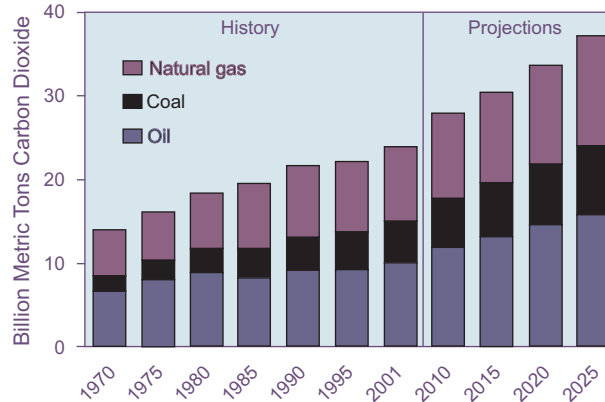


Figure 12. World Carbon Dioxide Emissions by Fossil Fuel, 1970-2025 (EIA, 2004).

3. Problems facing the nuclear power

The limited prospects for nuclear power today are attributable, ultimately, to five unresolved problems: economics, waste management, safety, proliferation, and public acceptance (MIT, 2003).

3.1. ECONOMICS

Nuclear power will succeed in the long run only if it has a lower cost than competing technologies. This is especially true as electricity markets become progressively less subject to economic regulation in many parts of the world. A “merchant” cost model developed in Interdisciplinary MIT study “The future of nuclear power” (MIT, 2003) compares the constant or “levelized” price of electricity over the life of a power plant that would be necessary to cover all operating expenses and taxes and provide an acceptable return to investors (TABLES I and II).

The authors (MIT, 2003) draw the conclusions:

- The U.S. government should cost share for site banking for a number of plants, certification of new plant designs by the Nuclear Regulatory Commission, and combined construction and operating licenses for plants built immediately or in the future.
- The government should recognize nuclear as carbon-free and include new nuclear plants as an eligible option in any federal or state mandatory renewable energy portfolio (i.e., a “carbon-free” portfolio) standard.
- The government should provide a modest subsidy for a small set of “first mover” commercial nuclear plants to demonstrate cost and regulatory feasibility in the form of a production tax credit.

TABLE I. Comparative power costs (MIT, 2003).

Case (year 2002 \$)	Real levelized cost (cents/kWe-hr)
Nuclear (LWR)	6.7
plus reduce construction cost 25%	5.5
plus reduce construction time 5 to 4 years	5.3
plus further reduce O&M to 13 mills/kWe-hr	5.1
plus reduce cost of capital to gas/coal	4.2
Pulverized coal	4.2
CCGT ^a (low gas prices, \$3.77/MCF)	3.8
CCGT (moderate gas prices, \$3.77/MCF)	4.1
CCGT (high gas prices, \$3.77/MCF)	5.6

^aGas costs reflect real, levelized acquisition cost per thousand cubic feet (MCF) over the economic life of the project; CCGT – Combined-Cycle Gas Turbine.

TABLE II. Carbon tax cases levelized electricity cost (MIT, 2003).

cents/kWe-hr	\$50/tonne C	\$100/tonne C	\$200/tonne C
Coal	5.4	6.6	9.0
Gas (low)	4.3	4.8	5.9
Gas (moderate)	4.7	5.2	6.2
Gas (high)	6.1	6.7	7.7

3.2. WASTE MANAGEMENT

The management and disposal of high-level radioactive spent fuel from the nuclear fuel cycle is one of the most intractable problems facing the nuclear power industry throughout the world. No country has yet successfully implemented a system for disposing of this waste.

The following propositions can be made:

- Governments should augment its focus on geologic disposal with a balanced long-term waste management R&D program.
- A research program should be launched to determine the viability of geologic disposal in deep boreholes within a decade.
- A network of centralized facilities for storing spent fuel for several decades should be established in nuclear energy producing countries and internationally.

3.3. NONPROLIFERATION

Nuclear power should not expand unless the risk of proliferation from operation of the commercial nuclear fuel cycle is made acceptably small.

- The International Atomic Energy Agency (IAEA) should focus overwhelmingly on its safeguards function and should be given the authority to carry out inspections beyond declared facilities to suspected illicit facilities.
- Greater attention must be given to the proliferation risks at the front end of the fuel cycle from enrichment technologies.
- IAEA safeguards should move to an approach based on continuous materials protection, control and accounting using surveillance and containment systems, both in facilities and during transportation, and should implement safeguards in a risk-based framework keyed to fuel cycle activity.
- Fuel cycle analysis, research, development, and demonstration efforts must include explicit analysis of proliferation risks and measures defined to minimize proliferation risks.
- International spent fuel storage has significant nonproliferation benefits for the growth scenario and should be negotiated promptly and implemented over the next decade.

3.4. SAFETY

MIT analyzers believe the safety standard for the global growth scenario should maintain today's standard of less than one serious release of radioactivity accident for 50 years from all fuel cycle activity. This standard implies a ten-fold reduction in the expected frequency of serious reactor core accidents, from 10^{-4} /reactor year to 10^{-5} /reactor year.

The reactor designs should include the elements of intrinsic and passive safety.

Nuclear facilities should be hardened to possible terrorist attack.

- The governments should, as part of their near-term R&D program, develop more fully the capabilities to analyze life-cycle health and safety impacts of fuel cycle facilities and focus reactor development on options that can achieve enhanced safety standards and are deployable within a couple of decades.

3.5. PUBLIC ATTITUDES TOWARD NUCLEAR POWER

Expanded deployment of nuclear power requires public acceptance of this energy source. Presently a majority of Americans and Europeans oppose building new nuclear power plants to meet future energy needs. Though, their number is slowly decreasing with the time.

The surer way to cultivate public acceptance of nuclear power is through the improvement of the technology itself. Much of the change would come through education about the high price of alternative energy sources, such as solar and wind. The other possible source of change in public attitudes is the connection between global warming and fossil fuels.

- The public is unlikely to support nuclear power expansion without substantial improvements in costs and technology.

4. New nuclear power plant designs

To overcome the nuclear energy problems the efforts of technicians, politicians, and scientists should be united. In this section we discuss in brief the last years progress in technical area, in reactor design.

It is convenient to classify the evolution of nuclear technology in terms of design generations, even if the boundaries between the generations are not necessarily distinct, Fig. 13 (IEA, 2002; GIF-IV, 2002). In the early period of nuclear power development, many types of reactor designs were proposed with a wide range of coolants (e.g., light water, heavy water, organic liquids, liquid metals, molten salts, gases), fuel materials (e.g., uranium-235, uranium-238/plutonium-239, thorium-232/uranium-233, oxides, carbides, or

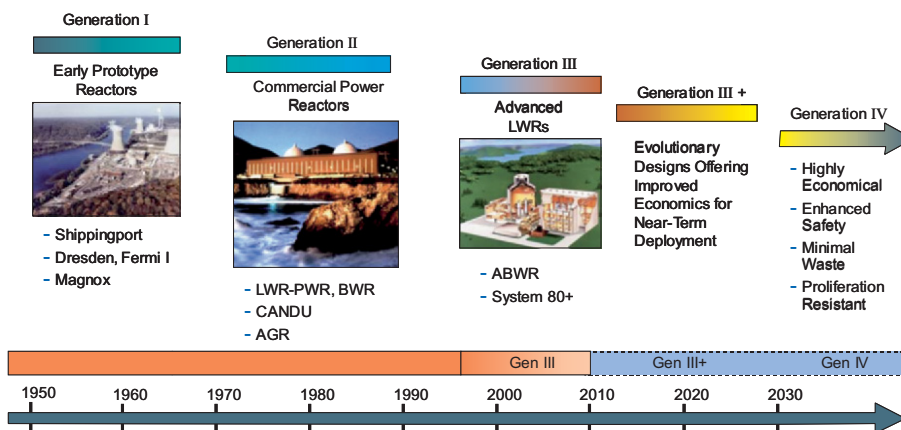


Figure 13. Design generation of nuclear power reactors (IEA, 2002; GIF-IV, 2002).

metal alloys), and system configurations. Based on these early reactor designs, a number of prototypes and demonstration plants were built and operated. These one-of-a-kind plants form **Generation I**. Most of them have been shut down for many years, but they were valuable tools for exploring the potential of nuclear energy.

Gradually, technical challenges and economic considerations narrowed the choices for commercial development to relatively few designs. These **Generation II** plants were the first to be commercially successful. Usually larger than those of Generation I, Generation II plants typically generate 700-1300 megawatts and are mainly cooled by light water. There are two types of LWRs: pressurized water reactors (PWRs) and boiling water reactors (BWRs). These and other main Generation II reactors are listed in TABLE III (Hore-Lacy, 2003).

The role of nuclear power in the national electricity production can be seen from the graph in Fig. 14 (WNA, 2005).

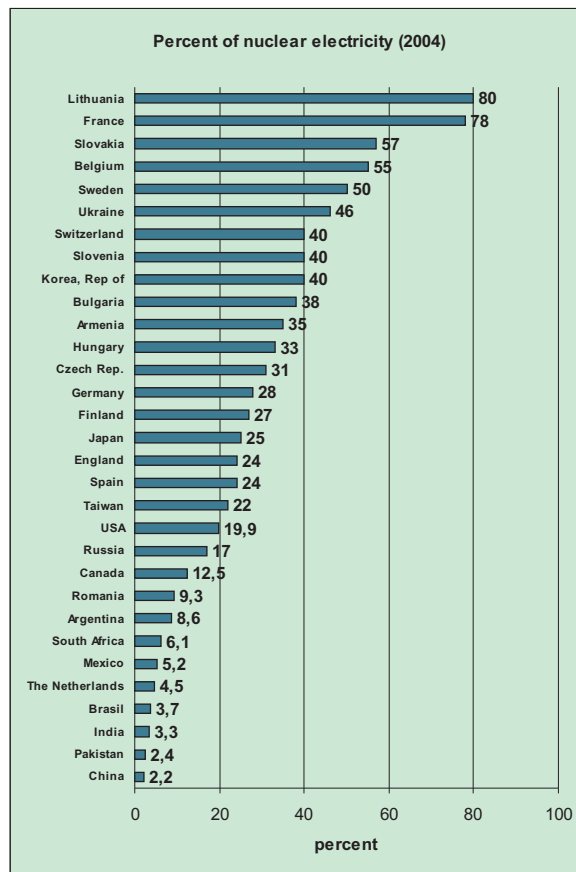


Figure 14. Nuclear percent in national electricity (2004) (Source: WNA (WNA, 2005)).

TABLE III. Nuclear power plants in commercial operation (end 2003) (Hore-Lacy, 2003).

Reactor type	Main Countries	Number	GWe	Fuel	Coolant	Moderator
Pressurised Water Reactor (PWR)	US, France, Japan, Russia	263	237	enriched UO ₂	water	water
Boiling Water Reactor (BWR)	US, Japan, Sweden	92	81	enriched UO ₂	water	water
Gas-cooled Reactor (Magneox & AGR)	UK	26	11	nat. U (metal), enriched UO ₂	CO ₂	graphite
Pressurised Heavy Water Reactor 'CANDU' (PHWR)	Canada	38	19	natural UO ₂	heavy water	heavy water
Light Water Graphite Reactor (RBMK)	Russia	17	13	enriched UO ₂	water	graphite
Fast Neutron Reactor (FBR)	Japan, France, Russia	3	1	PuO ₂ and UO ₂	liquid sodium	none
TOTAL		439	361			

5. Third Generation

Several designs, termed **Generation III**, have been now developed that represent more-or-less evolutionary advances over the reactors of the second generation. The main departure from second-generation designs is that many incorporate passive or inherent safety features², which require no active controls or operational intervention to avoid accidents in the event of malfunction. These designs include both LWR and GCR concepts. The first of Generation III design, General Electric Co's Advanced BWR (ABWR), has achieved a measure of commercial success. Two are in operation in Japan, and several others are under construction in Japan and Taiwan.

Third-generation reactors have (UIC, 2005):

- a standardized design for each type to expedite licensing, reduce capital cost and reduce construction time,
- a simpler and more rugged design, making them easier to operate and less vulnerable to operational upsets,

² Traditional reactor safety systems are "active" in the sense that they involve electrical or mechanical operation on command. Some engineered systems operate passively, e.g., pressure relief valves. Both require parallel redundant systems. Inherent or full passive safety depends only on physical phenomena such as convection, gravity or resistance to high temperatures, not on functioning of engineered components.

TABLE IV. Generation III and III+reactors.

Light water reactors	
ABWR (Advanced Boiling Water Reactor)	IRIS (Int. Reactor Innovative & Secure)
AP-600 & AP-1000	System 80+
APR-1400	SWR-1000
BWR 90+	VVER-1500 (V-448) Russia
EPR (European Pressurised Reactor)	VVER-640 (V-407) Gidropress, Russia
ESBWR	
Heavy water reactors	
ACR (Advanced Candu Reactor)	AHWR (Advanced Heavy Water Reactor)
CANDU-9	CANDU X
High-temperature gas reactors	Fast neutron reactors
AHTR (Advanced High-Temperature Reactor (Molten salt reactor))	BN-800, Russia
BREST, Russia	Super-PRISM, General Electric

- higher availability and longer operating life – typically 60 years,
- reduced possibility of core melt accidents,
- minimal effect on the environment,
- higher burn-up to reduce fuel use and the amount of waste,
- burnable absorbers (“poisons”) to extend fuel life.

The names of Generation III and III+ reactors are listed below in TABLE IV. TABLE V presents main parameters of some large size reactors (UIC, 2005).

There is revival of interest in small and simpler units for generating electricity from nuclear power, and for heat production. The interest is driven both by a desire to reduce capital costs and to provide power away from main grid systems. The technologies involved are diverse, but two leading ones use high temperature helium to drive turbines directly (TABLE VI). Several Generation III small size designs are being well advanced, TABLE VII (UIC, 2005a).

6. Generation IV. Generation IV International Forum (GIF)

There are anticipated potentially more revolutionary nuclear reactor concepts that will require substantial R&D to be realized over a couple of decades or

TABLE V. Large size advanced reactors (Generation III) (UIC, 2005).

Country (Developer)	Reactor	Size MWe	Design Progress	Main Features
US-Japan (GE-Hitachi-Toshiba)	ABWR	1300	Commercial operation in Japan since 1996-7. In US: NRC certified 1997, FOAKE	Evolutionary design; More efficient, less waste; Simplified construction (48 months) and operation
South Korea (derived from Westinghouse)	APR-1400 (PWR)	1400	NRC certified 1997, further developed for new S.Korean Shin Kori 3 & 4, expected to be operating 2010	Evolutionary design; Increased reliability; Simplified construction and operation
USA (Westinghouse)	AP-600, AP-1000 (PWR)	600, 1100	AP-600: NRC certified 1999, FOAKE; AP-1000 NRC design approval 2004	Passive safety features; Simplified construction and operation; 3 years to build; 60-year plant life
Japan (Utilities, Westinghouse, Mitsubishi)	APWR	1500	Basic design in progress, planned at Tsuruga	Hybrid safety features; Simplified construction and operation
France-Germany (Framatome ANP)	EPR (PWR)	1600	Confirmed as future French standard, French design approval; to be built in Finland	Evolutionary design; Improved safety features; High fuel efficiency; Low cost electricity
USA (GE)	ESBWR	1390	Developed from ABWR, pre-certification in USA	Evolutionary design; Short construction time; Enhanced safety features
Germany (Framatome ANP)	SWR-1000 (BWR)	1200	Under development, pre-certification in USA	Innovative design; High fuel efficiency; Passive safety features
Russia (OKBM)	V-448 (PWR)	1500	Replacement for Leningrad and Kursk plants	High fuel efficiency; Enhanced safety
Russia (Gidropress)	V-392 (PWR)	950	Two being built in India, Likely bid for China	Evolutionary design; 60-year plant life; Enhanced safety features
Canada (AECL)	CANDU-9	925-1300	Licensing approval 1997	Evolutionary design; Single stand-alone unit; Flexible fuel requirements; Passive safety features
Canada (AECL)	ACR	700, 1000	ACR-700: pre-certification in USA; ACR-1000 proposed for UK	Evolutionary design; Light water cooling; Low-enriched fuel; Passive safety features

TABLE VI. Small size Generation III reactors (UIC, 2005a).

Light water small reactors	Small high-temperature gas reactors
KLT-40, Russia	HTTR (High-Temperature Test Reactor)
VBER, Russia	PBMR (Pebble Bed Modular Reactor)
ABV, Russia	South Africa GT-MHR (Gas Turbine - Modular Helium Reactor)
CAREM	Russia-USA VHTR - Very High Temperature Reactor

TABLE VII. Small-to-medium Generation III reactors with development well advanced (UIC, 2005a).

Model	Capacity and type	Developer, country
CAREM	27 MWe PWR	CNEA & INVAP, Argentina
KLT-40	35 MWe PWR	OKBM, Russia
MRX	30-100 MWe PWR	JAERI, Japan
IRIS-50	50 MWe PWR	Westinghouse, USA
SMART	100 MWe PWR	KAERI, S.Korea
NP-300	100-300 MWe PWR	Technicatome, France
Modular SBWR	50 MWe BWR	GE & Purdue University, USA
PBMR	165 MWe HTGR	Eskom, South Africa, et al.
GT-MHR	285 MWe HTGR	Gen. Atomics (USA), Minatom (Russia) et al.
BREST	300 MWe LMR	RDIPE (Russia)
FUJI	100 MWe MSR	ITHMSO, Japan-Russia-USA

so. Being successful they will offer significant improvements in performance. These projects have been named **Generation IV** (GIF-IV, 2002). Whereas some of the concepts are quite new, others represent enhanced revivals of old ideas.

Ten countries — Argentina, Brazil, Canada, France, Japan, the Republic of Korea, the Republic of South Africa, Switzerland, the United Kingdom, and the United States — have agreed in 2000 on a framework for international cooperation in research for a future generation of nuclear energy systems, known as Generation IV.

6.1. GOALS FOR GENERATION IV NUCLEAR ENERGY SYSTEMS

Sustainability-1 Generation IV nuclear energy systems will provide sustainable energy generation that meets clean air objectives and promotes long-term availability of systems and effective fuel utilization for worldwide energy production.

Sustainability-2 Generation IV nuclear energy systems will minimize and manage their nuclear waste and notably reduce the long-term stewardship burden, thereby improving protection for the public health and the environment.

Economics-1 Generation IV nuclear energy systems will have a clear life-cycle cost advantage over other energy sources.

Economics-2 Generation IV nuclear energy systems will have a level of financial risk comparable to other energy projects.

Safety and Reliability-1 Generation IV nuclear energy systems operations will excel in safety and reliability.

Safety and Reliability-2 Generation IV nuclear energy systems will have a very low likelihood and degree of reactor core damage.

Safety and Reliability-3 Generation IV nuclear energy systems will eliminate the need for offsite emergency response.

Proliferation Resistance and Physical Protection-1 Generation IV nuclear energy systems will increase the assurance that they are a very unattractive and the least desirable route for diversion or theft of weapons-usable materials, and provide increased physical protection against acts of terrorism.

6.2. GENERATION IV NUCLEAR ENERGY SYSTEMS

The Generation IV roadmap process culminated in 2003 in the selection of six Generation IV systems, TABLE VIII (UIC, 2005b).

1. Gas-Cooled Fast Reactor System (GFR)
2. Lead-Cooled Fast Reactor System (LFR)
3. Molten Salt Reactor System (MSR)
4. Sodium-Cooled Fast Reactor System (SFR)
5. Supercritical-Water-Cooled Reactor System (SCWR)
6. Very-High-Temperature Reactor System (VHTR)

TABLE VIII. Generation IV Nuclear Energy Systems (UIC, 2005b).

	neutron spectrum (fast/ thermal)	coolant	temperature (°C)	pressure*	fuel	fuel cycle	size(s) (MWe)	application
GFR	fast	helium	850	high	U-238+	closed, on site	288	electricity & hydrogen
LFR	fast	Pb-Bi	550-800	low	U-238+	closed, regional	50-150, 300-400, 1200	electricity & hydrogen
MSR	epithermal	fluoride salts	700-800	low	UF in salt	closed	1000	electricity & hydrogen
SFR	fast	sodium	550	low	U-238 & MOX	closed	150-500, 500-1500	electricity
SCWR	thermal or fast	water	510-550	very high	UO ₂	open (thermal), closed (fast)	1500	electricity
VHTR ³	thermal	helium	1000	high	UO ₂ , prism or pebbles	open	250	hydrogen & electricity

7. Conclusions

- In view of the future shortage of fossil carbon fuels the nuclear option should be retained and even developed, especially because it is an important carbon-free source of power.
- Despite the achieved progress, none of the problems restraining the nuclear energy is solved definitively. Nuclear community should perform a great deal of work.
- The future of nuclear power is connected to breeder technology. Thus inevitably the nonproliferation questions should be first resolved.
- Russia with its huge nuclear technology potential is at the forefront of the current progress. The shortage of financing, however, hinders the development.
- Ukraine, without such potential, needs tense international cooperation in R&D. The Ukrainian government is lacking in national nuclear strategy. It exists only as a project.

References

- Alazard-Toux, N. and Bensaid, B. (2004) *Crude oil and natural gas liquids*, Survey of Natural Resources, World Energy Council, London, WEB: <http://www.worldenergy.org/wec-geis/publications/reports/ser/oil/oil.asp>.
- Benka, S. G. (2002) The Energy Challenge, *Physics Today* **55**, no.4, 38–39.
- Clerici, A. (2004) *WEC Survey of Energy Resources 2004*, World Energy Council, Energy Resources Committee, London, WEB: <http://www.worldenergy.org/wec-geis/congress/powerpoints/clericia0904.pps>.
- EIA (2004) *International Energy Outlook 2004*, DOE/EIA-0484(2004), April 2004, Energy Information Administration, Office of Integrated Analysis and Forecasting, U.S. Department of Energy, Washington, DC 20585, WEB: <http://www.eia.doe.gov/oiaf/ieo/index.html>.
- GIF-IV (2002) *A Technology Roadmap for Generation IV Nuclear Energy Systems*, Issued by the U.S. DOE Nuclear Energy Research Advisory Committee and the Generation IV International Forum, GIF-002-00. 03-GA50034.
- Hore-Lacy, I. (2003) *Nuclear Electricity*, 7th edition, Published by the Uranium Information Centre Ltd. and the World Nuclear Association, Chapter 3, Available on the WEB: <http://www.uic.com.au/ne3.htm>.
- Hore-Lacy, I. (2003a) *Nuclear Electricity*, 7th edition, Published by the Uranium Information Centre Ltd. and the World Nuclear Association, Introduction, Available on the WEB: <http://www.uic.com.au/ne.htm>.
- Knapp, R. (2004) *Coal (Including Lignite)*, Survey of Natural Resources, World Energy Council, London, WEB: <http://www.worldenergy.org/wec-geis/publications/reports/ser/coal/coal.asp>.

- IEA (2002) *Key world energy statistics from the IEA*, International Energy Agency, France, WEB: <http://www.iea.org>.
- MIT (2003) *The future of nuclear power*, Interdisciplinary MIT study, Massachusetts Institute of Technology, ISBN 0-615-12420-8.
- Storm, P. K. (2004) *Natural Gas*, Survey of Natural Resources, World Energy Council, London, WEB: <http://www.worldenergy.org/wec-geis/publications/reports/ser/gas/gas.asp>.
- UIC (2005) *Advanced Nuclear Power Reactors*, UIC Nuclear Issues Briefing Paper #16, Uranium Information Centre, April 2005, WEB: <http://www.uic.com.au/nip16.htm>.
- UIC (2005a) *Small Nuclear Power Reactors*, UIC Nuclear Issues Briefing Paper #60, Uranium Information Centre, January 2005, WEB: <http://www.uic.com.au/nip60.htm>.
- UIC (2005b) *Generation IV Nuclear Reactors*, UIC Briefing Paper #77, Uranium Information Centre, April 2005, WEB: <http://www.uic.com.au/nip77.htm>.
- Underhill, D. H. (2004) *Uranium: Part I*, Survey of Natural Resources, World Energy Council, London, WEB: <http://www.worldenergy.org/wec-geis/publications/reports/ser/uranium/uranium.asp>.
- WNA (2004) *Uranium production figures, 1995-2003*, Information and Issue Briefs, World Nuclear Association, June 2004, WEB: <http://www.world-nuclear.org/info/uprod.htm>.
- WNA (2004a) *Supply of Uranium*, Information and Issue Briefs, World Nuclear Association, August 2004, WEB: <http://www.world-nuclear.org/info/inf75.htm>.
- WNA (2004b) *Uranium Markets*, Information and Issue Briefs, World Nuclear Association, October 2004, WEB: <http://www.world-nuclear.org/info/info/inf22.htm>.
- WNA (2005) *World Nuclear Power Reactors 2003-05 and Uranium Requirements*, World Nuclear Association, Information and Issue Briefs, March 2005, WEB: <http://www.world-nuclear.org/info/reactors.htm>.
- Yokobori, K. (2003) *Overview*, World Energy Council, Energy Resources Committee, London, WEB: <http://www.worldenergy.org/wec-geis/publications/reports/ser/overview.asp>.

FAST REACTOR BASED ON THE SELF-SUSTAINED REGIME OF NUCLEAR BURNING WAVE

S.P. Fomin (sfomin@kipt.kharkov.ua), Yu.P. Mel'nik, V.V. Pilipenko
and N.F. Shul'ga

*NSC Kharkov Institute of Physics and Technology,
1, Akademicheskaya str., Kharkov 61108, Ukraine*

Abstract. An approach for description of the space-time evolution of self-organizing nuclear burning wave regime in a critical fast neutron reactor has been developed in the effective multigroup approximation. It is based on solving the non-stationary neutron diffusion equation together with the fuel burn-up equations and the equations of nuclear kinetics for delayed neutron precursor nuclei. The calculations have been carried out in the plane one-dimensional model for a two-zone homogeneous reactor with the metal U–Pu fuel, the Na coolant and constructional material Fe.

Key words: nuclear burning wave, fast neutron reactor, non-stationary diffusion equation, effective multigroup approximation

PACS: 28.41T, 28.52N

1. Introduction

The work is devoted to developing the physical foundations of the new perspective conception of the safe fast reactor (FR). This FR is a new type of long-life operation reactor with the so-called inner safety. This type of inherent safety prevents the appearance of reactivity-initiated accidents in FR by virtue of the physical principles that underlie its design. The FR in distinction from conventional fast reactors has no initial excess reactivity. Therefore, it does not need any reactivity control. Another important peculiarity of FR under consideration is that it operates till the end of its life without any refueling or fuel shuffling. In FR of this type natural or depleted uranium can be used as its fuel, except for the active zone of the initial critical assembly that serves as an ignition region. Thorium can also be useable instead of uranium. The level of fuel burn-up can be essentially high. The FR also has an important merit from the point of view of nuclear proliferation. It does not need a human access during its operation time and so can be placed underground.

The FR operation is based on the non-linear self-organizing regime of the nuclear burning wave (NBW) that arises owing to a high conversion ratio from fertile to fissile materials in the FR. Feoktistov (1989) was the first to

show up this regime in the framework of a schematic one-dimensional model of FR with the U–Pu fuel cycle. In a self-similar approach he proved the existence of the NBW and estimated the velocity of its propagation. However, Feoktistov's model of FR has essential faults. In this model, the equilibrium and critical plutonium densities were considered as certain phenomenological parameters whereas in reality they depend on both the neutron cross-sections and characteristic neutron spectrum. This scheme was restricted to a maximally simplified set of burn-up equations that involved only four components of the nuclear transformation chain and did not take into account the fission products, constructional materials and coolant.

The concept of NBW was further developed in the framework of multi-group diffusion approximation in (Sekimoto et al., 2001). A stationary equilibrium regime of nuclear burn-up (named CANDLE) was studied in the cylindrical model of FR using the self-similar solution approach. Calculations were carried out for a lead-bismuth-eutectic cooled FR with metallic uranium fuel employing a long nuclide chain in the burn-up equations. It was shown that in this steady-state regime the NBW moved with a constant velocity along the reactor without changing its shape.

Teller (1997) considered a long-life FR of a prolate form with fuel of the U-To cycle. He sought for a solution of the problem using the Monte-Carlo based approach. The burning process had the form of a running NBW that started in the ignition zone. Then this wave propagated beyond the ignition zone in an axial direction during the life of reactor.

The mechanism of self-organizing regime in the FR, was also explored in the framework of the quasi-diffusion approach with the help of mathematical modeling in (Gol'din et al., 1995). In the one-dimensional model of FR it was shown that this regime (called as self-adjusting neutron-nuclide regime) could be initiated inside its core at certain conditions. However, as it follows from the results Gol'din et al., this regime does not go over into the NBW regime in the non-stationary scheme considered. The reactor starts to damp earlier than the wave is created.

In our previous work (Fomin et al., 2005), the possibility of creation of a self-organizing regime in the form of a running NBW was proved for a model of critical FR close to a real situation. The requirements of the wave initiation and evolution in space and time were studied. To describe the space-time evolution of NBW, an approach has been developed in the framework of one-group approximation. It includes the non-stationary diffusion equation for neutron transport, the burn-up equations for fuel components and the equations of nuclear kinetics for precursor nuclei of delayed neutrons. Certain properties of the NBW regime were studied, such as the mechanism of reactivity feedback and stability of the NBW regime relative to distortions of the neutron flux.

The calculations have shown that the regime of running NBW can be observed when one uses the effective one-group cross sections obtained by averaging the group cross sections over the group neutron spectrum integrated over the length of the initial critical assembly of FR. It should be noted that the NBW regime did not arise if for this purpose the group neutron fluxes at each space point of the initial critical assembly were used (cf. Gol'din et al.).

In both cases the effective one-group microscopic cross sections remained unchanged during the lifetime of the FR. As a matter of fact, the group neutron fluxes essentially change inside the FR during its operation time. Therefore, the effective one-group microscopic cross sections must also be changed according with this space-time alteration of the neutron spectrum with time.

The purpose of the present paper is to study the influence of the space-time alteration of the group neutron fluxes on the process of NBW initiation and propagation inside the FR under consideration. This can be done considering the multigroup criticality problem at every moment of the FR operation time. The corresponding calculations will be performed in the framework of effective multigroup approximation, which is a modified version of the approach developed in Fomin et al.

2. The calculation scheme

For the description of space-time evolution of the self-organizing NBW in a critical FR it is necessary to solve the set of equations in partial derivatives that includes the non-stationary diffusion equation, the equations of fuel burn-up and the equations of nuclear kinetics.

Hereafter, these equations are written in the one-group approximation for the case of the plane one-dimensional model of FR under consideration.

The non-stationary diffusion equation with taking into account delayed neutrons can be written as

$$\frac{1}{v} \frac{\partial \Phi}{\partial t} - \frac{\partial}{\partial x} \left(D \frac{\partial \Phi}{\partial x} \right) + \Sigma_a \Phi - (1 - \bar{\beta}) (\nu_f \Sigma_f) \Phi = \sum_l \sum_i \lambda_l^i C_l^i, \quad (1)$$

where $\Phi(x, t)$ is the scalar neutron flux, $\Sigma_\alpha(x) = \sum_j \sigma_\alpha^j N_j(x)$ is the macroscopic cross section of the neutron reaction of the α -type (the index α corresponds to the reactions of neutron absorption (a) and fission (f)), $N_j(x)$ is the concentration of j -th nuclide at the point x ; σ_α^j is the corresponding effective one-group microscopic cross section for the j -th nuclide; $\nu_f \Sigma_f = \sum_j \nu_f^j \sigma_f^j N_j(x)$, ν_f^j is the mean number of neutrons produced at a single nuclear fission event for the j -th fissile nuclide; $\beta = \sum_j \beta_j (\nu_f \Sigma_f)_j / \nu_f \Sigma_f$ is the effective fraction of delayed neutrons, $\beta_j = \sum_i \beta_j^i$, and β_j^i , C_j^i and λ_j^i are

the portion of delayed neutrons, the concentration and decay constant of the precursor nuclei in the i -th group of the j -th fissile nuclide, correspondingly; $D(x) = 1/(3\Sigma_{tr}(x))$ is the diffusion coefficient, $\Sigma_{tr}(x)$ is the macroscopic transport cross-section, v is the one-group neutron velocity.

We use the boundary conditions of the third kind for the flux $\Phi(x, t)$ that take into account the presence of an external neutron flux j_{ex} falling onto the left boundary of FR while the right boundary is free

$$\Phi(0, t) - 2D(0, t) \left. \frac{\partial \Phi(x, t)}{\partial x} \right|_{x=0} = 2j_{ex}, \quad (2)$$

$$\Phi(L, t) + 2D(L, t) \left. \frac{\partial \Phi(x, t)}{\partial x} \right|_{x=L} = 0. \quad (3)$$

These conditions are valid for any moment of time within the considered time interval $0 \leq t \leq T$. Besides, the scalar neutron flux in the corresponding critical assembly $\Phi_0(x)$ is chosen as an initial condition for $\Phi(x, t)$ at the moment $t = 0$ for all values x from the space interval $0 \leq x \leq L$.

The burn-up equations describe changing the fuel components with time according to the chain of nuclear transformations. In the case of FR with the U–Pu fuel cycle we consider the chain including only 10 nuclides, whose numeration is presented in TABLE I, to facilitate writing down corresponding equations

$$\frac{\partial N_l}{\partial t} = -(\sigma_{al}\Phi + \Lambda_l) N_l + (\sigma_{cl}\Phi + \Lambda_{(l-1)}) N_{(l-1)}, \quad l = 1 \dots 8, \quad (4)$$

$$\frac{\partial N_9}{\partial t} = \Lambda_6 N_6, \quad (5)$$

$$\frac{\partial N_{10}}{\partial t} = \sum_{l=1,4,5,6,7} \sigma_{fl} N_l \Phi, \quad (6)$$

where $\sigma_{al} = \sigma_{cl} + \sigma_{fl}$, σ_{cl} is the microscopic cross section of radiation neutron capture by the l -th nuclide, $\Lambda_l = \ln 2/T_{1/2}^l$ and $T_{1/2}^l$ are the decay constant and half-life of the l -th nuclide.

TABLE I. The numeration of nuclei in the ^{238}U - ^{239}Pu transformation chain.

No	1	2	3	4	5	6	7	8	9	10
Nucleus	^{238}U	^{239}U	^{239}Np	^{239}Pu	^{240}Pu	^{241}Pu	^{242}Pu	^{243}Am	^{241}Am	FP

The pair of fission fragments produced at every fission event is considered to be one nuclide that we denote by the symbol FP (fission products).

At the initial moment of time the values of nuclide concentrations are

$$N_1(x, t = 0) = N_1^0(x). \quad (7)$$

In the scheme studied we neglect the burn-up of nuclei ^{239}U , ^{239}Np , ^{241}Am , ^{243}Am ($\sigma_{a2} = \sigma_{a3} = \sigma_{a8} = \sigma_{a9} = 0$) because the decrease of their concentrations due to the absorption reactions is small as compared with the processes that have been considered. The changes of the fission fragments as a result of neutron absorption also were not considered.

The NBW regime is a slow process in which the scalar neutron flux Φ varies very weakly during the characteristic decay time of the precursor nuclei that emit delayed neutrons (see, for example, Fomin et al.). In this case, for the nuclear kinetic equations can be used the approximation of one equivalent group of delayed neutrons

$$\frac{\partial C_l}{\partial t} = -\lambda_l C_l + \beta_l (\nu_f \Sigma_f)_l \Phi, \quad (8)$$

$$C_l(x, t = 0) = C_l^0(x), \quad (9)$$

where $\lambda_l = \beta_l / \Sigma_i (\beta_l^i / \lambda_l^i)$.

The complete statement of the non-stationary problem considered above includes the set of 16 non-linear partial differential equations and the corresponding initial and boundary conditions for them as well. We have solved this set of the equations using the finite-difference method. To apply the finite-difference technique, we introduce a rectangular mesh with steps h and τ (uniform for x and variable for t) in the range of the variables x and t . The FR length L was divided into M intervals of a spatial calculation mesh. We have found the solutions of the set of algebraic equations obtained from Eq. (1) in this way using, like in Fomin et al., the implicit Crank-Nicolson difference scheme (Crank et al., 1947). This symmetric-in-time scheme shows an unconditional stability at any relation between space and time steps. It has the approximation of the second order of accuracy in h and τ .

The solution of the burn-up equations (4)-(6) and equations of nuclear kinetics (8) has been simplified assuming that the effective one-group cross sections and the neutron flux Φ are constant during the time intervals τ . As for the constancy of cross-sections, this assumption is well fulfilled for the FR conditions because of a weak sensitivity of the effective cross-sections to changes in the fast neutron energy spectrum. The assumption for Φ can be easily satisfied by choosing sufficiently small time intervals τ , within which the flux value should be taken as $\Phi = (\Phi_n + \Phi_{n+1})/2$, where Φ_n is the flux value at the time layer n . This fact allowed us to obtain an approximate analytical solution of Eqs. (4)-(6) and (8) for the concentrations of the corresponding nuclides at every node of the space mesh for the new time layer $n + 1$ via the solution for layer n (see for details Fomin et al.).

It should be noted that the implicit finite-difference scheme that was used for solving the set of algebraic equations under consideration is non-linear. The neutron flux has been found using the method of successive approximations, in which its values at a new time layer were determined by an iteration procedure (see Fomin et al.).

The expression for the equilibrium concentration of plutonium can be written as (see, for example, Gol'din et al.)

$$\bar{N}_{eq} = \frac{\Lambda_3 N_3}{(\sigma_f^4 + \sigma_c^4 + \sigma_{(n,2n)}^4) \Phi}. \quad (10)$$

where $\sigma_{(n,2n)}^4$ is the cross section of the (n,2n) reaction for ^{239}Pu .

For calculations of the effective one-group microscopic cross sections we used the group neutron fluxes Φ^g (g is the number of neutron energy group) for the initial critical assembly, found from solving the stationary multigroup problem. The calculations were performed in the 26-group approximation using the group neutron constants from (Abagyan et al., 1981). The method of averaging the group cross-sections when passing from a greater number of energy groups to a smaller one is well known (see, for example, Walter et al.). We have used the approach that takes into account the requirement of conservation of rates of corresponding reactions during this procedure.

The scheme of passing from the group microscopic cross sections to the effective one-group cross sections is defined by the relations

$$\sigma_\alpha^l = \sum_{g=1}^{26} \frac{\sigma_\alpha^{gl} \Phi^g}{\Phi_S}, \quad \Phi_S = \sum_{g=1}^{26} \Phi^g, \quad (11)$$

where Φ_S is the neutron flux summed over 26 groups, the index α corresponds to the reactions of neutron capture (c), fission (f) and scattering (s).

The one-group neutron velocity is given by

$$\frac{1}{v} = \frac{1}{\Phi_S} \sum_{g=1}^{26} \frac{\Phi^g}{v^g}, \quad (12)$$

where v^g is the neutron velocity for the group g .

When averaging the transport cross section σ_{tr} , the requirement of conservation of the neutron leakage value was taken into account, which leads to the following expression

$$\sigma_{tr}^l = \sum_{g=1}^{26} \sigma_{tr}^{gl} D^g \Phi^g / \sum_{g=1}^{26} D^g \Phi^g. \quad (13)$$

3. Results and discussion

We have carried out a series of calculations of the NBW regime in the critical FR using the developed procedure of numerical solution of the set of non-linear algebraic equations under consideration. The FR core length, $0 \leq x \leq L$, is divided into $M = 200$ intervals of the spatial calculation mesh. We impose boundary conditions (3), (4) on the scalar neutron flux $\Phi(x, t)$. To create a neutron field in the system, that has to initiate the process of nuclear burning, we assume that the left boundary of the system is exposed to an external neutron flux coming from a source of certain intensity j_{ex} .

We consider a two-zone homogeneous FR with a metal U–Pu fuel of porosity $p = 0.8$ (see figure 1). In the first zone (near the left edge of the reactor) the fuel consists of uranium enriched with plutonium (the ignition zone). The second zone (the breeding zone), adjacent to the ignition one, is filled with ^{238}U (the presence of ^{235}U was neglected in the present FR model). Both zones also include the constructional material Fe and the Na coolant. The plutonium concentration in the enriched zone was chosen so as to be less than the equilibrium plutonium concentration and was equal to 10% of the concentration of fuel nuclei. The isotope composition of plutonium in the fuel was chosen to be as follows:

$$^{239}\text{Pu} : ^{240}\text{Pu} : ^{241}\text{Pu} : ^{242}\text{Pu} = 0.70 : 0.22 : 0.05 : 0.03.$$

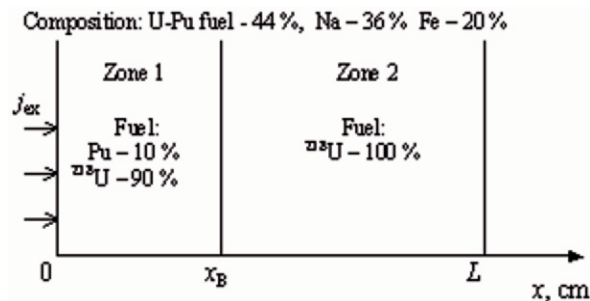


Figure 1. The initial critical assembly of FR.

The sharp boundary between the zones that exists at the initial moment of time would be quickly diffused with time. Therefore, to simplify the calculations, the U–Pu fuel distribution is assumed in the form of the Fermi step function with the parameters x_B and Δ defining the distribution width and diffuseness, respectively (see Fomin et al.).

The initial space distribution of the neutron field corresponding to the neutron flux of the critical FR was normalized so that the averaged energy production density in the enriched zone was equal to $10^{-8} \text{ kW cm}^{-3}$. The intensity of the external neutron flux falling onto the left boundary of FR, which

initiates the burning process, has been chosen to be $j_{ex} = 6 \cdot 10^{11} \text{ cm}^{-2} \text{ s}^{-1}$ for all variants of calculations.

We have chosen the following volume fractions of components in each zone: for the nuclear fuel $F_{fu} = 44\%$, the constructional material $F_{Fe} = 20\%$ and the coolant $F_{Na} = 36\%$. These values of volume fractions were taken to correspond to the composition of actual reactors.

In one of the variants that we have calculated in (Fomin et al., 2005) the corresponding effective one-group microscopic cross sections $\sigma_{\alpha}(x)$ were calculated (see (11)) using the multigroup neutron fluxes $\Phi_0^g(x)$ obtained for the initial critical assembly under study. During the reactor operation period considered in our non-stationary calculation, the values of effective microscopic cross sections $\sigma_{\alpha}^l(x)$ (dependent on the space variable) considered to be unchanged, as it was done in (Gol'din et al., 1995). In this case the variation of the effective one-group cross sections according to the change of neutron spectrum with time was not taken into account. As result the running NBW does not arise, although a little shift of maxima in the space distributions of neutron flux and power is observed. In the reactor, the self-organized regime of nuclear burning is established for a certain time period, being similar to the so-called self-adjusting neutron-nuclide regime that was described in Gol'din et al.

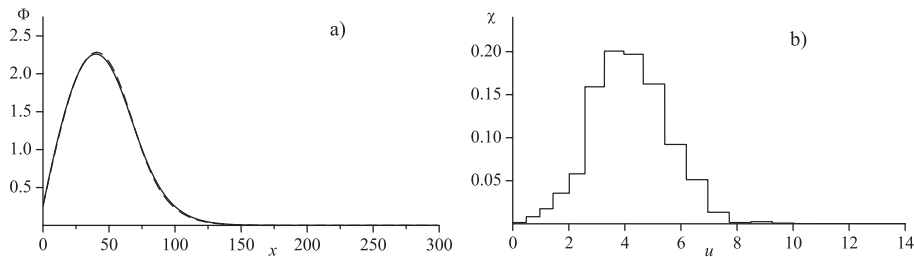


Figure 2. a) The space distribution of neutron flux Φ (in arbitrary units, x in cm) summed over 26 groups (solid curve) and calculated in the one-group approach (dashed curve); b) the neutron spectrum χ averaged over the FR length via lethargy $u = \ln(10.5/E_n)$, where E_n is the neutron energy in MeV.

In the present paper we take into consideration the variation of neutron flux and the effective one-group cross sections in the FR with time. Therefore, at each time layer we solved the multigroup problem for fluxes in the critical FR assembly whose composition changes according to the burn-up equations. In the calculations that are described below, the group neutron fluxes $\Phi^g(x)$ found for the corresponding critical assemblies were used to obtain the effective one group cross sections. Thus, during the whole lifetime of FR the cross sections were corrected in the correspondence to the neutron spectrum alteration that occurred.

Figure 2 presents the results of the calculations of scalar neutron fluxes in a critical assembly of FR that were carried out in the 26-group approximation with the parameters $x_B = 70.5 \text{ cm}$, $\Delta = 4.7495 \text{ cm}$ and $L = 300 \text{ cm}$. These parameter values correspond to $k_{eff} = 1$ for the given variant of FR.

A comparison of the calculation results for the summed neutron flux $\Phi_S(x)$ with the corresponding flux $\Phi(x)$ calculated in the one-group approximation with the effective cross sections $\sigma_\alpha^l(x)$ obtained using the 26-group fluxes $\Phi^g(x)$ is made in figure 2a. As can be seen, the results of calculations in the multigroup approach and in the considered variant of the one-group calculations are close to each other. Therefore, this one-group calculation reproduces the result obtained for the neutron flux in the multigroup approximation in a sufficiently accurate way.

As can be seen from figure 2b, the maximum of the energy spectrum of the considered FR with the metal fuel lies in the region of 200 keV (on the axis of ordinates we plot the integral neutron flux normalized to unity). It should be noted that, depending on the reactor composition, essential distinctions in spectra can be observed, especially in the low energy part. For example, the calculations show that when passing to the oxide fuel a considerable softening of the spectrum occurs in the low energy region. It can also be seen that at neutron energies lower than 10 keV that corresponds to the energy groups with numbers less than 12 the flux rapidly drops. Therefore, the neutrons in FR do not practically get to the thermal energy region. At the energies higher than 1 MeV the form of the calculated multigroup spectrum approaches to that of the fission neutron spectrum.

We have found approximate solutions of the non-stationary problem under consideration in the effective multigroup approach. This approach is based on the above-obtained result that the neutron flux in a critical FR summed over all groups does not practically differ from the one-group flux calculated with the effective cross sections obtained as described above. In this case, the values of effective one-group cross sections at each space point are corrected at each time layer according to the fuel composition that changes with time. The effective cross sections define the coefficients of the implicit Crank-Nicolson difference scheme for the non-stationary one-group diffusion equation. Thus, the scalar one-group neutron flux was found using the procedure developed in Fomin et al. for the numerical solution of the corresponding set of non-linear algebraic equations.

Figure 3 presents the results of calculations of the main characteristics that describe the burning process in FR. It can be seen that the neutron flux Φ and the density of energy production P change with time. By the 100-th day Φ and P reach their maximum values that are approximately 10^3 times higher as compared with their values for the first day of reactor operation (cf. the corresponding curves t_1 and t_3 in figures 3a and 3b). The flux rise

is determined by the expansion of the ignition zone (zone 1 in figure 1) due to the production of additional amount of ^{239}Pu in the breeding zone (zone 2 in figure 1) by means of the reaction of neutron capture by ^{238}U with two successive β -decays $^{239}\text{U} \rightarrow ^{239}\text{Np} \rightarrow ^{239}\text{Pu}$ with the characteristic time $t \approx 2.5$ days (see figure 3c).

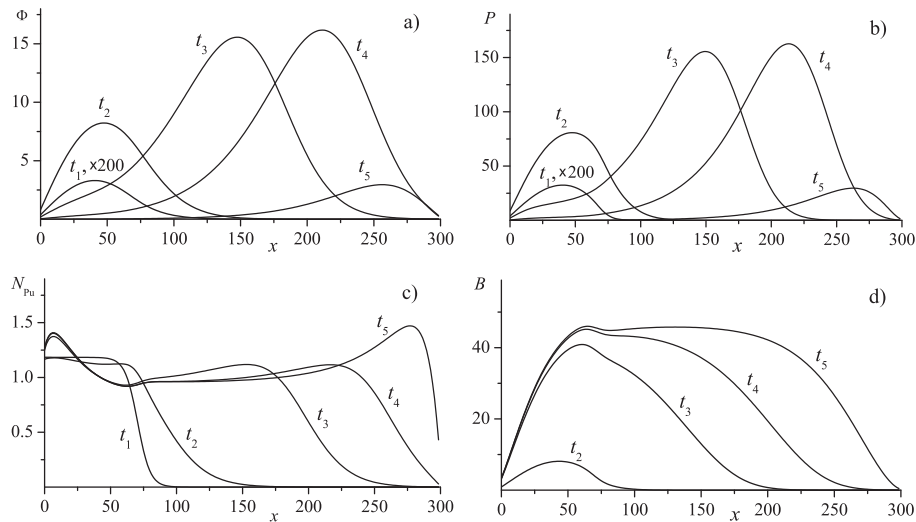


Figure 3. The NBW regime in FR: a) the scalar neutron flux $\Phi(x)$ ($\times 10^{17} \text{ cm}^{-2} \text{ s}^{-1}$); b) the power density $P(x)$ (kW cm^{-3}); c) the ^{239}Pu concentration $N_{\text{Pu}}(x)$ ($\times 10^{21} \text{ cm}^{-3}$); d) the fuel burn-up depth $B(x)$ (%) for $t_1 = 1$, $t_2 = 80$, $t_3 = 120$, $t_4 = 140$ and $t_5 = 170$ days (x in cm).

Along with production of ^{239}Pu the accumulation of large amount of fission products occurs in FR. This leads to the increase of neutron absorption in the system that stops further flux rise after $t \approx 100$ days. After this moment the space profiles of $\Phi(x)$ and $P(x)$ do not practically change moving with an almost constant velocity $V \sim 3 \text{ cm/day}$ (see figure 4a) along the x -axis through the breeding zone until they do not reach the right boundary of FR (cf. corresponding curves for t_3 and t_4 in figures 3a and 3b). This stage of the neutron flux evolution in the reactor properly speaking represents the NBW regime.

In the NBW regime the FR is automatically sustained in a state close to the critical one during a long time. For the 3 m long FR under consideration the NBW stage goes on during about forty days (see figures 3a and 3b). The self-organizing NBW regime is determined by the nuclear processes, in which the burn-up of the produced ^{239}Pu excess occurs instantaneously, whereas the increase of its concentration by means of two successive β -decays of ^{239}U and ^{239}Np nuclei is a relatively slow process. Therefore, the described

processes implement an intrinsic reactivity feedback that ensures the reactor operation stability during a long time period (see the discussion in Fomin et al.).

The width of NBW profile is determined by the critical parameters of the FR and for the chosen FR composition it is about 70 cm (see figures 3a and 3b). The length of the considered reactor (3 m) is enough to demonstrate the genesis of the NBW and the beginning of its slow propagation along the reactor. Reaching the right boundary of FR the NBW dies out during about 80 days. Characteristic NBW profiles for this stage are presented for the moment $t_5 = 170$ days, which are featured by considerably lower values of the neutron flux and energy production.

After the extinction of the reactor, plutonium and the nuclear fission products are distributed with a practically uniform concentration over the whole length of the reactor core, except for the regions close to its boundaries (see figure 3c). By the extinction moment the fuel burn-up depth reaches a high level of 40 – 50% (see figure 3d). It can be seen from figure 3 that in the breeding zone an intense accumulation of plutonium occurs and the isotope that burns up is practically ^{238}U .

The effect of the sharp changing the neutron flux in FR, in particular, due to turning the external flux j_{ex} off after 10 days is demonstrated in figure 4 and figure 5. One can see that the velocity V and neutron flux integrated over the reactor length Φ_I calculated without turning the external flux j_{ex} off increase more rapidly than in the case when the source of this flux is turned off after 10 days from the moment of its turning on.

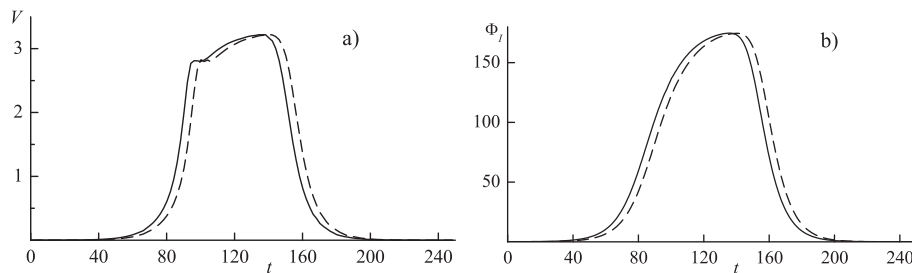


Figure 4. The NBW velocity $V(\text{cm d}^{-1})$ (a) and the integral neutron flux $\Phi_I (\times 10^{18} \text{ cm}^{-1} \text{ s}^{-1})$ (b) versus time (days). Solid curves were calculated without turning j_{ex} off, the dashed ones are for j_{ex} turned off at $t_{off} = 10$ days. The conditions correspond to figure 3.

It follows from figure 5 that at the moment of turning the external neutron flux off the magnitude of the integral flux in the reactor first decreases. This decrease is followed by an increase of the flux magnitude and then by oscillations that are gradually damped. Therefore, the reactor itself quenches the

arising perturbation in approximately 30 days at the very beginning stage of the NBW genesis. Turning the external flux source off at a later time moment (after 30 days, for example) does not practically affect the integral neutron flux behavior. Thus, the self-organized burning regime that arose before the moment of turning j_{ex} off is stable.

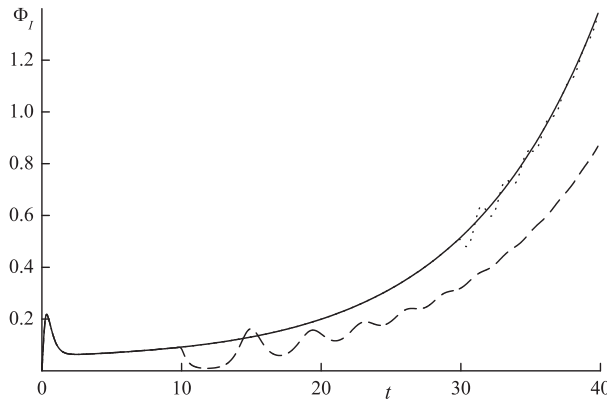


Figure 5. The integral neutron flux Φ_I ($\times 10^{18} \text{ cm}^{-1} \text{ s}^{-1}$) at the initial stage of burning versus time (days). The solid curve was calculated without turning j_{ex} off, the dashed one is for j_{ex} turned off at $t_{off} = 10$ days and the dotted one is for j_{ex} turned off at $t_{off} = 30$ days. The conditions correspond to figure 3.

If we increase the external flux intensity by an order of magnitude, then the curves for the wave velocity and integral neutron flux in the FR are similar to those shown in figure 4 but are shifted down in time. Although the perturbation of the integral neutron flux that arises when the more intense external flux is turned off is much greater, the picture of the damped oscillations of this perturbation is similar to the one shown in figure 5. The amplitude and duration of these oscillations are essentially greater than in the previous case, nevertheless the stability of the regime of our interest is not violated.

4. Conclusions

The feasibility of creating a self-organizing non-linear regime in the form of a running wave of nuclear burning in a critical FR is studied.

The solution of the corresponding non-stationary problem was found in the framework of effective multigroup diffusion approach. The approach takes into account the variation of the effective one-group cross sections according to the alteration of the group neutron spectrum with time that corresponds to the real situation. This allowed us to describe the peculiarities of the NBW regime in the FR.

Taking into account the neutron spectrum alteration effects leads to qualitative changes of the space-time behavior of the scalar neutron flux, as compared with the results obtained in (Gol'din et al., 1995). In contrast to Gol'din et al., the NBW arises in the FR. Its front moves with an approximately constant velocity from the ignition zone boundary towards the region with low plutonium concentration.

In the FR of length 3 m under consideration the self-organizing nuclear burning regime can be divided into three time periods: the NBW genesis stage (≈ 100 days), the NBW propagation stage (≈ 40 days) and the extinction stage (≈ 80 days).

In the NBW regime FR sustains in a state close to the critical one without any control during a fairly long time (in principal years depending on the reactor length). An intrinsic reactivity feedback is governed by the non-linearity of the NBW regime. This feedback prevents the reactor from the runaway regime and ensures the stable evolution of the self-organizing NBW process.

The average fuel burn-up of about 50% can be attained inside the FR.

The present results show a notable stability of the NBW regime to distortions of the neutron flux.

It should be noted that the values of the neutron flux and density of energy production in the hypothetical FR under consideration are rather high. To obtain more realistic parameters of the FR that would be applicable from the practical point of view, it is necessary to use more complete mathematical models for the description of the NBW regime. Of great interest would also be similar investigations for the FR with the thorium-uranium fuel.

References

- Abagyan, L. P. et al. (1981) *Group Constants for Calculations of Reactor and Shielding*, Moscow, Energoizdat (in Russian).
- Crank, J. Nicolson, P. (1947) A practical method for numerical evaluation of solutions of partial differential equations of the heat-conduction type, *Proc. Camb. Phil. Soc.* **43**, 50-67.
- Feoktistov, L. P. (1989) Neutron-fissioning wave, *Dokl. Akad. Nauk SSSR* **309**, 864-867 (in Russian).
- Fomin, S. P., Mel'nik, Yu. P., Pilipenko, V. V., Shul'ga, N. F. (2005) Investigation of Self-Organization of the Non-Linear Nuclear Burning Regime in Fast Neutron Reactors, *Annals of Nuclear Energy* **32**, 1435-1456.
- Goldin, V. Ya., Anistratov, D. Yu. (1995) Fast neutron reactor in a self-adjusting neutron-nuclide regime, *Mathematical Modelling* **7**, 12-32 (in Russian).
- Sekimoto, H., Ryu, K., Yoshimura, Y. (2001) CANDLE: The New Burnup Strategy, *Nucl. Sci. Engin.* **139**, 306-317.
- Teller, E. (1997) Nuclear Energy for the Third Millennium, *Preprint UCRL-JC-129547*, LLNL.
- Walter, A. E., Reynolds, A. B. (1981) *Fast Breeder Reactors*, New York, Pergamon Press.

ON THE SUBCRITICAL AMPLIFIER OF NEUTRON FLUX BASED ON ENRICHED URANIUM

V.A. Babenko^a, V.I. Gulik^b, L.L. Jenkovszky^a, V.N. Pavlovich^b, E.A. Pupirina^c

^a*Bogolyubov Institute for Theoretical Physics, National Academy of Sciences of Ukraine, Kiev*

^b*Institute for Nuclear Research, National Academy of Sciences of Ukraine, Kiev*

^c*Institute of the NPP Safety Problems, National Academy of Sciences of Ukraine, Kiev*

Abstract. Further progress in nuclear power engineering to large extent will depend on the solution of two basic problems: improvement of the safety level and on the efficient transmutation of the long-lived radioactive waste. Possible solutions of these problems consist in the construction of subcritical systems capable to multiply neutrons from an external source.

In the present paper we examine the main aspects of the construction of such systems, with emphasis on the choice of the neutron source and optimization of the parameters of the subcritical system. We calculate the neutron flux amplification factor for a one-zone spherical systems made of enriched uranium, water solution of the enriched uranium, and for the spherical enriched uranium system with a reflector.

1. Introduction

Studies by different authors [1, 2] show that the construction of accelerator-driven subcritical systems is a promising way in nuclear power engineering. Such systems enable to improve the safety level and to work out efficient methods of transmutation of long-lived radioactive waste.

The theoretic background of the accelerator-driven subcritical systems can be found e.g. in Ref. [3]. Preliminary results of our studies were published (in Russian) in Ref. [3].

Here we investigate the amplification of the neutron flux by a number of subcritical systems, namely by a homogeneous spherical assembly made of enriched uranium, by a homogeneous spherical assembly made

of water solution of enriched uranium, and by a homogeneous spherical assembly made of enriched uranium and containing a beryllium reflector.

2. Description of the assemblies

The main objective of our investigation is to establish the basic features in the behaviour of the amplification factors of neutron flux and energy depending on primary features of the assembly - such as the nuclide composition, energy of neutrons of the external source, effective multiplication factor of the system, ratio of nuclear concentrations. Studies of such model assemblies is of interest for a better understanding of amplification properties of more complicated systems and for the optimization of their parameters. Even such simple systems show a number of nontrivial properties concerning amplification of neutron flux. In particular, the amplification factors have nonmonotonic behaviour depending on the uranium enrichment and on the ratio of the nuclear concentrations (H/U). We choose the physical systems to be slightly subcritical, namely we fix the value of the neutron effective multiplication factor of each system to be equal $k_{eff} = 0.99$.

We consider a point-like isotropic source of neutrons with energy of $14MeV$ to be the “external” source, which is located at the centre of a spherical subcritical assembly. Although realistic neutron sources from $D - T$ reactions are neither isotropic nor monoenergetic, the simplified model we use is rather typical and it is frequently used. The geometric dimensions (radius) of the assembly are fixed by the requirement that the effective multiplication factor of the system be equal to some specified value, which is slightly less than unity, i.e. the assembly should be slightly subcritical. Calculations of the amplification factors and other physical characteristics of the systems under consideration were performed with the help of the neutron Monte Carlo transport code MCNP-4C [4], which employs the latest ENDF/B-VI nuclear data library.

Our choice of the neutron source energy, $14MeV$, was motivated by two factors. Firstly, there are two possibilities to obtain neutrons from the interaction of accelerated charged particles with matter, namely with the help of the $D - T$ reaction and by means of a spallation process. Spallation reactions produce neutrons from the interaction of fast charged particles (for example, protons with energy $\sim 1GeV$) with nuclei of heavy metals (for example, with a mixture of lead and bismuth) [5]. Fusion reaction may be accomplished with the help of

deuteron accelerators working at the energy $100 - 200\text{KeV}$ and with a currents $\sim \text{Ampere}$. Such a current is capable to yield a neutron flux equivalent to the neutron flux produced by proton accelerators with energy $\sim 1\text{GeV}$ and a current $\sim \text{mA}$. Any project based on $D-T$ reaction costs a few times less than the one based on spallation. Secondly, spallation neutrons have a rather wide energy spectrum with the maximum between $200 - 300\text{MeV}$. Neutron cross-sections in this region, however, are not known sufficiently well and they are not available for all nuclides needed. Since relevant cross-section libraries in this energy range are missing, calculation with the neutron source from spallation process is problematic. At the same time the neutron source with the energy of 14MeV , resulting from a $D - T$ reaction, is available technically, the neutron cross-sections in this energy range being well known and collected in relevant libraries. Therefore we find important studies of the efficiency of transmutation with 14-MeV neutrons and the compare of the results with those, obtained with spallation neutrons.

3. Results

First we consider a one-zone homogeneous spherical assembly made of enriched uranium. We fix the value of the neutron effective multiplication factor of the system at $k_{eff} = 0.99$. Any variation of the uranium enrichment w in the isotope ^{235}U , at a fixed value of k_{eff} , results in a change of the assembly radius R . To be more specific, the decrease of the uranium enrichment results in the decrease of the multiplication factor of an infinite medium k_{∞} , and hence the radius of the system should increase in order to keep the value of $k_{eff} = 0.99$ constant.

As already mentioned, we consider the external source of neutrons to be point-like, isotropic and monoenergetic with the energy $E_0 = 14\text{MeV}$. It is located at the centre of a spherical assembly. We define the flux amplification factor q as the ratio of the total number of neutrons passing through the external boundary surface in a time unit N_S , to the intensity of the neutron source I_0 , i.e. to the number of neutrons emitted by the source in a time unit $q = N_S/I_0$. It will be convenient to choose the intensity of the neutron source to be equal to unity, $I_0 = 1\text{n/sec}$, i.e. our results are normalized to be per starting single neutron from the source. The amplification factors, obviously, does not depend on the normalization. We define the energy amplification factor G as the ratio of the total energy deposition in the system to the source energy E_0 .

We study the dependence of the flux amplification factor q and the energy amplification factor G on the uranium enrichment w_{U235}

for the system under consideration. The results of our calculations are presented in Table 1 together with the calculated values of the multiplication factor of an infinite medium k_∞ , of the radius of the assembly R , of the mean neutron flux in the volume $\bar{\Phi}$, and of the neutron flux through the external boundary of the system Φ_S . The values of the fission density ρ_{fis} (which means the number of fissions per volume unit), and the total number of fissions in the system N_{fis} are also presented.

Table 1. Physical properties of a one-zone spherical amplifier of neutron flux made of enriched uranium, as functions of the uranium enrichment. The value of the neutron effective multiplication factor of the system is fixed at $k_{eff} = 0.99$. The external neutron source, which is pointlike, isotropic and monoenergetic, is located in the centre of the system. The energy of the source is $E_0 = 14MeV$, and the intensity of the source is $I_0 = 1n/sec$.

$w_{U235},$ %	k_∞	$R,$ cm	$\bar{\Phi},$ $n/cm^2 \cdot sec$	$\Phi_S,$ $n/cm^2 \cdot sec$	$\rho_{fis},$ $1/cm^3 \cdot sec$	$N_{fis},$ 1/sec	G	q
6	1.07	85.81	$4.99 \cdot 10^{-3}$	$2.29 \cdot 10^{-4}$	$2.89 \cdot 10^{-5}$	76.46	988.61	21.19
7	1.18	56.38	$1.59 \cdot 10^{-2}$	$1.23 \cdot 10^{-3}$	$1.04 \cdot 10^{-4}$	78.42	1013.94	49.03
8	1.26	45.34	$2.74 \cdot 10^{-2}$	$2.69 \cdot 10^{-3}$	$2.02 \cdot 10^{-4}$	78.72	1017.79	69.50
9	1.34	39.13	$3.83 \cdot 10^{-2}$	$4.38 \cdot 10^{-3}$	$3.11 \cdot 10^{-4}$	78.19	1010.89	84.38
10	1.41	35.05	$4.82 \cdot 10^{-2}$	$6.17 \cdot 10^{-3}$	$4.28 \cdot 10^{-4}$	78.33	996.54	95.12
20	1.82	20.81	$1.15 \cdot 10^{-1}$	$2.39 \cdot 10^{-2}$	$1.83 \cdot 10^{-3}$	77.08	892.29	130.34
30	2.01	16.38	$1.59 \cdot 10^{-1}$	$4.00 \cdot 10^{-2}$	$3.53 \cdot 10^{-3}$	64.85	838.16	135.01
40	2.12	13.93	$2.00 \cdot 10^{-1}$	$5.68 \cdot 10^{-2}$	$5.63 \cdot 10^{-3}$	63.81	824.67	138.53
50	2.20	12.32	$2.45 \cdot 10^{-1}$	$7.55 \cdot 10^{-2}$	$8.28 \cdot 10^{-3}$	64.77	837.09	143.81
60	2.25	11.13	$2.93 \cdot 10^{-1}$	$9.62 \cdot 10^{-2}$	$1.15 \cdot 10^{-2}$	66.60	860.60	149.86
70	2.29	10.22	$3.46 \cdot 10^{-1}$	$1.19 \cdot 10^{-1}$	$1.54 \cdot 10^{-2}$	68.96	891.14	156.54
80	2.32	9.49	$4.12 \cdot 10^{-1}$	$1.48 \cdot 10^{-1}$	$2.05 \cdot 10^{-2}$	73.30	947.15	167.36
90	2.35	8.88	$4.76 \cdot 10^{-1}$	$1.77 \cdot 10^{-1}$	$2.61 \cdot 10^{-2}$	76.42	987.39	175.19
100	2.37	8.36	$5.67 \cdot 10^{-1}$	$2.17 \cdot 10^{-1}$	$3.38 \cdot 10^{-2}$	82.92	1071.31	190.52

The main features of the system were found to be as follows. The flux amplification factor q depends monotonically on the enrichment and it increases with the increase of the enrichment. At the same time the energy amplification factor G , depending on enrichment, decreases,

reaching a minimum, followed by a subsequent rise (see Table 1 and Figs. 1, 2). To scrutinize this phenomenon, we have calculated also the fission density and the total number of fissions in the system (see Table 1). The fission density monotonically increases with the growth of the enrichment, while the total number of fissions has the same dependence on the enrichment as the energy amplification factor G . Such a behaviour may be explained as follows. Inasmuch as we fix the neutron effective multiplication factor, we have a large volume of

Table 2. Total mean free path of neutrons in the medium and mean free path before the fission as functions of the uranium enrichment for a one-zone homogeneous spherical assembly made of the enriched uranium.

$w_{U235}, \%$	R, cm	L_{tot}, cm	L_{fis}, cm	L_{fis}/R
6	85.81	2.04	172.71	2.01
7	56.38	2.07	151.75	2.69
8	45.34	2.09	135.65	2.99
9	39.13	2.12	122.88	3.14
10	35.05	2.14	112.49	3.21
20	20.81	2.27	63.00	3.03
30	16.37	2.35	44.99	2.75
40	13.93	2.40	35.48	2.55
50	12.31	2.45	29.54	2.40
60	11.13	2.48	25.44	2.29
70	10.22	2.50	22.43	2.19
80	9.49	2.53	20.12	2.12
90	8.88	2.55	18.27	2.06
100	8.36	2.56	16.76	2.00

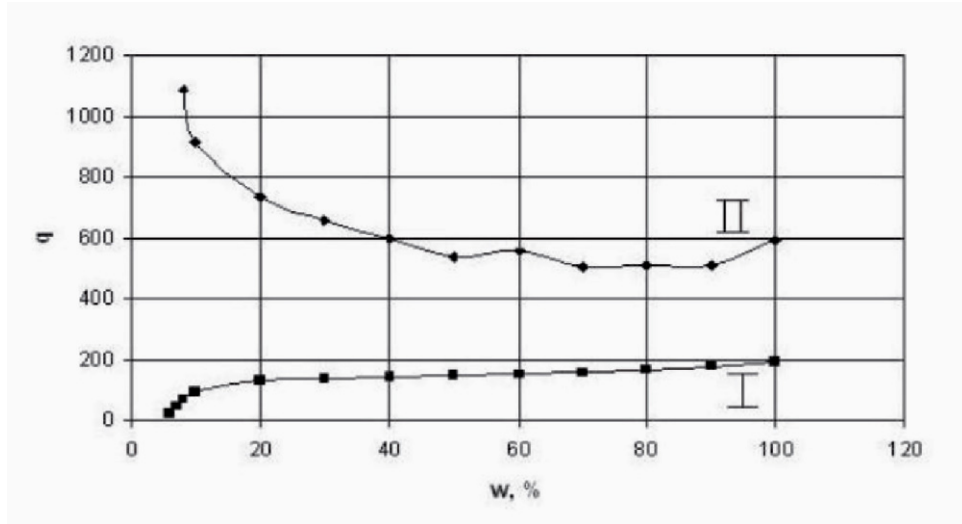


Figure 1. The neutron flux amplification factor versus the uranium enrichment. I — system without any reflector, II — system with beryllium reflector.

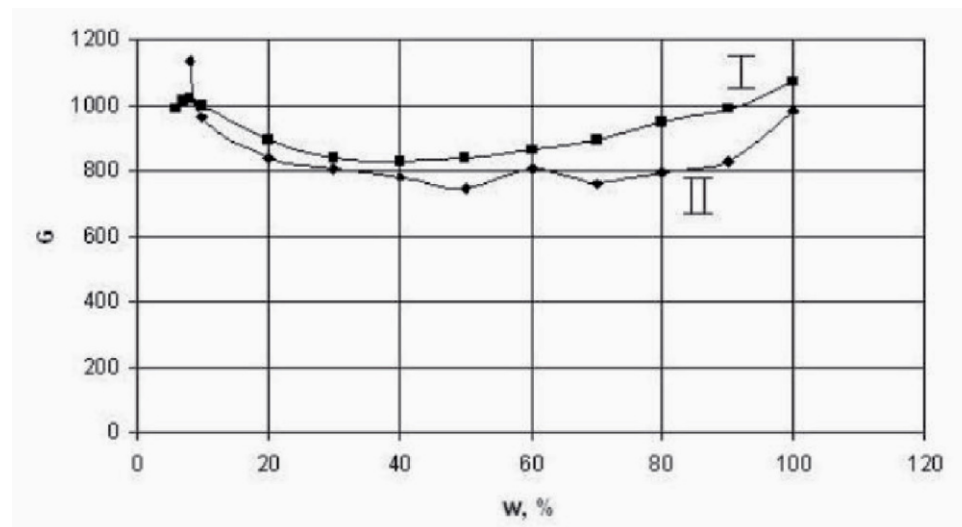


Figure 2. The energy amplification factor versus the uranium enrichment. I — system without any reflector, II — system with beryllium reflector.

the system at low enrichment and most of neutrons have time to be absorbed. By increasing the enrichment, the dimensions of the system decrease and part of the neutrons simply do not have time to interact with uranium (see Table 2 support this phenomenon). Here L_{tot} is a total mean free path of neutrons in the medium, L_{fis} is the mean free

path before the fission. We thus conclude that the maximal amplification factor will appear in the system with dimensions exceeding the neutron mean free path before the fission ($1/\Sigma_{fis}$).

It should be noted that while the flux amplification factor q is falling slowly in the range of the enrichment between 100 and 20 percents, it starts decreasing drastically below $w < 20\%$. So, it is advantageous to choose the enrichment of the system to be slightly greater than 20%.

In a similar way, we consider a one-zone spherical assembly involving water solution of the enriched uranium. At fixed value of $k_{eff} = 0.99$, the radius of the assembly R will change, depending on the ratio of nuclear concentrations of the moderator (hydrogen) and the fuel (uranium) - H/U . The main parameters necessary for calculations were determined similarly to the first system.

We have calculated the flux amplification factor q and the energy amplification factor G as functions of the ratio of nuclear concentrations H/U , sometimes called "moderation parameter". The results of calculations are presented in Table 3, together with the values of the radius of the system R , the volume of the system V , the mean free path of the neutron L_{tot} , and the neutron mean free path before the fission L_{fis} .

The main features of this system were found to be the following. The dependence of the flux amplification factor q on the ratio of nuclear concentrations H/U shows a nonmonotonic behaviour (see Fig. 3). First, as the moderation parameter H/U increases, q starts increasing very slowly, but then it jumps at the value of the moderation parameter $H/U = 0.5$. Subsequently q increases and reaches a maximum at $H/U = 2 - 3$, whereupon it starts decreasing. This dependence also has a jump at values $H/U = 15$ and $H/U = 50$. Thus, the dependence of the flux amplification factor on the moderation parameter has a pronounced maximum at $H/U = 2 - 3$. This result can be used to construct feasible assemblies. The energy amplification factor G has a similar dependence on the moderation parameter H/U , the only difference being that there is a minimum at $H/U = 500$, followed by a slight increase.

We have also calculated the properties of the subcritical system with a reflector. The spherical system under consideration is made of a core involving enriched uranium and a beryllium reflector 50cm thick. The parameters of the system were chosen similarly to the previous cases to achieve the fixed value of neutron effective multiplication factor $k_{eff} = 0.99$.

Table 3. Amplification factors and other physical characteristics as functions of the moderation parameter for a one-zone spherical assembly involving water solution of the enriched uranium.

H/U	R, cm	V, cm^3	q	G	L_{fis}, cm	L_{tot}, cm
0.0001	8.377	2462.37	171.233	960.2714	16.84524	2.577012
0.0005	8.382	2466.79	171.744	962.7500	16.85188	2.576257
0.001	8.388	2472.09	168.829	947.2500	16.8506	2.576097
0.005	8.401	2483.60	176.630	991.0214	16.88639	2.572807
0.01	8.414	2495.15	172.063	967.3500	16.92226	2.567789
0.05	8.553	2620.86	180.124	1018.071	17.22229	2.531544
0.1	8.708	2765.95	192.501	1095.579	17.57097	2.487461
0.5	9.691	3812.36	275.874	1652.207	19.54832	2.197037
1	10.528	4887.94	348.202	2188.836	21.06218	1.972522
2	11.622	6575.54	419.654	2814.507	22.94609	1.735358
3	12.315	7823.33	348.351	2426.221	24.2008	1.612303
4	12.782	8747.52	223.486	1591.136	25.11427	1.535745
5	13.109	9436.20	172.750	1245.621	25.84373	1.482758
10	13.831	11082.8	89.8052	659.0771	27.98335	1.350692
15	14.043	11600.3	53.2601	385.8764	29.21852	1.293725
20	14.128	11812.2	46.2400	331.7121	30.09629	1.258828
25	14.174	11928.0	43.2266	308.2293	30.66048	1.231354
30	14.206	12008.9	31.5489	221.4721	31.41745	1.219358
35	14.236	12085.2	26.0852	180.8243	32.05519	1.206755
40	14.263	12154.1	27.0735	187.1864	32.44564	1.190629
45	14.293	12230.9	24.409	167.5779	32.91605	1.180125
50	14.328	12321.0	23.1536	158.4000	33.31658	1.169539
100	14.658	13192.1	12.9954	85.06857	37.25373	1.110468

200	15.545	15734.8	9.717	63.45700	43.02007	1.024013
300	16.465	18697.1	8.37102	55.90264	47.9047	0.963363
400	17.435	22200.1	7.24806	49.82293	52.84375	0.921062
500	18.455	26328.8	7.13538	51.27821	57.04997	0.881092
600	19.558	31337.3	7.00582	53.19929	61.16092	0.848517
700	20.718	37250.5	6.88028	55.348	65.15647	0.821667
800	22.008	44560.9	6.851	58.94607	69.03865	0.798449
900	23.375	53498.7	7.0863	66.07914	72.50314	0.776008
1000	24.925	64862.6	6.91704	69.80257	76.39028	0.759799

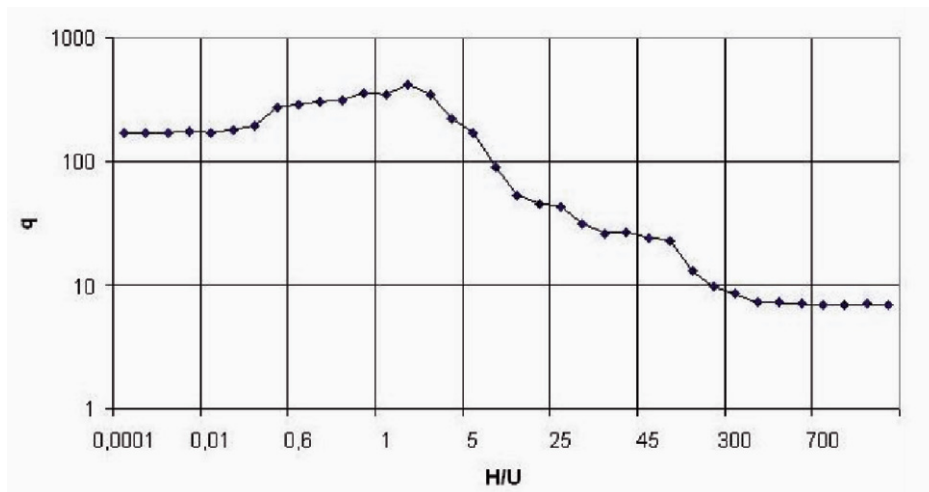


Figure 3. Neutron flux amplification factor versus the moderation parameter for a one-zone spherical assembly involving water solution of the enriched uranium.

The increase of the flux amplification factor q amounts to 3–5 times for the system with beryllium reflector. At the same time, the nature of the q -dependence on the enrichment also changes (Fig. 1). As to the energy amplification factor G , it does not change neither by magnitude, nor by the character of its dependence (Fig. 2). The last fact is due to decrease of the fission volume of the system with a reflector at fixed value of $k_{eff} = 0.99$.

4. Conclusion

Thus, even a very simple one-zone subcritical system makes possible a neutron flux amplification by 1 to 2 orders of magnitude and energy amplification by 2 to 3 orders. Another interesting result is that relatively low enrichments (10% – 20%) yield energy amplifications close to those at high enrichment, which is very advantageous from the economical point of view. The flux amplification factor varies insignificantly in the interval of enrichments between 20% and 40%, but decreases drastically at smaller enrichments. Hence a system of a 20% enrichment in uranium-235 can serve as a reasonable amplifier both in flux and energy.

A subcritical system involving water solution of uranium-235 enables one to obtain better values of amplification factors as compared to a system made of metallic uranium. These values amount to $q = 420$ for the flux amplification factor, and $G = 2800$ for the energy amplification factor.

A system with a reflector enables one to increase the flux amplification factor 3 – 5 times compared to a similar system without any reflector. The flux amplification factor reaches the value $q = 500 - 900$ in this case, and the energy amplification factor reaches the value $G = 800 - 1000$.

The results on the enhancement of the amplification factors of subcritical neutron-multiplying systems make only part of our research program. The characteristics of more advanced multi-zone systems, as well as the possibility to use alternative fissile materials will be studied in the future. In particular, two-zone systems are of great interest since the utilization of a booster involving a material with $k_{\infty} > 1$ makes it possible to increase the amplification factor significantly [6]. However, even the present stage of the study shows that subcritical neutron-multiplying assemblies are promising alternatives to the reactors as powerful sources of neutrons, suggesting various applications in nuclear physics and nuclear power engineering.

References

- 1 C. Rubia et al., CERN/AT/95-44(ET) (1995).
- 2 C. D. Bowman, *Annu. Rev. Nucl. Part. Sci.* **48**, 505 (1998).
- 3 V. A. Babenko, L. L. Jenkovszky, V. N. Pavlovich, E.A. Pupirina, *VANT* **6**, 13 (2002) (in Russian).

- 4 J. F. Briesmeister, Ed., "MCNP - A General Monte Carlo N-Particle Transport Code, Version 4C", LA-13709-M (2000).
- 5 Accelerator driven systems: Energy generation and transmutation of nuclear waste. IAEA, 1997.
- 6 H. Daniel, Yu.V. Petrov, Nucl. Instr. and Meth. in Phys. Res. A **373**, 131 (1996).

TRANSMUTATION OF FISSION PRODUCTS AND MINOR ACTINIDES IN A SUBCRITICAL ASSEMBLY DRIVEN BY A NEUTRON GENERATOR

H.I. Kiyavitskaya^a, I.G. Serafimovich^a, V.V. Bournos^a,
Yu.G. Fokov^a, S.V. Korneev^a, S.E. Mazanik^a,
A.A. Adamovich^a, C.C. Routkovskaia^a, A.V. Koulikovskaya^a,
A.M. Khilmanovich^b, B.A. Martsynkevich^b, T.N. Korbut^b,
S.E. Chigrinov

^a *Joint Institute for Power & Nuclear Research-Sosny,
NAS, Belarus, Minsk, acad. A.K. Krasin str., 99*

^b *B.I. Stepanov'Institute of Physics,
NAS, Belarus, Minsk, pr. Skaryny, 68*

Abstract. The use of low energy accelerators and neutron generators to investigate the physics of multiplying systems, driven by high energy ($E_p = 0.6 - 2.0\text{GeV}$) particles accelerators is discussed. The prospects of the subcritical facility "Yalina" driven by a neutron generator, to study sub-critical systems driven by an external neutron sources is investigated.

1. Introduction

The application of high energy accelerators in reactors is based on the utilization of high-energy spallation reactions for neutron production on targets with $A > 150$ (Pb, Bi, W, U, Pb-Bi), with subsequent multiplication of produced neutrons in sub-critical blankets ($k_{eff} \sim 0.9-0.98$) [1, 2, 3, 4]. In such systems high neutron flux densities ($\Phi \sim 10^{15}-10^{17}$ n/(cm²·s) can be achieved, which is one of the main conditions for the transmutation of radioactive nuclides. Experimental studies at sub-critical systems now are only planned since they are complicated, expensive and time-consuming; moreover they cannot be realized with the existing accelerators since most of them have inappropriate beam parameters. Therefore experimental studies of various aspects of ADS on the basis of low energy accelerators – cyclotrons, microtrons, as well as deuterium and tritium ions accelerators representing neutron generators of high intensity – are of great importance [5].

2. Interaction of high-energy radiation with matter

The interaction of high-energy particles in the energy range from several MeV to 10 GeV is a very complicated process involving a large number of heavy particles (n, p, π -mesons) with electromagnetic interactions, nuclear reactions, formation and development of nuclear cascade involved [6]. The propagation of the high-energy radiation through a dense medium is accompanied mainly by two types of interactions: the electromagnetic and nuclear ones. The main part of the energy losses occurs due to ionization. The nuclear interaction results in the production of new particles whose number and characteristics depend on the properties the initial particle. The development of a nucleon-meson (intranuclear) cascade depends on the medium characteristics, as well as on the energy and type of the primary particles. The development of intranuclear cascade attenuates as new particles with lower energy are produced, and finally it results in the scattering, moderation and absorption of neutrons. In fissionable media such a chain of nuclear reactions includes also fission of heavy nuclei by high energy particles and by neutrons of evaporation and fission spectra too.

As shown by theoretical and experimental studies, the main part of the spectrum of neutrons emitted from neutron-producing lead target of ADS contain neutrons in the energy range $E_n < 15\text{--}20$ MeV. By irradiating the targets containing fissionable nuclei (Th, U, Pu,...), a substantial contribution to the neutron component in the energy range of 1–2 MeV will be made by neutrons generated in fission reactions, so the energy distribution of the neutron flux density will be defined by the material composition of the medium. The fraction of high energy particles will obviously decrease as the target size increases due to the reduction of the number of elastic and inelastic interactions, and the spectrum of neutrons escaping from heavy targets will be defined mainly by 15–20 MeV neutrons formed mainly at the slow evaporation stage of a nuclear reaction. It should be noted that starting from the mechanism of pre-equilibrium and cascade stages of nuclear reactions, that are defined by properties of two-particles N-N and π -N interactions, one should expect that in the energy range corresponding to these stages of reactions $15 \text{ MeV} \leq E_n \leq 70 \text{ MeV}$ the spectra will also be

identical. In the 14 MeV neutron interaction the pre-equilibrium (fast) and equilibrium stages can also be excluded. So, it should be expected that the distribution dN/dE will be the same as in the high-energy range. Thus, one should expect that the leakage spectra from extended heavy targets irradiated by 14 MeV neutrons or by high energy protons ($E_p \approx 0.8-2.0$ GeV) will be the same in the energy range of $E_n < 15-20$ MeV. It results in the independence of neutron spectra upon the type of the projectile particle and the material of the target. In this connection the distribution of neutrons with $E_n < 15-20$ MeV escaped from the targets will be identical both for 14 MeV neutrons and for protons with energy about some GeV:

$$F(E_i) = \frac{E_p^2}{N_{sp} E_i} \frac{dN_i}{dE_i}, \quad (1)$$

where E_i is the energy of neutrons escaping from thick targets; E_p is the energy of projectile particle; N_{sp} is the number of neutrons escaping from a target with energy $E_n < 15-20$ MeV. This conclusion is demonstrated by Fig. 1-3.

So, the main contribution to $d^2\sigma/dEd\Omega$ comes from neutrons of low energies ($E_n < 15-20$ MeV) whose energy distribution is close to "the evaporation" spectrum – in contrast to the high-energy part that formed due to the cascade and pre-equilibrium stages. It is obvious that the fraction of the cascade particles is determined by the target dimension, and will decrease with increasing dimensions. The similarity of $d^2\sigma/dEd\Omega$ distributions in the energy range $E_n < 15-20$ MeV provides a principal possibility for the application of proton $E_p < 100-150$ MeV and deuterium ions accelerators, where the main contribution to nucleon cascade comes from the reaction $d+A \rightarrow n + \dots$ and electron accelerators (microtrons) in which spallation neutrons source is formed due to photo-spallation reactions $\gamma+A \rightarrow n+X$ for investigations of the ADS-technology. The evidence for the independence of the energy distribution of neutrons generated in spallation reactions in extended heavy targets upon the energy of primary proton beam are the results of experimental investigations of ^{129}I , ^{237}Np transmutation by relativistic protons ($0.5 < E_p < 7.4$ GeV) carried out at JINR (Dubna, Russia). It was found that the transmutation rates of $^{129}\text{I}(n,\gamma)^{130}\text{I}$ and $^{237}\text{Np}(n,\gamma)^{238}\text{Np}$ related to one neutron generated in neutron-producing Pb target do not depend on the proton energy. It should be stressed that these considerations became

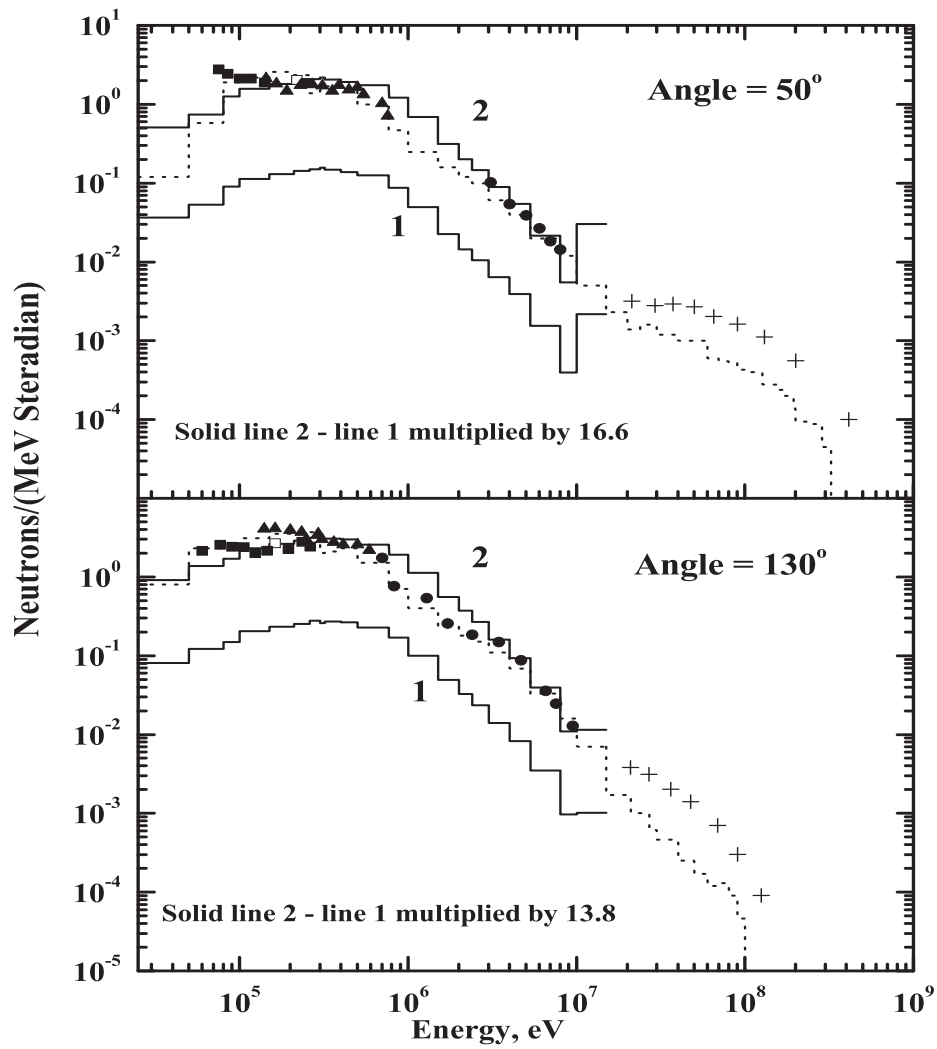


Figure 1. Comparison of the experimental and calculated spectra of neutrons from Pb target (D=15 cm, L=30 cm) irradiated by 1.5 GeV protons and 14.1 MeV neutrons [7]. Histograms are results of calculations with the computer code LAHET [8]. The dots are experimental data [9]

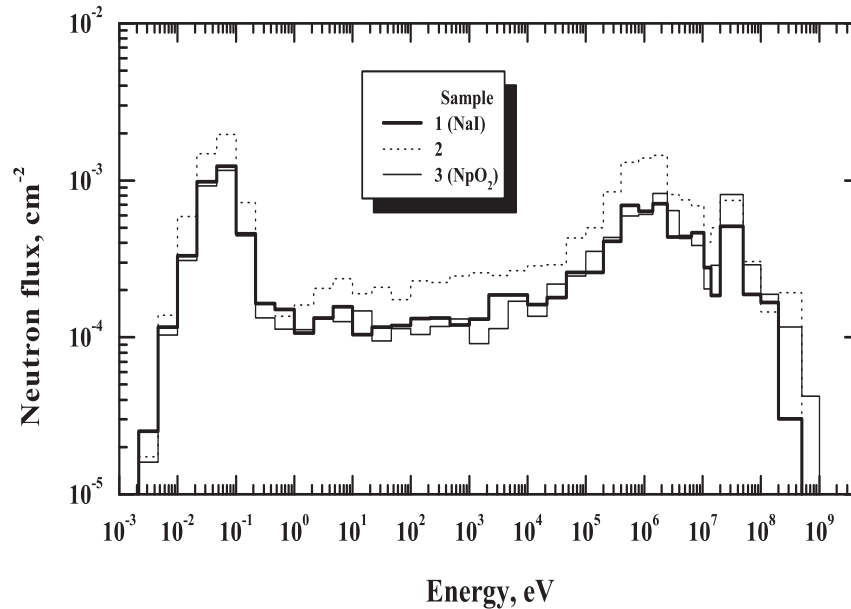


Figure 2. Calculated energy distributions averaged over the sample volumes at relevant sites. The normalization was performed per one 3.7 GeV proton.

a basic argument for setting up the subcritical facility “Yalina” to carry out experimental investigations of sub-critical systems driven by external neutron sources. The facility consists of sub-critical assembly driven by a neutron generator operating both in continuous and pulse modes.

3. Sub-critical facility “Yalina”

According to the generally accepted principles of the ADS-technology [1, 4, 5], any experimental facility consists of deuterium ions accelerator with Ti ^3H or Ti ^2H targets (neutron generator), a sub-critical assembly loaded by uranium dioxide (10% of ^{235}U), a polyethylene moderator and a Pb neutron-producing target, irradiated by neutrons with energy 14.1 or 2.5 MeV (Fig. 4).

The sub-critical assembly of “Yalina” facility is uranium-polyethylene multiplying system ($k_{max} < 0.98$), located inside a graphite reflector of parallelepiped configuration with side a dimension of 1000 and 1200 mm, arranged of high purity “reactor graphite”

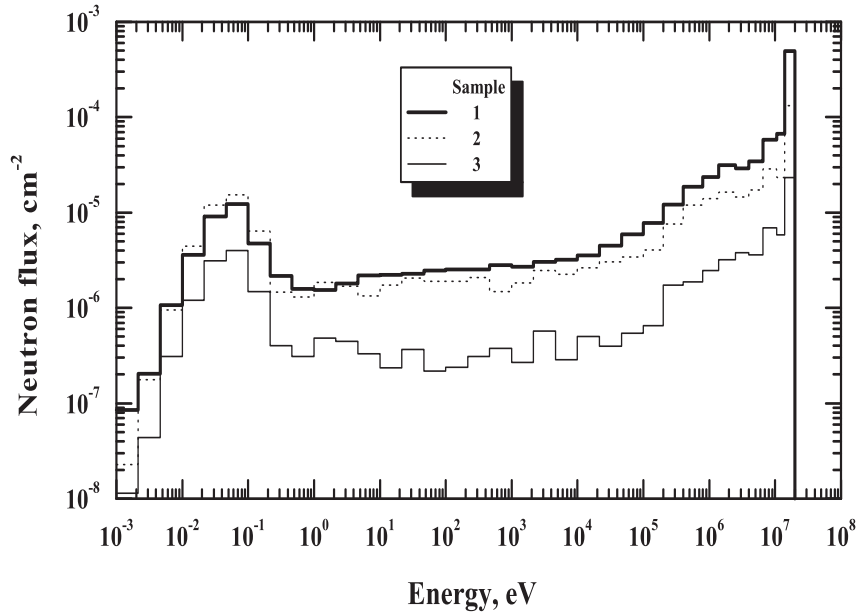


Figure 3. The same as in Fig. 2 but for neutrons as incident particles. The energy and the angle were sampled from distribution relevant to the reaction ${}^3\text{H}(\text{d},\text{t}){}^4\text{He}$ for E_d equal to 250 keV. The normalization was performed per one neutron.

blocks ($200 \times 200 \times 500$ mm). The core of the assembly has a of parallelepiped configuration too ($400 \times 400 \times 600$ mm) and consists of “bare” polyethylene sub-assemblies, where the fuel rods of EK-10 type (UO_2 of 10% enrichment by ${}^{235}\text{U}$) are located. On the whole, the fuel subassembly contains of 9 blocks (in height) made of polyethylene ($\rho = 0.927$ g/cm³) ($80 \times 80 \times 63$ mm) and 16 fuel rods of EK-10 – type located in channels ($D = 11$ mm). At the core center a neutron-producing Pb target is located, made of 12 blocks (in height) with side dimensions $80 \times 80 \times 50$ mm, that reminds a fuel subassembly by shape and size. The graphite reflector (thickness ~ 500 mm) is covered from outside by Cd-layer (1mm thickness). At distances $R = 50$ mm, 100 mm, 150 mm from the core center three experimental channels ($D = 25$ mm) are situated for the location of samples of radioactive targets and various detectors for the measurement of neutron flux density functionals. For the same purpose two axial channels ($D = 25$ mm) are located in a graphite reflector at distances 250 mm and 358 mm; by $Z = H/2$

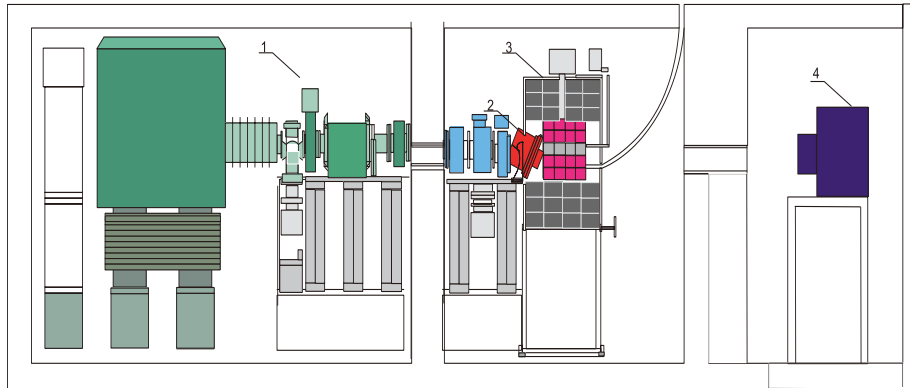


Figure 4. Sub-critical facility “Yalina”: 1 – neutron generator; 2 – Ti^3H (TiD) target system; 3 – sub-critical assembly; 4 – gamma-spectrometer.

and another radial channel ($D = 25$ mm) is located. On the whole, the core of the sub-critical assembly contains 20 fuel subassemblies, 4 control rods and Pb target of the same shape as fuel subassembly.

4. Neutron generator NG-12-1

The neutron generator is a linear accelerator of deuterium ions produced at duoplasmatron and accelerated to energies $E_d = 250$ keV. The accelerator magnet system separates D^+ those ions that by means of electromagnetic lenses are directed towards the Ti^3H or TiD targets, where in reactions $\text{d}(\text{T}, \text{n})^4\text{He}$ and $\text{d}(\text{D}, \text{n})^3\text{He}$ neutrons are generated with energies $E_n = 13\text{--}15$ MeV and $E_n = 2.5\text{--}3.0$ MeV, respectively. At present, highly effective water-cooled targets with diameters 230 and 45 mm are used in experimental programs.

The energy distribution of neutrons in the sub-critical systems is the main parameter that defines most of the ADS-technology characteristics, above all the transmutation of minor-actinides and long-lived fission fragments. In Fig. 5 the neutron spectrum in the energy range 0.3 – 13.0 MeV measured at the core center with the application of the developed method is compared with the spectrum calculated by the MCNP code [10].

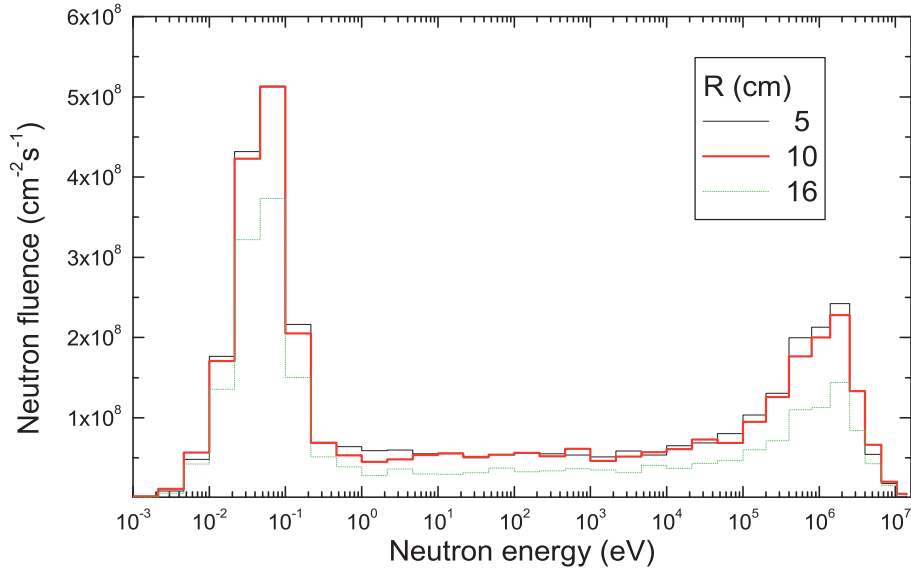


Figure 5. Energy distribution of neutrons flux in the sub-critical assembly “Yalina”.

The results of our calculations agree with the experimental data. One of the main characteristics of the thermal neutron spectrum is the cadmium ratio R_{Cd} that demonstrates the contribution of thermal neutrons to the total neutron spectrum. The comparison of the calculated and experimental data on radial distribution of cadmium ratio for reactions $^{237}\text{Np}(n,\gamma)^{238}\text{Np}$ and $^{243}\text{Am}(n,\gamma)^{244}\text{Am}$ in the core driven by external neutron source $d(T,n)^4\text{He}$ located outside the core ($Z = -38\text{ cm}$) is shown in Fig. 6.

Radionuclides ^{237}Np and ^{243}Am (NpO_2 and AmO_2 samples) were placed into cadmium containers (1.5 mm) and then located at central part of the core experimental channels. The samples were irradiated in the core of the sub-critical assembly during 3 hours. Analysis of the obtained results shows that calculated data agree well with experimental ones that confirms the applicability of MCNP-4B code and evaluated nuclear data libraries for estimation of MA and LLFP transmutation rates in sub-critical systems with thermal neutron spectrum.

One of the main aspects of the ADS-technology is the transmutation of MA and LLFP. In this respect “Yalina” the facility due

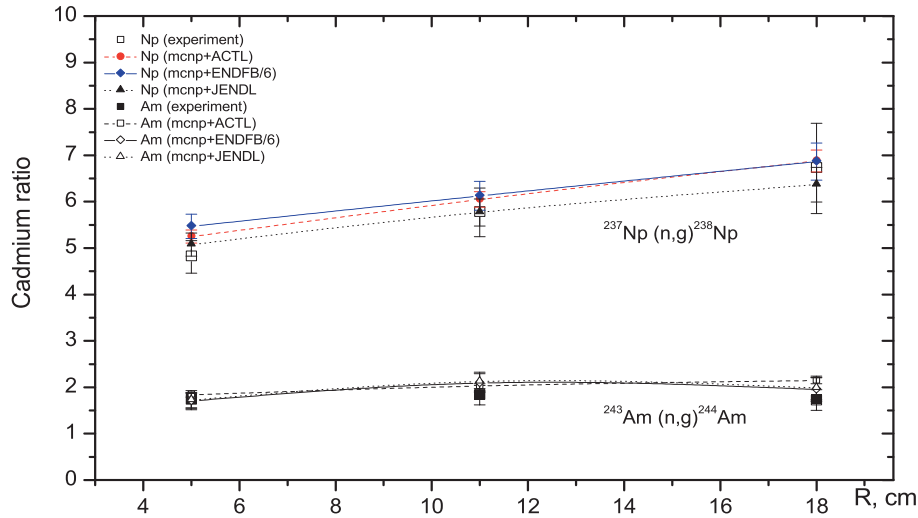


Figure 6. Radial distribution of Cd ratio of reactions $^{237}\text{Np}(n,\gamma)^{238}\text{Np}$ and $^{243}\text{Am}(n,\gamma)^{244}\text{Am}$ ($N_r=280$, $Z_s=-38$ cm, $E_n=14$ MeV)

to high neutron flux density in the core, the possibility of a core sub-criticality level variation ($0.90 < k_{eff} \leq 0.98$), the application of various neutron sources and configurations “external neutron source–core” gives a unique opportunity for the investigation of the details of the MA and LLFP transmutation in ADS with thermal a neutron spectrum that is of special interest for testing computer codes and evaluated nuclear data libraries. The calculated and measured spatial distributions of $^{129}\text{I}(n,\gamma)^{130}\text{I}$, $^{237}\text{Np}(n,\gamma)^{238}\text{Np}$ and $^{243}\text{Am}(n,\gamma)^{244}\text{Am}$ reaction rates in the core loaded by 280 fuel rods in the case when the sub-critical assembly is driven by a neutron generator operating with a DT-target located outside the core at the distance 38 cm from it’s center are presented Fig. 6.

5. Conclusion

The possibility of the application of low-energy accelerators and neutron generators for investigations in the field of physics of multiplying system driven by high-energy ($E_p \sim 0.6-2.0$ GeV) particle accelerators has been shown. A distinctive feature of the created

facility is the possibility to vary the core configuration to carry out experiments by sub-criticality levels up to $k_{eff} \leq 0.98$, application of various neutron external sources [^{252}Cf ; $\text{D}(\text{D},\text{n})^3\text{He}$; $\text{D}(\text{T},\text{n})^4\text{He}$] with various locations relative to the core center.

References

- 1 C.D. Bowman, Accelerator Driven Systems in Nuclear Energy. Role and Technical Approach: Report ADNA/97-013. ADNA Corporation/ Los Alamos.- New Mexico, 1997.
- 2 R.G. Vasilkov, V.I. Goldanskiy, V.L. Gelepov, V.P. Dmitriyevskiy, Electronuclear Method of Neutron Generation, Atomic Energy, 1970.-V.29, N 3. -P.151 – 158. (In Russian)
- 3 C. Rubbia, J.O. Rubio, S. Buono et al., CERN – group. Conceptual Design of a Fast Neutron Operated High Power Energy Amplifier, Accelerator Driven Systems: Energy Generation and Transmutation of Nuclear Waste: Status Report/ IAEA-TECDOC-985.-Vienna, 1997, P. 187 – 312.
- 4 M. Salvatores, M. Martini, I. Slessarev et al. MUSE-1: a First Experiment at MASURCA to Validate Physics of Sub-critical Multiplying Systems Relevant to ADS, IAEA-Techdoc-985.- Vienna, 1997, P. 430 - 436.
- 5 S.E. Chigrinov, H.I. Kiyavitskaya, Yu.G. Fokov et al., The Research on Accelerator Driven Systems at the NAS of Belarus, IAEA –TM-25032, TWG-FR/108.-49.- Vienna, 2002.
- 6 S.E. Chigrinov, H.I. Kiyavitskaya, A.M. Khilmanovich et al., Experimental Research of the Transmutation of Long - Lived Fission Products and Minor – Actinides in a Sub-critical Assembly Driven by a Neutron Generator, In Proc. ADTTA'96-Conf.-Kalmar, Sweden, 1996, P.737-744.
- 7 A.N. Kalinovskiy, N.V. Mokhov, Yu.P. Nikitin, Transport of High Energy Particles through a Matter, Moscow, Energoatomizdat, 1985, p. 248 (In Russian).
- 8 R.E. Prael, H. Lichtenstein, User Guide to LSC: the LAHET Code System: Report LAUR-89-3014, Los Alamos National Laboratory, 1989.
- 9 R.R. Fullwood, J.A. Cramer, R.A. Haarman et al., Neutron Production by Medium Energy Protons on Heavy Metal Targets: Report LA-4789 UC-34, Los Alamos, New Mexico, 1972.
- 10 J.F. Briesmeister, MCNP – A General Purpose N-Particle Transport Code, Version 4B: Report LA-12625-M/ Los Alamos National Laboratory, 1997.

EXPERIMENT AND RADIATION SAFETY AT COLLIDERS

V. Pugatch*

Institute for Nuclear Research, National Academy of Science of Ukraine,

Prospekt Nauki 47, 03680, Kiev-28, Ukraine

Abstract. The emphasis is made on the novel radiation monitoring systems at colliders based on the Metal Foil Detector technology. The radiation monitoring systems for the HERA-B experiment (DESY, Hamburg) as well as for the Silicon Tracker of the LHCb experiment (CERN, Geneva) are described. The micro-strip Metal Foil Detector used for the beam profile monitoring is briefly presented.

1. Introduction

The radiation safety at collider experiments is an important issue for their success. There are well tested devices used for the radiation monitoring discussed in details elsewhere [1]. We shall concentrate ourselves in this article on the novel approach to the radiation monitoring based on the Metal Foil Detector (MFD) technology developed recently [2]. The MFD is on the way to become the thinnest detector ever built for the monitoring of the high energy particle fluxes as far as 10-50 nm thickness saturates SEE yield which is high enough for the MFD operation, meanwhile. There are few MFD advantages.

- Extremely low mass (up to few tens nano-meter thickness) of the detecting material;
- Simple structure (thin metal foils supported by the isolating frame) at any shape and size;
- Low operating voltage;
- Simple read-out electronics (charge integrators and scalers);
- High radiation tolerance;
- Perfect long term performance without any maintenance;
- Low costs.

* E-mail address: *Valery.Pugatch@cern.ch*

Metal Foil Detector

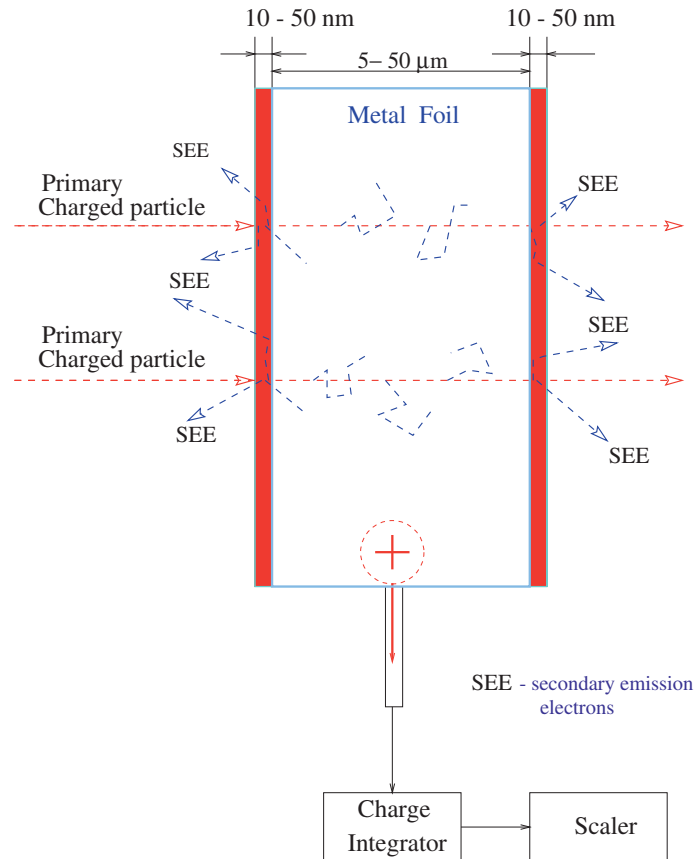


Figure 1. Scheme of a single-layer Metal Foil Detector.

MFDs proved to be a reliable tool for the charged particle radiation monitoring in a wide range of applications [2].

2. Metal Foil Detector principle

Physics and registration principles of the Metal Foil Detector (MFD) are as follows. Fast particles hitting a metal foil initiate Secondary Electron Emission (SEE). SEE occurs at (Fig. 1) 10-50 nm layers of both metal sensor surfaces [3, 4]. Auxiliary (two accelerating and two grounding) foils hermetize the sensor from both sides and stabilize the SEE yield, which is measured by a sensitive Charge Integrator with built-in current-to-frequency converter. This reduces the external

impact, essentially. Stable operation of the SEE monitor has been established under the impact of fluence of 10^{20} protons/cm² [5]. The first SEE monitor has been built in 1955 [6]. To our knowledge the principle has not been explored for the radiation monitoring with a large area sensors, placed in an atmosphere. We present here some of the MFD prototypes and real devices built and tested at accelerators and colliders of KINR (Kiev), DESY (Hamburg), M.P.I. für Kernphysik (Heidelberg) and CERN (Geneva). The fast single-charged particle fluxes exceeding few thousands per second per MFD sensor were reliably measured.

3. MFD for the Radiation Monitoring at the HERA-B experiment

The HERA storage ring at DESY (Hamburg) accumulates 920 GeV protons (≈ 80 mA) and 27 GeV positrons (≈ 30 mA). At its four straight sections it houses four experiments. H1 and ZEUS are the experiments with colliding e-p beams. The HERMES experiment deals with the electron beam scattered at an internal polarized gas target whereas the HERA-B experiment utilizes the proton beam scattered at internal multi-wire target. A single-layer MFD-structure was explored for the multi-target steering at the HERA-B experiment [7]. To provide an effective reconstruction of vertices the Interaction Rate (up to 40 MHz, by design) has to be equally distributed over 8 targets being operated simultaneously in the proximity to the beam core (2-3 mm). The HERA-B targets are thin conductive ribbons connected through the UHV feedthroughs to charge integrators. While scintillating counters are sensitive to the non-target background, Charge Integrators respond to the corresponding individual target-beam interaction, only. It was observed that hodoscopes could have omitted huge spikes in the IR (a saturation of the photo-multiplierlast dinodes). If not accounted properly this might lead to the wrong determination of the delivered luminosity and in worst cases to the radiation damage of expensive equipment. To provide a fully automatic operation of the target the Target Control System (TaCoS) has been developed. User interaction is limited to choosing the interaction rate and the desired target configuration only. The most important features of TaCoS are the following:

- insertion and retraction of targets.
- stabilization of the interaction rate;
- equal distribution of the interaction rate over the operated targets;

- emergency handling (to prevent the target system and the detector from being damaged by unintentionally high rates);
- an easy to communicate graphical user interface.

The main feedback signals for TaCoS are provided by the overall interaction rate measured by hodoscopes and partial interaction rates measured by the charge integrators. In an ≈ 10 Hz steering loop TaCoS compares these rates with the anticipated ones given by the user. If the rate is too small the targets are moved closer towards the beam center, in case the rate is too large TaCoS retracts the targets. A proper step-size is calculated internally using a set of predefined parameters and the actual relative rate deviation.

For radiation safety issue the TaCoS handles any emergency situation with the highest priority and starts to retract the targets as soon as any spike in the rate occurs or any failure inside the system is detected. In case the data exchange is interrupted all targets are automatically retracted to their end-switches. The same action occurs if the hard-wired emergency-out button is pressed. This provides the maximum possible security in case of computer problems. Another security aspect is the experiment protection against unintentional high rates. Spikes in the interaction rate are handled by an efficient emergency system: if the interaction rate exceeds a given threshold all operated targets are immediately retracted. The background rate measured by a setup of scintillating counters upstream of the experiment is also used to detect background emergency situation. An external data (HERA and other experiments etc.) are read from various online data servers, stored in online databases and used for monitoring and (if needed) correction in the target system operation. The online monitoring is very essential, for the operation of the target as well as for the coordination with other groups. All rate information together with the target positions are stored in online database servers.

The five-layer MFD technology (Fig. 2) has been used for the radiation monitoring at HERA-B. To minimize the Coulomb multiple-scattering 12 sectors (inner radius - 20 mm, outer one - 220 mm) of sensor foils as well as auxiliary components were manufactured out of 50 μm thick Al foils. The MFD Luminosity monitor has been installed around the beam pipe at the exit window of the Vertex Detector System. A perfect linear and stable response of the MFD monitors to the IR measured by hodoscopes in the range up to 140 MHz has been established. Similar MFD Luminosity and Radiation Monitoring System are under construction for the LHCb experiment [12].

The sensitivity of the MFD to the radiation flux is determined by the sensitivity of the charge integrators as well as by fluctuations of the

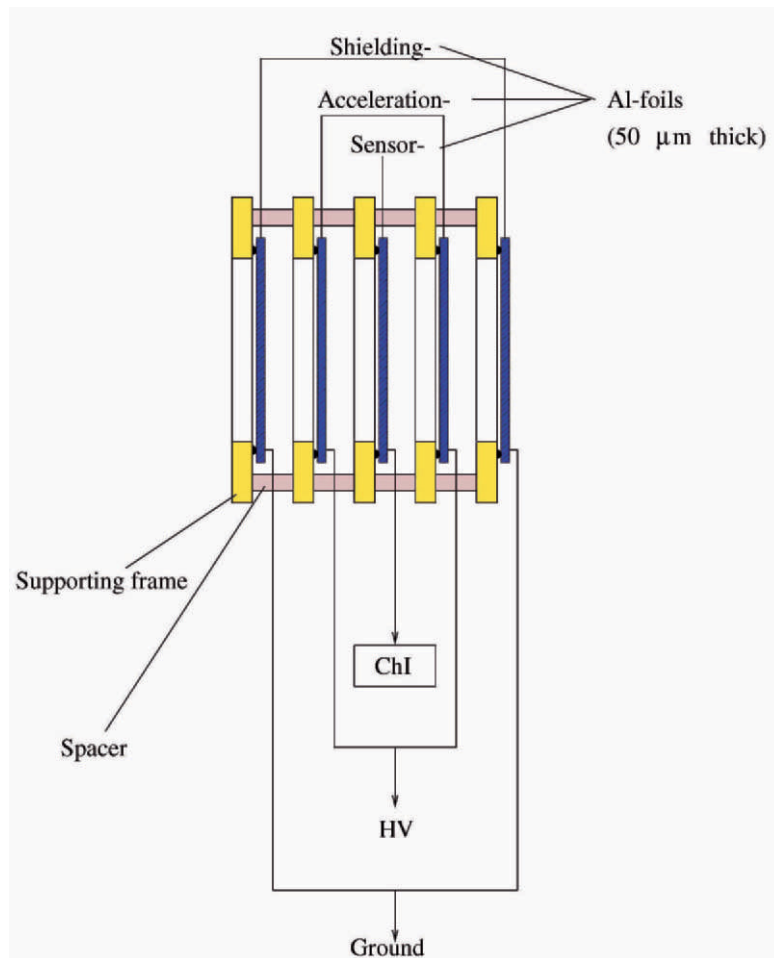


Figure 2. Five-layer MFD structure. ChI - charge integrator: HV - accelerating voltage.

charge at their input due to the leakage currents, temperature/humidity impact, r/f pick-up etc. The charge collection efficiency was significantly improved by placing from both sides of the sensor accelerating foils biased by positive voltage. To reduce the impact of external fields two additional (well-grounded) foils are the part of the final five-layer MFD structure.

The MFD sensitivity increased by a factor of 5 when ramping up the accelerating voltage from 0 to 20 V where it went into saturation [11] in a perfect agreement with the expected prevailing yield of low-energy secondary electrons. Five-layer MFD structure has been also applied for the measurement of the fluence distribution of 21 MeV protons (Tandem generator, M.P.I. für Kernphysik, Heidelberg) used for

the radiation hardness studies ([13]) of the HERA-B silicon microstrip detectors.

The multi-layer MFD technology of the MIP fluxes monitoring has been also implemented to build a Beam Profile Monitor (BPM) for characterization studies of the silicon microstrip detectors for the the LHCb Inner Tracker at CERN [12]. 16 X- and 16 Y-sensors (Al, 50 μm thick, 5 mm wide, 6 mm pitch) covering the area of 96 x 96 mm² were connected by 3 m long cables to Charge Integrators. The X- and Y-sensors were separated (3 mm distance) by accelerating and shielding Al foils.

The MFD monitor of much less size (32 Al strips, 10 μm wide with a 32 μm pitch deposited onto the 20 μm thick Si-wafer) has been designed and tested for the online control, positioning and focusing 32 MeV alpha-particles at the M.P.I. für Kernphysik (Heidelberg) Tandem generator for Single-Event-Upset studies of the BEETLE micro-chip.

4. MFD for the Radiation Monitoring at the LHCb experiment

Particle fluences expected at the LHCb are high enough to make a hazardous impact onto the performance of the LHCb Silicon Tracker [9] sensors as well as read-out electronics. In particular, the level of the radiation load in the region of the IT2-station will reach 60 kGy (after 10 years of operation). Silicon micro-strip sensors for the Silicon Tracker (ST) will be connected to the Beetle readout chip. Both these components should be protected against their loss as a result of an unexpected radiation incident (change of the beam trajectory, partial beam loss in the region of the detector etc.). Thus, it is necessary to measure an absorbed radiation dose on-line and archive the measured data necessary for adequate evaluation and tuning of the silicon sensor biasing voltage [13]. It is the task for the Radiation Monitoring System (RMS). The data measured by the RMS have to be transferred to the LHC and LHCb shift crews. Graphical User Interface will allow selection of the 'Nominal Interaction Rate', 'Warning' and 'ALARM' levels of the IR as well as 'Interaction Point' allowed range. The software for the ST RMS read-out electronics will allow for:

- Interaction Rate Monitoring;
- Interaction Point Monitoring;
- Generation of WARNING and ALARM messages;
- Tuning of the data taking periods;
- Monitoring/correction of the ChI baseline and/or background contribution;

RMS position at the IT-2 .

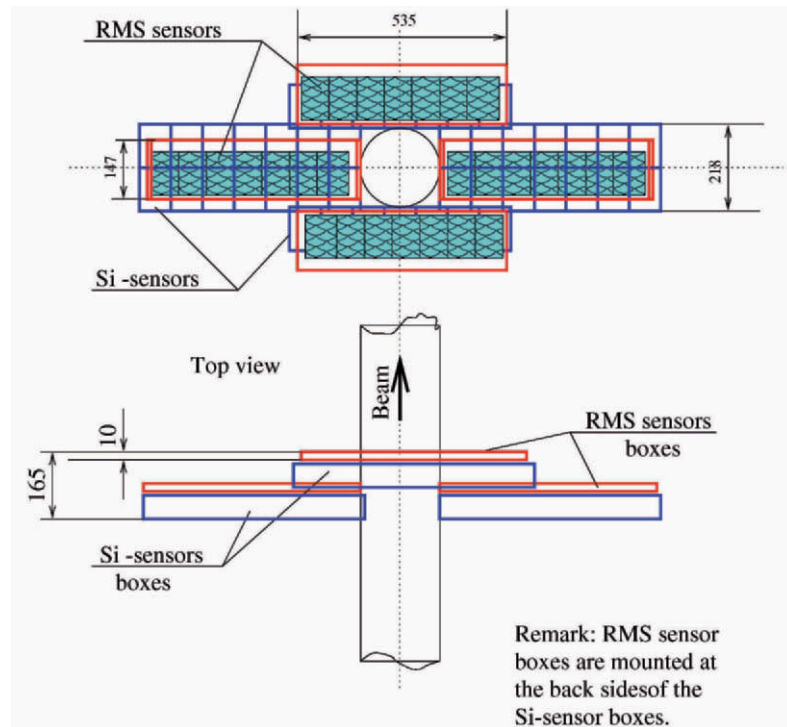


Figure 3. Schematic view of the RMS for the IT-2 station of the LHCb experiment.

- Background subtraction;
- On-line data presentation;
- Off-line data storage

The schematic view of the RMS for the IT-2 station of the LHCb experiment is shown in Fig. 3.

The 28 sensors of the RMS are read-out by the sensitive charge integrators. Currently used charge integrators have the sensitivity of 1 kHz per 1 pA, while their own output frequency fluctuations are at the level of 1-2 Hz. The output fluctuations of the charge integrator connected to a sensor by a long cable may increase up to ≈ 100 Hz due to shot noise as well as due to r/f pick-up and varying background contribution. Yet, it has been demonstrated that a correction for those factors is possible by measuring the MFD response during the time of a particles spill and between spills. This allows for the measurement of the fast charged particle fluxes exceeding $5 \times 10^3 \text{ s}^{-1}$ per MFD sensor.

The lowest expected flux at the silicon sensor of the IT-2 station is by an order of magnitude higher. Concerning the radiation hardness of the MFD readout electronics it is worthwhile to mention that the NIM crate with charge integrators used for the Luminosity monitor as well as for the HERA-B targets readout stood over 3 years of HERA-B operation in close vicinity to the Interaction Region (the accumulated dose at 1.5 m away from the target setup has been evaluated at the level of \approx few krad. There was no failure in the charge integrators operation induced by the radiation impact. The expected dose at the LHCb bunker after 10 years of operation will be in the range of few hundred rad, only.

Concerning the design of the Emergency RMS (ERMS) or Beam Conditions Monitor based on the MFD-sensors the MFD sensors manufactured out of 25 μm Al foils of two sizes, (78 x 110) mm^2 and (110 x 110) mm^2 , should be positioned symmetrically around the beam pipe and fixed at the forward/backward walls of the silicon boxes of the TT station. Such a geometry allows monitoring of the charged fluxes and rather precise monitoring of the beam conditions. In particular, any shift of the interaction point exceeding 10 μm could be recognized by the ERMS by means of the asymmetry method tested in HERA-B environment [14]. A sensitivity of the asymmetry method of the MFD Luminosity Monitor for different interaction point position (HERA-B targets separated in space by 3 mm) is illustrated in Fig. 4. Fig. 4 shows dependence of the Up-Down vs Left-Right asymmetries on the position of different targets. As one may see, there is an essential difference of the detector acceptance for different targets (up to \approx 7 %). There is a bias by \approx 20 % for the Left-Right asymmetry and \approx 6 % for the Up-Down asymmetry. The origin of this bias is in the non-axial beam position inside the beam-pipe. Thus, measuring this bias one can provide a permanent monitoring of the position of the Interaction Point in the (X - Y) plane. Comparing the measured data with the allowed region limits the ERMS could provide warning/alarm messages.

Below some figures are given for the radiation monitoring at the LHCb site for the emergency case. Currently used MFD have a sensitivity of 9 kHz per 1 MHz Interaction rate. Translating this into the number of counts per MIP one gets (from the HERA-B prototype and LHCb test beam studies) (3.0 +/- 0.3) *times* 10^{-2} counts/MIP. For the MFD output frequency fluctuations at the level of 150 Hz (20 m long, 5 mm in diameter coaxial cable between the sensor and charge integrator, or \approx 2000 pF) this means that the lowest detectable flux will be in the range of 5×10^3 MIP/s. Thus, if the LHCb Interaction Rate would grow up, let us say, to 100 MHz, the particle flux over

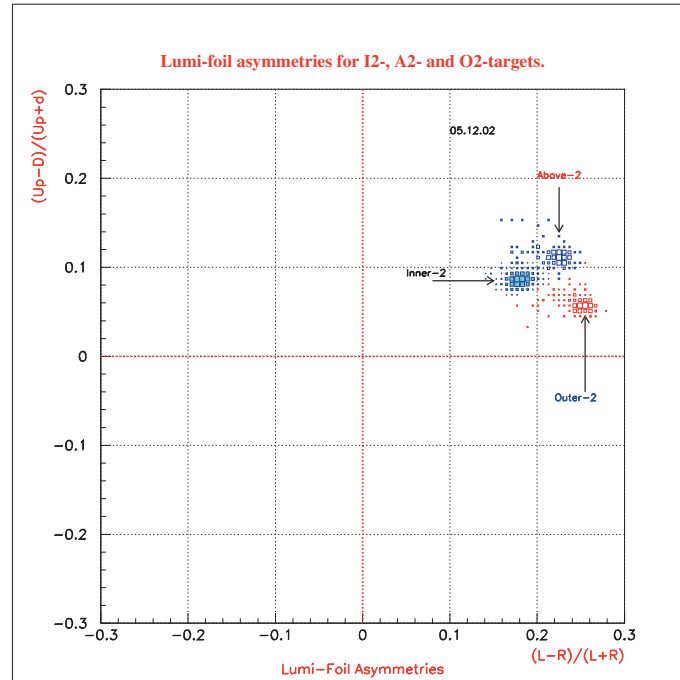


Figure 4. The asymmetries measured by the Up-Down and Left-Right sectors of the Metal Foil Detector monitoring ring.

the closest to the beam pipe RMS IT-2 sensor reaches the level of 1.2×10^8 MIP. Consequently, the output frequency of the corresponding charge integrator should be at the level of 3.6 MHz. For the integration over $40 \mu\text{s}$ this should produce 144 counts at the MFD output. This signal is large enough in comparison with expected natural fluctuations (few counts) to guarantee a proper indication of the emergency case. An aluminum ladder with two large area MFD ($40 \times 35 \text{ cm}^2$, each) has been built and tested as a prototype for the Emergency RMS. The metal frame with windows for the sensors has been strengthened by the nylon wires of 0.5 mm in diameter to support Al sensor as well as auxiliary foils ($25 \mu\text{m}$ thick). An electric contact to foils has been made by a silver glue (in addition fixed by an epoxy glue for mechanical rigidity). The ERMS was characterized at KINR by the intensive ^{90}Sr β -source and at the KINR LINAC test beam facility (5 MeV electron beam) having demonstrated the designed performance.

5. Micro-strip MFD for the Radiation Monitoring

There is an obvious request to focus the colliding beams at micrometer level to get the highest luminosity of the experiment. Many other developments in fundamental and applied research require non-destructive 'on-line' profile monitoring of micro-beams. For low intensity beams a proper approach could be realized by using silicon micro-strip detectors successfully progressing last two decades. Manufacturing technology allows for a position resolution at sub-micron level. Yet, radiation hardness aspect makes this approach rather limited. We report here briefly on the new approach to the microbeam profiling based on the micro-strip MFD technology. The sensors were prepared by means of micro-electronics technology and plasma-chemistry etching. To isolate a metal film from the wafer the dielectric layers were grown up on both sides of a wafer. At first, the silicon oxide (0.1 - 0.3 μm thick) was grown up covered later by 0.2 μm thick silicon nitride. A thin (0.1 μm) titanium layer was deposited onto dielectric layers. Afterward, nickel (0.5 μm) layers covered finally by silver layers (0.6 μm) served as films for the photo-lithography shaping of the strip pattern as well as contacting lines and pads. A window from the back side has been created for the plasma-chemistry etching. The KINR plasma-chemical reactor with variable ion energy has been used. The initial etching speed was in the range of 2.5 $\mu\text{m}/\text{min}$ at the ion energy of 80 eV and discharge current of 10 A. When the silicon wafer thickness approached 50-100 μm the etching speed was slowed down to 0.3 $\mu\text{m}/\text{min}$ by decreasing the current to 4 A and the ion energy to 20 eV. In this way the MMFD has been manufactured with 32 self-supporting strips (20 μm width, 70 μm pitch) which survived in the operating window with a diameter of 8 mm.

The strips were bonded to the ceramics based pitch adapter and connected by a flexible Kapton isolated cable to the 50 pin-connector and through the additional cable via the UHV feedthroughs to Charge Integrators housed inside the NIM crate (3 mm coaxial cables fed the signals from the flange with UHV feedthroughs). Fig. 5 shows the MMFD setup mounted on the ceramics and aluminium supporting frames together with 50-pin connector at its base. Tests performed at the Tandem Generator of the Max-Planck-Institut fuer Kernphysik (Heidelberg) as well as at the HASYLAB (DESY, Hamburg) have illustrated a reliable operation of the micro-strip MFD indicating that the thinnest detectors for the precise on-line radiation monitoring have become available [15].

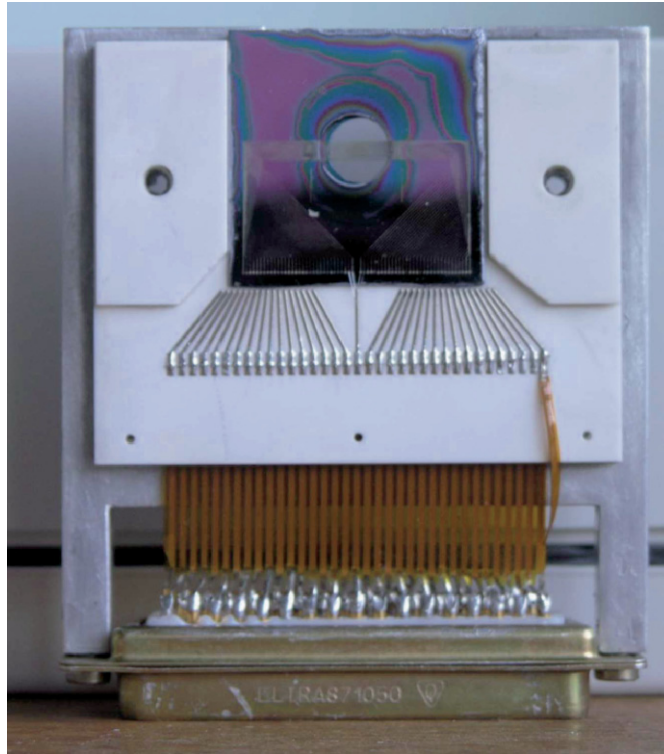


Figure 5. General view of the MMFD. Silicon substrates are glued to a ceramics supporting frames. Pitch adapting lines are made on the ceramics to feed the signals to/out strips via Kapton cable and 50-pin connector.

6. Conclusion

New type of the radiation monitoring systems based on the Metal Foil Detector technology has been successfully developed. The established advantages of the MFD for charged particle fluxes monitoring are as follows: extremely low mass (up to few tens nano-meter thickness) of the detecting material; simple structure (thin metal foils supported by the isolating frame); low operating voltage, which provides nearly total charge collection; simple read-out electronics (charge integrators and scalers); high radiation tolerance; perfect long term performance. The developed MFD technology proved to be a reliable tool for the charged particle radiation monitoring at colliders as well as in a wide range of other applications.

Acknowledgments

The author acknowledges the valuable contribution into the MFD preparation by the personnel of the Mechanical and Electronics workshops of the M.P.I. für Kernphysik, Heidelberg. The results presented are due to the effort of the HERA-B Target Group and the LHCb Silicon Tracker Group members, frank discussions with whom are appreciated. I use this opportunity to express the gratitude to the directorate of the Max-Planck-Institut für Kernphysik for the financial support and hospitality extended to me and my family during the course of these studies in Heidelberg.

References

- 1 <http://lhc-radwg.web.cern.ch/LHC-radwg/>
- 2 V. Pugatch et al., *Nucl. Instr. Meth.*, **A535** (2004) 566
- 3 E.J. Sternglass *Phys.Rev.*, **108** (1957) 1
- 4 H. Rothard, K.O. Groeneweld, J. Kemmler, in: *Springer Tracts in Modern Physics, Springer, Berlin*, (1992) 97
- 5 V.A. Vjalitsin, I.A. Prudnikov, I.R. Ryabuhov, *Pribori i Tehnika Eksperimenta*, **No. 3** (1967) 36
- 6 G.W. Tautfest, H.R. Fechter, *Rev. Sci. Instrum.*, **Vol. 26, No. 8** (1955) 229
- 7 E. Hartouni et al., HERA-B, *Technical Design Report*, DESY-PRC 95/01 (1995)
- 8 The LHCb Collaboration, *LHCb Inner Tracker Technical Design Report*, CERN/LHCC 2002-029, Nov. 8th, (2002) 83
- 9 The LHCb Collaboration, *LHCb Technical Design Report*, CERN/LHCC 2003-030, LHCb TDR 9, Sep. 9th, 2003
- 10 C. Bauer et al., *Nucl. Instr. Meth.*, **A 418** (1998) 65
- 11 V. Pugatch, K.T. Knoepfle, Yu. Vassiliev. *Nucl. Phys.* **A 701** (2002) 204
- 12 A. Franca Barbosa et al., LHCb Inner Tracker Technical Design Report, CERN/LHCC 2002-029, Nov. 8th, (2002)
- 13 V. Pugatch et al., *Nuovo Cimento*, **A 112** (1999)
- 14 C. Hast et al., *Nucl. Instr. Meth.*, **A354** (1995) 224
- 15 V. Pugatch et al., *European Workshop DIPAC-05. 6-8 June 2005, Lyon, France* (Proceedings to be published.)

AUTHOR INDEX

- A. Adamovich, 265–274
D. Anchishkin, 3–26
D. Artemenkov, 189–200
V. Babenko, 253–264
B. Barbashov, 125–136
D. Belozorov, 217–238
V. Bournos, 265–274
T. Čechák, 207–216
S. Chigrinov, 265–274
L. Davydov, 217–238
Yu. Fokov, 265–274
S. Fomin, 239–251
M. Gazdzicki, 27–39
M. Gorenstein, 49–67
V. Gulik, 235–263
L. Jenkovszky, 253–263
A. Kaidalov, 69–79
I. Karnaukhov,
A. Khilmanovich, 265–274
H. Kiyavitskaya, 265–274
J. Klusoň, 207–216
T. Korbut, 265–274
S. Korneev, 265–274
A. Koulikovskaya, 265–274
V. Kozhuharov, 81–90
B. Martsynkevich, 265–274
Yu. Mel'nik, 239–251
S. Lukashevich, 91–97
N. Maksimenko, 91–97
S. Mazanik, 265–274
I. Mishustin, 99–111
G. Orlova, 189–200
V. Pavlovich, 253–263
V. Pervushin, 125–136, 201–204
V. Pilipenko, 239–251
A. Polini, 137–147
V. Pugatch, 275–286
E. Pupirina, 253–263
C. Routkovskaia, 265–274
I. Serafimovich, 265–274
N. Shulga
V. Simak, 149–160
O. Utyuzh, 175–187
G. Wilk, 175–187
Z. Włodarczyk, 175–187
A. Zakharov, 125–136, 201–204
P. Zarubin, 189–200
V. Zinchuk, 125–136, 201–204

SUBJECT INDEX

- Actinides, 265, 271
- Accelerator, 34, 35, 36, 84, 113, 115, 116, 122, 137, 192, 253–255, 265, 267, 268, 269, 271, 273, 277
- ADS, 265–267, 269, 271, 273
- Background, 277, 278, 280, 281
- Beryllium, 84, 254, 258, 259, 261
- Baryon, 31, 32, 49, 61–63, 66, 99, 100, 110, 143
- Bootstrap, 50–59
- Bose-Einstein correlations, 175
- Clustering, 203
- Collider, 138, 149, 153, 159, 160, 275, 277, 285
- Compton scattering, 91, 92, 94,
- Critical point, 27, 50
- Deconfinement, 27, 49, 99
- Deep inelastic scattering, 69, 137
- Diffraction, 70, 73–75
- Dose, 207
- Duality, 161, 164
- Effective multigroup
 approximation, 239
- Elastic scattering, 69–71, 118, 137
- Emulsion, 203
- Factorization, 139
- Fast neutron reactor, 239
- Fission, 192, 240–244, 247, 248, 249, 256, 257, 259, 261, 265, 266, 271
- Flavour physics, 81
- Fluctuations, 27, 99, 175
- Fragmentation, 99, 189, 203
- Freeze-out, 5, 31–33, 107
- Fuel shortage, 217
- Generation III reactors, 217
- Generation IV reactors, 217
- Global warming, 217
- Gluon, 27, 28, 30, 32, 49, 50, 53, 54, 57, 59, 61, 63, 64, 66, 69, 70, 73, 75, 99, 106, 110, 138–140, 160
- Hadron, 161, 162, 166, 176, 178–181, 183, 185
- HERA, 70, 137
- Hydrodynamic equation, 3, 4, 12
- Kaon physics, 81
- MCNP, 254, 271, 272
- Meson, 5, 30, 81, 82, 105, 132, 140, 142, 169–171, 194–196, 266
- Multiplication factor, 254–257, 259
- Neutron flux, 241–258, 261, 262, 266, 270, 273
- Neutrons, 192, 240–243, 247, 253–255, 257, 258, 262, 265–272
- Non-stationary diffusion equation, 239
- Nuclear burning wave, 239
- Nuclear energy, 217
- Nuclear interactions, 69, 71, 76, 77, 198
- Nuclear power, 207, 210, 211, 217, 223, 226–231, 253, 262
- Nuclear power plant, 207
- Nuclear reactors, 217
- Nuclear safety, 205
- Nucleon, 5, 33–36, 44, 70–72, 74, 76, 91, 93, 94, 105, 107, 118, 175, 189, 190, 191, 193, 194, 197, 199

- Phase transition, 4, 25, 29, 30, 32, 49, 50, 52, 54, 56–59, 62–66, 99, 101, 102, 104, 107, 109, 110, 193, 198
- Photon, 44, 69, 70, 72–74, 83–85, 87, 88, 91, 92, 94, 95, 97, 137, 154, 201, 203, 207, 214, 215
- Pomeron, 70, 72–77
- QCD, 31, 32, 50, 63–70, 161, 163, 166
- Quantum chromodynamics, *see*
- Quark, 27, 28, 30, 32, 49, 50, 53, 54, 56, 57, 59, 61, 63, 64, 66, 69, 70, 72, 73, 75, 82, 100, 101, 105, 106, 110, 138–140, 143–145, 147, 149–158, 161–165, 169, 173
- Quark-gluon plasma, 27, 70, 99, 110
- Radioactive waste, 211, 213, 215, 253
- Rare decays, 81
- Rates portable monitor, 207
- Reflector, 253, 254, 258, 259, 261, 262, 270
- Regge trajectory, 73
- Relativistic nuclear collisions, 27
- Resonance, 15, 44, 55, 91, 143, 144, 169, 170–173, 195, 196
- RHIC, 27, 28, 30, 32, 35, 36, 37, 69, 71, 75–77, 104, 110
- Scintillation detector, 207
- Shadowing, 69–71, 74, 77
- Spend fuel, 207
- Spent fuel storage facility, 207
- Sub-critical systems, 265, 269, 271, 272
- Tensor meson, 169
- Transmutation, 253, 255, 265, 267, 271–273
- Uranium, 207–211, 221–224, 229, 240, 245, 251, 253–262, 269
- Uranium mining, 207
- Uranium ore, 207